University of Nevada, Reno

Cyclic Plastic Deformation, Fatigue, and the Associated Micro-Mechanisms in Magnesium: from Single Crystal to Polycrystal

A dissertation submitted in partial fulfillment of the

requirements for the degree of

Doctor of Philosophy in Mechanical Engineering

by

Qin Yu

Dr. Yanyao Jiang/Dissertation Advisor

December, 2014

THE GRADUATE SCHOOL

We recommend that the dissertation
prepared under our supervision by

QIN YU

Entitled

Cyclic Plastic Deformation, Fatigue, And The Associated Micro-Mechanisms In Magnesium: From Single Crystal To Polycrystal

be accepted in partial fulfillment of the
requirements for the degree of

DOCTOR OF PHILOSOPHY

Yanyao Jiang, Ph.D., Advisor

Kwang J. Kim, Ph.D., Committee Member

Kam K. Leang, Ph.D., Committee Member

Ronald F. Gibson, Ph.D., Committee Member

Dhanesh Chandra, Ph.D., Graduate School Representative

David W. Zeh, Ph. D., Dean, Graduate School

December, 2014

Abstract

Magnesium and its alloys have received substantial interests as the government initiatives on energy saving and environment protection demand an increasing use of lightweight materials in structural parts, especially in transportation industries. A good understanding of fatigue behavior in magnesium is critical to ensure the reliability and durability of the magnesium components. Unlike the body centered cubic and face centered cubic metals, fundamental knowledge concerning the cyclic deformation and fatigue in hexagonal close packed magnesium is limited. The current research aims at a better understanding of the micro-mechanisms associated with the cyclic deformation and fatigue of magnesium. Magnesium single crystal was chosen to study the fundamental twinning/detwinning process while extruded polycrystalline pure magnesium was studied for the fatigue damage mechanisms.

Cyclic deformation and the corresponding morphology evolution of $\{10\,\bar{1}\,2\}$ twinning–detwinning–retwinning are, for the first time, characterized in magnesium single crystal under fully reserved strain-controlled tension-compression utilizing *in situ* optical microscopy. As loading cycles are increased, the activity of twinning–detwinning–retwinning gradually decreases. Microscopy after fatigue shows that the matrix region having experienced repeated twinning-detwinning cannot be completely detwinned to its original crystal orientation. Fragmented secondary tension twins are found to result from twin-twin interactions. Various twin-twin interaction structures exist in fatigued magnesium single crystal: quilted-looking twin structure, "apparent crossing" twin structure, and double tension twin structure. According to the

crystallography of magnesium, twin-twin interactions are classified into Type I for two twin variants sharing the same <11$\bar{2}$0> zone axis and Type II for two twins with different zone axes. For Type I twin-twin interactions, one twin does not transmit across the twin boundary and into the other twin. For Type II twin–twin interactions, one twin can transmit into the other only under some special loading conditions. In most cases, twin transmission does not occur but, instead, twin-twin boundaries form that contain boundary dislocations.

The formation mechanism of the twin-twin boundary is proposed based on the reaction of twinning dislocations. Twin-twin boundary is a low-angle tilt boundary for Type I co-zone twin-twin interaction whereas it adopts a high-index crystallographic plane for Type II twin-twin interaction according to a geometry analysis. Twin-twin boundary dislocations can be inferred by reactions of twinning dislocations associated with the two twin variants. An "apparent crossing" twin structure is a consequence of twin-twin boundary formation. Under reversed loading subsequent to twinning, detwinning is retarded and secondary twinning can be activated at the twin-twin boundary for Type II twin-twin interaction.

The fatigue damage mechanisms in magnesium were studied in extruded coarse-grained polycrystalline pure magnesium through fully-reversed strain controlled tension-compression along its extrusion direction. Twinning/detwinning dominates the cyclic deformation at high strain amplitudes while dislocation slips are responsible for the cyclic deformation at low strain amplitudes. Microcrack initiation and early-stage crack growth strongly depend on cyclic loading magnitude. During most of fatigue life at twinning-dominated strain amplitudes, microcracks are incessantly initiated with

limited propagation on both grain boundary and twin boundary. At slip-dominated strain amplitudes, microcracks are initiated predominantly by grain boundary cracking. Both intergranular and transgranular modes are observed for early-stage crack propagation. Early-stage transgranular propagation is dominated by cracking at twin boundaries at twinning-dominated strain amplitudes. At dislocation slip-dominated strain amplitudes, early-stage transgranular propagation is found to occur on the $\{\bar{1}2\bar{1}0\}$ crystal planes, which is driven by alternative slip mechanism on two sets of second-order pyramidal <*a*> slip system.

Dedication

To my beloved parents, father Mr. Shiwang Yu and mother Mrs. Youqin Qin.

Acknowledgment

I must first express my earnest gratitude to my advisor, Professor Yanyao Jiang. I owe huge debts of gratitude to Professor Jiang in every sense during the past seven years. His professional expertise, enthusiastic dedication, inspiring advice, sustaining encouragement, considerate care, and greatest tolerance have been deeply imprinted on my heart and cannot be erased from the memory in my remaining life. Professor Jiang not only teaches me knowledge but also nourishes me with the meaning of life. My next deepest acknowledge must be given to Dr. Jian Wang, my mentor at Los Alamos National Laboratory (LANL). Dr. Wang's insightful advice, patient tutoring, and generous support to me can never be overestimated. This dissertation work can never be accomplished without Professor Jiang and Dr. Wang. My sincere thanks go to Dr. Ronald F. Gibson, Professor Dhanesh Chandra, Professor Kwang J. Kim, Professor Kam K. Leang, for all the advice and helps they provide to current research, and for serving as the dissertation committee members.

I would like to show my warmest appreciation and gratitude to Dr. Carlos N. Tom é at Los Alamos National Laboratory (LANL), for the inspiring and creative discussion between us, for his continuous encouragement, and for his generous support. I would like to thank Dr. Rodney J. McCabe at Electron Microscopy Laboratory (EML), Los Alamos National Laboratory (LANL), for his kindness in helping me with microscopy experiments, and for his continuous encouragement. I would also like to thank Dr. Nan Li at Center for Integrated Nanotechnologies (MPA-CINT), Los Alamos National Laboratory (LANL), for every help he provided to me in carrying out microscopy experiments.

My sincere gratefulness is given to Dr. Jixi Zhang. I cannot forget the constructive discussion, continuous encouragement, and every help that Dr. Zhang has provided me, during his stay as a postdoctoral scholar at the University of Nevada, Reno (UNR). Special thanks go to Dr. Sergiy Kalnaus at Oak Ridge National Laboratory (ORNL). As a former senior group member in Mechanical Behavior Laboratory (MBL) at UNR, Dr. Kalnaus is always ready to offer helps and suggestions which I must appreciate sincerely. I would like to express my gratitude to all the other group members in Mechanical Behavior Laboratory (MBL), Dr. Fei Ding, Dr. Tianwen Zhao, Dr. Miaolin Feng, Dr. Ying Xiong, Dr. Rong Zhu, Dr. Sanlong Zheng, Dr. Fenghua Wang, Ms. Feifei Fan, Mr. Shuai Dong, Mr. Mark Wehner, Mr. Conan Song, and Mr. Jimmie Mar, for the friendship and their kind helps during the past seven years. Mr. Tony Berendsen is acknowledged for his expertise and effort in helping machining the gripping system and the testing specimen. I am also thankful to all my friends at Los Alamos National Laboratory (LANL), Dr. Hui Li, Dr. Shengtai Li, Dr. Shihai Feng, Dr. Yongqiang Wang, Dr. Huamiao Wang, Dr. Cheng Sun, Dr. Shuai Shao, Dr. Weizhong Han, Dr. Shijian Zheng, Dr. Li Chen, and Dr. Yun Xu, for their kindness, and all the considerate care and helps.

Financial support provided by the Office of Basic Science (DE-SC0002144 and W-7405-ENG-36) is gratefully acknowledged. Current research also benefits from the use of Center for Integrated Nanotechnologies (CINT) Sandia Core Facility, under user proposal (RA2013A0027).

Finally, the utmost acknowledge goes to my beloved parents, father Mr. Shiwang Yu and mother Mrs. Youqin Qin, and my aunt Mrs. Fengzhu Yu. I owe enormous

debts of gratitude to their sustainable support and encouragement. Their love and sacrifice deserve far more than what I can return.

Table of Contents

List of Tables

List of Figures

Nomenclature

$\mathbf{a_1},\mathbf{a_2},\mathbf{c}$	Basis vectors for the rhombohedral system
$\mathbf{a_1},\mathbf{a_2},\mathbf{a_3},\mathbf{c}$	Basis vectors for the hexagonal system
$\mathbf{A_1^*},\mathbf{A_2^*},\mathbf{C}^*$	Reciprocal basis vectors for the rhombohedral system
$\mathbf{a_1^*},\mathbf{a_2^*},\mathbf{a_3^*},\mathbf{c}^*$	Reciprocal basis vectors for the hexagonal system
a	Norm of basis vectors ($\mathbf{a_1},\mathbf{a_2},\mathbf{a_3}$) in the rhombohedral and hexagonal systems
A_{twin}	Twin area fraction
b_l	Burgers vector of the impinged twining dislocation
b_A	Burgers vector of the TTB_A boundary dislocation
b_O	Burgers vector of the TTB_O boundary dislocation
$b_{tw}^{T_i}$	Burgers vector of the primary twinning dislocation
$b_{tw}^{T_{ij}}$	Burgers vector of the secondary twinning dislocation
b_r	Burgers vector of the residual dislocation
$BG(\varphi)$	Background error in the measured pole intensity
c	Norms of the basis vector ($\mathbf{c}$) in the rhombohedral and hexagonal systems
d_{HKL}	Interplanar spacing of a set of $(H\ K\ L)$ crystal planes

$\mathbf{e_1},\mathbf{e_2},\mathbf{e_3}$	Basis vectors for the orthonormal coordinate system to represent the crystal coordinate system
f_{twin}	Twin volume fraction
$(H\ K\ L)$	Miller indices in the reciprocal lattice to represent a set of crystal plane
$\{H\ K\ L\}$	Miller indices to represent a family of crystal planes which are equivalent with respect to a crystal symmetry
$(h\ k\ i\ l)$	Miller-Bravais indices in the reciprocal lattice to represent a set of crystal plane
$\{h\ k\ i\ l\}$	Miller-Bravais indices to represent a family of crystal planes which are equivalent with respect to a crystal symmetry
$I_{meas}(\varphi,\psi)$	Measured pole intensity
$I_{corr}(\varphi,\psi)$	Corrected pole intensity
$I_{norm}(\varphi,\psi)$	Normalized pole intensity
K_1	Twinning plane
K_2	Conjugate twinning plane
ΔK	Stress intensity factor range
$\mathbf{L}$	Transformation matrix from the rhombohedral coordinate system ($\mathbf{a_1},\mathbf{a_2},\mathbf{c}$) to the orthonormal coordinate system ($\mathbf{e_1},\mathbf{e_2},\mathbf{e_3}$)
m_i	Unit vector of the slip/twinning plane normal with respect to the sample coordinate system
M	Matrix region

n_i	Unit vectors of the slip/twinning direction with respect to the sample coordinate system
$N(hkil)$	Normal of the X-ray diffraction plane
N_{sep}	Separation fatigue life
$\mathbf{r}$	Arbitrary direction in the direct lattice
$\mathbf{r}^*$	Vector in the reciprocal lattice lies along the normal of a set of parallel planes (HKL) in the direct lattice
$(\mathbf{r}, \theta)$	Angle/axis pair to represent an orientation
S	Plane of twinning shear
s	Magnitude of twinning shear
S_i	Secondary twin region
T_i	Primary tension twin variant
T_{ij}	Secondary tension twin variant
$[U\,V\,W]$	Miller indices in the direct lattice to represent an arbitrary direction
$\langle U\,V\,W \rangle$	Miller indices to represent a family of directions which are equivalent with respect to a crystal symmetry
$[u\,v\,t\,w]$	Miller-Bravais indices in the direct lattice to represent an arbitrary direction
$\langle u\,v\,t\,w \rangle$	Miller-Bravais indices to represent a family of directions which are equivalent with respect to a crystal symmetry
$U(\varphi)$	Defocusing error in the measured pole intensity

$\mathbf{x}, \mathbf{y}, \mathbf{z}$	Basis vectors for the orthonormal coordinate system to represent the sample coordinate system
β_i	Geometry factor to represent the thickness of a tension twin variant
$\overline{\beta}$	Geometry factor to represent the twin thickness averaged among six tension twin variants
δ_{ij}	Kronecker delta
$\varepsilon_{p,mean}$	Mean plastic strain in a loading cycle
η_1	Twinning direction
η_2	Conjugate twinning direction
σ_{twin}	Stress at the mean plastic strain in the twinning reversal
σ_{detwin}	Stress at the mean plastic strain in the detwinning reversal
$\left(\frac{d\sigma}{d\varepsilon_p}\right)_{twin}$	Plastic moduli at the mean plastic strain in the twinning reversal
$\left(\frac{d\sigma}{d\varepsilon_p}\right)_{detwin}$	Plastic moduli at the mean plastic strain in the detwinning reversal
$(\varphi_1, \Phi, \varphi_2)$	Bunge Euler angles
φ	Azimuth angle
ψ	Polar angle

1. Introduction

Magnesium, as the lightest structural metal with a density of 1.74 g/cm^3, is the third-most-used structural metal, following iron and aluminum [1, 2]. The density of magnesium is only 22 percent as that of iron (7.87 g/cm^3) and 64 percent of aluminum (2.70 g/cm^3). Two forms of magnesium alloys can be processed: casting and wrought (rolled, extruded, and forged). Compared to the casting counterpart, a wrought magnesium alloy is usually free of casting defects, exhibiting higher mechanical strength and superior fatigue resistance [3, 4]. In addition, wrought magnesium alloys possess multiple intriguing physical and mechanical properties such as excellent thermal conductivity, high strength-to-weight ratio, excellent damping capability, and good recyclability. All of these characteristics make magnesium and its alloys potential lightweight structural materials in aircraft, automotive, and electronics industries [5, 6].

Despite a rising interest in magnesium alloys, main restrictions for wrought magnesium alloys to be widely utilized are their low ductility and poor formability at room temperature [1, 2]. With a hexagonal close packed (HCP) crystal structure, magnesium has a reduced number of slip systems compared to body centered cubic (BCC) and face centered cubic (FCC) metals. The limited slip systems make plastic deformation in magnesium more difficult. To maintain the compatibility of local plastic deformation, twinning is usually activated as an additional deformation mechanism. The combined effects of two major inelastic deformation modes and their interactions result in unique mechanical responses under monotonic loading: tension-compression yielding asymmetry [7], anisotropic plastic hardening [8], and low

ductility [9, 10]. Such an unusual plastic behavior of wrought magnesium alloys and a low room-temperature formability are not desirable for engineering applications. However, the potential benefits in energy saving and environment protection continue to drive research and development in magnesium alloys particularly in aerospace and automobile industries [5, 6].

1.1 Significance and Motivation

When wrought magnesium alloys are used as structural components in transportation industries, the parts in service are inevitably subjected to repeated loading. Cyclic loading will induce localized permanent structural changes in the material. Progressive accumulation of such irreversible structural changes will result in initiation and growth of microcracks and eventually lead to final failure of the structural component [11–15]. Fatigue failure can bring about catastrophic incidents that cost billions of dollars and losses of human lives. Therefore, to ensure the reliability and durability of magnesium structural components, it is vital to understand the inelastic deformation and failure mechanisms of magnesium under cyclic loading.

In the last two decades, common characteristics of cyclic deformation of wrought magnesium alloys were extensively studied and identified, including the asymmetric stress-strain hysteresis loop, the mean stress effect, and the pseudoelasticity phenomenon. These macroscopic features of cyclic plasticity in magnesium are mainly attributed to the operation of a critical deformation mechanism: twinning/detwinning process. Although some efforts have been made to study the role of twinning/detwinning process on cyclic deformation of magnesium alloys, most of the work was limited to microscopic examinations of twins after fatigue loading. The only

work which links cyclic deformation with the real-time twinning/detwinning behavior was conducted by Wu et al. [16, 17] in ZK60 magnesium alloy utilizing *in situ* neutron diffraction technique. The neutron beam characterizes a three-dimensional material volume which contains millions of grains. The experimentally obtained *in situ* twinning/detwinning evolution reflects a statistical response averaged on a volume of many grains. No information regarding the kinetic evolution of twinning/detwinning process together with the twin-twin interaction under cyclic loading were revealed. Therefore, there exists a tremendous gap between the macroscopic observations of cyclic deformation of magnesium and the detailed localized fundamental microscopic mechanisms.

On the aspect of fatigue damage mechanisms in magnesium, several experimental observations and analyses were made on crack initiation and propagation in magnesium alloys experienced high-cycle fatigue [18–21]. Most of the experimental observations were made on the testing specimen after fatigue fracture occurred. Therefore, controversies exist in the modes of crack initiation and propagation. There is no clear picture showing the fatigue damage development in magnesium and its associated mechanisms under cyclic loading magnitudes dominated by different cyclic deformation mechanisms.

1.2 Research Objectives and Outlines

The current research aims to investigate the principle microscopic mechanisms responsible for cyclic plastic deformation and fatigue failure in magnesium. Emphases are placed on a fundamental understanding of the twinning/detwinning process in magnesium, and to obtain a clear picture of fatigue damage processes associated with

different cyclic deformation mechanisms in magnesium. The following goals are expected to be achieved:

I. To explore the local twin structure changes and their interactions related to the twinning/detwinning process in magnesium.
II. To analyze the microscopic process related to the formation and interaction of the observed twin structures and to address their effects on the macroscopic responses of cyclic deformation in magnesium.
III. To clarify the fatigue damage processes in magnesium under cyclic loading at magnitudes dominated by different controlling mechanisms.
IV. To explore major modes of microcrack initiation and early-stage propagation and to study the mechanisms responsible for these modes.

It is expected that experimental characterization and theoretical analysis of the microstructural changes will enhance the understanding of fundamental physical processes underlying cyclic deformation and fatigue in magnesium. The revealed micro-mechanisms are also anticipated to be implemented into physical-mechanism based constitutive model and fatigue model to better predict the mechanical behavior in HCP materials under cyclic loading condition.

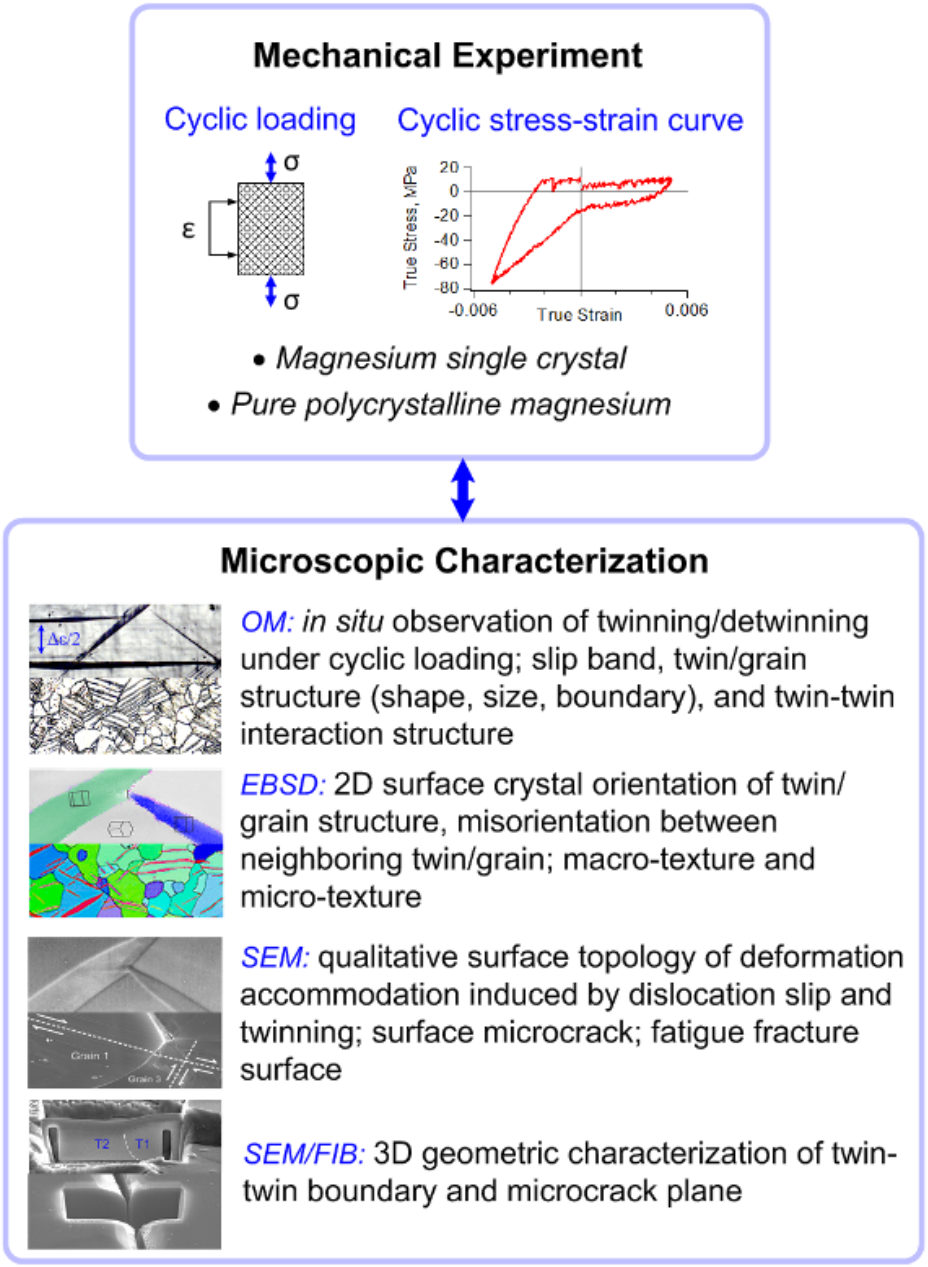

Figure 1 Schematic illustration of tasks and methods in current research.

To achieve these goals, experimental efforts are made in two interrelated parts: mechanical experiment and microscopic characterization. Figure 1 shows the major experimental methods that are used in current research. To reveal the detailed twinning/detwinning process, magnesium single crystals oriented for easy twinning

and detwinning were chosen as the study material subjected to fully reversed strain controlled tension-compression utilizing *in situ* optical microscopy (OM) technique. Cyclic stress-strain curve for tension twinning/detwinning were measured. The real-time evolution of twin structure were directly observed. Local geometric and crystallographic information regarding twin structures and their interaction were further revealed in companion specimens by utilizing advanced microscopy techniques such as scanning electron microscopy (SEM), electron backscatter diffraction (EBSD), and SEM/focused ion beam nanofabrication (SEM/FIB). To investigate the fatigue mechanism in magnesium, fully reversed tension-compression experiments were carried out in extruded coarse-grained polycrystalline pure magnesium at strain amplitudes dominated by different deformation modes. The development of fatigue damage were studied by charactering microcracks on companion testing specimens interrupted at different stages of fatigue life. With detailed crystallographic and geometric analysis, mechanisms of fatigue crack initiation and early-stage propagation in magnesium were enlightened.

The main content of the dissertation is divided into three parts. In the first part (Chapter two), the crystallography and plastic deformation modes in magnesium are described. Historic and current research status in twin-twin interaction is examined. The state of the art of plastic deformation and fatigue in magnesium single crystal and magnesium polycrystal is also described in Chapter two.

In the second part (Chapter three), mechanical experiments and microstructure observations for magnesium single crystal subjected to cyclic tension-compression are described. Characteristics of cyclic deformation and the corresponding *in situ*

observations of twinning/detwinning behavior are presented. After the termination of the cyclic loading experiment, microscopic features of microcracks, slip band extrusion, residual twins, and twin-twin interaction structures are examined. In Chapter four, detailed theoretical analysis of twin-twin interaction is carried out based on crystallography of magnesium and the dislocation theory. The feasibility of twin transmission in magnesium is clarified. The formation mechanism and the configuration of twin-twin boundaries are studied. Influences of twin-twin boundary on the subsequent twinning and detwinning process are also discussed.

The third part (Chapter five) describes the fatigue damage development in extruded coarse-grained polycrystalline pure magnesium by using companion specimens interrupted at different stages of fatigue life. Development of microcracks from initiation to final fracture are obtained at two strain amplitudes dominated by different cyclic deformation mechanisms. Modes of crack initiation and early-stage propagation in magnesium are summarized. Possible micro-mechanisms associated with the microcrack initiation and early-stage propagation are proposed with an emphasis on their dependence of the cyclic loading magnitude.

Conclusions obtained from the research are summarized in Chapter six. Recommendations for future research related to magnesium are outlined.

2. Literature Review

2.1 Crystallography and Deformation Modes in Magnesium

2.1.1 Crystallography of Magnesium

Magnesium has a hexagonal close packed (HCP) crystal structure. Its direct lattice with one atom at each point is visualized in Figure 2 [22]. The primitive hexagonal unit cell has three basis vectors $\mathbf{a_1},\mathbf{a_2},\mathbf{c}$ in the rhombohedral system. With $|\mathbf{a_1}| = |\mathbf{a_2}| = a = 3.203$ Å and $|\mathbf{c}| = c = 5.200$ Å, the c/a ratio is 1.624. Two atoms are positioned in the primitive unit cell at coordinates 0 0 0 and $\frac{2}{3}\frac{1}{3}\frac{1}{2}$ in the rhombohedral system. If all the atoms are assumed to be hard spheres, the hexagonal structure can generate a stacking sequence of ABABAB (Figure 2a). When these hard spheres are closely packed, the ideal c/a ratio is $\sqrt{8/3} = 1.633$. It is obvious that the c/a ratio (1.624) of magnesium is smaller than the ideal c/a ratio (1.633). A description of the representations of crystal direction and crystal plane in HCP crystal structure is presented in Appendix A.1.

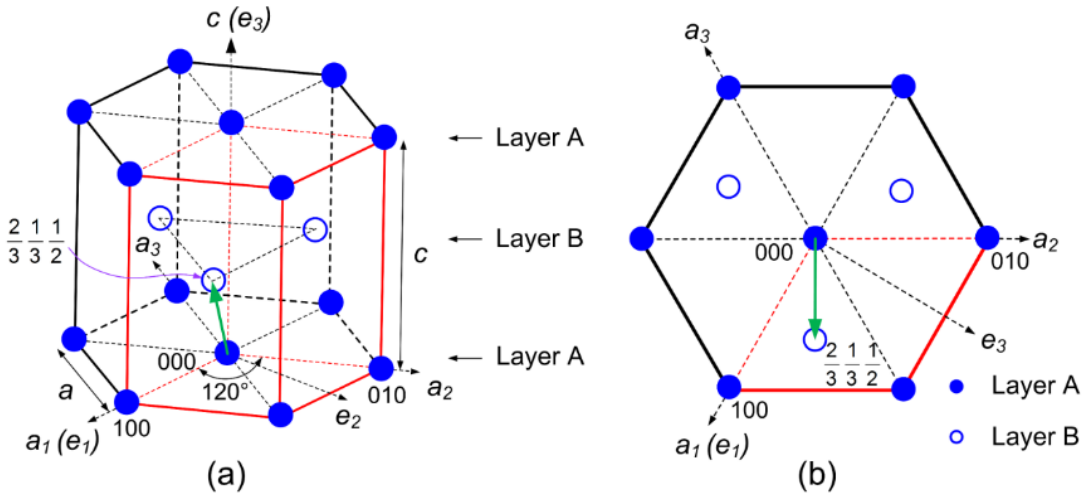

Figure 2 Hexagonal close packed crystal structure of magnesium (primitive hexagonal unit cell is outlined in red color) [22]: (a) three-dimensional view; (b) two-dimensional projection on the basal plane.

Three important zone axes exist in magnesium [22]: $\langle 0001 \rangle$, $\langle 10\bar{1}0 \rangle$, and $\langle \bar{1}2\bar{1}0 \rangle$. The three zone axes and their associated zone planes are schematically shown in Figure 3 and listed in Table 1. The $\langle 0001 \rangle$ zone includes all the $\{hki0\}$ planes that are perpendicular to the basal plane. The $\langle \bar{1}2\bar{1}0 \rangle$ zone contains all the $\{10\bar{1}n\}$ planes (Figure 3b) naming Type I planes. When $n=0$, the $\{10\bar{1}0\}$ planes are called the prism planes of Type I. The $\langle 10\bar{1}0 \rangle$ zone contains all the $\{1\bar{2}1n\}$ planes (Figure 3c), referred to as Type II planes. When $n=0$, the $\{1\bar{2}10\}$ planes are called prism planes of Type II. If n is not equal to zero, the $\{10\bar{1}n\}$ and $\{1\bar{2}1n\}$ planes are known as pyramidal planes of Type I and Type II, respectively.

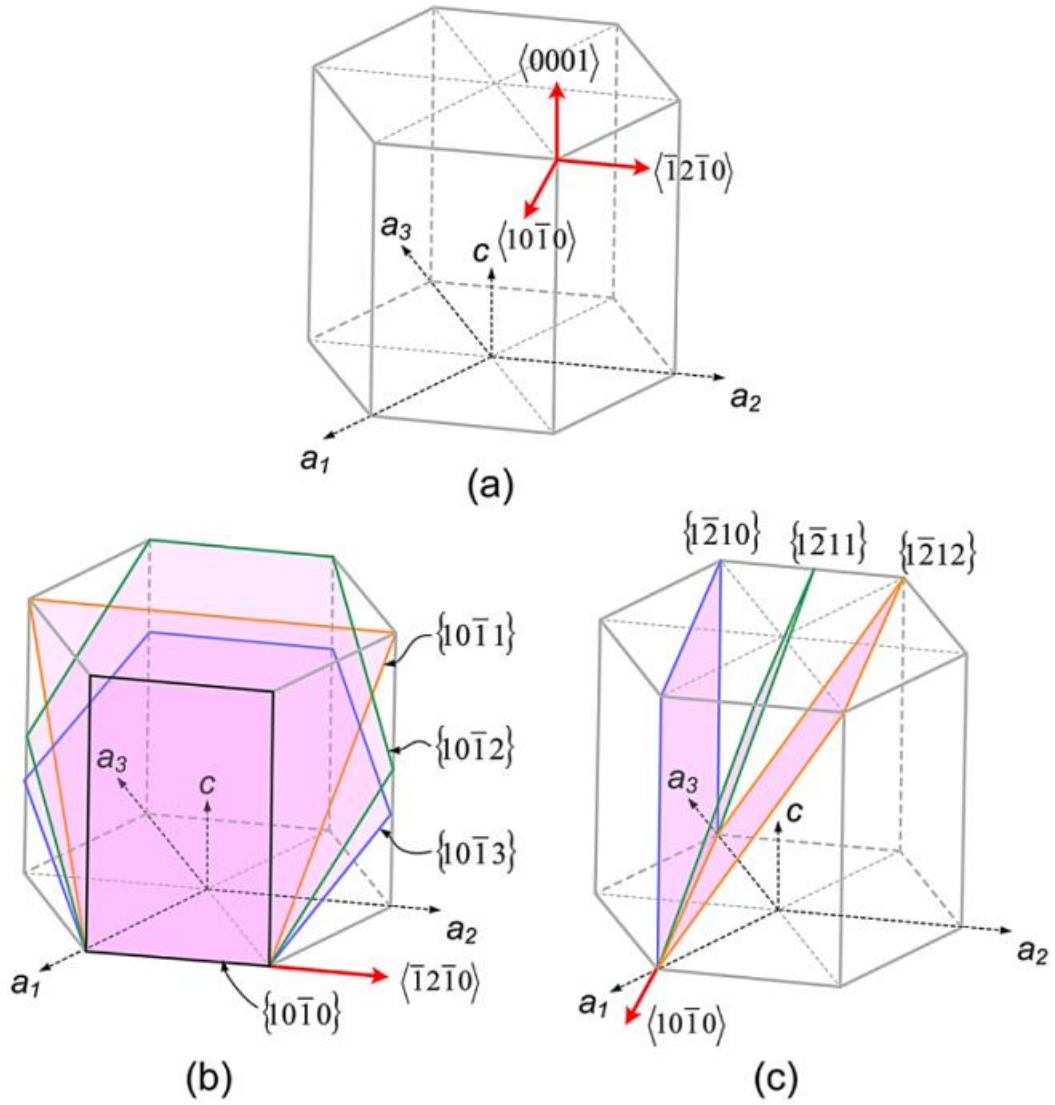

Figure 3 Important zone axes and zone planes in magnesium [22]: (a) three important zone axes $\langle 0001 \rangle$, $\langle \bar{1}2\bar{1}0 \rangle$, and $\langle 10\bar{1}0 \rangle$; (b) $\langle \bar{1}2\bar{1}0 \rangle$ zone axis and the associated $\{10\bar{1}n\}$ zone planes; (c) $\langle 10\bar{1}0 \rangle$ zone axis and the associated $\{1\bar{2}1n\}$ zone planes.

Table 1 Important zone axes and zone planes in magnesium [22].

Zone axes	Zone planes	Specific planes	Plane name	Type
$\langle 0001 \rangle$	$\{hki0\}$	-	-	-
$\langle \bar{1}2\bar{1}0 \rangle$	$\{10\bar{1}n\}$	$\{10\bar{1}0\}$	Prism	I
		$\{10\bar{1}1\}$	1st-order pyramidal	
		$\{10\bar{1}2\}$	2nd-order pyramidal	
		$\{10\bar{1}3\}$	3rd-order pyramidal	
$\langle 10\bar{1}0 \rangle$	$\{1\bar{2}1n\}$	$\{1\bar{2}10\}$	Prism	II
		$\{1\bar{2}11\}$	1st-order pyramidal	
		$\{1\bar{2}12\}$	2nd-order pyramidal	

2.1.2 Slip Modes in Magnesium

Common slip modes (or systems) in magnesium at room temperature are $<11\bar{2}0>$ ($<a>$) slip on the $\{0001\}$ basal plane, $<11\bar{2}0>$ ($<a>$) slip on the $\{10\bar{1}0\}$ prism plane, $<11\bar{2}0>$ ($<a>$) slip on $\{10\bar{1}1\}$ first-order pyramidal plane, and $<11\bar{2}3>$ ($<c+a>$) slip on $\{11\bar{2}2\}$ second-order pyramidal plane [22, 23]. The slip direction and slip plane for each slip system are visualized in Figure 4. The experimentally obtained values of the critical resolved shear stress (CRSS) associated with each slip system are also listed in Table 2. For arbitrary homogeneous deformation having its component along the *c*-axis, five independent slip systems must be activated according to the von Misses criterion [24]. Figure 4 shows that the basal $<a>$, prism $<a>$, and first-order pyramidal $<a>$ slip systems allow for plastic accommodation only within

the basal plane. Henceforth, the $<c+a>$ type slip must be activated. Nevertheless, as listed in Table 2, the ratio of the CRSS for the nonbasal $<c+a>$ slip over that for the basal slip is in the order of 10^2, which means that the nonbasal $<c+a>$ slip is very difficult to be activated at room temperature. Noting that the CRSS for tension twinning is ~2 MPa [25], tension twinning is usually activated instead of the nonbasal $<c+a>$ slip to accommodate the deformation along the *c*-axis.

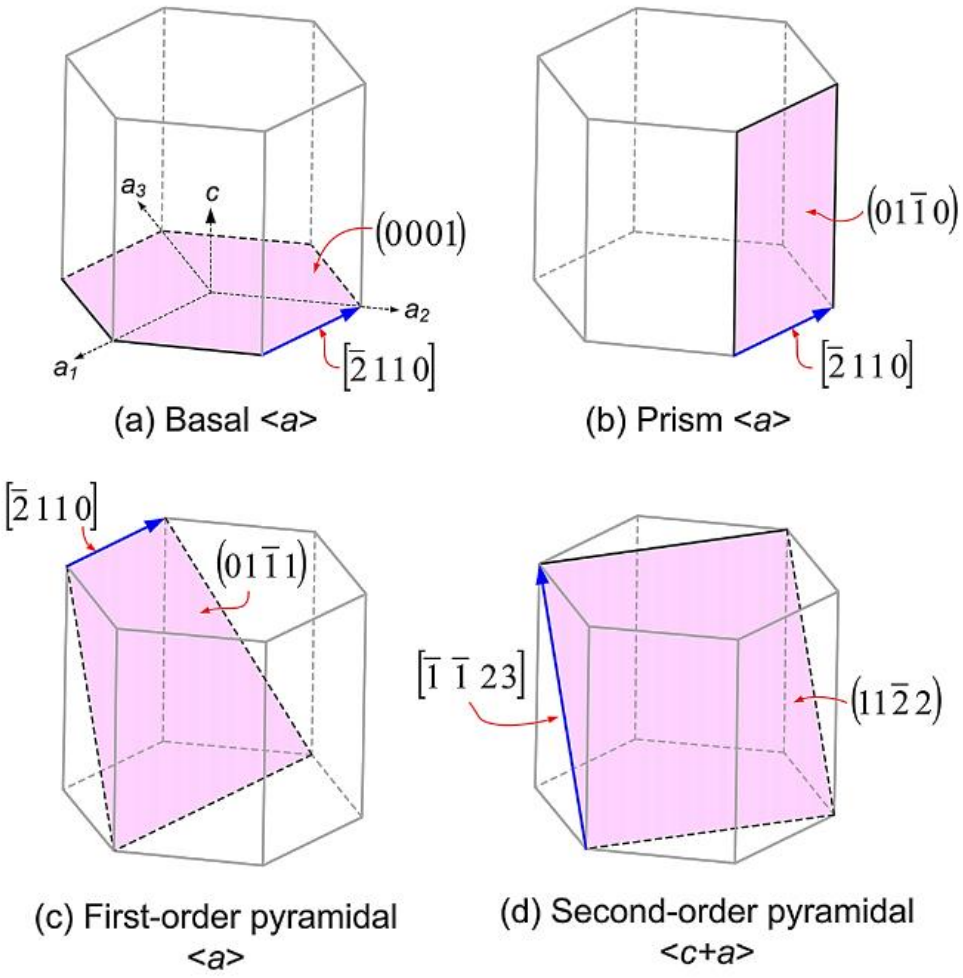

Figure 4 Typical slip modes (or systems) in magnesium [22, 23] at room temperature: (a) basal $<a>$; (b) prism $<a>$; (c) first-order pyramidal $<a>$; (d) second-order pyramidal $<c+a>$.

Table 2 Typical slip systems and their critical resolved shear stress in magnesium at room temperature [22, 23].

Burgers vector type	Slip system	Slip direction	Slip plane	Independent number of slip system	CRSS (MPa) at 300 °K
$<a>$	Basal $<a>$	$<11\bar{2}0>$	$\{0001\}$	2	0.81 [26] 0.76 [27] 0.45 [28] 0.78 [29] 1.07 [30]
	Prism $<a>$	$<11\bar{2}0>$	$\{10\bar{1}0\}$	2	39.2 [31] ~18 [32] ~8 [33]
	First-order pyramidal $<a>$	$<11\bar{2}0>$	$\{10\bar{1}1\}$	4	3.92 [27] 0.51 [28]
$<c+a>$	Second-order pyramidal $<c+a>$	$<11\bar{2}3>$	$\{11\bar{2}2\}$	5	~40 in Figure 12 [34]

2.1.3 Twinning Modes in Magnesium

In addition to dislocation slips, twinning is another important inelastic deformation mode associated with lattice shear. Figure 5 schematically illustrates the difference between the shear accommodation by dislocation slips and that by twinning. Unlike the shear caused by dislocation slips, the shear deformation induced by twinning is uniformly distributed over a reoriented crystal volume rather than localized on discrete slip planes [35]. Detailed discussions of the crystallography of twinning were covered

by papers of Cahn [36], Partridge [22], and recently Christian and Mahajan [37]. The following brief description of crystallography of twinning and twinning elements is based on these review papers.

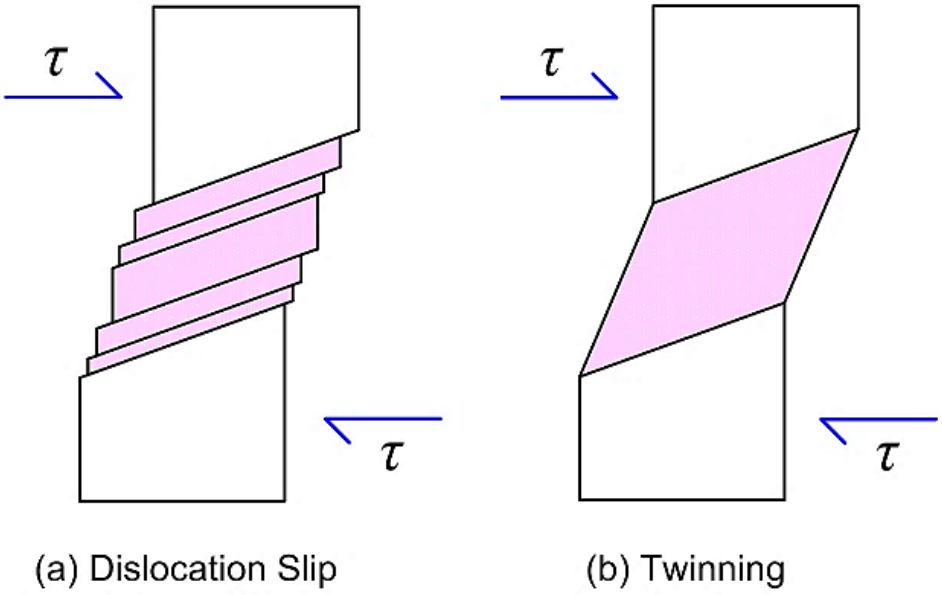

Figure 5 Schematic illustration of difference between shear deformation associated with dislocation slips (a) and twinning (b) [35].

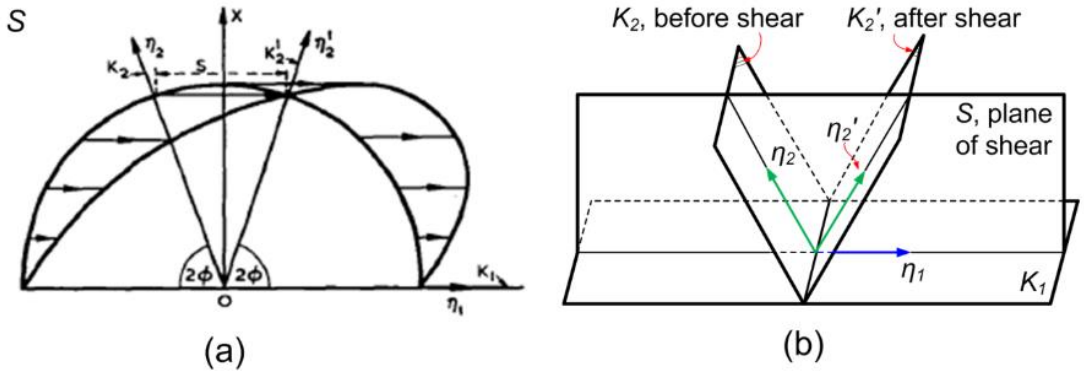

Figure 6 Twinning elements associated with the original sphere and the distorted ellipsoid caused by the twinning shear [22, 35]: (a) projection onto the plane of shear, *S*; (b) three-dimensional view.

As schematically illustrated in Figure 6, twinning shear brings about a distortion of the original sphere (the matrix lattice) into an ellipsoid (the twin lattice). There are four twinning elements associated with the original sphere and the distorted ellipsoid: plane K_1, direction η_1 lying on plane K_1, plane K_2, and direction η_2 lying on plane K_2. Twinning shear aligns along the η_1 direction within plane K_1. Plane K_1 and direction η_1 are referred to as the twinning plane and the twinning direction, respectively. The K_1 plane remains undistorted after twinning. Plane K_2 and direction η_2 are the conjugate twinning plane and the conjugate twinning direction, respectively. After twinning shear, plane K_2 and direction η_2 are rotated to plane $K_2^{'}$ and direction $\eta_2^{'}$ in the twinned lattice and both keep undistorted. As seen in Figure 6b, direction η_2 is rotated to direction $\eta_2^{'}$ lying on plane *S*. Plane *S* is called "plane of twinning shear" and can be defined as the plane containing both direction η_1 and direction η_2. The magnitude of the twinning shear "*s*" can be calculated by the acute angle (ϕ) between plane K_1 and plane K_2:

$$s = 2\cot(2\phi) \tag{1}$$

The plastic strain accommodated by a twin volume can be calculated from the twinning shear *s*:

$$\varepsilon_{p(ij)}^{tw} = f_{twin} \cdot s \cdot \left(\frac{m_i n_j + n_i m_j}{2} \right) \tag{2}$$

where $\varepsilon_{p(ij)}^{tw}$ is the plastic strain accommodated by twinning. f_{twin} is the twin volume fraction and *s* is the magnitude of twinning shear. $\frac{m_i n_j + n_i m_j}{2}$ is the Schmid factor of the specific twinning mode. m_i and n_i are the unit vector of the twinning plane normal and the unit vector of the twinning direction with respect to the sample coordinate system, respectively.

For all twinning modes, the matrix lattice and the twin lattice can be related by a reflection operation about the K_1 plane. If the twin lattice is resulted from a matrix lattice through a 180-degree rotation about the normal to the K_1 plane, the twin is referred to as *Type I Twin*. If the reflection about the K_1 plane is realized through a 180-degree rotation about the direction η_1, the twin is termed as *Type II Twin*. In an HCP structure, plane K_1, direction η_1, plane K_2, and direction η_2 can be irrational. However, if plane K_1, direction η_1, plane K_2, and direction η_2 in Type I twin are rational, the twin is known as a *Compound Twin*. Twinning modes discussed in magnesium for the current research are known as compound twins.

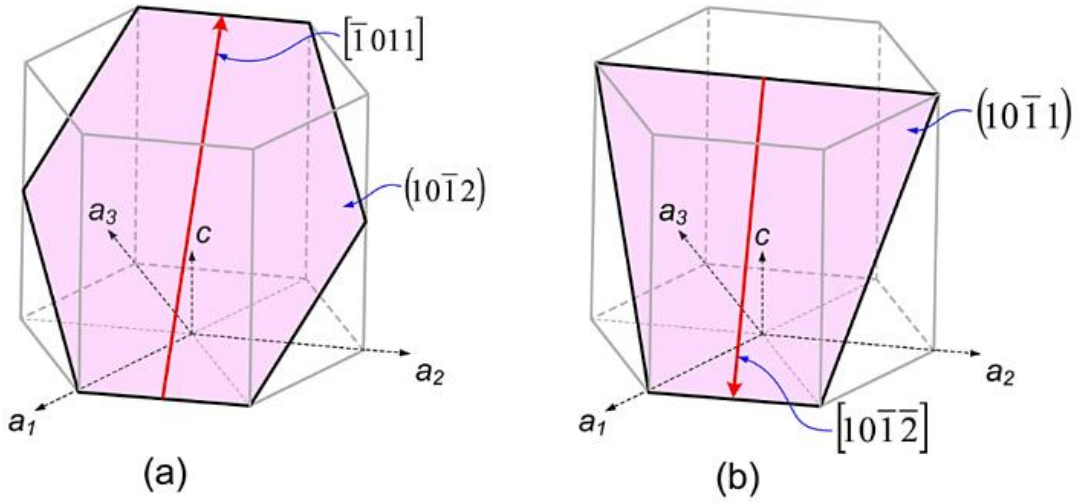

Figure 7 Twinning elements of primary twinning modes in magnesium at room temperature: (a) $\{10\bar{1}2\}<\bar{1}011>$ tension (or extension) twin; (b) $\{10\bar{1}1\}<10\bar{1}\bar{2}>$ compression (or contraction) twin.

Primary Twinning in Magnesium: Typical primary twinning modes in magnesium at room temperature are $\{10\bar{1}2\}<\bar{1}011>$ tension (or extension) twin and $\{10\bar{1}1\}<10\bar{1}\bar{2}>$ compression (or contraction) twin (Figure 7). Twinning elements for tension and compression twins together with their experimental obtained CRSS values at room temperature are listed in Table 3. Both tension and compression twins can accommodate deformation along the *c*-axis. As seen in Table 3, $\{10\bar{1}2\}<10\bar{1}1>$ tension twin has a CRSS value much lower than that of $\{10\bar{1}1\}<10\bar{1}\bar{2}>$ compression twin at room temperature. Therefore, tension twin is the most easily activated twinning mode and plays a critical role in the plastic deformation of magnesium and its alloys.

Table 3 Twinning elements and critical resolved shear stress for $\{10\bar{1}2\}<\bar{1}011>$ tension twin and $\{10\bar{1}1\}<10\bar{1}\bar{2}>$ compression twin at room temperature.

K_1	η_1	K_2	η_2	Shear plane *S*	Twinning shear ($\gamma = 1.624$ for HCP Mg)	CRSS (MPa) at 300 °K
$\{10\bar{1}2\}$	$<\bar{1}011>$	$\{10\bar{1}\bar{2}\}$	$<10\bar{1}1>$	$\{1\bar{2}10\}$	$\frac{\lvert\gamma^2-3\rvert}{\gamma\sqrt{3}} = 0.129$	2 [25] 2.7-2.8 [38] 2.4 [39] 5.5 [33]
$\{10\bar{1}1\}$	$<10\bar{1}\bar{2}>$	$\{10\bar{1}\bar{3}\}$	$\{30\bar{3}2\}$	$\{1\bar{2}10\}$	$\frac{4\gamma^2-9}{4\gamma\sqrt{3}} = 0.138$	114 [40] 75-130 [32]

Shape changes and crystal reorientation associated with tension twin and compression twin in magnesium are shown in Figure 8, where the out-of-plane direction points along the $[\bar{1}2\bar{1}0]$ direction. Since $c<\sqrt{3}a$ in HCP magnesium, $\{10\bar{1}2\}<\bar{1}011>$ twinning is favored by tension along the *c*-axis (Figure 8a) or, equivalently, compression normal to the *c*-axis. The crystal reorientation by tension twinning results in an angle of 86.4 degree between the basal plane pole in twinned lattice and that in matrix lattice (Figure 8a). For $\{10\bar{1}1\}<10\bar{1}\bar{2}>$ twinning, *c*-axis compression or tension perpendicular to the *c*-axis can be accommodated, as shown in Figure 8b. Compression twinning reorients the basal pole in the matrix lattice 56.2 degree about the $<\bar{1}2\bar{1}0>$ zone axis to the basal pole in the twin lattice.

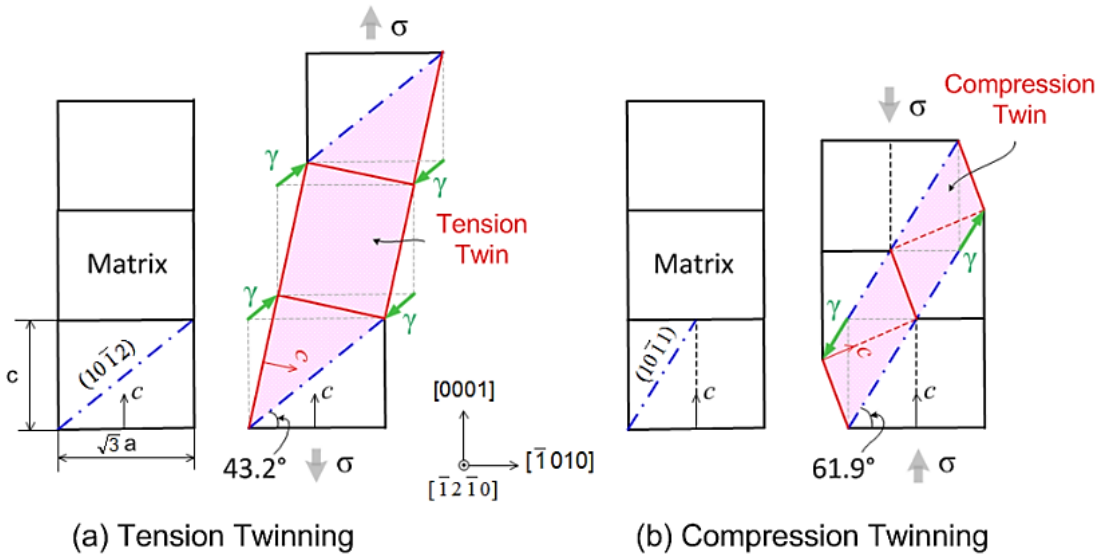

Figure 8 Twinning shear, shape change, and the crystal reorientation associated with primary twinning in magnesium: (a) $\{10\bar{1}2\}<\bar{1}011>$ tension twin; (b) $\{10\bar{1}1\}<10\bar{1}\bar{2}>$ compression twin.

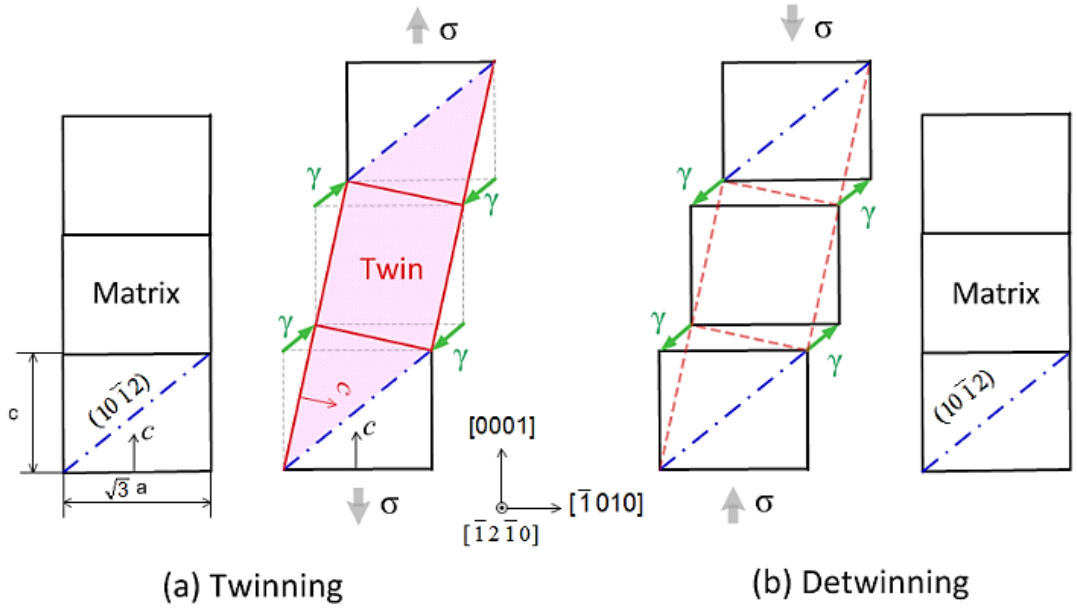

Figure 9 Twinning under tension along the *c*-axis and detwinning under reversed loading in magnesium.

As previously discussed, twinning under tension along the *c*-axis of the matrix (or under compression parallel to the basal plane) reorients the basal pole in the matrix lattice 86.4 degree about the $<\bar{1}2\bar{1}0>$ zone axis to that in the twin lattice. If the subsequent loading reverses its direction, a secondary twinning with the same variant as that of primary twinning can occur in the twin lattice as a reverse lattice shuffle. This process is termed as "*detwinning*," as schematically illustrated in Figure 9. As observed in experiments, detwinning is observed as a shrinkage of the previously developed twin by the reverse motion of the twinning boundary [39].

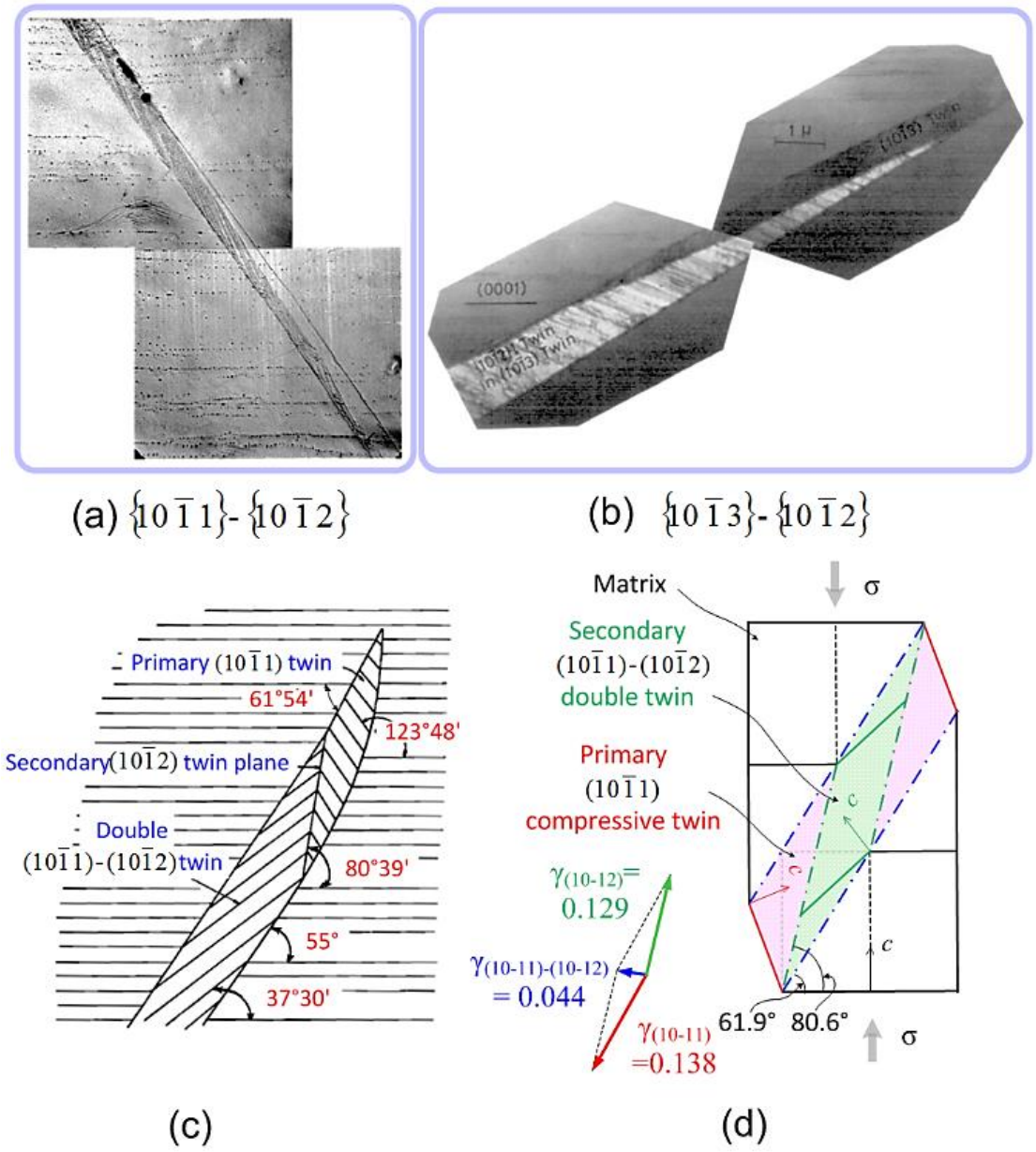

Figure 10 Compression-tension double twin in magnesium: (a) $\{10\bar{1}1\}-\{10\bar{1}2\}$ double twin [41]; (b) $\{10\bar{1}3\}-\{10\bar{1}2\}$ double twin [42]; (c) schematic drawing of the experimentally observed $\{10\bar{1}1\}-\{10\bar{1}2\}$ double twin [43]; (d) twinning shear, shape change, and crystal reorientation associated with $\{10\bar{1}1\}-\{10\bar{1}2\}$ double twinning.

Compression-Tension Double Twinning in Magnesium: $\{10\bar{1}1\}$ and $\{10\bar{1}3\}$ compression twinning is well known as a deformation mode which can accommodate *c*-axis compression [32, 40, 43, 44] or tension parallel to the basal plane [25, 32, 41, 43–47]. Since the stress required to activate compression twins is very large due to its high magnitude of CRSS (75~130 MPa in Table 3), $\{10\bar{1}1\}-\{10\bar{1}2\}$ or $\{10\bar{1}3\}-\{10\bar{1}2\}$ compression-tension double twinning [25, 32, 40, 41, 43–47] can occur. Compression-tension double twinning is a secondary $\{10\bar{1}2\}$ tension twinning occurring inside the primary $\{10\bar{1}1\}$ or $\{10\bar{1}3\}$ compression twin (Figure 10a and Figure 10b). Experimental observations reveal that the boundary of double twin usually deviates 5~8 degrees from that of the primary compression twin [43], as shown in the schematic drawing of the observed $\{10\bar{1}1\}-\{10\bar{1}2\}$ double twin (Figure 10c). Figure 10d illustrates the twinning shear associated with the compression-tension double twin. When the compression twin first occurs under an external compression along the *c*-axis in the matrix, the interior of the compression twin favors a secondary tension twinning. Combining the primary twinning shear of 0.138 along the $\left[10\bar{1}\bar{2}\right]$ direction with respect to the matrix and the secondary twining shear of 0.129 along the $\left[\bar{1}011\right]$ direction inside the compression twin, a strain of 0.044 can be resulted. The direction of the resultant strain vector lies nearly perpendicular to the double twin boundary. Therefore, once compression-tension twinning occurs, the displacement normal to the double twin boundary causes a cleavage in the double twin boundary, leading to rapid fracture of the material.

Twin-Twin Interaction: When multiple variants of a twinning mode are activated, they inevitably meet and interact each other. Therefore, a twin-twin interaction is a common phenomenon observed in deformed metals. Early studies of twin-twin interaction were mostly limited to materials with orthotropic [36], tetragonal [48], and cubic [49–52] crystal structures. Less attention was paid to HCP crystals [53–56]. During the past two decades, HCP materials have been received a great attention. Studies on twin-twin interaction in HCP structures were frequently reported [181–205]. Three typical twin-twin interaction structures have been found: (1) quilted-looking twin structure consisting of twins arrested at other twin boundaries [36, 39, 56–74], (2) "apparent crossing" twin structure which links twins impinging independently on each side of twin lamella [75, 76], and (3) double twin structure that results from secondary twin being nucleated at twin-twin interfaces [36, 48, 50, 51, 53–56, 74, 77–81].

Cahn [36] first reported the quilted-looking twin structure in plastically deformed α-uranium with an orthotropic structure. Quilted-looking twin structure (refer to Figure 7 in Ref. [36]) can be described as a locked network of different twin variants, where one twin is arrested at another twin boundary. No twin transmission exists in the blocked twin-twin pair. A similar quilted-looking twin structure was observed by Robert and Partridge [56] in HCP magnesium. The twin-twin boundary formed between two $\{10\bar{1}2\}$ twin variants was identified as a common interface bisecting two twinning planes. It was pointed out that a local rotation of twin lattice in the vicinity of the contact site could be resulted from a stress relaxation process across the contact interface accompanying the formation of the common interfaces between two twins. Recently, such quilted-looking twin structure is frequently found in HCP metals in

different metalworking conditions or mechanical experiments, such as monotonic loading [181–190], rolling and extrusion [67, 73, 74], surface treatment [69, 71, 72], and cyclic loading [39, 68–70].

Compared to the quilted-looking twin structure, "apparent crossing" twin structure was much less reported [75, 76]. In this twin structure, two twins impinge independently on each side of a barrier twin, where the region in the barrier twin which links the two impinging twins experiences a slight crystal rotation. The "apparent crossing" twin structure was recently observed in an AZ31 magnesium alloy subjected to plane strain compression along the direction perpendicular to the extrusion direction [75] and in an AZ31 magnesium alloy rolled sheet with inhomogeneous coarse and fine grains compressed perpendicular to the normal direction [76].

A double twin structure refers to a composite twin where a secondary twin having the same twinning mode as primary twinning is activated inside a primary twin. The secondary twin is usually found to be either connected to or close to the impingement of the incident primary twin. Cahn [36] first observed a crossing-like double twin structure in α-uranium. An impinging twin was observed to transmit a pre-existing twin through a secondary twin path. Cahn [36] proposed a continuity condition stating that two constraints are required for creating a crossing-like double twin structure: (1) the traces of the impinging twin and the secondary twin in the K_1 plane of the barrier twin must be parallel; (2) the direction and magnitude of twinning shear must be identical in the impinging and secondary twins. However, the second constraint had been questioned in early days when it was applied to other materials such as tetragonal tin [48], FCC cobalt-iron alloy [50, 51], HCP zinc [53], HCP zirconium [54], and HCP

magnesium [55, 56]. Recently, a double tension twin structure was observed in HCP magnesium [74, 77–81].

Microstructures in association with twin-twin interaction were found to correlate with mechanical hardening [60, 61, 64–66]. Jiang et al. [60] and Yang et al. [61] reported that multiple twin variants and twin-twin intersections were often associated with the deformation stage with a higher strain hardening rate in an AZ31 magnesium alloy subjected to compression along the extrusion direction. Oppedal et al. [64] and Ma et al. [65] found that multivariate and multifold twins were activated to accommodate large straining and the subsequent twin-twin interaction contributed to significant strain hardening. El Kadiri et al. [66] compared the twin growth behavior in two grains that contain different number of twin variants. The authors found that a higher twinning nucleation rate was exhibited in a grain containing twin-twin interaction with two variants while the twinning propagation rate was faster in the grain having only a single twin variant.

2.2 Current State-of-the-Art

2.2.1 Cyclic Plasticity and Fatigue – Magnesium Single Crystal

Single crystal is an ideal form of material to study the fundamental mechanisms of deformation and fracture. Compared to polycrystalline alloys, complex influences of grain boundaries, secondary phase, grain size, and alloying elements in solution on mechanical behavior can be eliminated. The orientation of a single crystal can be properly designed to study a single deformation mode. The resolved shear stress and

shear strain on a specific slip/twinning system can be accurately determined. Potentially activated slip/twinning systems can be easily identified.

Most experimental studies on magnesium single crystal were concentrated on exploring the operative slip/twinning modes under monotonic loading along a specific crystal orientation [25, 27, 28, 30, 32, 34, 40, 41, 43–47, 82–94]. Relative prevalence of deformation mechanism or fracture mechanism is strongly dependent upon the crystal orientations and loading modes. Very limited experimental studies have been conducted on cyclic plastic deformation [95, 96] and fatigue [97–106] in magnesium single crystals.

Work on cyclic plasticity of magnesium single crystal has been limited to crystals oriented for basal slip at limited range of strain amplitudes. Stevenson and Sande [95] carried out fully reversed total strain-controlled tension-compression experiments on magnesium single crystals. The angle between the loading axis and the *c*-axis is greater than 45°. Two strain amplitudes of 0.18% and 0.9% were studied. Cyclic plastic deformation at low plastic strain amplitude was controlled by single cyclic basal slip. At a higher plastic strain amplitude, duplex cyclic basal slip occurs in all crystal orientations. Cyclic hardening rate and the saturation stress increase with increasing plastic strain amplitude.

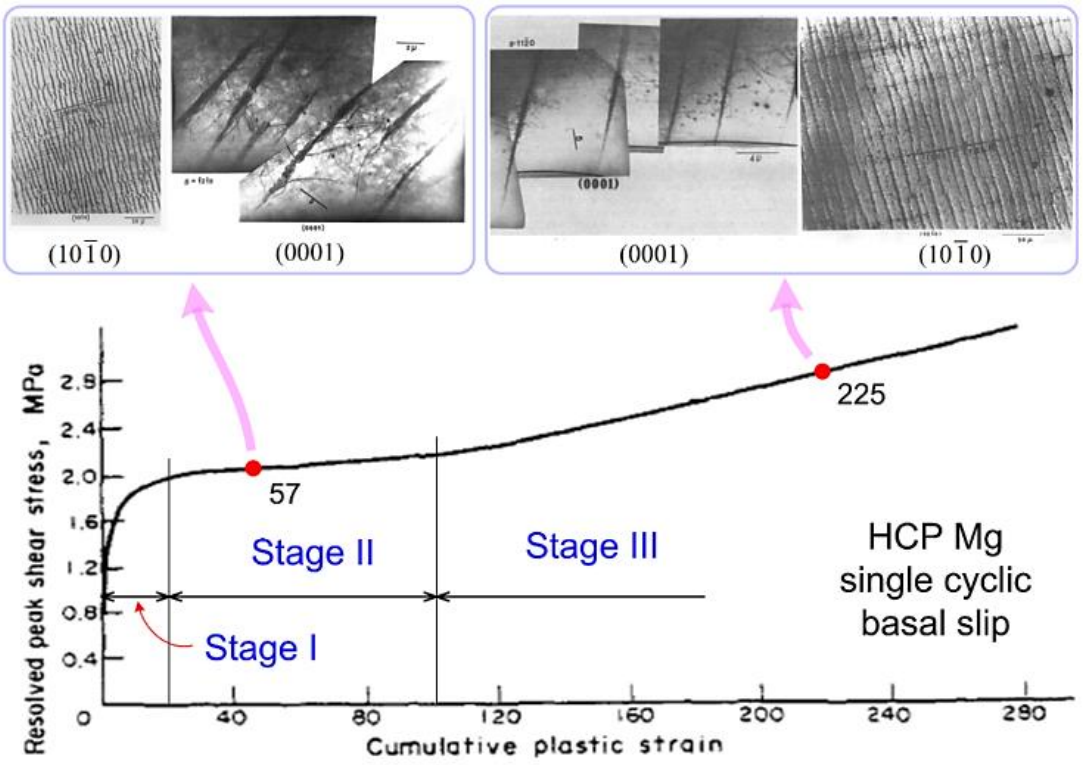

Figure 11 Cyclic stress-cumulative plastic strain curve oriented for single cyclic basal slip in magnesium single crystal showing three stages and the dislocation wall structures associated with Stage II and Stage III cyclic hardening [96].

Following Stevenson and Sande's work [95], Kwadjo and Brown [96] characterized the cyclic stress-cumulative plastic strain (CSPSC) curve for single basal slip by carrying out plastic strain-controlled tension-compression experiments on magnesium single crystals at the plastic strain amplitudes between 0.1% and 0.8% at 78 K and 300 K. Three stages are exhibited on the CSPSC curve (Figure 11): Stage I with rapid increasing of cyclic hardening rate in the range of cumulative plastic strain from 0 to 20; Stage II ($20 < \varepsilon_{c,p} < 100$) having relatively flat cyclic hardening rate; and Stage III ($\varepsilon_{c,p} > 100$) having increasing cyclic hardening rate. Transmission electron microscopy (TEM) observations of dislocation configuration were carried out on the

(0001) and $(10\bar{1}0)$ planes for the cumulative plastic strain of 57 (in Stage II) and 225 (in Stage III). In Stage II, dislocation clusters projected on the (0001) plane are irregular and generally aligned in the $[10\bar{1}0]$ direction. After cyclic hardened to Stage III, cluster arrays become more regular and the basal dislocation loops appear. The basal dislocation loops act as strong obstacles to the glide dislocation, which is responsible for the increased hardening in Stage III.

Very limited work was conducted on the fatigue and fracture of magnesium single crystals. Armstrong and Horne [97] first studied the fatigue fracture in magnesium single crystal by applying fully reversed shear stress on the basal plane at a constant amplitude at room temperature and -140 °C. Fatigue cracks were found to appear at the basal slip traces in the matrix near the twin boundary. The cause of fatigue cracks was attributed to the internal stress concentration occurred at the dislocations piled up at some twin barriers.

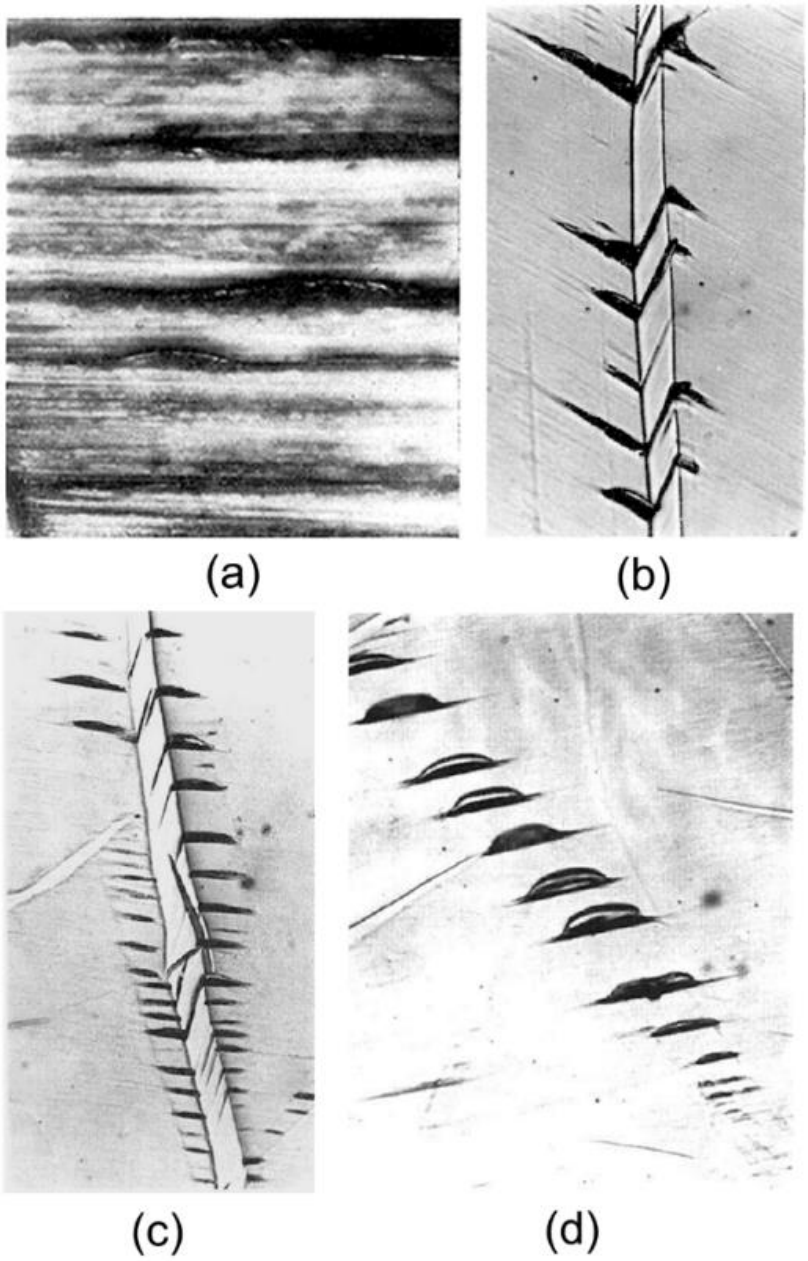

Figure 12 Fatigue extrusion developed in the coarse-grained polycrystalline magnesium under cyclic loading near the fatigue limit [100]: (a) extrusion bands developed along the basal slip steps; (b) extrusion developed from the basal slip traces within both the matrix and the twin; (c) extrusion preferably developed from the basal slip in the matrix near the twin boundary; (d) extrusion developed at position where the twin is detwinned.

A significant contribution regarding the origin of fatigue crack in magnesium was made by Partridge [98–101] who comprehensively studied the slip band extrusion and the cyclic twinning structure in coarse-grained polycrystalline pure magnesium at room temperature. Two types of experiments were designed: rotating-bending tests on cylinder specimens and reversed plane bending tests on plate specimens. In the fatigued specimen, numerous extrusions on basal slip band were developed in the matrix region inside the coarse grains. Smaller extrusion appeared as debris along the slip steps between the larger extrusions (Figure 12a). Partridge [100] further investigated the development of the fatigue extrusion with the existence of twins prior to fatigue loading. Three situations of pre-existing twins were designed: fully-developed twin (Figure 12b), partially detwinned twin (Figure 12c), and fully detwinned twin (Figure 12d). For the specimen where twins were fully developed prior to fatigue testing, the extrusions were developed from the basal slip traces within both the twin and the matrix. When the twin was partially detwinned prior to fatigue loading, the extrusion bands were developed preferably in the matrix adjacent to the twin boundary. When a twin was completely detwinned and was subsequently subjected to fatigue loading, extrusion developed from the basal planes at the original position of the twin.

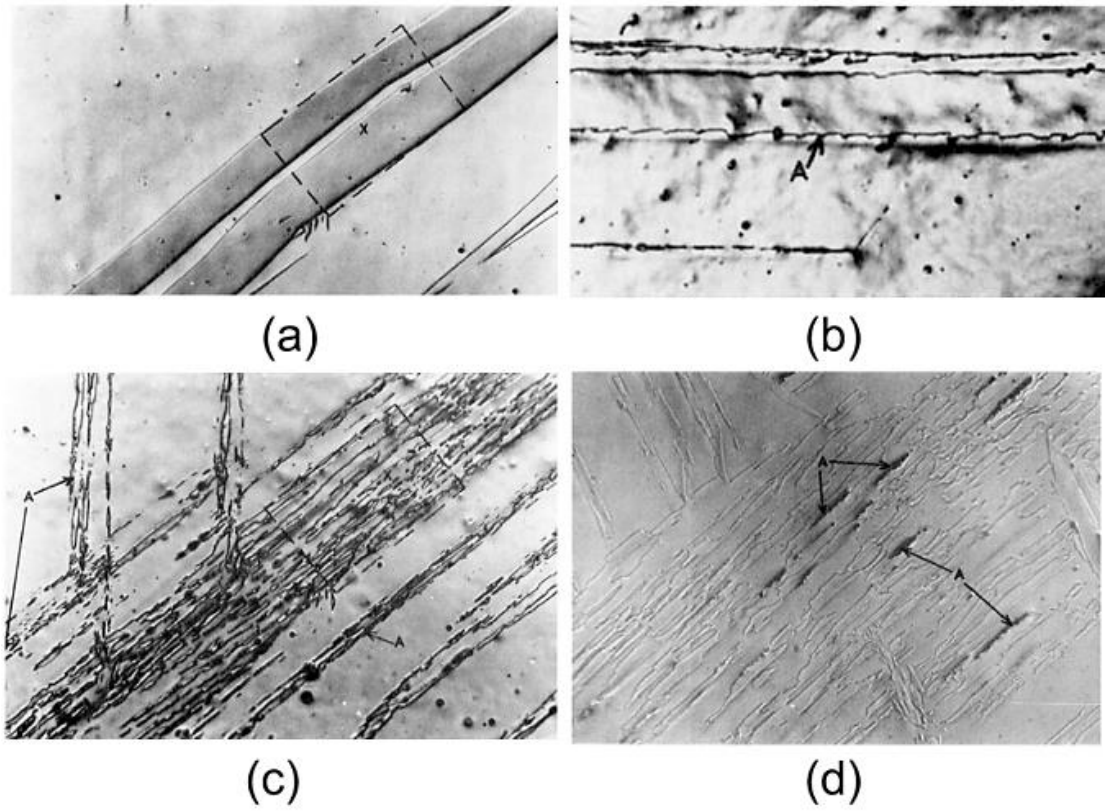

Figure 13 Cyclic twinning structures in coarse-grained pure polycrystalline magnesium at 25% of the fatigue life [101]: (a) twin prior to the fatigue test; (b) serrated twin boundary; (c) twin fragments; (d) microcrack developed at the interface of the fragmented twins.

Cyclic twinning structure in fatigued magnesium was investigated in pre-twinned plate testing specimen followed by reversed plane bending at a stress level which gave rise to the fatigue lives between 10^4 and 10^5 cycles. Slight surface polishing on one specimen stopped at the ~25% fatigue life revealed that the initially smooth twin boundary (Figure 13a) became severely serrated (Figure 13b). This is considered to be caused by the local non-uniform displacement of the twin boundary. Further removing the surface material by polishing revealed that cyclic stressing broke certain oriented

twins into smaller fragments with irregular shapes (Figure 13c). Microcracks were nucleated at the fragmented twin boundary and did not propagate significantly (Figure 13d). A schematic model based on the interaction between the twin boundary and the localized cyclic stressing was proposed by Partridge [101] to explain the phenomenon of twin fragmentation. However, such an explanation was solely based on the mechanical interaction between the twin boundary and the cyclic stressing. No information regarding the crystal orientation of the twin fragments was considered.

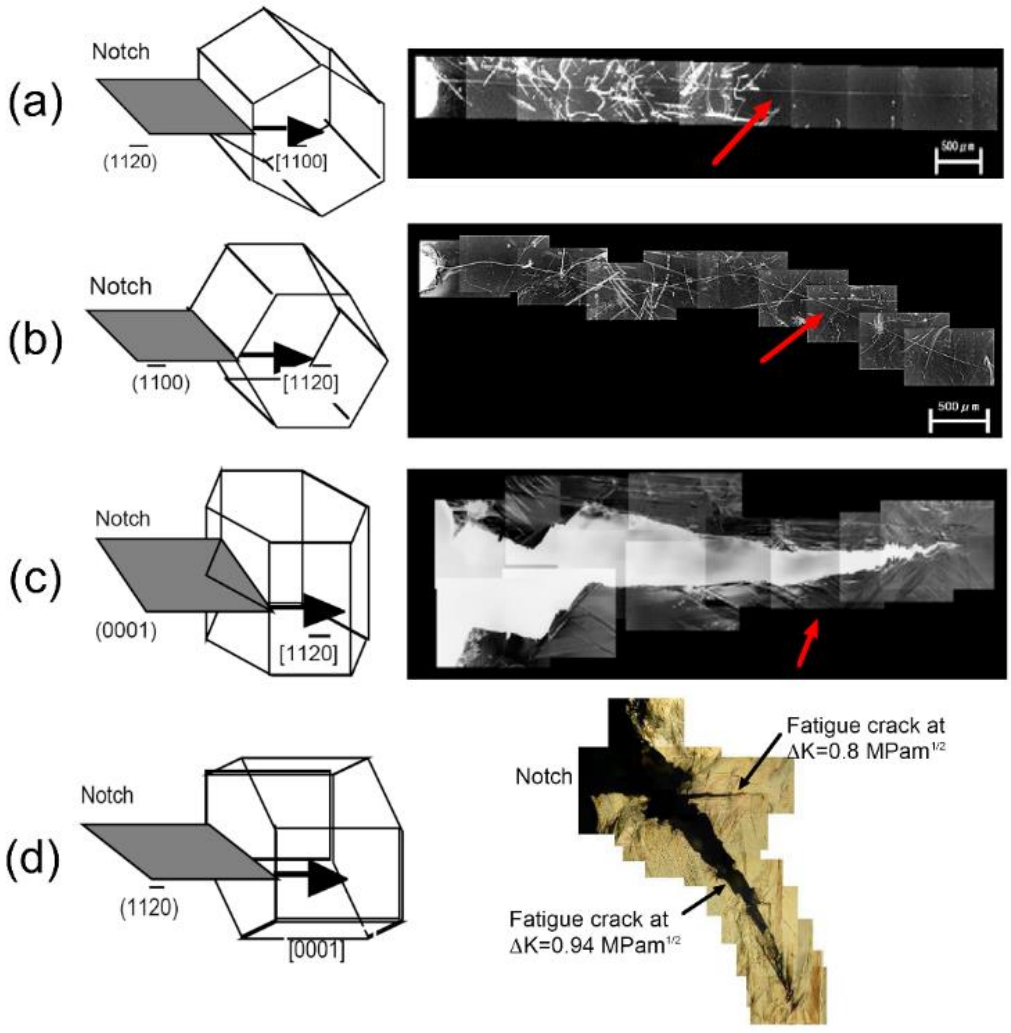

Figure 14 Effect of crystal orientation on fatigue crack growth in magnesium single crystal [103].

Recently, fatigue crack growth in magnesium single crystal was studied by Ando et al. [102–106] utilizing compact tension specimen under four different crystal orientations: notch plane on the $(11\bar{2}0)$ plane and the growth direction along $[1\bar{1}00]$ (Orientation A, Figure 14a), notch plane on the $(1\bar{1}00)$ plane and the growth direction along $[11\bar{2}0]$ (Orientation B, Figure 14b), notch plane on the (0001) plane and the growth direction along $[11\bar{2}0]$ (Orientation C, Figure 14c), and notch plane on the $(11\bar{2}0)$ plane and the growth direction along [0001] (Orientation D, Figure 14d). It is interesting to find that in both Orientations A and B, the fatigue crack plane is parallel to the $(11\bar{2}0)$ plane. In Orientation C, the fatigue crack propagates alternatively on the basal plane and on the tension twinning plane. In Orientation D, the fatigue crack growth is arrested at $\Delta K < 0.7 MPa(m)^{1/2}$ but propagated parallel to the basal plane at $\Delta K \geq 0.8 MPa(m)^{1/2}$. Based on the TEM observations of the <*c*+*a*> dislocations near the crack surface, Ando et al. [103] proposed that the fatigue crack in Orientation A and B was driven by alternating shear due to two intersecting second-order pyramidal slips at a lower ΔK. At a higher ΔK, the first-order pyramidal slip can be activated. The crack propagation could be proceeded by alternating shear on one second-order pyramidal slip plane and on a first-order pyramidal slip plane.

2.2.2 Cyclic Plasticity and Fatigue – Magnesium Polycrystal

Compared to single crystal, a study on cyclic deformation and fatigue failure of polycrystalline material has its practical and engineering significance. Unlike single crystal, grain boundaries exist in a polycrystalline aggregate. An individual grain has

its own preferred crystal orientation. The macroscopic mechanical response and the associated microscopic mechanisms can be different from those exhibited in a single crystal. Major influences of the grain boundary and grain orientation on the cyclic deformation and fatigue cracking must be taken into account.

Two forms of magnesium alloys can be processed: casting and wrought (rolled, extruded, and forged). Strong basal texture exists in the as-wrought magnesium alloys. The *c*-axes of most grains are aligned almost perpendicular to the extrusion or rolling direction [107, 108]. Tension twinning is favored in such oriented grains subjected to compression along the extrusion or rolling direction. When subsequent loading reverses its direction, detwinning occurs, i.e. the *c*-axis in the twinned lattice rotates back to align with that in the matrix. Due to this pole nature of twinning and the initial basal texture, wrought magnesium alloys show peculiar cyclic deformation behavior and fatigue properties.

During the last two decades, characteristics of cyclic deformation for wrought magnesium alloys have been extensively studied through fully reversed total strain-controlled (or plastic strain-controlled) tension-compression experiments at different strain amplitudes. The studied magnesium alloys include extruded AZ31 [109–115], rolled AZ31 [116–119], extruded AZ31B [120], rolled AZ31B sheet [121], extruded AZ61A [122–125], extruded AZ80 [109], extruded AM30 [126–128], extruded AM50 [129], and extruded ZK60 [130, 131] and ZK60A [16, 17, 132]. The stress-strain hysteresis loops at large strain amplitudes usually exhibit an asymmetric shape. When tension-compression is applied along the extrusion or rolling direction, the compressive reversal shows a normal concave-up shape whereas the tensile reversal appears to have

a concave-down first and subsequently concave-up sigmoidal shape. When tension-compression is along the direction normal to the rolled sheet plane, the asymmetric shape of the hysteresis loop is inversed. The asymmetric tensile and compressive reversals lead to a tensile (or compressive) mean stress which has a significant effect on the fatigue strength. Furthermore, a strong Bauschinger effect [133] is observed during the unloading from the tensile and compressive stress peaks. This phenomenon is regularly referred to as pseudoelasticity in magnesium alloys [134–138]. For the stabilized stress-strain hysteresis loops, features such as asymmetric shape, mean stress effect, and the pseudoelastic phenomenon are found to become more pronounced with increasing strain amplitudes.

Explorations of microstructural evolution during cyclic deformation in magnesium alloys were carried out by Brown et al. [139] and Wu et al. [16, 17, 132, 140] using *in situ* neutron diffraction, by Yin et al. [111] using electron backscattered diffraction (EBSD), and by Park et al. [118] using light microscope. All of these studies confirmed that the compressive reversal was dominated by activation of tension twins and the subsequent tensile reloading was associated with detwinning. Moreover, Brown et al. [139] and Wu et al. [16, 17, 132, 140] observed that with increasing number of loading cycles, the amount of twins in the compressive peak increased while the detwinning capacity under subsequent tensile reloading progressively exhausted. This evolving twinning/detwinning process resulted in an increased residual twin boundaries, which can be reflected from the enhanced tensile and compressive peak stresses with increasing number of loading cycles. Further direct observations were provided by Park et al. [118] through the comparison of the twin distribution in the half-cycle with

that in the first loading cycle via optical microscopy. The strain-amplitude dependence of the residual twins was investigated by Fan et al. [127], Li et al. [122], and Luo et al. [128] via optical microscopy. It was found that when the strain amplitudes were higher, more residual twins were observed in the fatigued specimens, and their size and shape were bigger and coarser.

Fatigue of magnesium alloys is usually characterized using the fatigue life curve. Earlier studies of wrought magnesium alloys frequently reported that the strain-life curves exhibited a smooth transition from the low-cycle fatigue regime to the high-cycle fatigue regime and the strain-life curves can be described well by the Basquin (stress-life curve) and Manson–Coffin (plastic strain-life curve) equations [110, 113, 114, 120, 126, 129]. Hasegawa et al. [110] found out that the Manson–Coffin relationship can nicely describe the fatigue lives of extruded AZ31 obtained under stress-controlled loading but failed to describe the fatigue lives obtained from the strain-controlled experiments. Matsuzuki and Horibe [112] observed that the fatigue data of extruded AZ31 exhibited a bilinear tendency in the Manson–Coffin curve, implying that the twinning/detwinning process was dominant at higher plastic strains amplitudes whereas dislocation slips were dominant at lower plastic strain amplitudes. Similar bilinear Manson–Coffin curves were observed in rolled AZ31 [116] and extruded AZ31 [115]. Luo et al. [128] indicated that the fatigue lives for extruded AM30 had an evident difference between the strain amplitudes above and below 0.3%. Li et al. [122] showed that the strain–life fatigue curve of extruded AZ61A displayed a detectable transition from the low cycle fatigue regime to the high cycle fatigue regime in the vicinity corresponding to a strain amplitude of 0.5%.

On the fundamental fatigue mechanism in magnesium alloys, Matsuzuki and Horibe [112] first noticed that the plastic strain-life curve could be described by a bilinear Coffin-Manson equation, which indicated a transition of the dominant cyclic deformation mechanism from twinning/detwinning at high strain amplitudes to the dominating dislocation slips at low strain amplitudes. A kink in the strain-life curve was recently observed [110]. Further examination of the residual twin distributions near and far away from the fracture surface suggested that crack initiation was associated with the cyclic deformation mechanism but crack propagation was influenced by the twinning/detwinning process. Tokaji et al. [18] observed that crack initiation for a rolled AZ31 magnesium alloy in high-cycle fatigue (HCF) regime was in either transgranular or intergranular mode and both initiation modes occurred in nearly equal amounts. Through the study of the surface and subsurface crack initiation sites near the fatigue endurance limit for a Mg–Zn–Y–Zr magnesium alloy, Xu et al. [19] attributed the surface and subsurface crack initiation to a competition between the intrusion/extrusion degree by cyclic slipping and the retarding effect of oxide film on the cyclic slip. As a supplementary mechanism of crack initiation, Yang et al. [20] emphasized the role of twin-involved cyclic deformation irreversibility and proposed twin band cracking as one specific crack initiation mechanism for extruded AZ31 in the HCF regime. Yin et al. [21] examined the residual twin distribution and the fracture morphology at the stable and unstable propagation zones on the fracture surface for an extruded AZ31 magnesium alloy. It was emphasized that the twinning/detwinning process played an important role in forming the fracture morphologies at the stable and unstable propagation zones.

2.3 Summary

Typical macroscopic features of cyclic plasticity and fatigue of magnesium alloys have been investigated through extensive cyclic loading experiments. No previous work has been carried out to study the cyclic deformation in magnesium single crystal oriented for easy twinning and detwinning. Efforts made on the relationship between the macroscopic behavior and the associated microscopic structural changes in magnesium are very limited. There is still no direct observation of the fundamental twinning/detwinning process which plays a critical role in the cyclic plastic deformation in magnesium. Kinetic evolution of twinning/detaining process together with the twin-twin interaction under cyclic loading were never studied and reported. As for polycrystalline magnesium, the detailed development of fatigue damage at different strain amplitude is not clear. The associated fatigue damage mechanisms regarding initiation of microcrack and its early-stage propagation modes still remain unanswered.

3. Cyclic Deformation of Single Crystal Magnesium

Cyclic deformation of magnesium single crystal was investigated by carrying out fully reversed strain-controlled tension-compression experiments along the [0001] and $[10\bar{1}0]$ directions in ambient air. For the [0001]-oriented magnesium single crystal, *in situ* optical microscopy (OM) revealed the fundamental morphology evolution of the $\{10\bar{1}2\}$ twinning-detwinning-retwinning process. With increasing loading cycles, the material exhibits cyclic hardening during which the activity of twinning-detwinning-retwinning progressively decreases. During detwinning at each loading cycle, residual twins are observed to form on the vicinities of the twin boundaries which have been fully expanded at the previous tensile peak. After termination of the fatigue test, microcracks were found on the boundaries of residual twins and on the basal slip band extrusions. Optical microscopy (OM) examination on the as-tested specimen surface revealed that basal slip band extrusion, serrated residual twin boundary, and fragmented twin-twin interaction sites are developed. Electron backscatter diffraction (EBSD) analysis shows that the material having experienced repeated twinning and detwinning cannot completely reverse to its original crystal orientation, which could be ascribed to the development of stable dislocation substructures due to dislocation-twin boundary interactions. Secondary twin fragments predominately occur at the interaction sites among primary twins and are more difficult to be detwinned as compared to the parent primary twins.

For the magnesium single crystal subjected to cyclic tension-compression in the $[10\bar{1}0]$ direction, plastic instability was found near the end of the first detwinning reversal. Twin-twin boundaries and secondary twins were induced by interaction of

primary $\{10\bar{1}2\}$ twins. Microcracks were developed at primary twin boundaries and twin-twin interaction sites. Final fracture was caused by cleavage cracking on $\{10\bar{1}1\}$-$\{10\bar{1}2\}$ double twin and shearing fracture on the basal plane.

3.1 Materials and Specimen Preparation

Magnesium single crystals were commercially acquired and the material was grown by using the Bridgman technique. Two crystal orientations were designed, aiming to maximize the activation of $\{10\bar{1}2\}<\bar{1}011>$ tension twin upon loading in one direction and to facilitate detwinning under the subsequent loading reversal. The relationships between the crystal coordinate system and the sample coordinate system for these two designed crystal orientations are schematically illustrated in Figure 15. In the figure, the "$oa_1a_2a_3c$" notation denotes a four-axis hexagonal crystal coordinate system. The "$oe_1e_2e_3$" notation represents a three-axis orthotropic crystal coordinate system fixed on the "$oa_1a_2a_3c$" coordinate, where the "e_1" axis is aligned along the "a_1" axis and the"e_3" axis is along the "c" axis. The sample coordinates fixed on the testing specimen are referred to as the "*OXYZ*" coordinates. The axial loading direction is aligned with the "*Z*" axis while the observation plane is parallel to the "*OYZ*" plane.

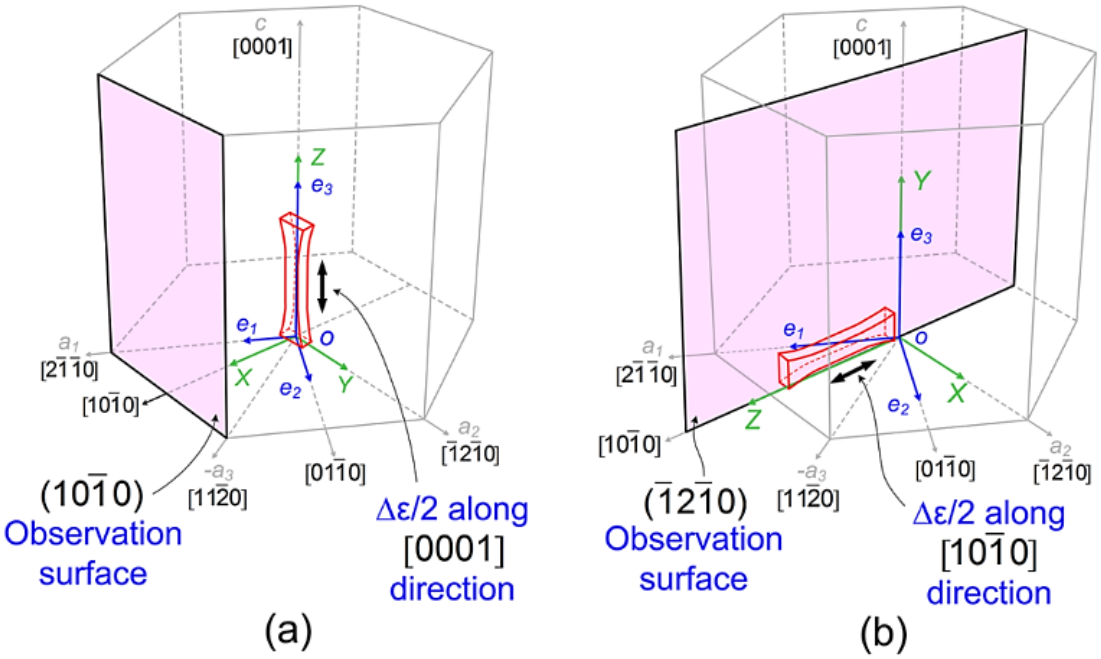

Figure 15 Geometry of magnesium single crystal testing specimen and the relationship between the crystal coordinate system and the sample coordinate system: (a) [0001] direction; (b) $[10\bar{1}0]$ direction.

For the crystal orientation in the [0001] direction (Figure 15a), the "*Z*" axis is aligned with the "*c*" axis. The "*X*" axis is rotated 30 degree from the "a_1" axis ($(2\bar{1}\bar{1}0)$). The observation surface "*OYZ*" is a $(10\bar{1}0)$ prism plane. For the crystal orientation in the $[10\bar{1}0]$ direction (Figure 15b), the "*Z*" axis is aligned with the $[10\bar{1}0]$ direction. The "*X*" and "*Y*" axes are aligned along the "a_2" ($(\bar{1}2\bar{1}0)$) and "*c*" ([0001]) axes, respectively. The observation plane "*OYZ*" is parallel to the $(\bar{1}2\bar{1}0)$ plane. Under tension along the [0001] direction, all the six tension twin variants are anticipated to be simultaneously activated because the Schmid factor for all six variants is 0.499. As for compression along the $[10\bar{1}0]$ direction, the Schmid factor is 0.499

for the $(10\bar{1}2)$ and $(\bar{1}012)$ twin variants while the value for the remaining four twin variants is 0.125. Accordingly, the $(10\bar{1}2)$ and $(\bar{1}012)$ twin variants are expected to be activated due to their higher value of Schmid factor.

Magnesium single crystals designed in these two orientations were fabricated into small dog-bone shaped plate specimens using electrical discharge machining (EDM) specially designed for soft single crystals. The machine used a relaxation circuit to keep the crystal damage-free and strain-free. The gage section of the testing specimen had a length of 7.5 mm with a square cross section of 3.0 mm × 3.0 mm. The design of specimen shape was intended to prevent buckling under fully reversed tension-compression loading. In order to facilitate *in situ* optical microscopy (OM) observations, one of the flat surfaces was ground carefully using SiC sanding papers with grit No. of 1200. Mechanical polishing using 6-μm and 1-μm MetaDi® diamond polycrystalline suspension pastes was followed. After mechanical polishing, the specimen surface was chemically polished using a solution consisting of 1 part of nitric acid, 2 parts of hydrochloric acid, and 7 parts of ethanol [141].

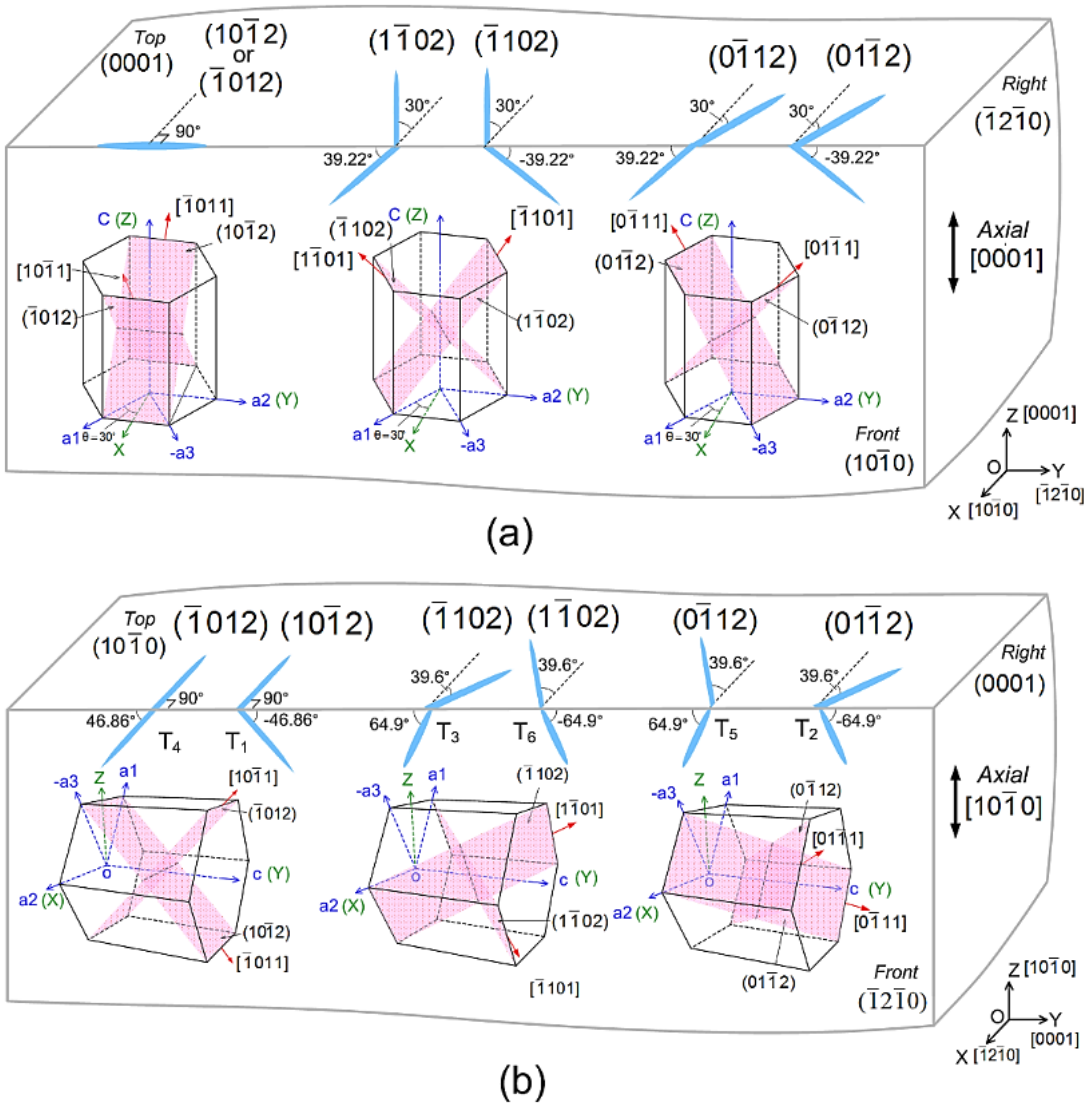

Figure 16 Projected orientations of $\{10\bar{1}2\}$ tension twin variants on the observation (front) surface and on the cross section (top) plane for magnesium single crystals in the two designed crystal orientations: (a) [0001] direction; (b) $[10\bar{1}0]$ direction.

In order to facilitate an identification of twin variants from the twin markings observed on the specimen surface, it is necessary to calculate the theoretical orientations of the six tension twin variants projected on the observation surface and on the cross section plane of the testing specimen in the two designed crystal

orientations. Figure 16 shows the theoretical projections of the $\{10\bar{1}2\}$ twin variants on the observation (front) surface and on the cross section (top) plane for the two designed crystal orientations. For the crystal orientation in the [0001] direction (Figure 16a), three orientations of twins can be observed on the observation surface ($(10\bar{1}0)$ prism plane): 0˚ with respect to the "*Y*" axis for the $(10\bar{1}2)$ or $(\bar{1}012)$ twin, 39.22˚ for the $(1\bar{1}02)$ or $(0\bar{1}12)$ twin, and -39.22˚ for the $(\bar{1}102)$ or $(01\bar{1}2)$ twin. On the cross section plane (the basal plane), twin $(10\bar{1}2)$ or $(\bar{1}012)$ has projections oriented with 0˚ rotated from the "*Y*" direction, -60.00˚ for twin $(1\bar{1}02)$ or $(\bar{1}102)$, and 60.00˚ for twin $(0\bar{1}12)$ or $(01\bar{1}2)$. For the crystal orientation in the $[10\bar{1}0]$ direction (Figure 16b), on the $(\bar{1}2\bar{1}0)$ observation plane, twins $(\bar{1}012)$ and $(10\bar{1}2)$ are projected having 46.86˚ and -46.86˚ rotations with respect to the "*Y*" direction ([0001]), 64.90˚ for twins $(\bar{1}102)$ and $(0\bar{1}12)$ and -64.90˚ for twins $(1\bar{1}02)$ and $(01\bar{1}2)$. On the $(10\bar{1}0)$ cross section plane, twins $(\bar{1}012)$ and $(10\bar{1}2)$ are projected having 0˚ rotations with respect to the "*X*" direction ($[\bar{1}2\bar{1}0]$), 39.60˚ for twins $(1\bar{1}02)$ and $(0\bar{1}12)$, and -39.60˚ for twins $(\bar{1}102)$ and $(01\bar{1}2)$. It is noted that the projected orientations of the six twin variants are calculated assuming an ideally designed crystal orientation as shown in Figure 16. In the real testing specimens, the axial loading direction and the observation plane can be slightly tilted from the designed crystal direction and plane. (The size of the inserted numbers is larger than 12. Need to be consistent.)

3.2 Mechanical Experiments and Microscopic Observations

The experimental setup for the cyclic deformation experiment of magnesium single crystal and the *in situ* optical microscopic (OM) observation is composed of two parts: a mechanical testing system and a long-distance light microscope, as shown in Figure 17. An Instron servohydraulic load frame was used for the cyclic loading experiments. The testing system has a load capacity of ±20 kN. It is equipped with the Instron 8800 electronic control, computer control, and data acquisition. The gripping system was specially designed to ensure an accurate alignment of the small testing specimen and to eliminate the premature cracking outside the gage section. An important consideration in the grip design was to enable both tension and compression forces to be applied on the small testing specimen. A specially designed strain-gaged extensometer was used for the direct measurement of the strain within the gage section of the testing specimen. The extensometer was designed in such a way that the contact of the extensometer with the specimen surface created a minimal local deformation on the surface of the testing material to ensure that fatigue failure occurred within the gage section. The extensometer had a range of ±9.15%.

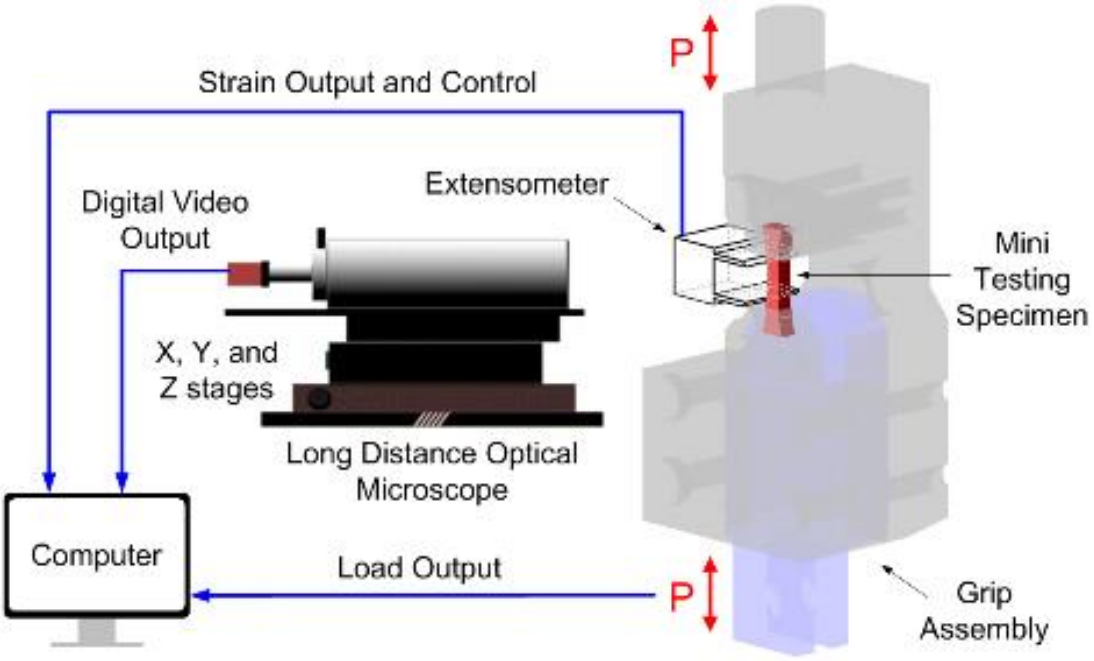

Figure 17 Experimental setup for cyclic deformation experiment of magnesium single crystal and *in situ* optical microscopic observation.

A long-distance travelling optical microscope (QM-100) equipped with a unique rotational and a high resolution charge-coupled device (CCD) camera was employed for *in situ* optical observation of the deformation and fatigue processes on the flat specimen surface during the cyclic loading experiment. The microscope together with the CCD camera can capture an image frame with a resolution of ~1 μm. The activities of twinning/detwinning process can be monitored. Real-time image frames were correlated directly to the data points on the simultaneously recorded stress-strain hysteresis loops. In addition, the twin volume fraction can be obtained from the image frame. The twin volume fraction f_{twin} is calculated from the twin area fraction A_{twin} by multiplying an average geometrical factor $\overline{\beta}$ that accounts for the true twin thickness:

$$f_{twin} = A_{twin}\overline{\beta} \quad (3)$$

where the twin area fraction A_{twin} is equal to the ratio of the total number of dark contrasted pixels (representing twins) over the total number of pixels within the observation region. $\overline{\beta}$ is an average geometry factor given by:

$$\overline{\beta} = \frac{1}{6}\sum_{i=1}^{6}\beta_i \quad (4)$$

where β_i (i =1, 2, 3…, 6) denotes the thickness factor for the six tension twin variants. Based on the crystal orientation as shown in Figure 16, the geometry factor for $(10\bar{1}2)$ and $(\bar{1}012)$ twin variants is identified to be 0.73 and the value for the $(1\bar{1}02)$, $(0\bar{1}12)$, $(\bar{1}102)$, and $(01\bar{1}2)$ twin variants is 0.90.

The cyclic deformation behavior of magnesium single crystal was investigated by carrying out fully reversed strain-controlled tension-compression in [0001] and [$10\bar{1}$ 0] directions in ambient air. For the magnesium single crystal oriented in the [0001] direction, a strain amplitude of 0.5% was used. The testing frequency was chosen to be 0.01 Hz. For the loading cycles when *in situ* images were recorded, the load-strain acquisition rate was 5 points per second and the corresponding video recording rate was 0.7 frame per second (fps). The true stress and true strain were calculated and reported. The cyclic deformation experiment was terminated after 5,019 loading cycles. The testing specimen was not fractured into two parts and was carefully unloaded from the compressive peak stress after the experiment was terminated. A macroscopic horizontal crack appeared on the specimen surface near the transition part from the gage section to the grip section. The as-tested specimen surface was first observed

using SEM for examination of microcrack development and OM for morphology examination of slip band and residual twin. To reveal the crystal orientations of the residual twins and the twin-twin interaction structures, the rough as-tested specimen surface was polished using 1-μm MetaDi® diamond polycrystalline suspension paste and etched with an etchant consisting of one-part of nitric acid and ten-part of distilled water. Surface material about 200 μm thick was removed. Electron backscatter diffraction (EBSD) scan with a step size of 0.5 μm was conducted on a surface area of 1,920 μm × 640 μm located within the gage section of the chemically polished specimen.

Cyclic deformation of magnesium single crystal oriented in the $[10\bar{1}0]$ direction was studied by carrying out fully reversed strain-controlled tension-compression experiments in ambient air at three strain amplitudes: 0.5%, 0.75%, and 1%. The strain rate was 4.0×10^{-4} /s when *in situ* OM was used to observe the specimen surface. A strain rate at 4.0×10^{-3} /s was used for the rest of the loading cycles. All the experiments started with a compressive loading reversal. In addition to *in situ* OM observation, EBSD characterization of twin structures was carried out in the specimens unloaded from the first and third compressive peaks at the strain amplitude of 0.75% and in the specimen unloaded from the 30^{th} compressive peak at the strain amplitude of 1%. After fatigue fracture, microcracks and the macroscopic fracture surfaces were examined using SEM and EBSD.

A $[10\bar{1}0]$-oriented magnesium single crystal specimen subjected to fully reversed strain-controlled tension-compression at a strain amplitude of 0.75% was used to further study detailed twin-twin boundaries and their influences on subsequent

twinning and detwinning. Twins were absent before the mechanical experiment. Loading in the $[10\bar{1}0]$ direction, twin variants $(10\bar{1}2)$ and $(\bar{1}012)$ that share the same $[\bar{1}2\bar{1}0]$ zone axis have the maximum Schmid factor of 0.499 and are expected to be more active than the other four twin variants which have a Schmid factor of 0.125, particularly during the initial several loading cycles. This offers the best situation to study the co-zone twin-twin interaction. The testing specimen was initially compressed until a peak strain of -0.75% was reached. After slightly unloaded from the compression peak strain to a strain of -0.725%, the specimen surface was examined by SEM and EBSD with a scan resolution of 0.5 μm. The testing specimen was subsequently subjected to fully reversed strain-controlled tension-compression at a strain amplitude of 0.75% for 30 loading cycles. During the cyclic loading, morphology change of the deformation twin was traced on the specimen surface using the *in situ* long-distance optical microscope. After fatigue loading, three dimensional geometric and crystallographic characters of twin-twin boundary were examined by utilizing SEM/focused ion beam (FIB) and transmission electron microscopy (TEM) techniques.

3.3 Cyclic Deformation and Morphology Evolution of Tension Twin in the [0001] Direction

Fully reversed strain-controlled tension-compression experiment was conducted at a strain amplitude of 0.5% for the magnesium single crystal in the [0001] direction. Direct *in situ* observations via OM together with the corresponding stress-strain response will be discussed in detail. To facilitate a discussion of the optical observation

of twins, twin variants on the $(1\bar{1}02)$, $(0\bar{1}12)$, $(\bar{1}102)$, and $(01\bar{1}2)$ twinning planes will be referred to as "inclined twins" and twin variants on the $(10\bar{1}2)$ and $(\bar{1}012)$ twinning planes will be cited as the "horizontal twins."

The cyclic deformation experiment starts with tension. Figure 18 shows the stress-plastic strain curve, twin volume fraction evolution, and the corresponding *in situ* optical micrographs at critical points during the initial tension loading reversal. Upon the tensile loading from the virgin state (Figure 18c), the material yields very quickly. This immediate yielding behavior can be attributed to the activation of basal slip. Although basal slip is not favorable in a perfectly *c*-axis aligned loading direction, a slight misalignment of the loading direction from the *c*-axis can easily lead to the activation basal slip due to its very low critical resolved shear stress (CRSS) of ~0.5 MPa. With further tensile loading, a careful examination of the stress–plastic strain curve (Figure 18a) reveals that at a stress of ~4.8 MPa corresponding to a total strain of ~0.0164%, the work hardening rate suddenly reduces to almost zero and the material starts to exhibit serrated plastic flow. Figure 18d (point P1 in Figure 18a) shows the appearance of two fresh-nucleated twins, an inclined $\{1\bar{1}02\}$ or $(0\bar{1}12)$ twin and a horizontal $(10\bar{1}2)$ or $(\bar{1}012)$ twin. The horizontal twin tip is blocked at the inclined twin boundary. Due to a relatively low video recording rate at 0.7 fps, the exact moment and site of twin nucleation are not captured in the observation window. Knowing that the Schmid factor of $\{10\bar{1}2\}$ tension twin is 0.499 under current loading direction, the CRSS for $\{10\bar{1}2\}$ twining is identified to be ~2.4 MPa. This value is higher than ~2 MPa reported by Reed-Hill and Robertson [25] but lower than ~5.5 MPa reported recently by Chapuis and Driver [33]. The inconsistent CRSS values reported

in the literature might be resulted from the unavoidable misalignment of crystal orientation and from the different testing conditions.

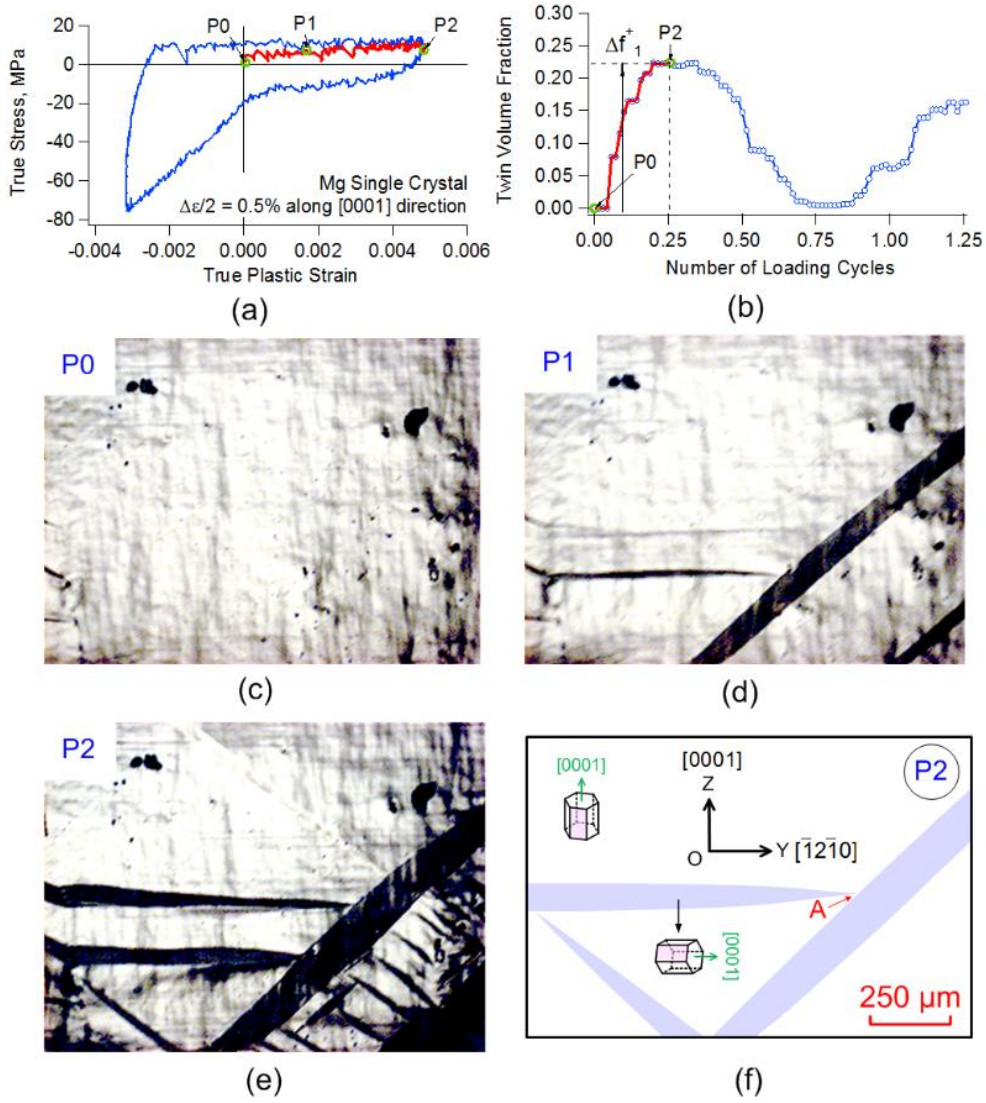

Figure 18 Stress-plastic strain curve, twin volume fraction evolution, and the corresponding *in situ* optical micrographs at critical points during the initial tension phase: (a) stress-plastic strain curve with the initial tension phase highlighted; (b) twin volume fraction evolution from P0 to P3 during the initial tension phase (in solid red color); (c, d, e) optical micrographs at points P0, P1, P2 in (a); (f) schematic illustration of twins at point P2.

During the plastic flow after the activation of tension twin, fresh twins continue to be nucleated at random sites. In the meantime, previously nucleated twins expand wider. A careful *in situ* observation of the twin growth indicates that, once the twin is nucleated, it first propagates very quickly in the direction parallel to the coherent twin plane, either cutting through the gage section or meeting some pre-existing twin boundaries. After a complete elongation, the twin expands along the direction normal to the coherent twinning plane to accommodate further tensile straining. The degree of twin expansion at the midway between the two twin tips is larger than that at the regions near the two twin tips. Consequently, a lenticular shape is resulted for tension twin. Compared to the speed of twin expansion, the twin elongation immediately following the twin nucleation is completed almost in a sudden. As seen in Figure 18a, the stress-plastic strain curve during this period proceeds by alternated small stress increment and drop, showing a serrated plastic flow with an overall zero work hardening rate. A similar serrated flow behavior is observed in single crystals of copper [142], iron [143], zinc, tin, and bismuth [144, 145]. The irregular flow behavior indicates that the plastic deformation in the gage section of the testing specimen was highly inhomogeneous. Knowing that the lattice rotation during twin growth has an internal stress relaxation effect [17, 146], the small macroscopic stress drop can be ascribed to the nucleation and growth of fresh twins. Meanwhile, with a misorientation angle of 86.3° between the basal plane in the twin and that in the matrix, the Schmid factor for basal slip in the twin is significantly increased compared to that in the matrix. Therefore, basal slip is to occur more likely in the twin than in the matrix. Strain hardening caused by the basal slip in the twin might contribute to the small stress increment right following the

stress drop. It is also suggested that, as a consequence of basal slip in the twin, the <*a*> type dislocation intends to converge and accumulate in the vicinity near the twin boundary inside the twin rather than inside the matrix. At the tensile peak of P2 (Figure 18e and Figure 18f), all the deformation twins are fully expanded. The only observed twin-twin interaction at that moment is that one twin tip is blocked by another twin boundary (arrow A in Figure 18f). No crossing-like twin-twin interaction structure is observed. Twin volume fraction is increased to ~0.22 from point P0 (virgin state) to point P2 (tensile peak strain of 0.5%), as shown in Figure 18b.

Upon unloading from the tensile peak at point P2, the stress-plastic strain curve immediately flows nonlinearly showing almost no linear part (Figure 19a). This phenomenon is regularly cited as a pseudoelasticity phenomenon in magnesium alloys [134–138]. This nonlinear flow right after unloading is usually attributed to partial shrinkage of the twins developed prior to unloading [134–138]. However, *in situ* optical images shows that no morphologic change of twins is detected during this unloading period until a compressive reloading stress of about -6 MPa (point P3 in Figure 19a) is reached. At point P3 with a compressive stress of approximately -6 MPa, slight shrinking of a horizontal twin is detected, signifying the advent of "detwinning" (comparing twins at the tensile peak stress (Figure 18e) to those at the stress of -6 MPa (Figure 19c)). Therefore, there is no direct experimental evidence showing that the nonlinear unloading behavior observed in a magnesium single crystal is due to partial detwinning. A reasonable hypothesis of the cause can be ascribed to the easy reverse movement of mobile <*a*> dislocations which are accumulated in the region near the

twin boundary. Another possible reason is that certain detwinning events do exist but are not captured in our observation window.

With further compressive reloading beyond point P3 in Figure 19a, the work hardening rate of the compressive flow keeps a gradually decreasing low value. *In situ* optical observations reveal that detwinning during this period can be described as a reverse movement of the expanded twin boundary in the thickness dimension. No shortening of the twin length is detected during detwinning. Moreover, unlike the sudden nucleation and fast growth of fresh twins, detwinning is a much slower and gradual process. During the low work-hardening portion from P3 to P4 (red highlighted portion in stress-plastic strain curve in Figure 19a), only ~34% of the previously developed twins are detwinned (see Figure 19b). If the plastic strain during the initial tension from P0 to P2 is assumed to be most accommodated by twinning, detwinning is not the sole deformation mode during the compressive reversal from P3 to P4. It is suggested that the remaining part of the plastic strain during this stage is accommodated by basal slip.

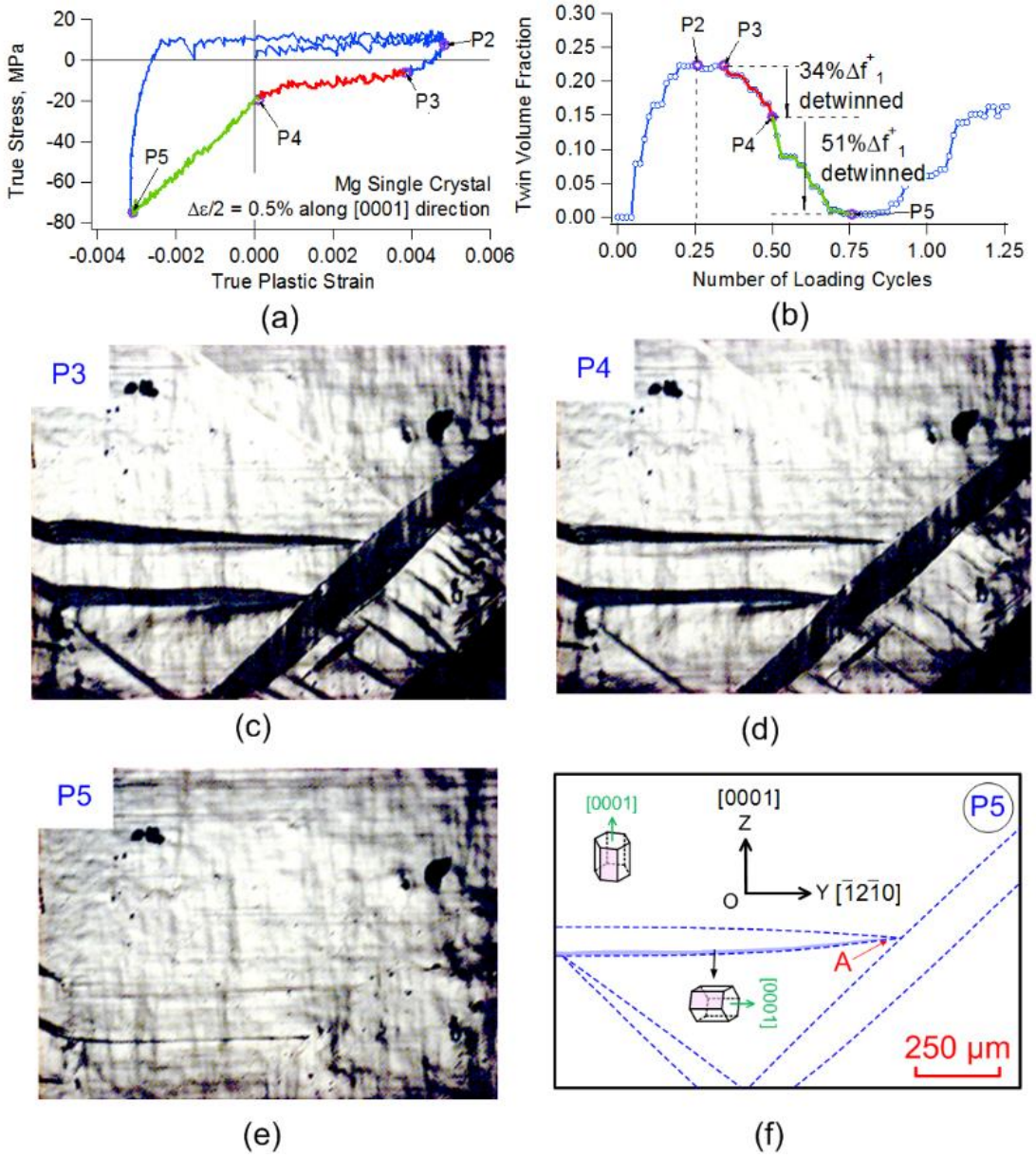

Figure 19 Stress-plastic strain curve, twin volume fraction evolution, and the corresponding *in situ* optical micrographs at critical points during the first compressive reversal: (a) stress-plastic strain curve with the compressive reversal highlighted; (b) twin volume fraction evolution from P3 to P5 during the compressive reversal (in solid red and green colors); (c, d, e) optical micrographs at points P3, P4, P5 in (a); (f) schematic illustration of twins at point P5.

With further compression from P4 to P5 (green highlighted part in stress-plastic strain curve in Figure 19a), detwinning continues. The most prominent difference between this period and that from P3 to P4 is the significantly increased work hardening rate. Since no markings of compression twins are observed within the stress range under compression, the increase of the work hardening rate can be attributed to the activation of nonbasal slip, most likely the 2nd pyramidal <*c*+*a*> slip. As indicated in Figure 19b, approximate 51% twin volume fraction which have been developed in the initial tension is detwinned during this period. At the compressive peak of P5 (Figure 19e and Figure 19f), most twins developed during the initial tensile phase are detwinned. However, a residual $(10\bar{1}2)$ or $(\bar{1}012)$ twin having a width of ~2 μm is observed (see Figure 19e).

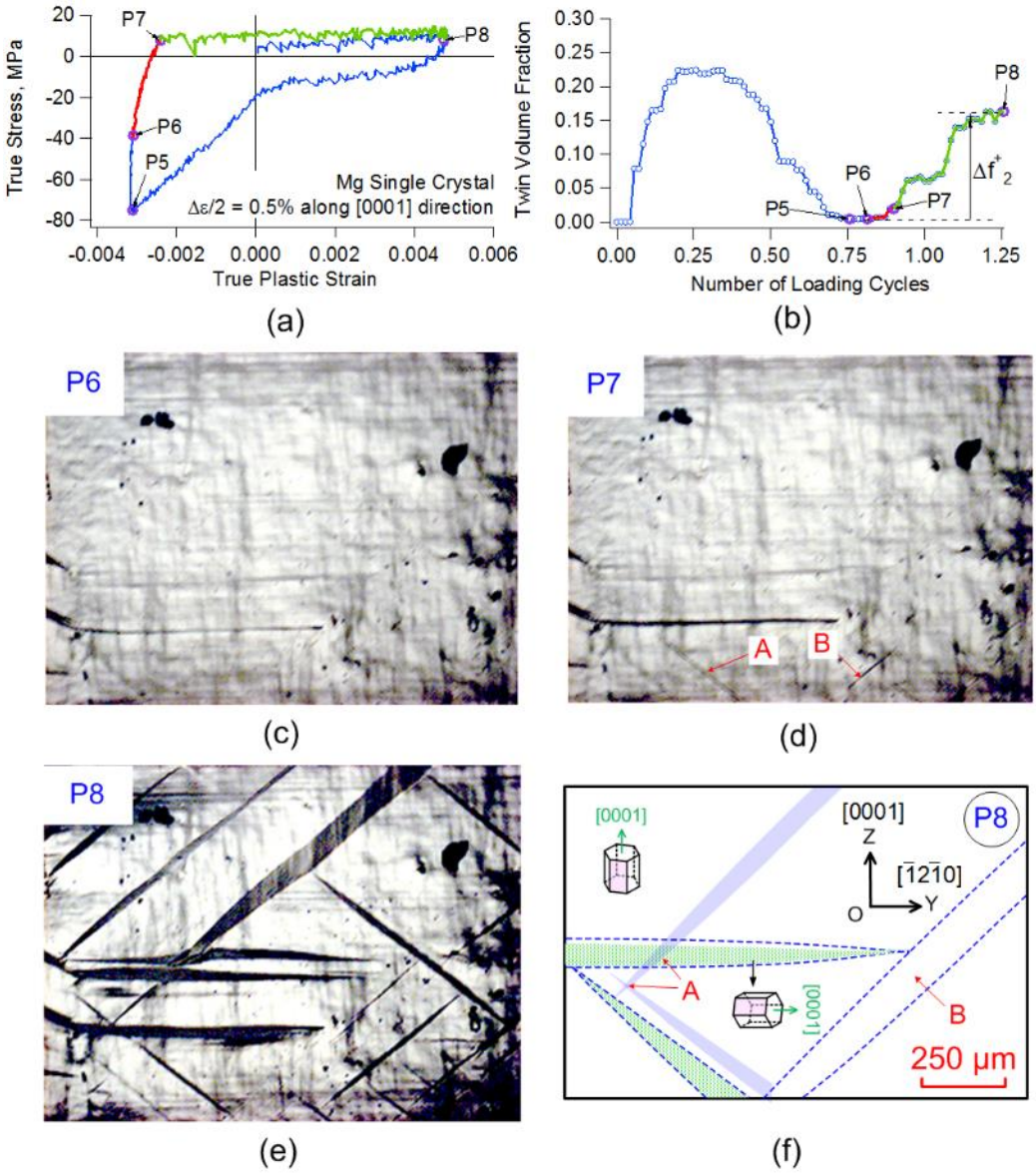

Figure 20 Stress-plastic strain curve, twin volume fraction evolution, and the corresponding *in situ* optical micrographs at critical points during the compressive unloading and tensile reloading: (a) stress-plastic strain curve with the compressive unloading and tensile reloading highlighted; (b) twin volume fraction evolution from P5 to P8 during the compressive unloading and tensile reloading (in solid red and green colors); (c, d, e) optical micrographs at points P6, P7, P8 in (a); (f) schematic illustration of twins at point P8.

During unloading from compressive peak P5 to a compressive stress of -40 MPa at P6, the residual twins observed at P5 keep unchanged (comparing twins at the compressive peak stress (Figure 19e) to those at the stress of -40 MPa Figure 20c). This observation can be confirmed by the unchanged twin volume fraction from P5 to P6 (Figure 20b). In the meantime, the stress-plastic strain curve remains approximately linear from P5 to P6 but become nonlinear after P6 (Figure 20a). The coincidence between the start of nonlinear portion and the start of twinning at a compressive stress of -40 MPa indicates that twinning is responsible for the nonlinear plastic flow during compressive unloading. Also, it is a direct evidence showing that twinning can be activated at a compressive external loading along the *c*-axis. The same observation was obtained by Wu et al. [17] using *in situ* neutron diffraction in ZK60 magnesium alloy. By measuring the internal stress, Wu et al. [17] reveal that although the residual twin is subjected to an external stress suppressing twinning, the internal stress exposed on the residual twin can result in an opposite effect, which drives twinning of the residual twin.

With further unloading beyond P6 until P7, slight expansion of the residual twin (comparing Figure 20c and Figure 20d) is observed. The twin volume fraction is increased by ~2% during this period. At point P7 with a tensile stress of ~7.8 MPa, the material yields abruptly. A careful observation indicates that one inclined twin reappears from its previous twinned-detwinned site (arrow A in Figure 20d). In addition, a fresh inclined twin is nucleated (arrow B in Figure 20d). From P7 to P8, the stress–plastic strain curve becomes serrated again. Fresh twins are nucleated again and grow in the same fashion as those during the initial tension. The widths of the

freshly developed twins during this period are smaller than those formed in the initial tension. The newly formed twins are not exactly the same ones from the initial tensile quarter. Some previously twinned and detwinned positions experience twinning again, which is termed as "retwinning." Retwinning is generally initiated at the center of the previously fully developed twinned area. However, some twinned–detwinned sites do not experience retwinning (arrow B Figure 20f). Expansion of the retwinning area has a slow speed similar to that of detwinning. The pre-expanded twin boundaries at the tensile peak stress are never exceeded by retwinning. As shown in Figure 20b, the twin volume fraction from P6 to P8 is increased by ~16%, smaller than that (~22%) from the initial tension. At the tensile peak P8, crossing-like twin-twin interactions (arrow A in Figure 20f) appear. One newly nucleated twin "penetrated" a retwinned area.

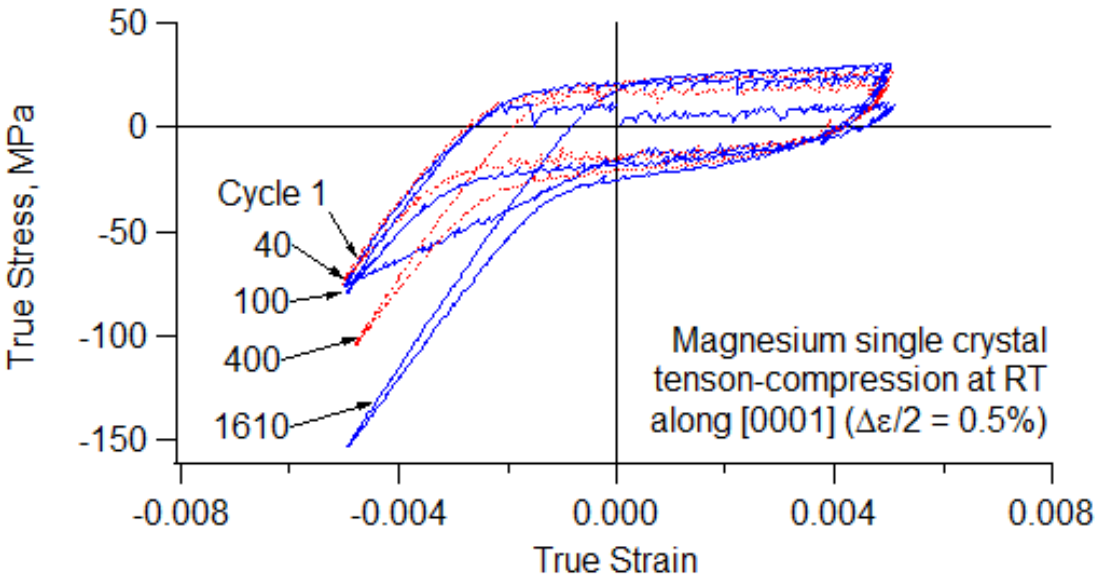

Figure 21 Cyclic stress-strain hysteresis loops from the first loading cycle to the 1610th loading cycle in magnesium single crystal under fully reversed tension-compression at strain amplitude of 0.5% in [0001] direction.

Figure 21 shows the cyclic stress-strain hysteresis loops from the first loading cycle to the 1610th loading cycle. It is clear that all the stress-strain hysteresis loops exhibit asymmetric shape showing three featured portions: twinning, detwinning, and detwinning accompanied by nonbasal slip. The tensile reversal shows a serrated flow shape with a very low work-hardening rate which starts at a tensile stress of approximate 8 MPa. During the compressive reversal at approximate -6 MPa, the stress-strain curve starts to flow with a low work hardening rate until most of the plastic strain produced in the previous tensile loading is reversed. This low work hardening portion is accompanied by detwinning where only about 50% twin volume fraction produced in the previous tensile loading is detwinned. For the remaining portion of the compressive reversal, the flow curve proceeds with a significantly increased work hardening rate until the compressive peak is reached. The largely increased work hardening rate is ascribed to the activation of nonbasal slip under the *c*-axis compression. It is noted that accompanying the nonbasal slip, detwinning and the residual twin formulation continue. The low work hardening portion in the compressive reversal is always terminated when ~50% twin volume fraction produced in the previous tensile reversal is detwinned.

Figure 22 shows the *in situ* optical observations at the tensile and compressive peak stresses corresponding to the cyclic stress-strain hysteresis loops shown in Figure 21. As the loading cycle increases, the volume fraction of the residual twins increases. Meanwhile, the width of the residual twins is significantly reduced. The formation of new twins persisted during the tensile reversal, and generally occurs close to the previously developed residual twins possessing the same orientation. A careful *in situ*

observation reveals that after detwinning is complete, one side or two sides of the twin area serves as the sources to form a narrow residual twin. This is evident by comparing the optical images at tensile and compressive peak stresses at the 40th cycle in Figure 22.

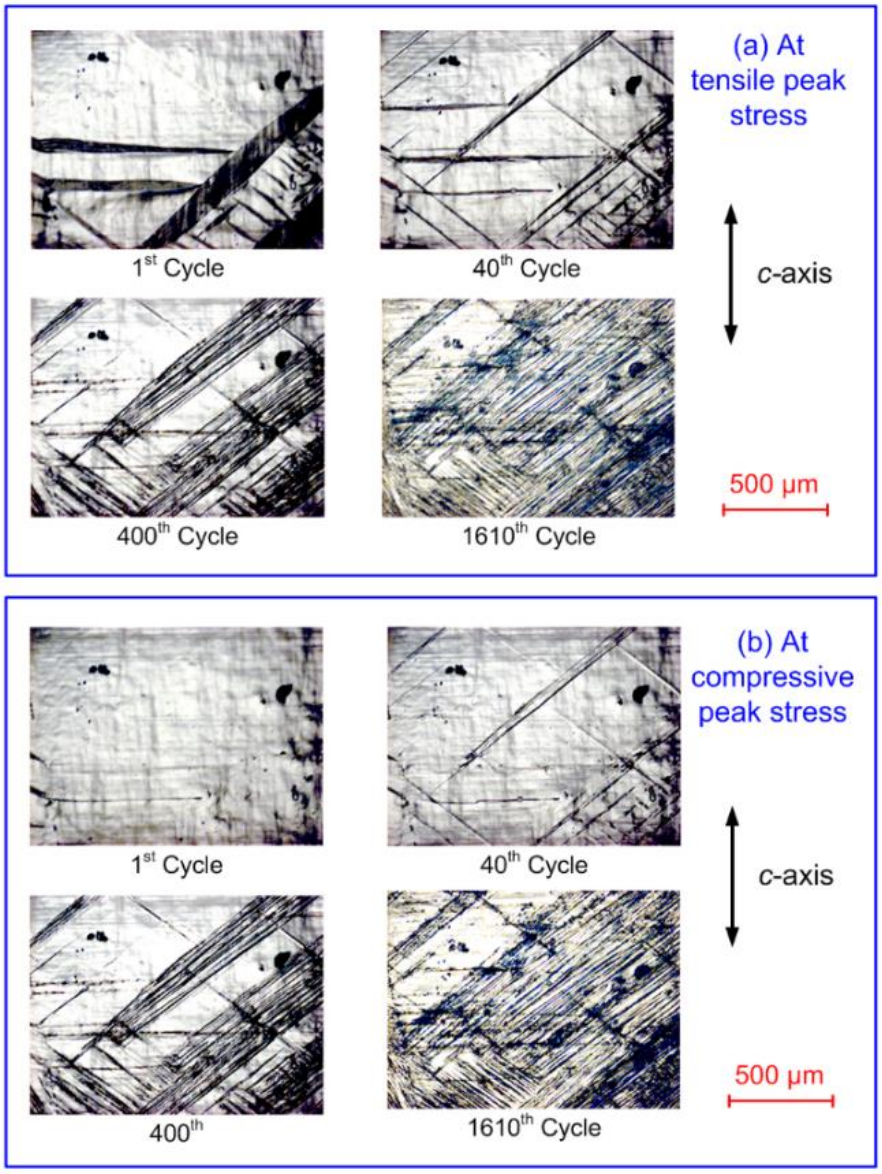

Figure 22 *In situ* optical microscopic observations at tensile peak stress (a) and compressive peak stress (b) corresponding to the cyclic stress-strain hysteresis loops shown in Figure 21.

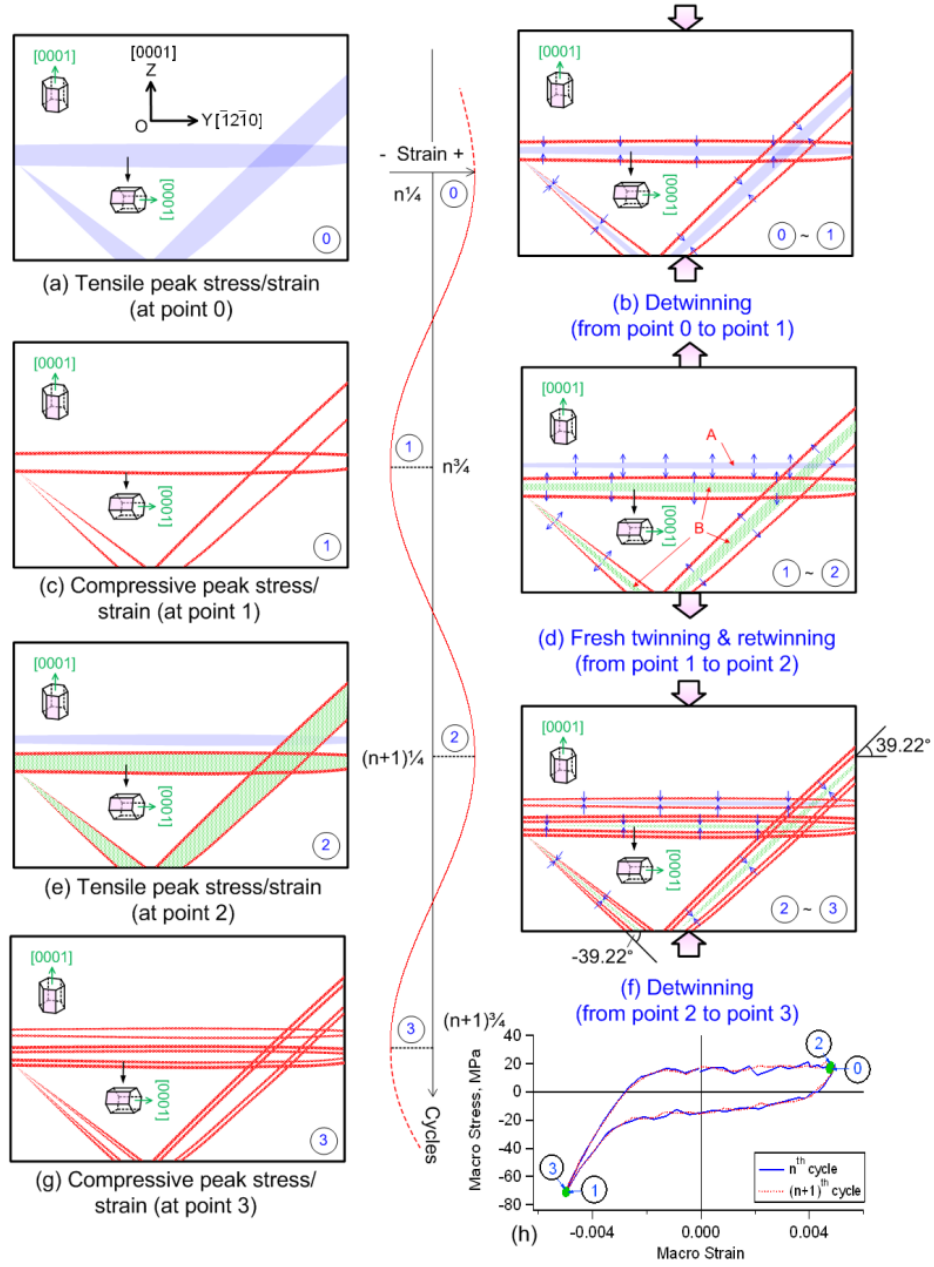

Figure 23 Schematic illustration of the development of residual twins during two consecutive loading cycles (the $(n)^{th}$ (previous) and $(n+1)^{th}$ (current) loading cycles): (a and c) tensile and compressive peaks at the nth loading cycle; (e and g) tensile and compressive peaks at the $(n+1)^{th}$ loading cycle; (b and f) detwinning during the n^{th} and $(n+1)^{th}$ loading cycles; (d) fresh twinning and retwinning; and (h) stress–strain hysteresis loops for the n^{th} and $(n+1)^{th}$ loading cycles.

To explain more clearly the development of the residual twin, two consecutive loading cycles (the n^{th} (previous) and $(n+1)^{th}$ (current) loading cycles) are considered and schematically illustrated in Figure 23. During the initial stage of compression (Figure 23b) from the tensile peak (Figure 23a) to the compressive peak (Figure 23c) at the n^{th} loading cycle, the twinned region with a thickness of ~2 to ~3 μm close to the pre-expanded twin boundaries at the n^{th} tensile peak is "pinned" and is generally unable to reorient their *c*-axes back to align with that of the matrix. With further compression, the twinned region lying beyond ~2 to ~3 μm away from the pre-expanded twin boundaries at the n^{th} tensile peak is found to be fully detwinned. Consequently, at the compressive peak of the n^{th} loading cycle (Figure 23c), the residual twins are found to have a width of 2~3 μm with their positions on the vicinities of the twin boundaries fully expanded at the n^{th} tensile peak (comparing Figure 23a and Figure 23c). During the subsequent tensile reloading (Figure 23d), fresh twins persist to be nucleated at the sites aligning closely with the residual twins formed earlier (arrow A in Figure 23d). Together with fresh twins, the detwinned areas during the n^{th} compressive reversal are able to be retwinned (arrow B in Figure 23d). As a result, at the tensile peak of the $(n+1)^{th}$ loading cycle (Figure 23e), a slightly increased twin area comparing with that at the n^{th} tensile peak is observed. A similar detwinning process which produced new residual twins is observed during the compression at the $(n+1)^{th}$ loading cycle (Figure 23f). It is noticed that a narrow band of matrix always exists between newly formed residual twins and those formed during the n^{th} compression reversal. By means of the schematically illustrated process, the accumulated residual twins are regarded as "propagating" over the entire gage section with increasing loading cycles (comparing

the image at the compressive peak of the 400th loading cycle and that of the 1610th loading cycle in Figure 22).

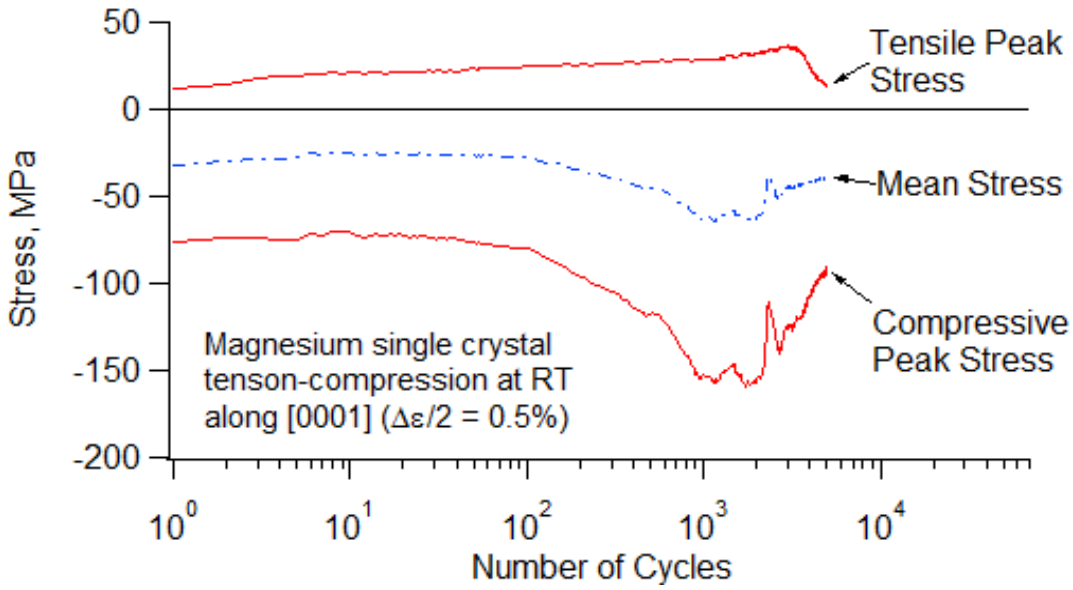

Figure 24 Variation of the tensile and compressive peak stresses with respect to number of loading cycles in magnesium single crystal subjected to fully reversed tension-compression at a strain amplitude of 0.5% in [0001] direction.

Figure 24 shows the variation of the peak stress responses with respect to the increasing number of loading cycles in magnesium single crystal loaded under fully reversed tension-compression at a strain amplitude of 0.5% in [0001] direction. With the increasing number of loading cycles, the tensile peak stress increases slightly while the compressive peak stress increases significantly (Figure 24). After approximately 1,000 loading cycles, cyclic hardening of the compressive peak stress becomes saturated. Cyclic hardening for both the tensile and compressive peak stresses is terminated after approximately 3,000 cycles. The cause of cyclic hardening can be associated to the considerable increase in residual twin boundary and residual twin

fragmentation as well as the increased densities of dislocation induced at the repeated twinned and detwinned matrix. Twin-twin interaction is also a critical mechanism responsible for the cyclic hardening of the material, which will be studied in detail in Chapter four.

As a consequence of cyclic hardening, the twinning and detwinning stresses increase while the number of twins involved in twinning and detwinning decreases until a saturation state is eventually reached [111, 120]. From the persistent asymmetric shape of the cyclic stress-strain hysteresis loops in Figure 21, it is noted that twinning/detwinning saturation is never reached but being approached, even though no detectable change of twins at tensile peak and compressive peak is observed when the number of loading cycles is greater than 1,600 cycles. After approximate 3,000 cycles, both the tensile and compressive peak stresses are found to decrease, indicating cyclic softening in the later stage of the cyclic loading. SEM observations suggest that the cyclic softening is caused by accumulation of microcracks which initiate at the residual twin boundaries and show limited propagation.

3.4 Microstructure Characterization of the Fatigued Specimen Loaded in the [0001] Direction

3.4.1 Scanning Electron Microscopy of Microcrack

Figure 25 shows the SEM examination of microcracks on the prismatic plane in the magnesium single crystal after termination of the experiment at the 5,019th loading cycle. In high magnified images (Figure 25c and Figure 25d), the residual twins are identified as dark narrow bands. The bright contrasted regions are locations where the

microcracks developed. In low magnified images (Figure 25a and Figure 25b), only the bright contrasted microcracks are visible. Microcracks are densely distributed over the entire gage section of the testing specimen with limited propagation.

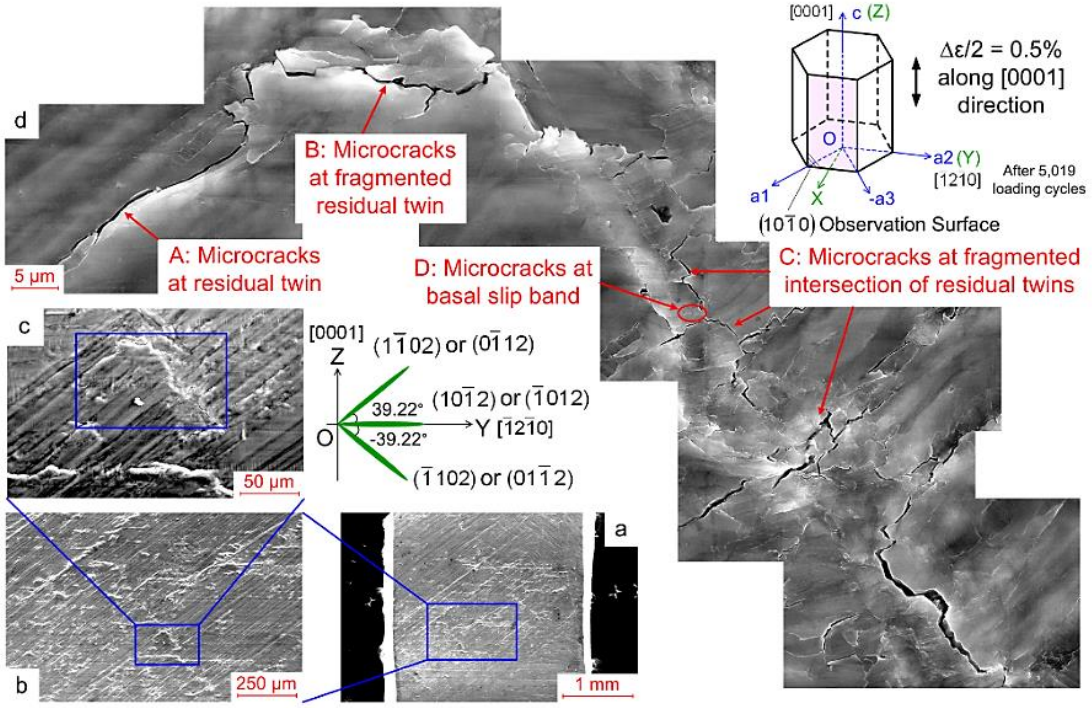

Figure 25 SEM observation of fatigue microcracks on the prismatic plane in magnesium single crystal subjected to fully reversed tension-compression at a strain amplitude of 0.5% in [0001] direction after 5,019 loading cycles: (a, b) low magnification; (c, d) high magnification.

The high magnification SEM image (Figure 25d) clearly shows that four types of microcracks are developed: (1) smooth long microcracks at the boundaries of inclined residual twins (A in Figure 25d); (2) serrated short microcracks at the boundaries of the fragmented horizontal residual twins (B in Figure 25d); (3) serrated short microcracks developed at the fragmented intersections of residual twins (C in Figure 25d); and, (4) short microcracks at the basal slip band (D in Figure 25d). The microcracks are

inhabited at the crystallographic planes of $\{10\bar{1}2\}$ tension twins or basal slip. The current observation of fatigue microcracks on the magnesium single crystal is consistent with the early results by Partridge [98–101] who demonstrated that fatigue cracks are developed at slip bands and twin fragments for coarse-grained polycrystalline magnesium.

3.4.2 Optical Microscopy of Slip Band and Residual Twin

Figure 26 shows the optical micrographs of the microstructures developed on the prism plane in the magnesium single crystal after 5,019 loading cycles. Several microstructural changes are observed on the prismatic plane: basal and prismatic slip bands (Figure 26a), basal slip band extrusion (Figure 26b), accommodation kinks (Figure 26c), and fragmented residual twins (Figure 26d). Basal slip bands and prismatic slip bands are observed to intersect in the matrix region which have experienced repeated twinning and detwinning (Figure 26a).

Prismatic slip bands, which are much fewer than the basal slip bands, are mostly found at narrow spacing between two neighboring residual twins and terminated at the neighboring twin boundaries. Unlike the close-spaced long basal slip bands, short prismatic slip bands are separated sparsely. The spacing of prismatic slip bands is approximately 2~3 times wider than that of basal slip bands. The observation of prismatic slip bands together with the crossed basal slip bands is an evidence that prism-basal cross-slip was activated at local regions during the high work hardening detwinning period.

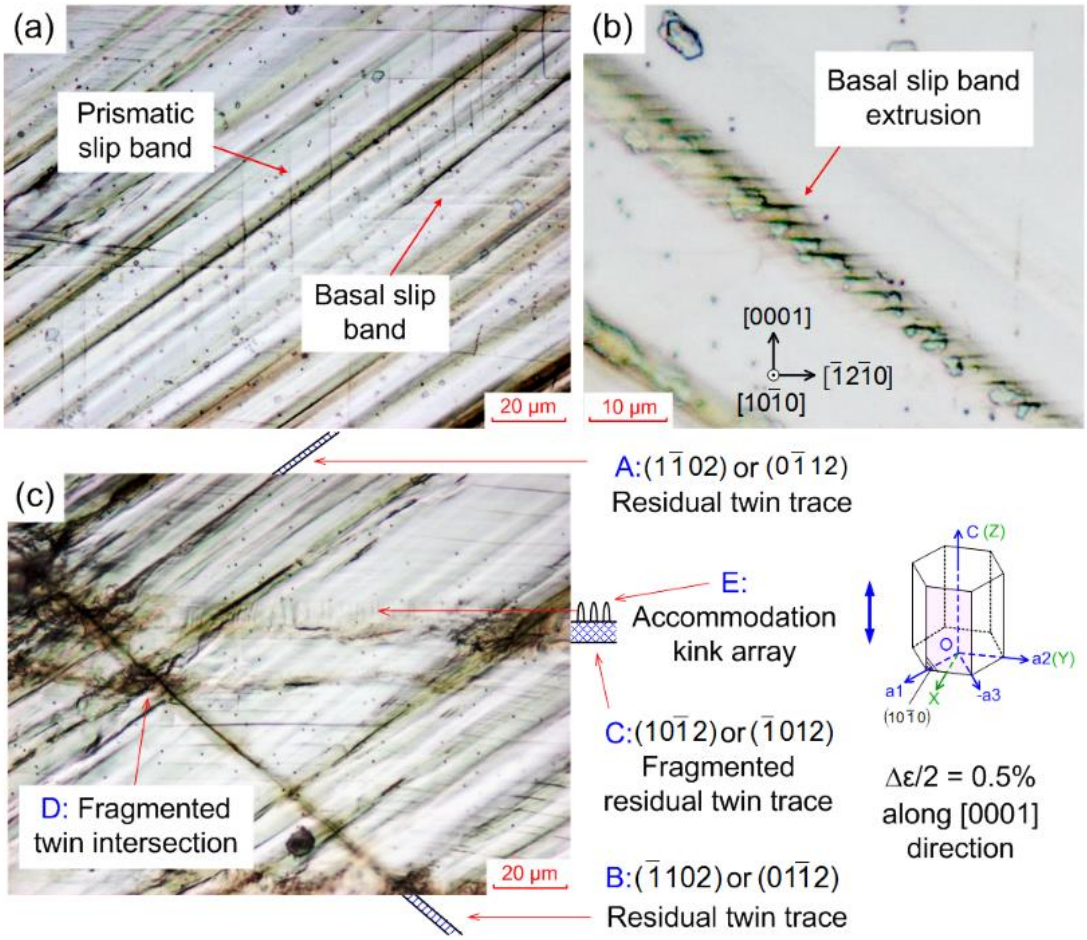

Figure 26 Optical micrographs of basal and prismatic slip bands (a), basal slip band extrusion (b), accommodation kinks (c), and fragmented residual twins (d) on the prismatic plane in the [0001]-oriented magnesium single crystal having experienced cyclic tension-compression at the strain amplitude of 0.5% for 5,019 loading cycles.

As shown in Figure 26b, slip band extrusions are found on the basal plane in a fully-detwinned matrix region. The spacing between the slip band extrusions is ~1.2 μm. The basal-slip band extrusions are constricted within the matrix region which has experienced repeated twinning and detwinning. This is indicated by the brown shaded region in Figure 26b, which delineates the original position of the twin. This result is consistent with Partridge's observation of extrusion at the region where a twin is first

detwinned and subsequently subjected to fatigue loading [100]. A model based on the glide of glissile prismatic dislocation dipole was proposed by Partridge [100] to explain the formation of extrusion.

Figure 26c shows the development of residual twins (arrow A, B, and C in Figure 26c). The observed residual twins in three orientations agree well with the theoretically predicted projections of the twin planes on the prism plane (Figure 16). The widths for all the residual twins are approximately ~1 to ~2 μm. Contrast to the relatively smooth boundaries of the inclined residual twins, the horizontal residual twins are broken into small fragments having serrated boundaries. At the interaction sites of different residual twin variants, fragmentation is found to develop more severely (arrow D in Figure 26c). Moreover, an array of close-spaced micro-accommodation kinks is found to attach vertically with the serrated boundaries of horizontal twins (arrow E Figure 26c). However, for the inclined residual twins, no such micro-accommodation kinks are observed. The detailed geometry and crystallography analysis of accommodation kinks formation on the sample surface is carried out by Robert and Partridge [56]. The observation of fragmentation of twins associated with the micro-accommodation kinks were also observed on coarse-grained polycrystalline magnesium by Partridge [101]. The author attribute the phenomena as a result of interaction between the twin boundary and the pinned dislocations at the twin boundary located in both the twin and the matrix under cyclic stressing. Although the proposed model can qualitatively explain the cause of serrated twin boundary, the fundamental mechanism of the fragmented twin-twin interaction sites is unknown. To reveal this mechanism, it is necessary to identify the crystal orientations at the twin-twin interaction area.

3.4.3 Electron Backscatter Diffraction Microscopy of Matrix, Residual Primary, and Secondary Twins

Following the OM examination on the specimen surface after fatigue loading, EBSD scan was conducted on a further polished and etched surface area of 1,920 μm × 640 μm located within the gage section of the testing specimen. A discrete (0001) pole figure generated from the EBSD data is presented in Figure 27. To facilitate a discussion, symbol T_i (i = 1 to 6) are used to stand for $(10\bar{1}2)$, $(01\bar{1}2)$, $(\bar{1}102)$, $(\bar{1}012)$, $(0\bar{1}12)$, and $(1\bar{1}02)$ primary twin variants, respectively. Also, T_{ij} (i, j = 1 to 6) are used to indicate a secondary tension twin T_j activated within the primary tension twin T_i.

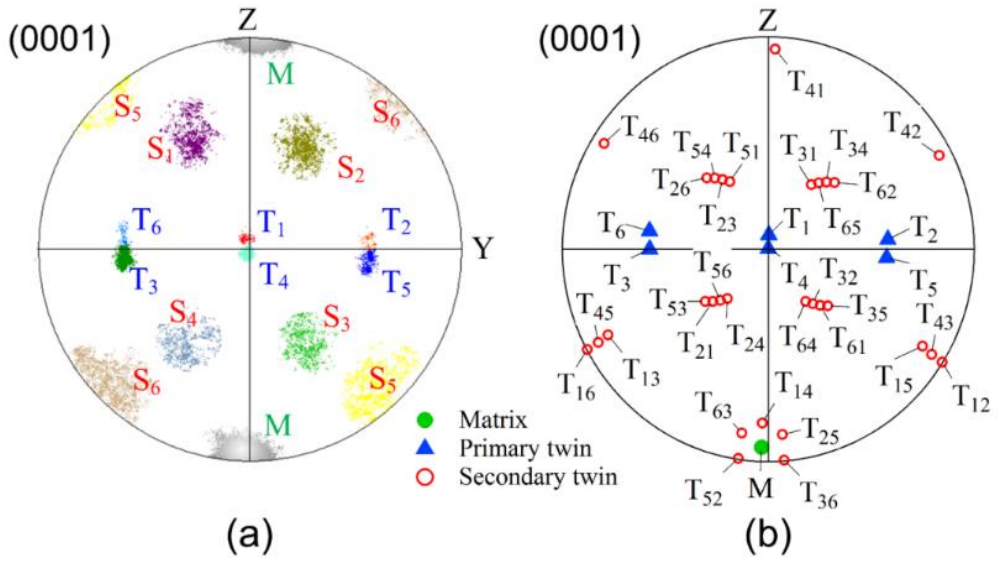

Figure 27 Texture development generated from the EBSD data scanned on the prismatic plane in the [0001]-oriented magnesium single crystal having experienced cyclic tension-compression at the strain amplitude of 0.5% for 5,019 loading cycles: (a) discrete (0001) pole figure with the converged pole regions highlighted in different colors; (b) the calculated (0001) pole figure of the original matrix (M), primary tension twins (T_i, i=1 to 6), and secondary tension twins (T_{ij}, i, j = 1 to 6).

As seen in Figure 27a, 13 regions are identified: the matrix region M, six primary twin regions T_i (i =1 to 6), and six secondary twin regions S_i (i =1 to 6). In order to distinguish the regions corresponding to the converged pole regions on the EBSD scan area, the 13 converged pole regions are selected and highlighted in different colors by choosing appropriate tolerances of misorientation angle. Tolerance of misorientation denotes the maximum deviating misorientation angle between the crystal orientation in the selected set and that at the selection point. Region M is selected with a tolerance of misorientation angle of 12 °, region T_i with 5 ° misorientation angle, and region S_i with 14 ° misorientation angle.

Table 4 Relationship between 13 converged (0001) pole regions in Figure 27a and the calculated (0001) poles of matrix, primary twins, and secondary twins in Figure 27b.

Converged (0001) pole region in Figure 27a	Calculated (0001) poles in Figure 27b
M	T_{ii}, T_{14}, T_{25}, T_{36}, T_{41}, T_{52}, T_{63}
T_i (i=1 to 6)	T_i (i = 1 to 6)
S_1	T_{26}, T_{23}, T_{51}, T_{54}
S_2	T_{31}, T_{34}, T_{62}, T_{65}
S_3	T_{32}, T_{35}, T_{61}, T_{64}
S_4	T_{56}, T_{63}, T_{21}, T_{24}
S_5	T_{12}, T_{15}, T_{46}, T_{43}
S_6	T_{16}, T_{13}, T_{42}, T_{45}

The relationship between the theoretical secondary twin poles shown in Figure 27b and the regions S_i shown in Figure 27a is summarized in Table 4. To identify the possible variants of secondary twin in the six secondary twin regions S_i in Figure 27a, a theoretical (0001) pole figure is calculated to show the pole locations of matrix, six

primary twins, and 36 secondary twins by stereographical projection method, as visualized in Figure 27b. The crystal orientations in the matrix area where twinning has never occurred are averaged to be the original matrix orientation. Bunge Euler angles of the original matrix are identified to be $(\varphi_1, \Phi, \varphi_2) = (88^\circ, 94^\circ, 58^\circ)$. In Figure 27b, the pole of the matrix is plotted as a green solid circle and is denoted by M. Poles of primary twins are plotted using blue solid triangles and are designated by T_i (i = 1 to 6). Poles of the secondary twins are plotted using red circles and are denoted by (T_{ij}, i, j = 1 to 6) (the secondary twin T_j forms within the primary twin T_i). When i = j, the orientation of the secondary twin is exactly the same as that of the original matrix, signifying detwinning through T_{ii}. It is worth mentioning that secondary twinning via $T_{i(i+3)}$ (i = 1, 2, 3) (T_{14}, T_{25}, T_{36}) and $T_{i(i-3)}$ (i = 4, 5, 6) (T_{41}, T_{52}, T_{63}) will reorient the primary twins back to the orientation close to that of the original matrix, where the deviation misorientation angle is 7.13 °(Figure 27b). The other secondary twins can be categorized into six groups. The maximum difference in the misorientation angle between two secondary twins is almost identical, 12.83 °in each group.

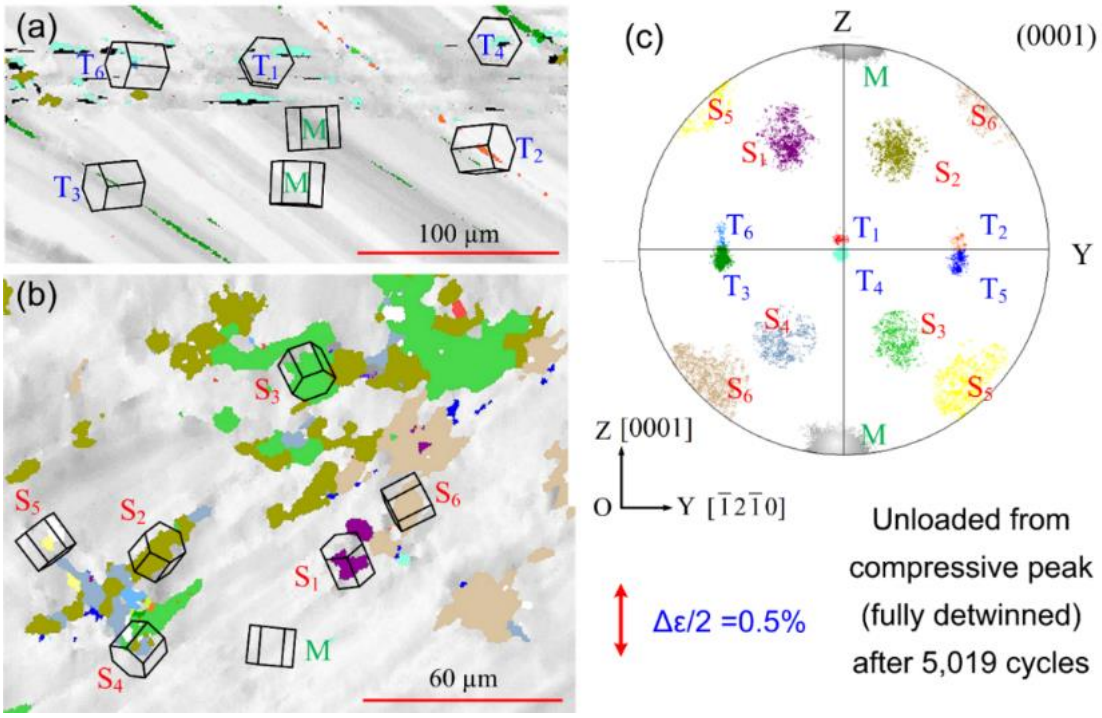

Figure 28 (a) Crystal orientation map showing matrix and residual primary tension twins with areas highlighted in different colors; (b) crystal orientation map showing residual secondary tension twins; (c) discrete (0001) pole figure with converged regions highlighted in colors corresponding to different material domains in (a) and (b).

Figure 28a and Figure 28b illustrate the crystal orientation maps of matrix, residual primary twin, and residual secondary twin, with different material domains highlighted in different colors. The colors are corresponding to different crystal orientation groups of matrix, primary tension twin, and secondary tension twins, as indicated in Figure 28c. Several features of twin structures developed after fatigue are clearly observed: (1) detwinned matrix regions having experienced repeated twinning/detwinning cannot fully reverse to the original orientation of the virgin state; (2) secondary twins are located at the intersection sites among primary twins and possess irregular shapes; and,

(3) a comparison of the volume fractions of primary and secondary twins suggests that detwinning of secondary twins is more difficult than that of primary twins.

Region M in Figure 28a is highlighted in white-grey gradient color. The white color represents the original matrix orientation of the virgin state. The darkest grey color in the gradient spectrum denotes the crystal orientations having a $12°$ misorientation angle from that of the original matrix orientation. The grey regions on the scan surface are narrow lamellar bands with three orientations that coincide with the projected orientations of the primary tension twins (Figure 28a). Referring to Figure 27 and Table 4, it is geometrically possible that the grey poles in region M with their crystal orientations having large misorientation angles with respect to that of the reference crystal could have been resulted from secondary twinning T_{14}, T_{25}, T_{36}, T_{41}, T_{52}, and T_{63}. However, if this type of secondary twinning had occurred, the inclined secondary twinning lamellar bands should lie in the primary twins. As experimentally observed, the grey lamellar bands only coincide with the orientations of the primary twin projections on the prismatic plane and no inclined bands are observed within these grey lamellar bands. In addition, detwinning (or secondary twinning T_{ii}) that chooses the same crystalline plane as that in primary twinning is more kinetically and energetically preferred. Therefore, it is believed that the grey lamellar bands are the crystalline regions that have experienced repeated primary twinning and detwinning but cannot fully reverse to the original matrix orientation after detwinned upon unloading.

Knowing that the grey lamellar bands are not completely reversed to the crystal orientation of the reference crystal after 5,019 loading cycles, it can be deduced that

there must involve immobile residual dislocations during twining/detwinning process. It is well established that in the material where dislocation slips act as the dominant mechanism of cyclic deformation, stable wall/cell dislocation structures and persistent slip bands (PSBs) develop as a result of the complex entanglement of immobilized dislocations [147]. Similarly, after repeated twinning/detwinning process, the glide dislocations within both the matrix and the twin can be activated, and can interact and react with the twin boundaries. Atomistic simulations regarding dislocation-twin boundary interactions show that most lattice dislocations cannot fully transmit the twin boundary in HCP materials [148–150]. As a result, the residual dislocations will be inevitably lose mobility and accumulate in the material. As a consequence of the complex interaction of the immobile dislocations after sufficient loading cycles, certain dislocation substructures can be developed and obstruct the material to completely rotate to either the completely twinned lattice or the original matrix lattice. This explains why the crystal orientation is not completely reversed to that of the original matrix when the material is detwinned. Further TEM characterization in these regions will help to reveal the immobilized dislocation structure and deepen the understanding of the twinning-detwinning mechanisms.

Region T_i (i=1 to 6) in Figure 28a correspond to the poles of six primary tension twin variants (Figure 28c) and are highlighted in red (T_1), aqua (T_4), navy (T_6), green (T_3), orange (T_2), and blue (T_5), respectively. All the residual primary twins are broken and fragmented, aligning aside the grey lamellar bands with three orientations. The degree of the fragmentation in horizontal T_1 and T_4 twins are more severe than that in

the other four inclined twin variants. This observation is consistent with the OM observation (Figure 26c).

The secondary twin regions S_i (i=1 to 6) in Figure 28b are highlighted in yellow, tan, lime, dark-yellow, light-blue, and violet, respectively. These regions are found severely fragmented with irregular polygonal shapes. Moreover, the secondary twin fragments are mainly located at the intersection areas where two or three different orientated lamellar bands in grey color are met. Since the lamellar bands in grey color represent the regions where primary twinning/detwinning process has occurred, it can be deduced that secondary twinning is activated during the interaction of primary twin variants under a certain local stress state. A procedure can be followed to identify the interacting primary twins by which a secondary twin is activated. Taking the secondary twin fragment S_2 in Figure 28b as an example, the elongated fragment is found to be located at a grey lamellar band oriented 39.22 ° with respect to the *Y*-axis. According to Figure 16a, the 39.22 ° inclined grey lamellar band is the projection of the primary twin T_5 or T_6. Referring to Figure 27 and Table 4, the crystal orientations in region S_2 can only be resulted from secondary twinning within primary twin T_3 or T_6. Therefore, T_6 is determined as the parent twin for the S_2 secondary twin fragment in Figure 28b. Additionally, it is noted that a -39.22 ° inclined grey lamellar band (T_2 or T_3 as indicated in Figure 28a) is connected to the S_2 fragment as well. It can be seen that this secondary twin fragment is activated during the interaction between primary twin T_6 and primary twin T_2 or T_3. Since S_2 fragment can only be T_{62} or T_{65}, it can be derived that T_{62} is the variant type of the S_2 fragment in Figure 28b. Such an analysis to identify the parent

twin and its interacting counterpart for the secondary twin fragment is not suitable for those secondary twin fragments having irregular shapes.

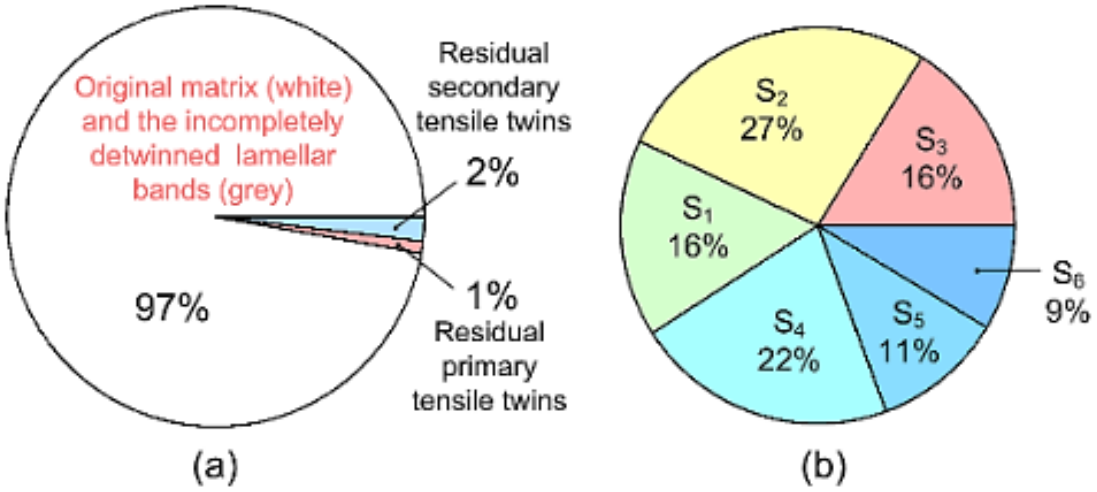

Figure 29 (a) Area fractions on the entire EBSD scan area; (b) area fraction of the residual secondary tensile twin region S_i.

Figure 29 shows the area fractions on the entire EBSD scan area. Approximately 97% of the scan area is the region where crystal orientations lie in the vicinity of the original matrix orientation with a maximum 12 ° misorientation angle (Figure 29a). This region contains two parts: the virgin material where twinning has never occurred and the narrow lamellar bands with an orientation incompletely detwinned to that of the matrix. The remaining ~3% of the scan area is composed of secondary twin fragments (~2%) and primary twins (~1%). It is interesting to note that the area fraction of secondary twin fragments is approximately twice as that of primary twins. It should be reiterated that when the experiment is terminated after 5,019 loading cycles, the specimen is unloaded from the compression peak where detwinning was completed. The smaller amount of residual primary twins than that of residual secondary twin fragments after detwinning indicates that primary twins are much easier to be

detwinned as compared to secondary twins. It is known that tension twinning makes the twin lattice reoriented nearly 90° to the matrix lattice. Therefore, if the external loading favors primary twinning (or detwinning), it will suppress secondary twinning (or detwinning). Accordingly, during the last loading step when primary twin is detwinned under compressive stress along the [0001] direction, secondary twin fragments will be generally subjected to *c*-axis tension without detwinning. Moreover, since the secondary twins are activated within the narrow lenticular primary twins, the pinning effect of primary twin boundary on the secondary twin dislocations will be more severe, which makes secondary detwinning more difficult. Figure 29b further shows a pie chart plotting the area fractions of different converged secondary twin regions S_i (refer to Figure 27). It is found that secondary twin fragments in six different orientation groups have almost uniform area fractions. Referring to Table 4, it is known that secondary twin fragments in regions S_1 can be equally activated in T_2 and T_5 (S_4 equally in T_2 and T_5, S_2 or S_3 equally in T_3 and T_6, S_5 or S_6 equally in T_1 and T_4). Therefore, it can be concluded that all the six primary twin variants have equal probability to activate secondary twins during their interaction with other primary twin variants under cyclic loading.

3.5 Cyclic Deformation and Fatigue Damage of Mg Crystal Loaded in the [$10\bar{1}0$] Direction

Figure 30 presents the stress-strain hysteresis loops for the magnesium single crystals subjected to fully reversed tension-compression in the [$10\bar{1}0$] direction at three strain amplitudes of 0.5%, 0.75%, and 1%, respectively. The stress-strain hysteresis

loops at the strain amplitudes under investigation are associated with three featured deformation modes: twinning-dominated, detwinning-dominated, and non-basal slips-dominated accompanied by detwinninng. Twinning occurs under the compressive reversal when the resolved shear stress exceeds the critical resolved shear stress (CRSS) for tension twinning. The CRSS to activate tension twin is identified from the initial compression phase. The directly measured value is 2.2~3.0 MPa, which is very close to that (~2.4 MPa) obtained in the [0001] direction [39]. Detwinning accompanies the entire sigmoidal shaped tensile loading reversal. At the inflection point of the sigmoidal curve, the strain hardening rate converts from a gradually decreasing low value to a rapidly increasing high value. The significant increase in the strain hardening rate is ascribed to the operation of non-basal slips [31]. By testing a notched plate under monotonic tension in the $[10\bar{1}0]$ direction, Reed-Hill and Robertson [31] observed the non-basal slip band traces on the specimen surface of magnesium single crystals. It was suggested that the non-basal slip occurring under tension in $[10\bar{1}0]$ direction was of duplex prismatic type [31].

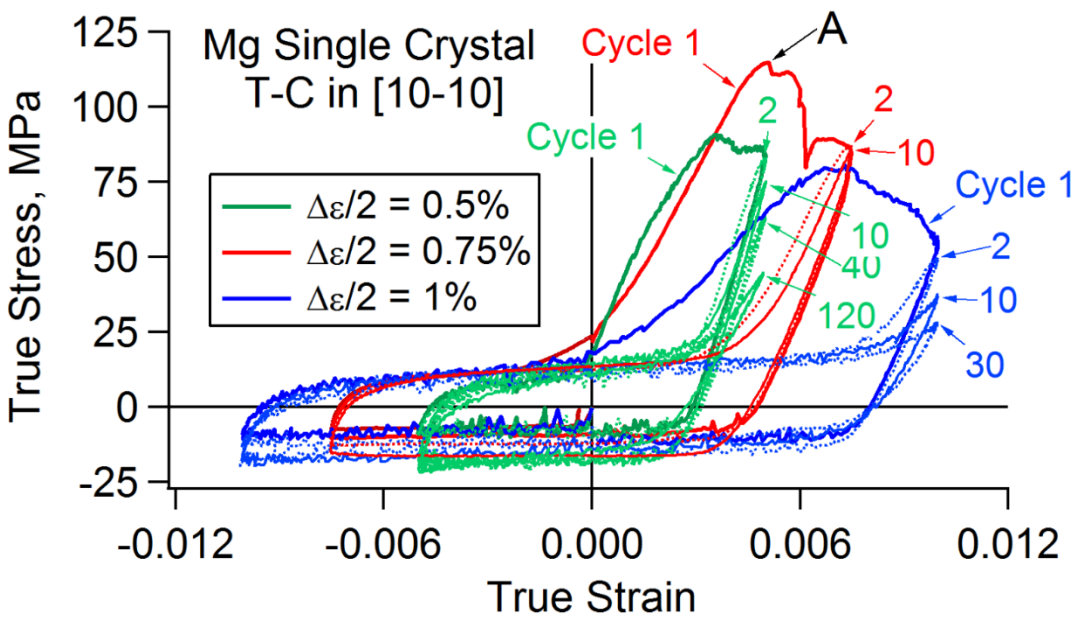

Figure 30 Stress-strain hysteresis loops of magnesium single crystals subjected to fully reversed tension-compression in $[10\bar{1}0]$ direction at strain amplitudes of 0.5%, 0.75%, and 1%.

A distinctive phenomenon of plastic instability, which is not observed in the [0001]-oriented magnesium single crystal, is discovered near the end of the first tensile reversal in the $[10\bar{1}0]$-oriented magnesium single crystal. To describe the phenomenon in detail, the specimen tested at $\Delta\varepsilon/2 = 0.75\%$ is taken as an example (red lines in Figure 30). Beyond the inflection point of the tensile loading reversal, the steady plastic flow proceeds smoothly but terminates at point A (see Figure 30, σ = ~115 MPa and ε = ~0.5%) where a sudden stress drop ($|\Delta\sigma_1|$ = 4 MPa) followed by a short flow plateau ($\Delta\varepsilon_1$ = 0.06%) occurs. At the end of the plastic flow plateau, a second rapid stress drop with a significant decrease in stress ($|\Delta\sigma_2|$ = 30 MPa) is observed. The second stress drop is followed by an immediate stress increment by 10 MPa and a subsequent plastic flow plateau ($\Delta\varepsilon_2$ = 0.09%), which continues until reaching the tensile peak strain of

0.75%. The currently observed unstable plastic flow is similar to the inhomogeneous plastic deformation associated with Lüders band propagation in carbon steels [183, 184] and the serration of the stress-strain curve (Portevin-Le Chatelier (PLC) effect) observed in aluminum alloys [185-187]. Unlike the high-frequent serration with small stress drop and increment (around 5 MPa in average) in the PLC effect, the magnitude of stress drop in the $[10\bar{1}0]$ magnesium single crystals is rather random, varying from ~4 MPa to as high as ~30 MPa. Moreover, both the stress increment and the plastic flow plateau can be followed after a stress drop. The underlying mechanisms of plastic instability might be related to dislocation-solute interaction (or dynamic solute aging) and dislocation-dislocation interaction [183-187]. Without the presence of solutes in the pure magnesium single crystals, the dislocation-solute interaction can be ruled out as a possible cause of the observed phenomenon and therefore, the dislocation-dislocation interaction can be a probable cause. Noting that such a plastic instability is not observed in the [0001]-oriented magnesium single crystal near the end of the first compressive reversal [39], it is conjectured that the involved non-basal dislocations could originate from the duplex prismatic slips rather than the second–order pyramidal slips. This speculation is enlightened by the experimental findings in magnesium single crystals that pyramidal slips operate under *c*-axis compression [34, 90] whereas duplex prismatic slips operate in $[10\bar{1}0]$-tension [31].

It is noticed that, different from wrought magnesium alloys [111], polycrystalline pure magnesium [188], and single crystal magnesium oriented in [0001] direction [39, 68], significant cyclic softening is observed in the $[10\bar{1}0]$ magnesium single crystal during tensile loading reversals. In addition, the maximum stress upon which plastic

instability occurs in the first tensile reversal is not a monotonic increasing function of the applied strain amplitude. These observed deformation features are likely associated with the dislocation-dislocation interactions which are influenced the initial amount of tension twinning created by the preceding compressive strain. Further studies are needed to determine the underlying mechanisms.

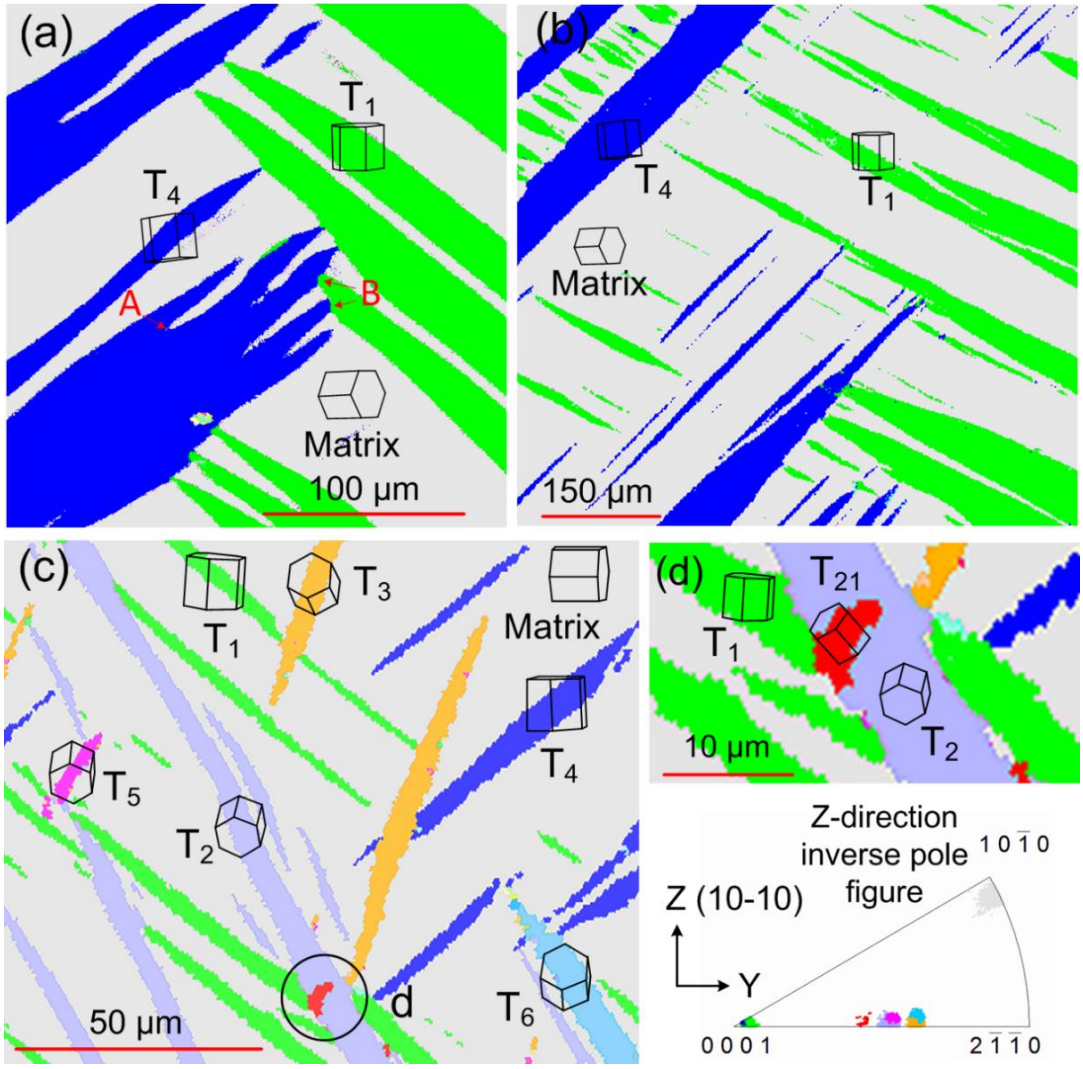

Figure 31 EBSD observation of twin structures: (a) unloaded from the first compressive peak at 0.75% strain amplitude; (b) unloaded from the third compressive peak at 0.75% strain amplitude; (c) unloaded from the 30th compressive peak at 1% strain amplitude; (d) magnified area in (c) showing secondary tension twin.

EBSD observations of twin structures are presented in Figure 31. All the twin structures represent a material state unloaded from the compressive peak stress where the material has been twinned. The *Z*-direction in the figure denotes the loading axis oriented in the $[10\bar{1}0]$ direction.

Figure 31a and Figure 31b show the twin structures in the material unloaded from the first and third compressive peaks, respectively, at $\Delta\varepsilon/2 = 0.75\%$. Two twin variants, T_1 and T_4 having a maximum SF of 0.499 and identical zone axis, are developed. In Figure 31a, lenticular-shaped twins are observed. The boundaries of two neighboring twins having the same variant meet and coalesce (arrow A in Figure 31a). When two twin variants meet, no twin transmission or penetration occurs but twin-twin boundaries (TTB) form (arrow B in Figure 31a) [160, 189]. In the specimen unloaded from the third compressive peak (Figure 31b), the number of twin lamellae and the number of TTBs are significantly increased. It is noticed that the absolute compressive peak stress increases from 9.36 MPa at the first loading cycle to 15.12 MPa at the third loading cycle (Figure 30). The positive correlation of the increased compressive peak stress and the multiplied TTBs suggests that TTB plays an effective role in the material hardening during cyclic deformation. To be specific, the incoming twinning dislocations (TDs) can be piled up at the barrier TTB, which exerts a repulsion force on the successive impinging TDs. To further grow the twin, a large stress that overcomes the backstress at TTBs is required. Such a hardening effect is amplified as more TTBs are developed.

Figure 31c illustrates the twin structures developed in the material unloaded from the 30^{th} compressive peak at $\Delta\varepsilon/2 = 1\%$. All six twin variants are observed. The

activation stress for T_2, T_3, T_5, and T_6 is larger than that for T_1 and T_4 since the SF of T_2, T_3, T_5, and T_6 is 0.125 which is lower than that (0.499) for T_1 and T_4. As a result, T_2, T_3, T_5, and T_6 can be only activated when the material is cyclically hardened during the later stage of cyclic deformation at a larger strain amplitude, such as the loading condition (N = 30 cycles, $\Delta\varepsilon/2$ = 1%) in Figure 31c. The development of all the six twin variants can lead to TTBs formation between either two co-zone twin variants (Type I) or two twin variants that do not share the same zone axis (Type II) [189]. The Type II twin-twin interaction can nucleate secondary tension twin at the TTB. A detailed analysis of the feasibility of secondary twin transmission will be presented in Chapter four. In the current study, the observation of secondary twins can be visualized in Figure 31c and Figure 31d. An EBSD analysis shows that a secondary twin T_{21} is developed at the TTB formed between two primary twins T_1 and T_2. It is established that the formation process of secondary tension twins is energetically unfavorable, which contributes to material hardening as well as the formation of TTBs [189]. To summarize, an experimental observation by EBSD in Figure 31 shows that the twinning-associated cyclic hardening in $[10\bar{1}0]$-oriented magnesium single crystal is due to the incessant formation of TTBs and secondary twins with the increasing number of loading cycles.

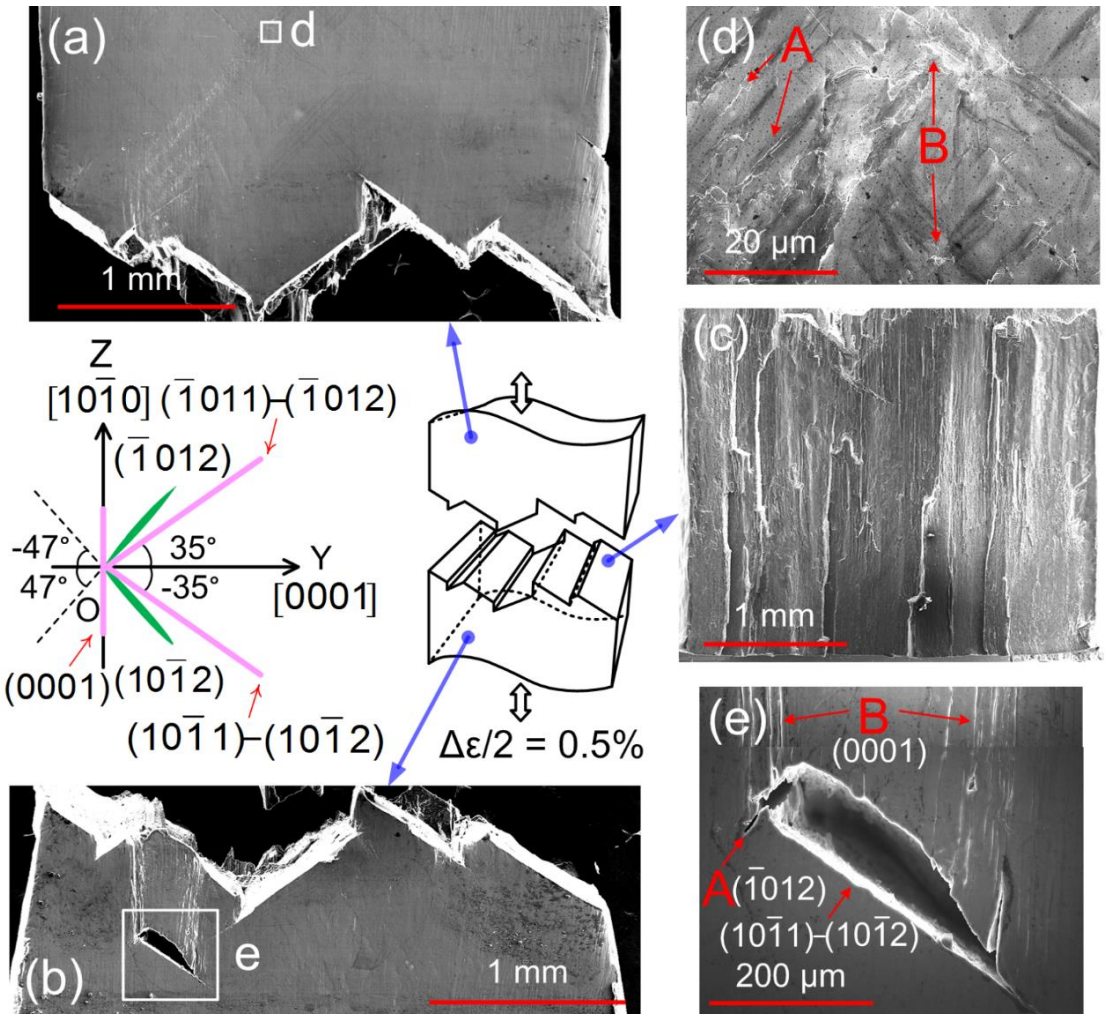

Figure 32 Microcracks and fracture surface in magnesium single crystal subjected to fully reversed tension-compression in [10$\bar{1}$0] direction: (a) and (b) specimen surface; (c) fracture surface; (d) microcracks; (e) cleavage cracking and shearing fracture.

An examination of fatigue damage and fracture surface in [10$\bar{1}$0]-oriented magnesium single crystal is illustrated in Figure 32. Since the specimen loaded at $\Delta\varepsilon/2 = 0.75\%$ and 1% were not separated into two parts, the specimen tested at $\Delta\varepsilon/2 = 0.5\%$ which was fractured into two parts is used to examine the fatigue damage. Figure 32 shows the SEM observations on the specimen surface (Figure 32a, Figure 32b, Figure 32d, and Figure 32e) and the fracture surface (Figure 32c). On the specimen surface

away from the macroscopic fracture surface (Figure 32d), microcracks are distributed mainly in two specific regions: the serrated primary twin boundaries (arrows A in Figure 32d) and the severely fragmented twin-twin interaction sites (arrow B in Figure 32d). The length of microcrack is very short (less than ~20 μm), implying that the microcrack propagation along twin boundaries and TTBs is limited. The current observation of microcrack is similar to that obtained in the [0001]-oriented magnesium single crystal [39].

A three dimensional profile of the macroscopic fracture surface is schematically reconstructed (middle, Figure 32). The macroscopic fracture surface consists of multiple cleavage-like flat facets. On the $(\bar{1}2\bar{1}0)$ specimen surface, straight markings projected from the cleavage facets form three inclination angles with respect to the [0001] direction (Figure 32a and Figure 32b): -35 °, 35 °, and 90 °. The projected straight markings coincide with the traces of the crystal planes $(30\bar{3}4)$, $(\bar{3}034)$, and (0001) on the $(\bar{1}2\bar{1}0)$ plane, as confirmed by the EBSD trace analysis. The crack facets $(30\bar{3}4)$ and $(\bar{3}034)$ are associated with cleavage-cracking along the boundary of $\{10\bar{1}1\}$-$\{10\bar{1}2\}$ double twin, and the crack facet (0001) is related to Mode-II shearing fracture of the basal plane. The cleavage cracking on $\{30\bar{3}4\}$ plane was first observed and studied by Reed-Hill and co-workers [25, 41, 46] in magnesium single crystal subjected to monotonic tension along the $[10\bar{1}0]$ direction. The $\{30\bar{3}4\}$ cleavage-cracking marking was revealed to align with the boundary of $\{10\bar{1}1\}$-$\{10\bar{1}2\}$ double twin, where $\{10\bar{1}1\}$ primary twin experiences a secondary $\{10\bar{1}2\}$ twinning. It was further found that the formation of double twin can lead to rapid cleavage cracking at the double twin boundary. The seminal work by Reed-Hill and co-workers [25, 41, 46]

sheds lights on the process of final fracture in the current experiment. As visualized in Figure 32e, an inclined macrocrack of $\{10\bar{1}1\}$-$\{10\bar{1}2\}$ twin type is connected to a microcrack (arrow A in Figure 32e). A trace analysis shows that the microcrack orientation coincides with the trace of $\{\bar{1}012\}$ crystal plane. The inclined microcracks are observed to predominantly align with the tension twin boundaries (Figure 32d). Therefore, the microcrack connected to the $\{10\bar{1}1\}$-$\{10\bar{1}2\}$ macrocrack was most likely originated from tension twin cracking. Knowing that a large CRSS is required to activate $\{10\bar{1}1\}$-$\{10\bar{1}2\}$ double twin [32], it can be inferred from Figure 32e that the double twin where the macrocrack is located is induced by the intensified stress field at the tip of the microcrack. The cleavage cracking at double twin can easily activate basal slips in the slightly-rotated crystals surrounding the crack. The locally aggravated basal slips can lead to Mode-II shearing fracture on the basal plane, as indicated by arrows B in Figure 32e.

3.6 Summary

Cyclic plastic deformation and direct observation of twinning-detwinning-retwinning evolution for $\{10\bar{1}2\}$ tension twins are, for the first time, reported in [0001]-orientated magnesium single crystal subjected to fully reversed tension-compression at a strain amplitude of 0.5%. A typical stress-strain hysteresis loop contains three featured deformation stages: twinning, detwinning, and detwinning accompanied by nonbasal slips. With increasing loading cycles, the activities for twinning/detwinning decrease but never exhaust. Cyclic hardening can be attributed to the accumulated barrier effect of the increased residual twin boundaries to the mobile

slip dislocations and twin-twin interaction. During detwinning, residual twins are found to form on the vicinities of twin boundaries which were fully expanded at the previous tensile peak.

Microstructural characterization of the [0001]-oriented magnesium single crystal after termination of the fatigue experiment shows microcracks develop at slip band extrusions, residual twin boundaries, and the intersection area of primary twins. The matrix regions in the magnesium single crystal having experienced repeated twinning and detwinning for sufficient number of loading cycles are unable to completely detwinned back to the original orientation of the matrix. The incapability of complete twinning/detwinning can be most likely attributed to the development of certain stable dislocation substructures due to glide dislocation-twin interaction under cyclic loading. Residual primary tension twins and residual secondary tension twins are found fragmented in small area fractions after detwinning. Secondary twin fragments have irregular shapes and can be activated in all six primary twin variants during the interaction of primary twins. They are predominantly located at the intersection sites and are more difficult to be detwinned compared to the detwinning of primary twins.

From the experimental investigation of cyclic deformation in $[10\bar{1}0]$-oriented magnesium single crystal subjected to cyclic tension-compression, a plastic instability phenomenon is found in the first tensile loading reversal where the initial detwinning process accompanied by non-basal slips approaches exhaustion. Two twin variants having the highest Schmid factor (SF) with an identical zone axis are activated in the early stage of cyclic deformation. The other four twin variants with a much lower SF can be activated as the material is cyclically hardened during the later stage of cyclic

deformation. The development of twin-twin boundaries and secondary tension twins effectively act as a twinning-induced hardening mechanism. Repeated twinning and detwinning can initiate microcracks with limited propagation at primary twin boundaries and twin-twin interaction sites. Final fracture of the $[10\bar{1}0]$ magnesium single crystal is dominated by the sudden cleavage cracking on $\{10\bar{1}1\}$-$\{10\bar{1}2\}$ double twin boundary and the shearing fracture on the basal plane.

4 Twin-Twin Interaction in Magnesium Single Crystal

Twin-twin interactions are frequently observed during twinning/detwinning process in cyclic deformation experiments for magnesium single crystal by *in situ* optical microscopy. They can affect the twinning and detwinning processes and play a critical role in cyclic hardening. This chapter is dedicated to analyzing the experimentally observed twin-twin interaction structures in the magnesium single crystal subjected to cyclic loading. Theoretical analyses of the twin-twin interaction are carried out based on crystallography of magnesium and the dislocation theory.

4.1 Crystallography of Twin-Twin Interaction

In HCP magnesium, three pairs of twin-twin interactions are crystallographically distinctive, $T_1 \leftrightarrow T_2$, $T_1 \leftrightarrow T_3$, and $T_1 \leftrightarrow T_4$, as illustrated in Figure 33a, Figure 33b, and Figure 33c, respectively. Symbols "$T_i \leftrightarrow T_j$" denote that an incoming twin T_i encounters a barrier twin T_j, and vice versa. The misorientation axis and angle for the three crystallographically distinctive twin-twin interactions are summarized in Table 5. For $T_1 \leftrightarrow T_4$ twin-twin interaction pair, the intersection line is parallel to the $[\bar{1}2\bar{1}0]$ direction (a_2-axis). The *c*-axis misorientation angle between T_1 and T_4 is 7.40°. $T_1 \leftrightarrow T_4$ twin-twin interaction is referred to as Type I co-zone twin-twin interaction. For $T_1 \leftrightarrow T_2$ and $T_1 \leftrightarrow T_3$ twin-twin interactions, the intersection lines are along $[\bar{2}\,\bar{2}\,43]$ and $[0\,\bar{2}\,21]$ directions, respectively. The *c*-axis misorientation angles about these axes are 79.98° for $T_1 \leftrightarrow T_2$ twin pair and 34.73° for $T_1 \leftrightarrow T_3$ twin pair, respectively. Since the two twin pairs do not share an *a*-axis, their interactions are referred to as Type II twin-twin interactions, with Type II(a) for $T_1 \leftrightarrow T_2$ and Type II(b) for $T_1 \leftrightarrow T_3$.

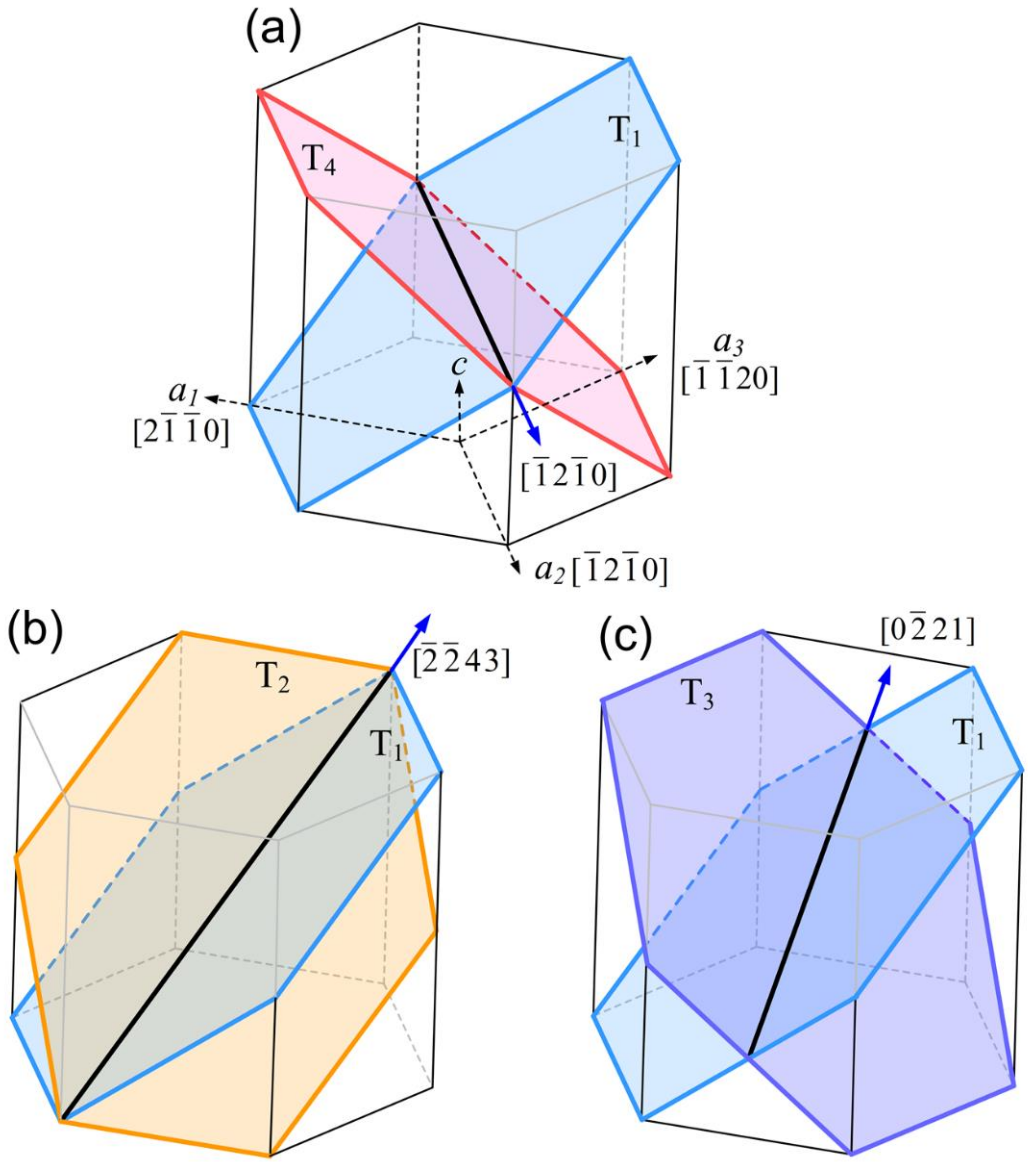

Figure 33 Crystallography of twin-twin interaction in magnesium: (a) Type I twin-twin pair $T_4 \leftrightarrow T_1$ with the intersection line along $[\bar{1}2\bar{1}0]$, (b) Type II(a) twin-twin interaction $T_2 \leftrightarrow T_1$ with the intersection along $[\bar{2}\,\bar{2}\,4\,3]$, and (c) Type II(b) twin-twin interaction $T_3 \leftrightarrow T_1$ with the intersection line along $[0\,\bar{2}\,2\,1]$.

Table 5 Three crystallographically distinctive twin-twin interaction pairs in magnesium and their misorientation relationships.

Type	Twin-twin pair	Misorientation axis (or intersection line)	Misorientation angle
I	$T_4 \leftrightarrow T_1$	$[\bar{1}2\bar{1}0]$	7.40 °
II(a)	$T_2 \leftrightarrow T_1$	$[\bar{2}\,\bar{2}\,43]$	79.98 °
II(b)	$T_3 \leftrightarrow T_1$	$[0\,\bar{2}\,21]$	34.73 °

4.2 Feasibility of Twin Transmission

The first critical question regarding twin-twin interaction is whether an impinging twin can transmit a barrier twin through a secondary twinning path within the barrier twin. To facilitate a discussion, the impinging twin is denoted as T_i and the barrier twin as T_j. If the impinging twin T_i transmits into twin T_j, a secondary twin T_{jk} forms inside twin T_j. Figure 34 shows an impinging twin T_4 approaching a previously formed twin T_1. Both twins can be activated by the stress state depicted in Figure 34, say tension along the *c*-axis or compression parallel to the basal plane. Following Cahn's first constraint [36], the trace of the impinging twin is parallel to the intersection line between two twins. The secondary twin could be either T_{11} or T_{14} inside twin T_1. For T_1 and T_4, the direction of the resolved shear stress on the twinning plane is denoted with a blue arrow and the twinning shear direction with a red arrow. In the matrix, they have the same direction (Figure 34) on the twinning plane. The twinned crystal is rotated 86.3 ° about the zone axis with respect to the matrix and the *c*-axis experiences tension in the matrix and compression inside twin T_1. As a consequence, the direction of the resolved shear stress on the secondary twin plane is opposite to the secondary

twinning shear direction. Therefore, secondary twinning or twin transmission does not occur for Type I twin-twin interaction.

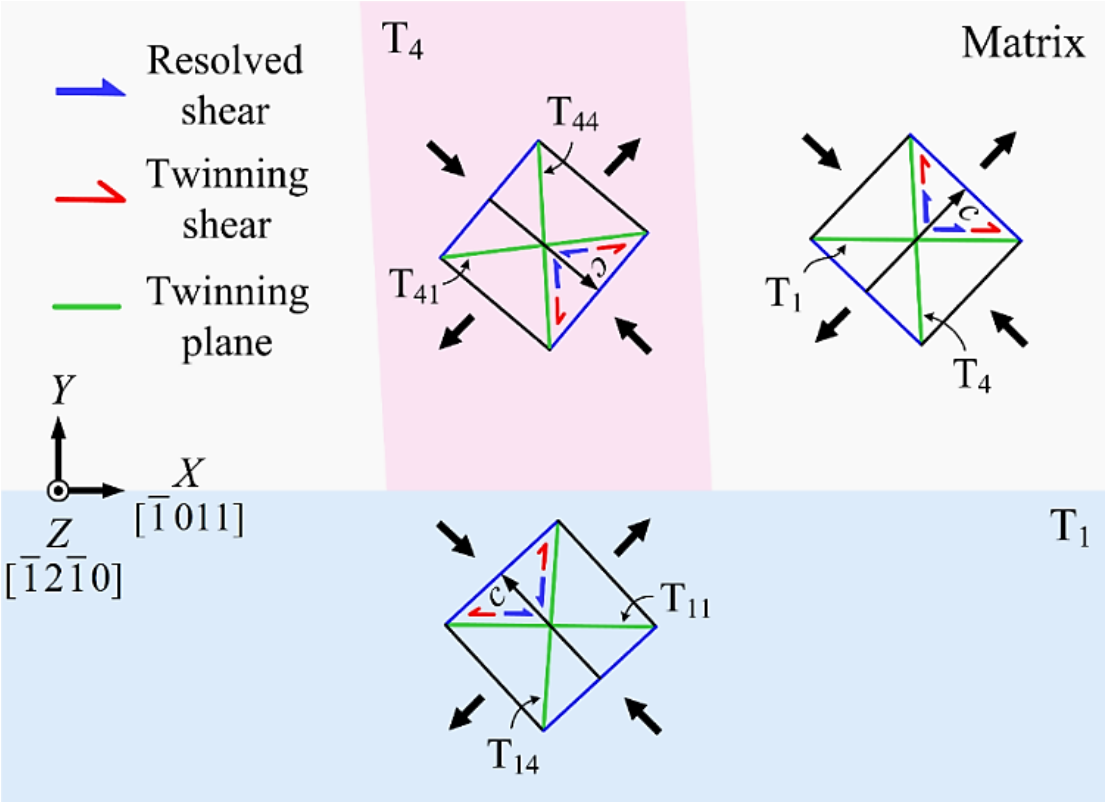

Figure 34 Schematic of Type I twin-twin interaction in magnesium showing the relation between the direction of the resolved shear stress and the direction of twinning shear on the primary T_1 and T_4 twin planes, and on the $\{10\bar{1}2\}$ twinning planes inside twin T_1. The external loading in the figure favors primary twin growth but not secondary twin transmission when twin T_4 impinges on twin T_1.

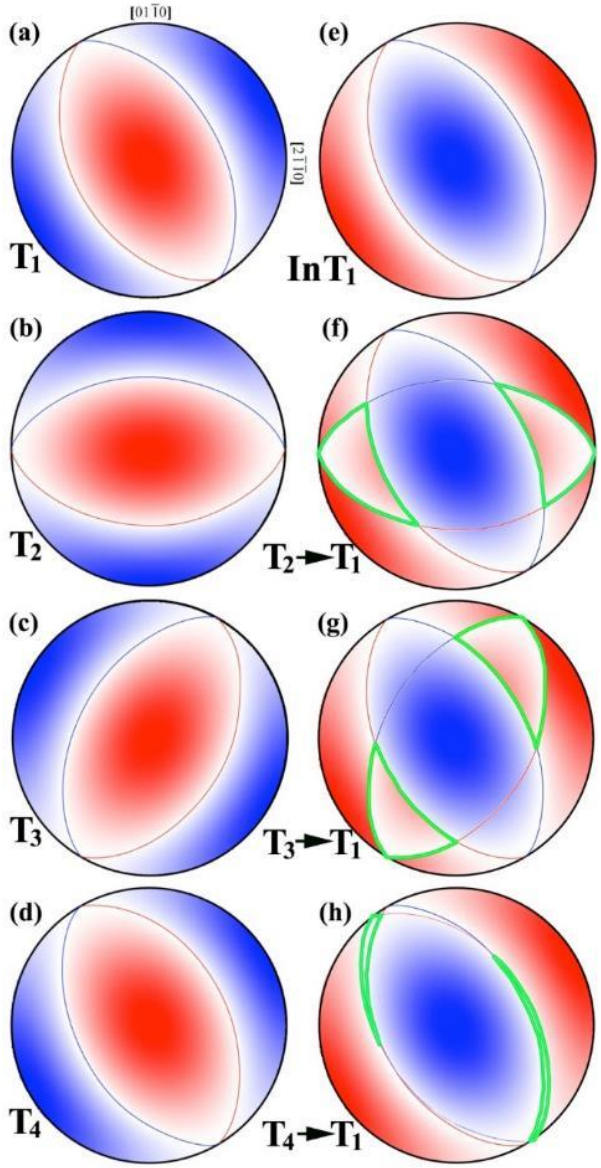

Figure 35 Inverse pole figures of Schmid factor of twinning systems in magnesium under a tensile axis. Red (blue) color identifies domains with positive (negative) resolved shear on a twinning system. Directions of potential activation stresses for activating: (a) twin T_1; (b) twin T_2; (c) twin T_3; (d) twin T_4, (e) twin T_1 after it has been reoriented; (f) twin T_2 inside twin T_1; (g) twin T_3 inside twin T_1; (h) twin T_4 inside twin T_1. The regions outlined by the green line represent the stress domain associated with the transmission of twin T_i into twin T_1.

A more general and rigorous analysis of twin transmission for Types I and II twin-twin interactions can be done using the Schmid criterion. A description of Schmid criterion is covered in Appendix A.2. Figure 35a to Figure 35d plot the Schmid factor (SF) of twins T_i (i=1…4) in an inverse pole figure for uniaxial tension applied on the parent HCP structure. A positive SF (red domain) is associated with the stress directions that induce a resolved shear along the positive shear direction and activate T_i twinning. Take twin T_1 as an example. If the SF is negative (blue domains), T_1 is not activated. Following reorientation of T_1, the *c*-axis reorients by nearly 90 degree and the SF of twin T_1 associated with the stress state changes sign (Figure 35e) for the twinned crystal (from red to blue, and vice versa), indicating that the stress state that activates twin T_1 cannot activate detwinning inside T_1. The following three cases correspond to Type I and II twins being able to propagate inside twin T_1. Each of twins T_2, T_3 and T_4 is associated with positive and negative domains of SF in the parent crystal. If T_i (i = 2, 3, and 4) can propagate into twin T_1 under certain stress, the stress direction must be projected onto superimposed red (positive SFs) domains when Figure 35b to Figure 35d are superimposed with Figure 35e, respectively. Such superimposed domains are sketched in Figure 35f to Figure 35h as red regions outlined by the green lines. It should be noticed that while the same stress states allow twins T_2 and T_3 to propagate into twin T_1, the SFs associated with these domains are very low. In practice, such a kind of twin-twin transmission has not been observed. As for twin T_4 propagation into twin T_1 (Figure 35h), the superimposed red domains is very small so that the likelihood of such a propagation is very low. This is also consistent with the experimental evidence presented.

4.3 Observations of Twin-Twin Structures in Magnesium Single Crystal

Through *in situ* OM and *ex situ* EBSD characterizations, three microstructural features are identified in association with twin-twin interactions in magnesium single crystal specimens: (1) quilted-looking twin structure, (2) "apparent crossing" twin structure, and (3) double twin structure. The microstructural features for the three twin interaction structures are shown from Figure 36 to Figure 38. The quilted-looking twin structure forms through the propagation and blocking of multiple twin variants (Figure 36). This structure has been widely observed in materials with HCP structures [53–56]. Figure 36a shows a quilted-looking twin structure in the specimen cyclically loaded along the $[10\bar{1}0]$ direction. The structure is composed of two twin variants, T_1 and T_4, that share the same zone axis. In the specimen cyclically loaded along the [0001] direction, six twin variants are activated. Figure 36b shows quilted-looking twin structure composing of four twin variants, T_1, T_2, T_3 and T_5. It is noticed that the quilted-looking structure prevents the propagation and growth of twins in association with the formation of twin-twin boundaries.

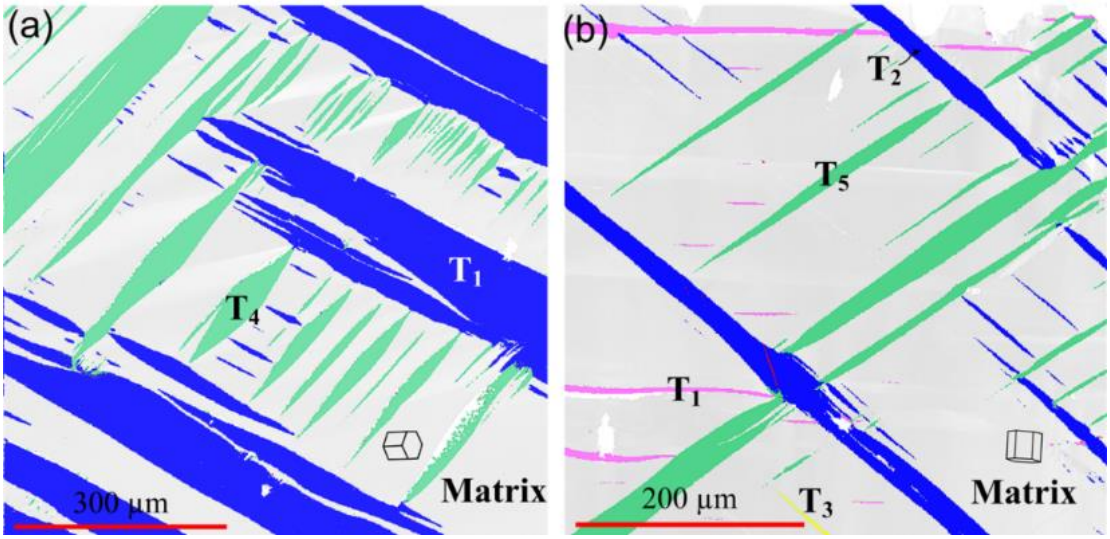

Figure 36 Quilted-looking twin structures in magnesium single crystal having experienced cyclic tension-compression: (a) in the specimen cyclically loaded along $[10\bar{1}0]$ direction; (b) in the specimen cyclically loaded along [0001] direction.

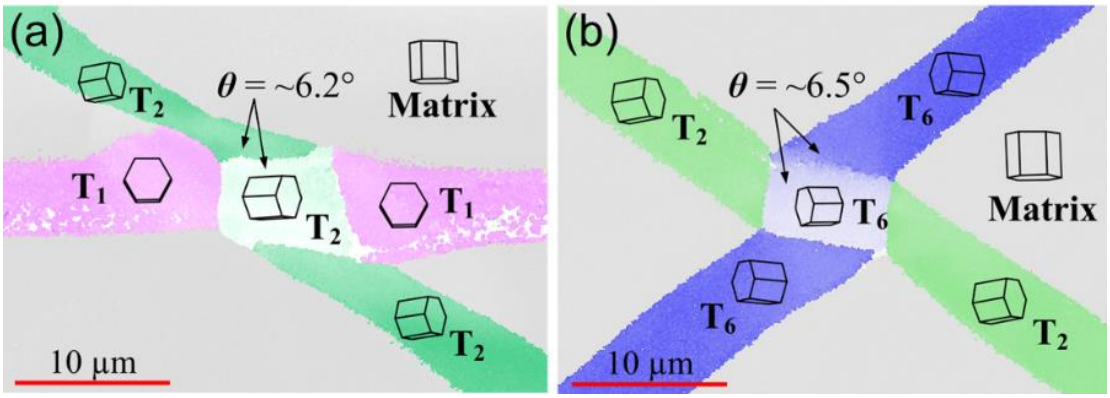

Figure 37 "Apparent crossing" twin structures in magnesium single crystal after cyclic loading along [0001] direction: (a) two T_1 twins and one T_2 twin; (b) two T_2 twins and one T_6 twin.

Figure 37 shows two "apparent crossing" twin structures observed experimentally. A closer observation reveals that neither impinging twin actually penetrates the barrier twin. Figure 37a shows two T_1 twins and one T_2 twin. The crystal orientation in the

intersection region has a *c*-axis misorientation angle of ~6.2° with respect to the crystal orientation in the T_2 twin away from the twin-twin interaction, indicating that the crystal in the intersection region belongs to T_2 twin but experiences a tilt induced by forming twin-twin boundaries. In Figure 37b, EBSD analysis shows three twins: two T_2 twins and one T_6 twin. The crystal orientation in the intersection region has a *c*-axis misorientation angle of ~6.5° with respect to the crystal orientation in the T_6 twin away from the twin-twin boundary. This is an indication that the crystal in the intersection region belongs to T_6 twin but experiences a tilt induced by dislocation formation at the twin-twin boundaries.

The results shown in Figure 34 clearly indicate that no twin crossing or transmission occurs upon the contact of one twin with another twin. This is different from the crossing twin-twin interaction structure in face-centered cubic structures [50, 51] where twin transmission can occur under monotonic loading because the face-centered cubic structure exhibits three sets of twinning dislocations on each twinning plane [151–153]. The twinned crystal can be further twinned by the glide of twinning dislocations under the same stress condition. For HCP structures, a crossing twin structure is unlikely because twinning is unidirectional with one set of twinning dislocation per twinning plane. According to a Schmid analysis in Type I twin-twin interaction (Figure 34), the twinned crystal cannot experience secondary twinning under the same stress because the twinning direction is opposite to the direction of the resolved shear stress in the twinned crystal. For Type II twin-twin interaction, the twinned crystal cannot be further twinned because the positive loading domains are characterized by very low Schmid factors (Figure 35). Therefore, crossing twin structures in the HCP structure

are unlikely a result of twin-twin interaction. This is evidenced in theEBSD analysis where among all twin-twin structures only “apparent crossing” twin structure was observed without crossing twin structure through secondary twinning. However, crossing twin structures could form if the local stresses depart substantially from the applied stress as a result of spatially distributed defects.

Double tension twin structure is the one in which a secondary tension twin forms inside another primary tension twin. There are two typical structures: one where the secondary twin does not connect another twin that interacts with the primary twin (Figure 38a and Figure 38b), and the other one is where the secondary twin does connect to another twin that interacts with the primary twin (Figure 38c and Figure 38d). Since secondary twins cannot occur inside a primary twin without changing the stress state in the primary twin, the double tension twin structure can occur either due to a change in the applied loading or due to local stresses resulting from other defects such as an interacting twin.

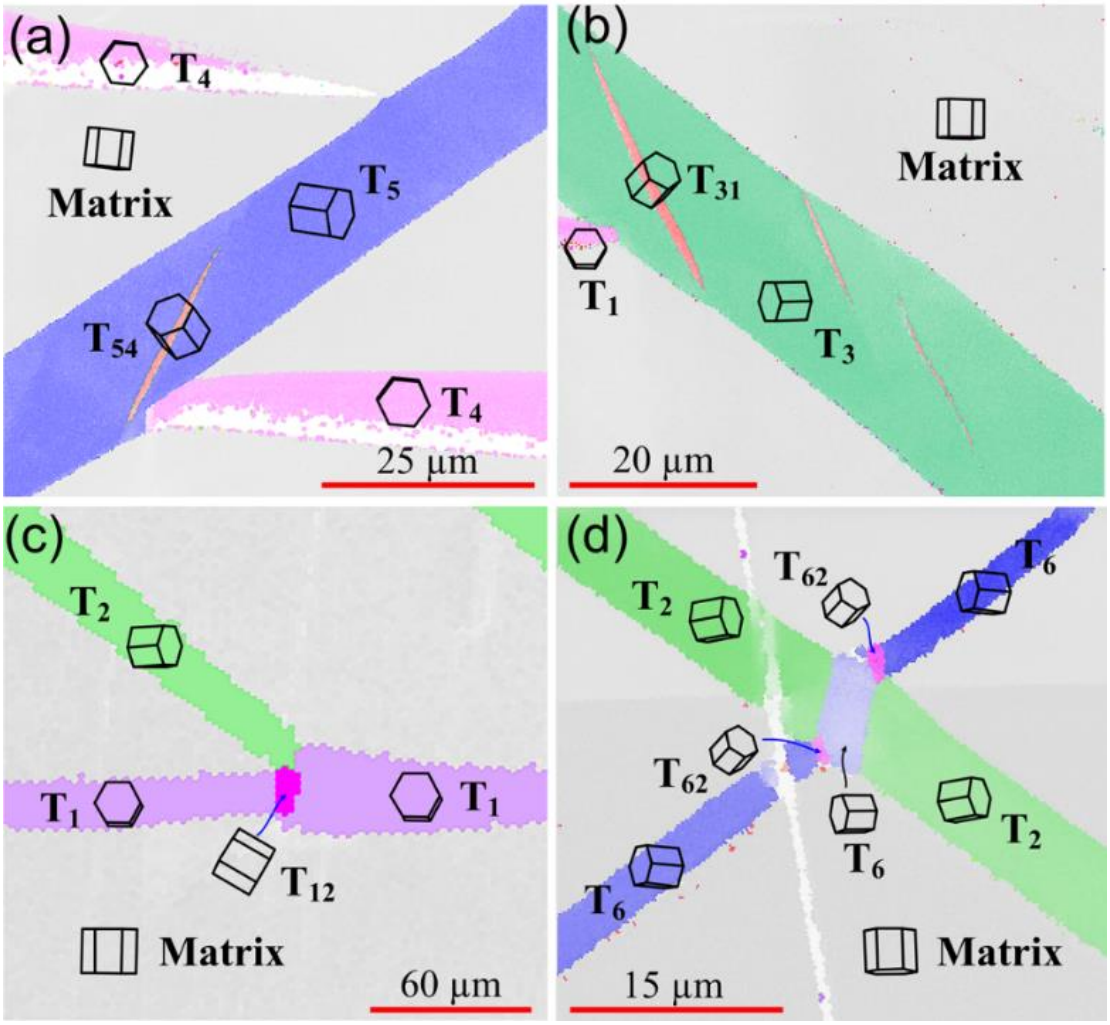

Figure 38 Double tension twin structures in magnesium single crystal cyclically loaded along [0001] direction. Secondary twin does not connect to an impinging twin: (a) a secondary twin T_{54} inside a primary twin T_5 and (b) three secondary twins T_{31} inside a primary twin T_3. Secondary twin connects to twin-twin boundaries: (c) a secondary twin T_{12} inside a primary twin T_1 and (d) two secondary twins T_{62} inside a primary twin T_6.

4.4 Twin-Twin Boundary

4.4.1 Formation of Twin-Twin Boundaries

When one twin encounters another twin, twin-twin boundaries (TTBs) form. Starting with Figure 39a where an incoming twin T_i approaches the T_j twin boundary, TTBs form through three possible mechanisms based on the reaction of twining dislocations (TDs), as visualized in Figure 39a to Figure 39d. The first mechanism corresponds to the *impinging* process (Figure 39b) where the front tip of twin T_i is blocked at the boundary of twin T_j. TDs associated with twin T_i impinge on the twin boundary of twin T_j. The twin-twin boundary that forms between these two twins is referred to as TTB_I, where the subscript "I" denotes **i**mpinging. The twin-twin boundary plane coincides with the T_j twinning plane and contains boundary dislocations that have the same character as the twinning dislocation associated with the incoming twin T_i.

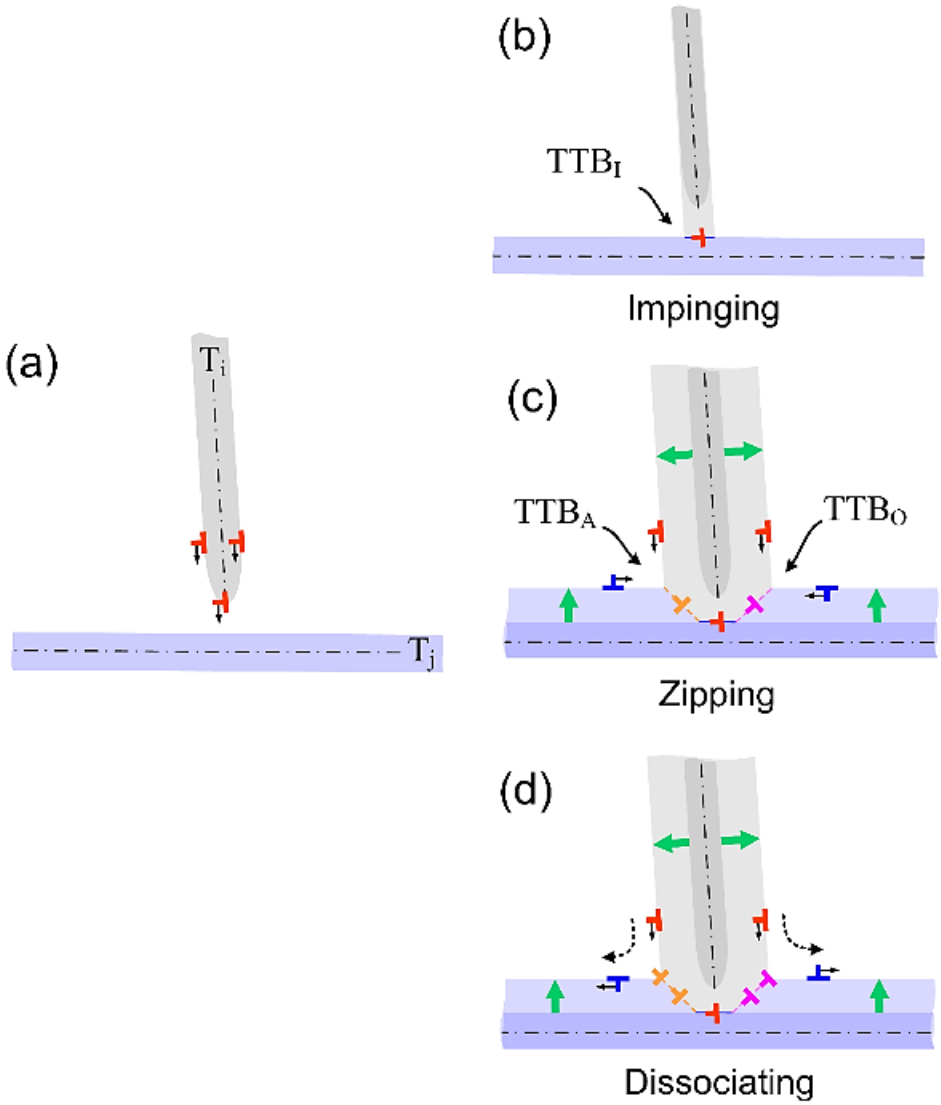

Figure 39 Formation mechanisms of twin-twin boundaries (TTBs): (a) a twin T_i is approaching the boundary of a pre-existing twin T_j ($i \neq j$); (b) the impinging mechanism where twinning dislocations (TD) impinge on the T_j twin boundary, forming TTB_I; (c) the zipping mechanism where TDs associated with these two twins zip to form junctions; (d) the dissociating mechanism where a TD associated with one twin dissociates into one TD associated with the other twin and leaves one junction. The light grey and light blue domains correspond to the T_i and T_j twins, respectively. The TDs are drawn in red (T_i) and blue (T_j) colors.

The second and third mechanisms are associated with the growth of two twins as shown in Figure 39c and Figure 39d. When both twins T_i and T_j grow through the glide of TDs, these TDs meet, react, and form junctions. The pile-up of these junctions forms a dislocation wall, referred to as the twin-twin boundary. Two types of twin-twin boundaries can form as schematically shown in Figure 39c and Figure 39d. Based on the angles between the two primary twinning planes, one twin-twin boundary is referred to as TTB_A corresponding to an **a**cute angle and the other is referred to as TTB_O corresponding to an **o**btuse angle. For the second mechanism, the formation of junctions is accomplished through *zipping* twinning dislocations associated with the two primary twins (Figure 39c). The Burgers vector of the junction is thus equal to the sum of the two TDs. In the case of a more common twin-twin boundary that forms between an incoming T_4 twin and a T_1 twin, the line sense of all twinning dislocations is oriented along the $[1\bar{2}10]$ zone axis. The reaction process can be expressed as:

$$\begin{aligned} b_{tw}^{T_4} + b_{tw}^{T_1} &\Rightarrow b_A \\ \lambda[10\bar{1}1] + \lambda[\bar{1}011] &\Rightarrow 2\lambda[0001] \end{aligned} \qquad (5a)$$

and

$$\begin{aligned} b_{tw}^{T_4} + b_{tw}^{T_1} &\Rightarrow b_O \\ \lambda[10\bar{1}1] + \lambda[10\bar{1}\,\bar{1}] &\Rightarrow 2\lambda[10\bar{1}0] \end{aligned} \qquad (5b)$$

where $b_{tw}^{T_1}$ has Burgers vector $\lambda[\bar{1}011]$ at the left of twin T_4 and $\lambda[10\bar{1}\,\bar{1}]$ at the right of twin T_4, where $\lambda = (3-\kappa^2)/(3+\kappa^2)$ (λ=0.064 for magnesium). b_A and b_O denote the Burgers vectors of the junctions in the twin-twin boundaries TTB_A and TTB_O, respectively.

In the third mechanism, the formation of TTBs is accomplished through *dissociating* the twinning dislocation of one twin into the twinning dislocation of the other twin plus a residual. As shown in Figure 39d, a TD associated with T_i glides towards the boundary of the T_j and dissociates into a TD associated with twin T_j. The residual is left at the intersection of these two twins, corresponding to a junction. Taking $T_4 \rightarrow T_1$ twin pairs as example, the dissociation process can be expressed as:

$$\begin{aligned} b_{tw}^{T_4} &\Rightarrow b_{tw}^{T_1} + b_A \\ \lambda[10\bar{1}1] &\Rightarrow \lambda[10\bar{1}\,\bar{1}] + \lambda[0001] \end{aligned} \qquad (6a)$$

and

$$\begin{aligned} b_{tw}^{T_4} &\Rightarrow b_{tw}^{T_1} + b_O \\ \lambda[10\bar{1}1] &\Rightarrow \lambda[\bar{1}011] + 2\lambda[10\bar{1}0] \end{aligned} \qquad (6b)$$

4.4.2 Configuration of Twin-Twin Boundaries

According to the three proposed mechanisms in Figure 39, the geometric and crystallographic aspects of the twin-twin boundaries including boundary planes and boundary dislocations were studied. Figure 40 shows the three-dimensional geometry for the three twin-twin interactions. T_1 is the pre-existing twin. T_2, T_3, and T_4 are the incoming twins. The coordinate system (*OXYZ*) is fixed to the T_1 twinning plane. The *X*-axis aligns with the T_1 twinning shear direction $[\bar{1}011]$ and the *Y*-axis is normal to the T_1 twinning plane. The *Z*-axis points out-of-paper parallel to the $[1\bar{2}10]$ zone axis.

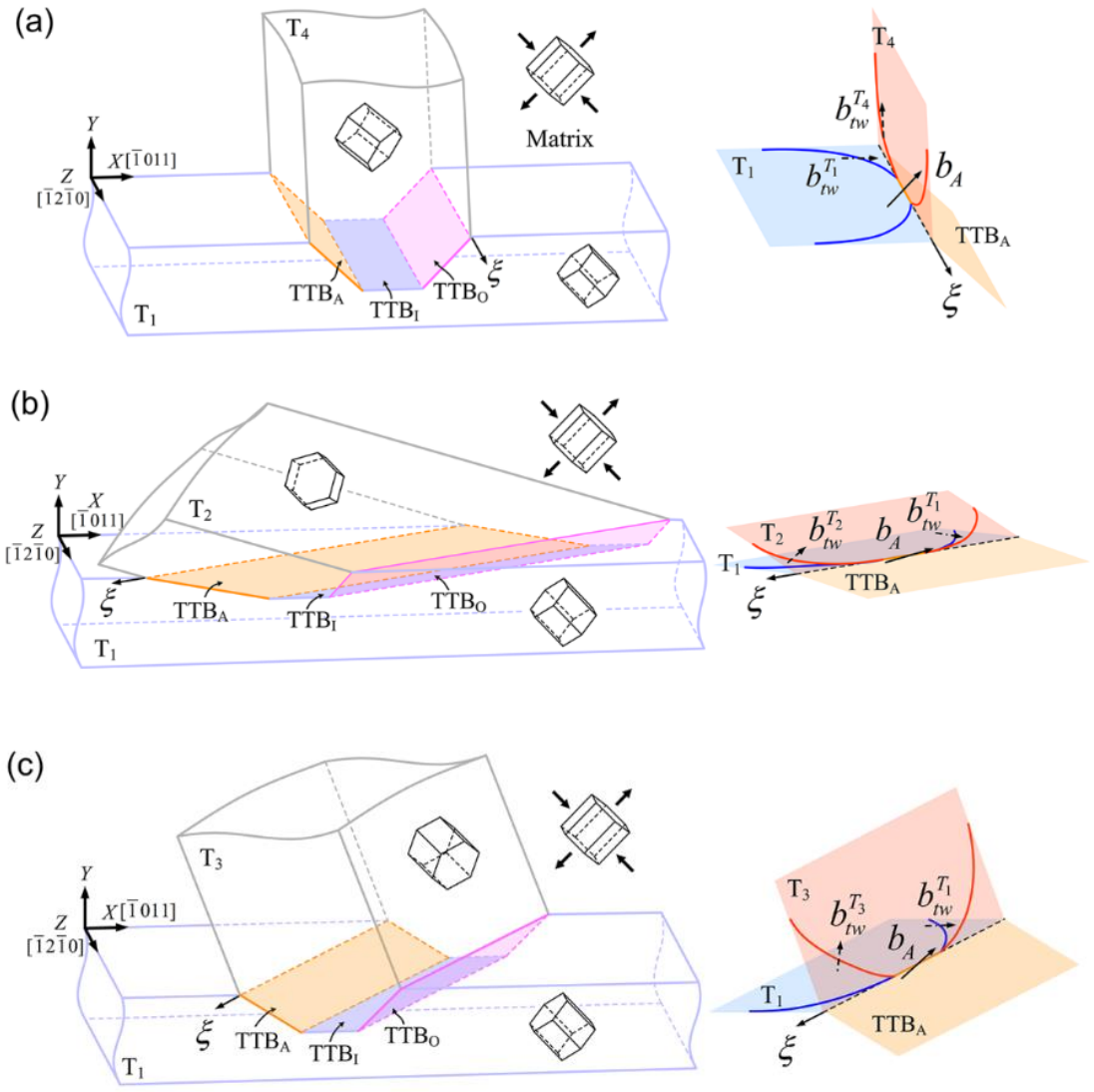

Figure 40 Twin-twin boundary planes and Burgers vectors of boundary dislocations for the three twin-twin interactions: (a) Type I $T_4 \leftrightarrow T_1$ twin interaction; (b) Type II(a) $T_2 \leftrightarrow T_1$ twin-twin interactions; (c) Type II(b) $T_3 \leftrightarrow T_1$ twin-twin interactions.

Table 6 Burgers vectors of the dislocations on twin-twin boundaries (TTB_I, TTB_A, TTB_O) for the three types of twin-twin interactions (all the vectors are described in the matrix crystal coordinate).

Twin pair	b_I	b_A	b_O	$2\|b_I\|^2/(\lambda a)^2$	$\|b_A\|^2/(\lambda a)^2$	$\|b_O\|^2/(\lambda a)^2$
$T_4 \leftrightarrow T_1$	$\lambda[10\bar{1}1]$	$2\lambda[0001]$	$2\lambda[10\bar{1}0]$	11.23	10.56	11.97
$T_2 \leftrightarrow T_1$	$\lambda[0\bar{1}11]$	$\lambda[\bar{1}\bar{1}22]$	$\lambda[1\bar{1}00]$	11.23	19.54	2.99
$T_3 \leftrightarrow T_1$	$\lambda[1\bar{1}01]$	$\lambda[0\bar{1}12]$	$\lambda[2\bar{1}\bar{1}0]$	11.23	13.54	9.00

Notes: b_I - Burgers vector of dislocation impinged on a pre-exiting twinning boundary; b_A and b_O - Burgers vectors of dislocations on the TTB_A and TTB_O twin-twin boundaries formed by reaction of twinning dislocations.

Table 6 summarizes the Burgers vectors of junctions (or boundary dislocations) in the twin-twin boundaries. b_I is the Burgers vector of the impinging TD associated with the incoming twin. b_A and b_O are the Burgers vectors that result from reaction of the TDs associated with two interacting twins. The elastic energy associated with these dislocations is proportional to the square of the magnitude of Burgers vector and is computed for the three twin-twin interactions in Table 6. It is found that the formation of TTB_A is energetically favorable while TTB_O is unfavorable for Type I twin-twin interactions. Conversely, the formation of TTB_O is energetically favorable while TTB_A is unfavorable for Type II twin-twin interactions. For example, the elastic energy associated with the left hand side of Equations (5a) and (5b) is proportional to $11.23(\lambda a)^2$ for Type I twin interactions according to Frank's law [151]. The right hand sides of Equations (5a) and (5b) are proportional to $10.56(\lambda a)^2$ and $11.97(\lambda a)^2$,

respectively, indicating that the reaction is favorable for forming TTB_A boundary and unfavorable for forming TTB_O boundary when only considering the change in line energy of the dislocations. The change in the elastic energy associated with the dislocation dissociation (Equations (6a) and (6b)) increases, indicating that the dissociation mechanism is energetically unfavorable. However, the formation of dislocation walls will further reduce the net elastic energy due to the core-core interactions among these dislocations [151]. Therefore, both TTB_A and TTB_O boundaries can form through the two mechanisms.

The twin-twin boundary plane is geometrically defined as the common interface bisecting two twinning planes. In practice, the twin-twin boundary plane can be slightly deviated from the common interface because of thermodynamically driven reconstruction to minimize interface energy, such as faceted or curved interfaces [154–156]. Nevertheless, the net Burgers vector of the boundary dislocations is unchanged according to the Frank-Bilby theory [154, 156–159] when the misorientation relationship between the two crystals remains unchanged. For a Type I co-zone twin-twin interaction (Figure 40a and Table 7), due to the twinning reorientation of the crystals, the boundary plane of TTB_O bonds the basal planes in the two twins, which is referred to as BB. The boundary plane of TTB_A binds the prismatic planes in the two twins, as being referred to as PP. These structures have been examined recently using atomistic simulations in magnesium [160]. The Burgers vector of the boundary dislocations is perpendicular to the TTB plane (Figure 40a), forming a boundary dislocation tilt wall. As a result, TTB_A and TTBo in Type I twin interactions can be characterized as low-angle symmetric tilt boundaries with a tilt angle of 7.4 º. As listed

in Table 7, for Type II(a) twin-twin interaction, a crystallographic analysis according to a common interface bisecting two twinning planes shows that the boundary plane of TTB_A is parallel to the $(11\bar{2}4)$ plane in the matrix and binds the $(5\bar{2}\bar{3}6)$ plane in T_1 twin and the $(\bar{2}5\bar{3}6)$ plane in T_2 twin. The boundary plane of TTB_O is parallel to $(1\bar{1}00)$ in the matrix and bonds the $(\bar{1}2\bar{1}2)$ plane in the T_1 twin and the $(\bar{2}11\bar{2})$ plane in T_2 twin. For Type II(b) twin-twin interaction, the boundary plane of TTB_A is parallel to the $(01\bar{1}4)$ plane in the matrix and binds the $(13\bar{5}\bar{8}6)$ plane in T_1 twin and the $(\bar{1}\bar{3}856)$ plane in T_3 twin. The boundary plane of TTB_O is parallel to the $(2\bar{1}\bar{1}0)$ plane in the matrix and binds the $(\bar{3}5\bar{2}14)$ plane in T_1 twin and the $(\bar{3}\bar{2}5\bar{1}\bar{4})$ plane in T_3 twin. As shown in Figure 40b and Figure 40c, the Burgers vector of the boundary dislocations has two components, one is perpendicular to the boundary plane and the other lies on the boundary plane and is not parallel to the intersection line (or junction line). Consequently, TTB_A and TTBo for Type II twin-twin interactions can be characterized to be tilt plus twist boundaries. The two bound crystal planes in the two twins are of the same type but twisted relative to each other.

Table 7 Plane normal to the twin-twin boundaries (TTB_I, TTB_A, and TTB_O) for three crystallographically distinctive twin-twin interaction pairs (the Miller-Bravais indices of the crystal planes are referred in different lattice domains as indicated in the table).

Twin-twin pair	TTB_I	TTB_A	TTB_O
$T_4 \leftrightarrow T_1$	$(10\bar{1}2)$ in matrix	(0001) in matrix $(10\bar{1}0)$ in T_1 $(\bar{1}010)$ in T_4	$(10\bar{1}0)$ in matrix (0001) in T_1 (0001) in T_4
$T_2 \leftrightarrow T_1$	$(10\bar{1}2)$ in matrix	$(11\bar{2}4)$ in matrix $(5\bar{2}\bar{3}6)$ in T_1 $(\bar{2}5\bar{3}6)$ in T_2	$(1\bar{1}00)$ in matrix $(\bar{1}2\bar{1}2)$ in T_1 $(\bar{2}11\bar{2})$ in T_2
$T_3 \leftrightarrow T_1$	$(10\bar{1}2)$ in matrix	$(01\bar{1}4)$ in matrix $(13\bar{5}\bar{8}6)$ in T_1 $(\bar{1}\bar{3}856)$ in T_3	$(2\bar{1}\bar{1}0)$ in matrix $(\bar{3}5\bar{2}14)$ in T_1 $(\bar{3}\bar{2}5\bar{1}\bar{4})$ in T_3

Notes: TTB_I - the boundary of a pre-existing twin; TTB_A - twin-twin boundary bisecting the acute angle between the two interacting twins; TTB_O - twin-twin boundary bisecting the obtuse angle between the two interacting twins. (A table should be within one pape if possible)

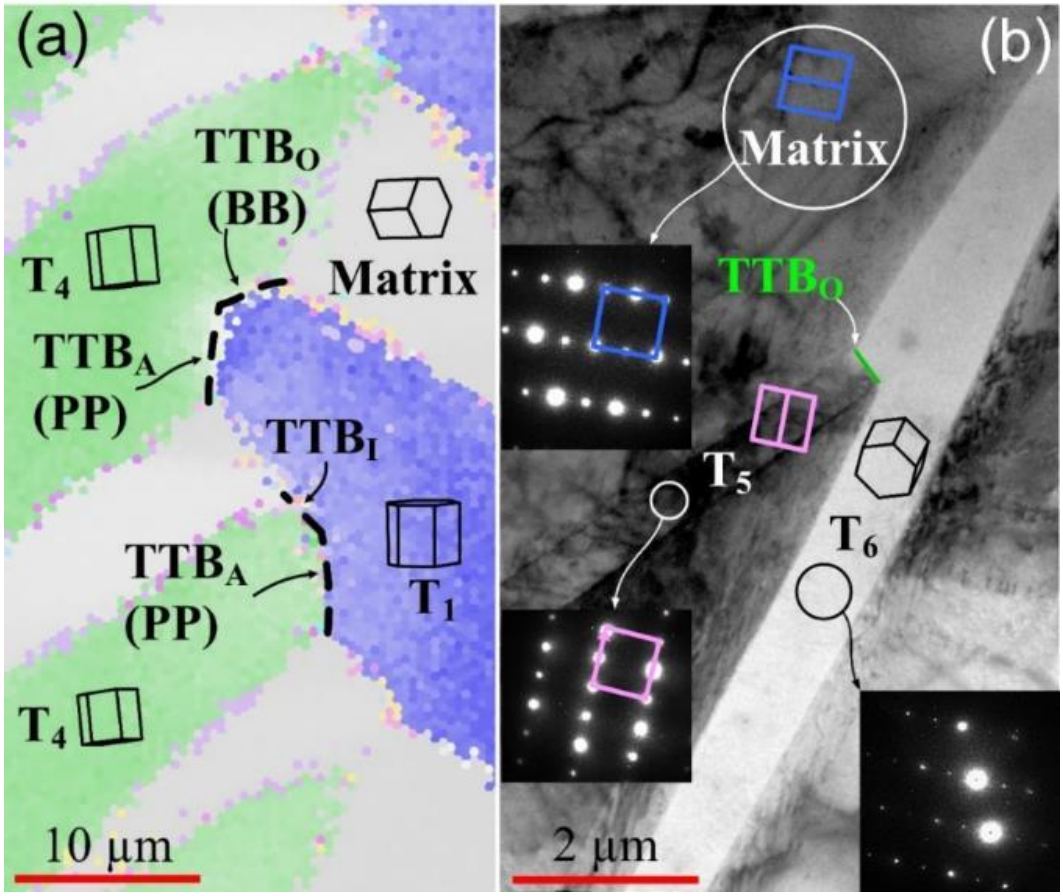

Figure 41 Experimentally observed twin-twin boundaries in magnesium single crystal: (a) EBSD orientation map of low-angle twin-twin boundaries, TTB_A (BB) and TTB_O (PP), in Type I co-zone twin interaction under initial compression in [10 $\bar{1}$ 0]-magnesium single crystal; (b) TEM bright field micrograph showing a TTB_O in Type II(a) twin-twin interaction.

TTBs associated with Type I co-zone twin-twin interaction are observed from the initial compression of the magnesium single crystal under [10 $\bar{1}$ 0] direction. Figure 41a shows TTBs between a T_4 twin and a T_1 twin. Twin-twin boundaries consist of low-angle TTB_O and TTB_A tilt boundaries with a misorientation angle of 6.6 ºmeasured by EBSD. The trace of the TTB_A boundary plane is close to traces of prism planes in

both twins and referred to as PP boundary. The TTB_O boundary plane trace is approximately parallel to the basal plane traces in both twins and referred to as BB boundary. Atomistic simulations of Type I co-zone twin-twin interactions [160] with empirical potential for magnesium have been used to examine the formation of PP and BB boundaries. Figure 41b is a TEM bright field micrograph showing a TTB_O boundary associated with Type II(a) twin-twin interaction. It is worth mentioning that no twin transmission is observed in either type of twin-twin interactions.

The three-dimensional geometry of a Type II(a) twin-twin boundary (TTB) is further studied to verify whether it is suitable to define the TTB as a common interface bisecting two interacting twinning planes. It can be reasonably assumed that the twin-twin interface is a three-dimensional (3D) plane located in the specimen with an arbitrary orientation, as shown in Figure 42a. The 3D twin-twin interface can be projected onto the specimen surface as well as the cross section plane (Figure 42a). For the trace of TTB on the specimen surface, SEM/EBSD can be used to characterize the surface geometry of TTB and the crystal orientation of its neighboring twins. As for the trace of TTB on the cross section plane, a SEM/FIB dual beam technique was used to cut off a thin TEM foil (~200 nm in thickness) containing the TTB. The TEM foil plane is parallel to the cross section plane. The foil under TEM was further examined so that the geometry and crystallography information of the TTB on the cross section plane can be obtained.

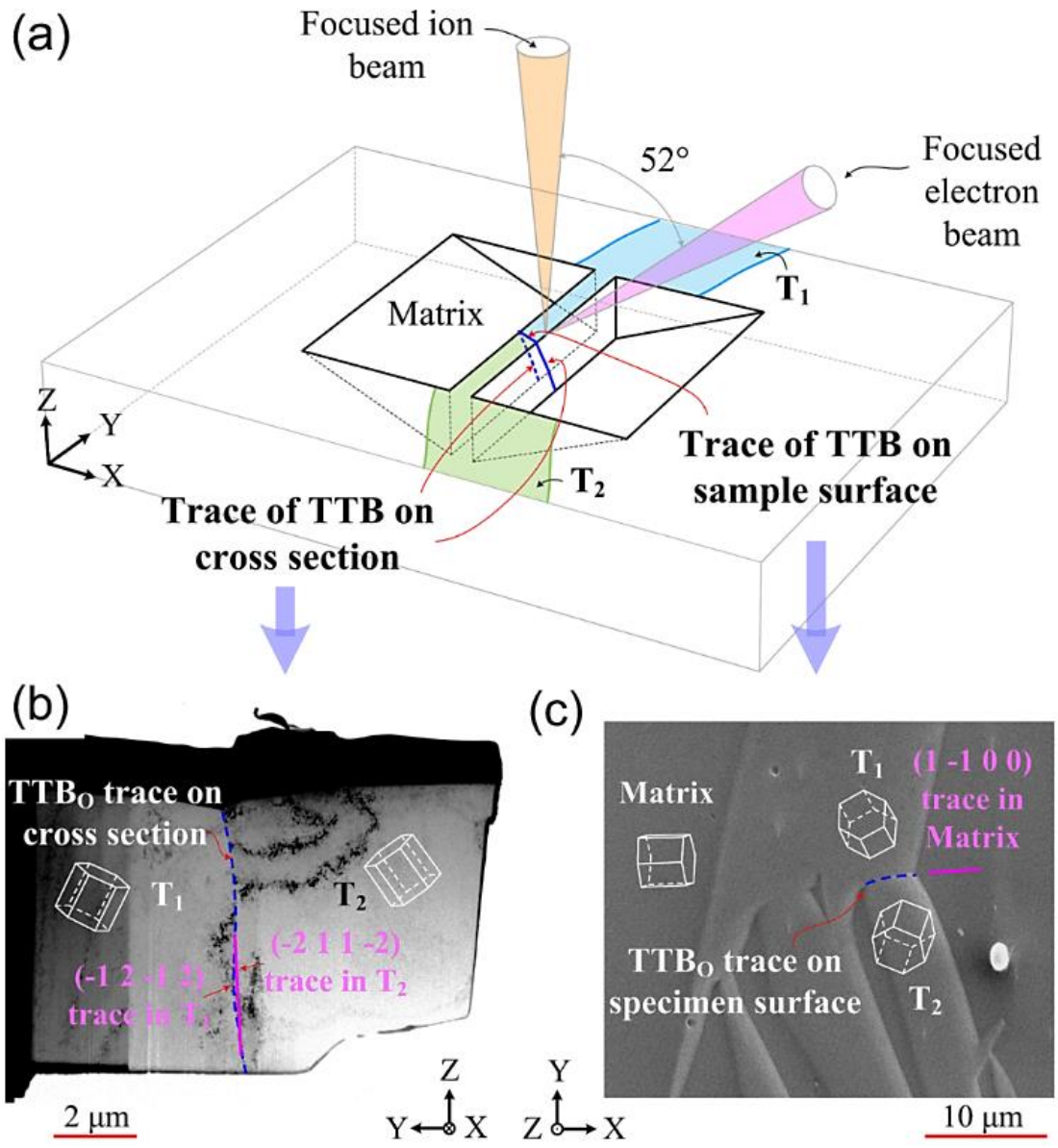

Figure 42 Three-dimensional geometry and crystallography information of a Type II(a) twin-twin boundary (TTB) characterized by SEM/FIB dual beam technique and TEM technique: (a) schematic of TEM foil fabrication by SEM/FIB nanofabrication through cross section and lifting out techniques; (b) TEM examination of TTB trace on the cross section plane (dashed blue line); (c) SEM and EBSD examinations of TTB trace on the specimen surface (dashed blue line).

The observation of TTB traces on the cross section plane and the specimen plane are shown in Figure 42b and Figure 42c, respectively. On the cross section plane, it can be clearly observed that the TTB is a slightly curved interface (dashed blue line in Figure 42b) between the neighboring twins T_1 and T_2. A crystallographic analysis shows that the trace of $(\bar{1}2\bar{1}2)$ plane in T_1 and the trace of $(\bar{2}11\bar{2})$ plane in T_2 coincide well with an imaginary line linking the starting point and the ending point on the curved twin-twin interface. On the specimen surface, an SEM/EBSD analysis reveals that the TTB trace aligns with the $(1\bar{1}00)$ trace in the matrix. The agreement of TTB trace with $(\bar{1}2\bar{1}2)$ trace in twin T_1 and $(\bar{2}11\bar{2})$ trace in twin T_2 on the cross section plane and the $(1\bar{1}00)$ trace in the matrix on the specimen surface confirms that a geometry abstraction of TTB as a common interface bisecting two twinning planes is acceptable.

4.4.3 Formation of "Apparent Crossing" Twin Structure

According to the experimental observations and theoretical analyses presented, $\{10\bar{1}2\}$ twins do not transmit into one another. The formation of the "apparent crossing" twin structures in Figure 37 is addressed here using an argument based on the formation of twin-twin boundaries. As shown in Figure 43a, two T_i twins impinge on each side of a T_j ($j \neq i$) twin. Figure 43b shows the formation of an "apparent crossing" twin structure accompanying the formation and growth of TTBs and the growth of these three twins. TTBs of all kinds are shown in Figure 43b. In fact, a different number or kind of TTBs could form due to the local stresses and difference in the kinetics and energetics aspects for TTBs formation. For example, two types of

TTBs are observed in Figure 37a and one type of TTB is observed in Figure 37b. Nevertheless, the intersection region visualized as the violet shaded area in Figure 43b is part of twin T_j but tilted 6.4 ° from twin T_j due to the existence of boundary dislocations according to interface dislocation theory [151].

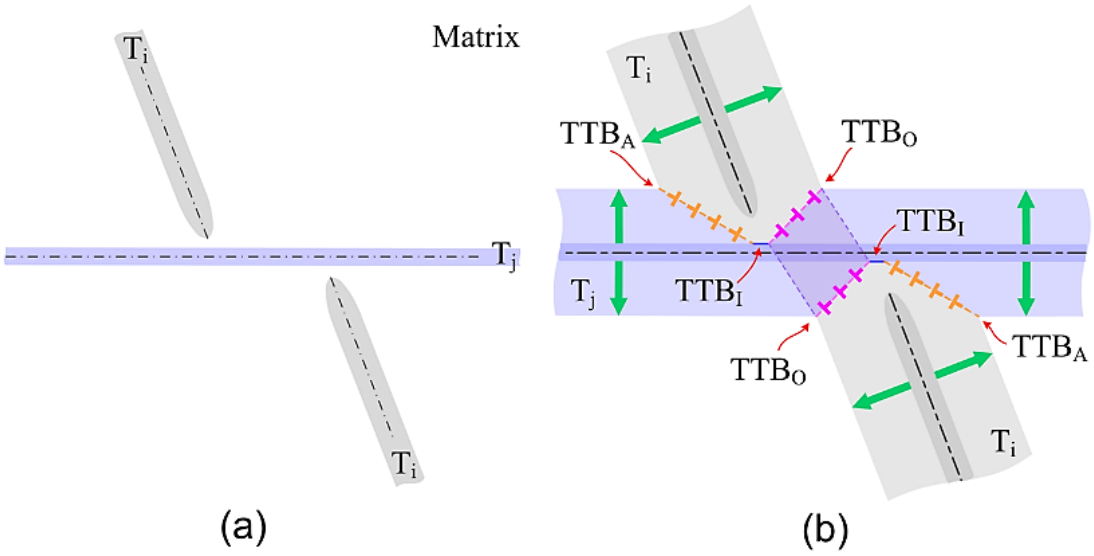

Figure 43 Formation mechanisms of "apparent crossing" twin structure: (a) a T_i twin encounters a pre-existing T_j twin from one side and another closely-aligned parallel T_i twin contacts the same T_j twin from the other side ($j \neq i$); (b) formation of twin-twin boundaries at both sides of T_j twin via the zipping and/or dissociating mechanisms. The dislocations on TTB_A and TTB_O are drawn in orange and pink colors, respectively. The green arrow indicates the direction of the twin boundary growth.

4.5 Influence of Twin-Twin Boundary on Twinning/Detwinning

4.5.1 Influence on Twinning

Once TTBs form, twinning dislocations associated with the incoming twin are blocked at the twin boundary and form boundary dislocations. Backstresses resulting

from the pileup of these boundary dislocations hinder the motion of twinning dislocations toward the TTB, producing a stronger repulsion force near the TTB. Further growth and propagation of twins thus requires a higher external stress, resulting in strain hardening during twinning.

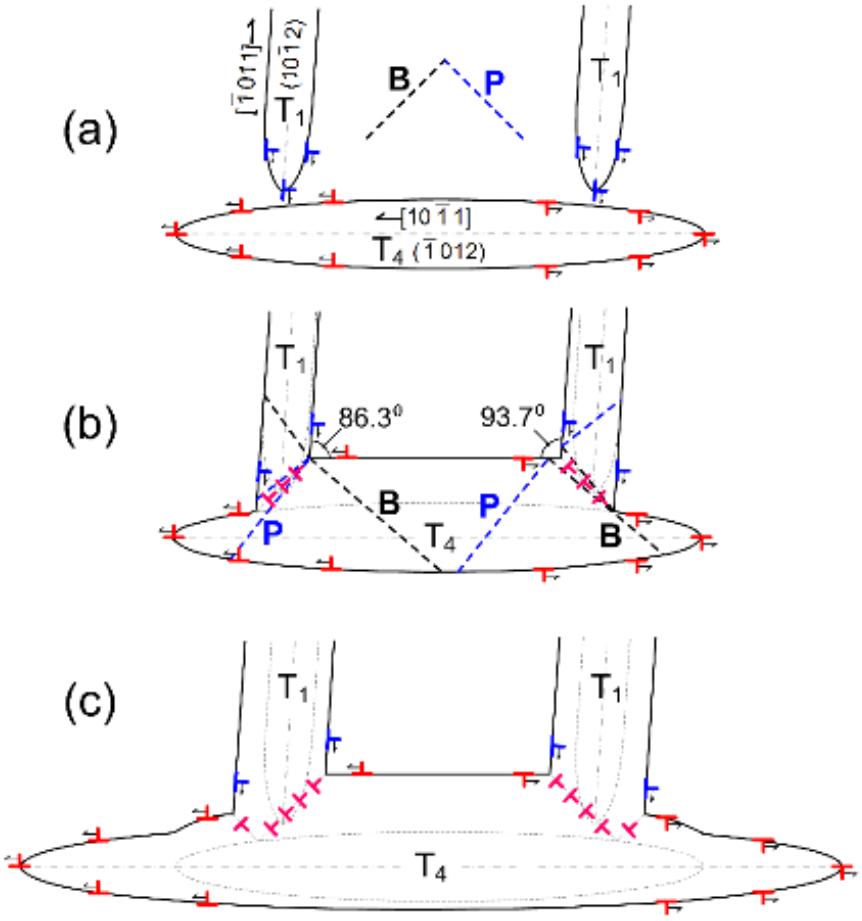

Figure 44 Formation of both PP and BB twin-twin boundaries (TTBs) when a $(10\bar{1}2)$ T_1 twin interacts a $(\bar{1}012)$ T_4 twin: (a) two twin variants before interact; (b) formation of a single tilt TTB (PP or BB); (c) further twin growth after the formation of a single TTB (PP or BB). Twinning dislocations are red for T_4 twin, blue for T_1 twin, and pink for twin-twin boundary dislocations. Blue and black dashed lines indicate prism plane (P) and basal plane (B), respectively.

Apart from the barrier effect caused by the pinned twinning dislocation at the barrier twin boundary, further twinning loading will produce a compound twin-twin boundaries which contains both the TTB_A and TTB_O, as observed in Figure 41a. It is noticed that both types of tilt TTBs (PP and BB for Type I) will form when one twin meets the other. The extension of a single tilt twin-twin boundary into a compound twin-twin boundary can be explained if further growth of T_1 and T_4 is accounted for by the reaction and dissociation of TDs, as schematically illustrated in Figure 44. With further growth of T_1 after formation of a single PP or BB tilt boundary (Figure 44b), a TD in T_1 can glide towards the tilt boundary, dissociating into a TD in T_4 and leaving a tilt boundary dislocation at the tilt boundary. As a result, the T_4 twin grows and the tilt boundary extends (Figure 44(c)), adding extra atomic layers on one side of the twin-twin junction and creating a "plateau." The required reaction involves a dissociation as expressed in Equation (6), which is energetically unfavorable and results in a strain hardening effect during further twin growth.

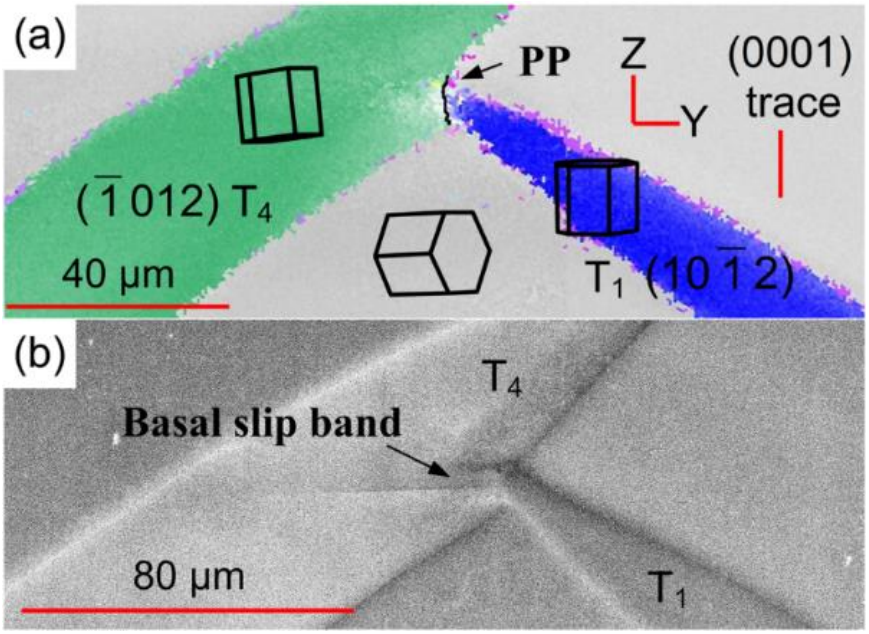

Figure 45 (a) High-magnification crystal orientation map showing the low-angle twin-twin boundary (PP) between T_1 and T_4 twins. (b) backscatter secondary electron (BSE) micrograph of the same region in (a) showing a basal slip band transmitted from the PP boundary.

It is worth pointing out that for Type I twin-twin interactions, the two twinned crystals have a low misorientation angle of about 7.4 °. As a result, glide planes in both crystals are nearly parallel and slip transmission for dislocation across TTBs is easy. For the easy basal slip in magnesium, basal dislocations from the incoming twin can transmit across TTB_O (PP) where the boundary plane is prismatic, forming a basal slip band in the barrier twin. This basal slip band emitted from PP boundary was observed in magnesium single crystal, as shown in Figure 45. When T_1 encounters T_4, a low-angle twin-twin boundary (PP, black line) forms (Figure 42a). Figure 45b is a backscattered secondary electron (BSE) micrograph taken at the same region as that in Figure 45a. A slip band connected with the twin-twin boundary is observed inside the

T_4 twin. The trace of the slip band aligns with the trace of the basal plane (0001) in T_4 twin, indicating that this slip band is of a basal type.

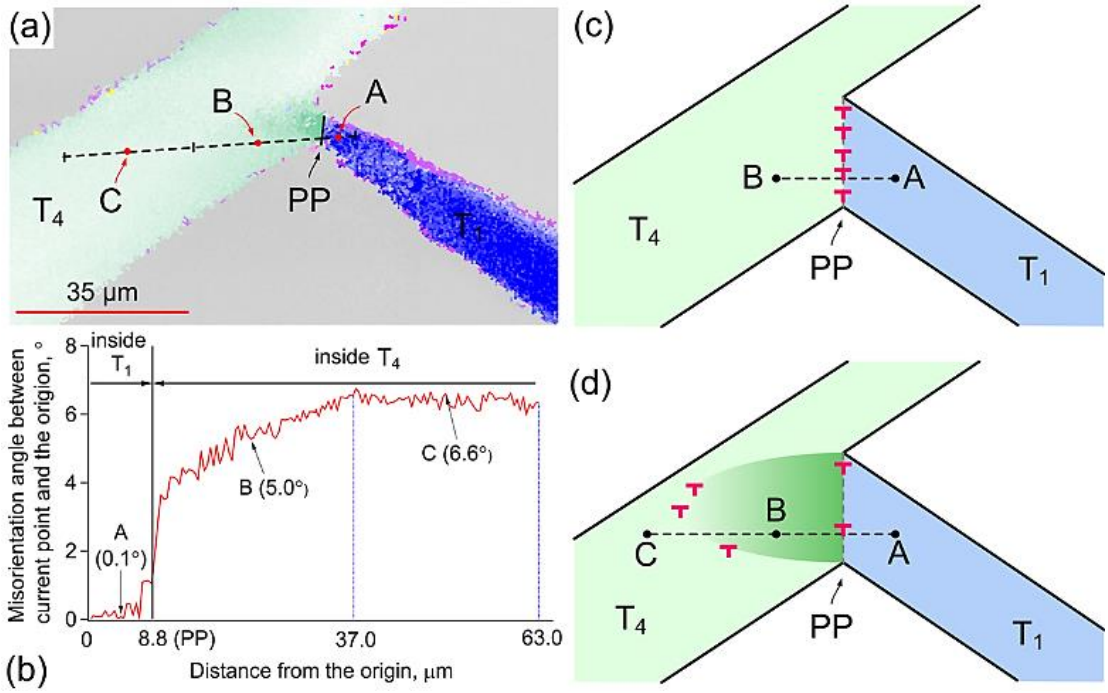

Figure 46 Misorientation change caused by a slip band transmitted from a tilt PP twin-twin boundary: (a) a straight path on the basal slip band area in the barrier twin across the PP boundary; (b) misorientation angle measured between the current point and the origin on the straight path shown in (a); (c) PP tilt boundary is formed but no basal slip occurs in T_4; (d) after basal slip band is formed in T_4.

Figure 46a and Figure 46b present a misorientation analysis in the transmitted slip band region based on the results obtained from an EBSD analysis. The misorientation angle between T_1 and T_4 is 6.6° but the slip band region (represented by point B) has misorientation angles of 5.1° with respect to twin T_1 (represented by point A) and 1.5° with respect to twin T_4 (represented by point C). There are two possible mechanisms in the formation of basal slip bands. First, a simple geometry analysis shows that the

angle between the basal planes in T_1 and T_4 is 7.4°. The coherent region associated with the tilt boundary facilitates slip transmission for basal dislocation from the T_1 twin to the T_4 twin, and prevents the formation of a secondary tension twin inside the T_4 twin because TDs in the T_1 twin cannot directly transform into TDs in T_4 twin. Second, Burgers vectors along the tilt boundary could reassemble, under stressing, into a boundary dislocation with a Burgers vector of $\frac{1}{2}[10\bar{1}0]$ accompanying the extension of the tilt boundary, reducing the chemical potential energy by forming more coherent segments along the tilt boundary [161, 162]. These reassembled boundary dislocations can further dissociate into basal dislocations or act as sources for nucleation and emission of basal dislocations. They are then emitted from the tilt boundary, forming a basal slip band. Accompanying the emission of basal dislocations from the tilt boundary, the tilt angle decreases, as schematically described in Figure 46c and Figure 46d. This is an energetically favorable process. For Type II twin-twin interactions, the two twinned crystals have large misorientation angles (>35°) and the traces of their glide planes with the boundary plane are not parallel. As a result, slip transmission is difficult.

4.5.2 Influence on Detwinning and Secondary Twinning

Under reversed loading, detwinning may occur as a reversal of the twinning process. For interacting twins, TTB dislocations can dissociate into twinning dislocations that glide on the twinning plane to cause the twin thickness to decrease. However, dissociation is an energetically unfavorable process based on the dislocation theory. It is expected that detwinning becomes more difficult with increasing loading cycles because more TTBs accumulated hinders detwinning. More interestingly, secondary

twins can initiate from TTBs, as observed in Figure 38c and Figure 38d. Experimental characterizations by EBSD reveal two microstructural mechanisms, both based on secondary twins nucleating at and propagating from TTBs: (1) secondary twins leading to "detwinning from inside" (T_{ii} in T_i and T_{jj} in T_j) and; (2) secondary twins where the secondary twin plane T_{ij} intersects with the primary twin planes T_i and T_j along the same intersection line.

Figure 47 schematically illustrates possible deformation modes under reversed loading. Figure 47a shows a general case of TTBs associated with the $T_i \rightarrow T_j$ twin interaction where three possible detwinning modes could operate. The first mode is associated with direct detwinning through dissociation/unzipping of boundary dislocations into twinning dislocations that glide on their associated twinning planes (Figure 47b). This process can be expressed as:

$$b_{TTB} \Rightarrow b_{tw}^{T_i} + b_{tw}^{T_j} \quad (7)$$

The second and third detwinning modes are associated with nucleation and propagation of secondary twinning inside the primary twins. In the second deformation mode (Figure 47c), the secondary twin variant is either T_{ii} or T_{jj}, that is, the same variant is activated in primary twin. In the third deformation mode (Figure 47d), the secondary twin variant is either T_{ij} or T_{ji}, that is, the variant of the other primary twin is active. Atomistic simulations and a theoretical analysis [163] show that a minimum stable twin nucleus requires simultaneous nucleation of multiple twinning dislocations. Correspondingly, the second deformation mode can be expressed as:

$$nb_{TTB} \Rightarrow nb_{tw}^{T_{ii}} + nb_{tw}^{T_{jj}} \quad (8)$$

The third mode is similar to the second mode but with different reactions:

$$nb_{TTB} \Rightarrow nb_{tw}^{T_{ij}} + nb_r \qquad (9a)$$

or

$$nb_{TTB} \Rightarrow nb_{tw}^{T_{ji}} + nb_r \qquad (9b)$$

where n is equal to 3 for the normal-twinning mechanism [163]. nb_r is the residual dislocations left on the TTB. Compared to the first mode where detwinning is accomplished through successive dissociation of boundary dislocations, the second and third modes involve multiple dislocations and are less energetically favorable.

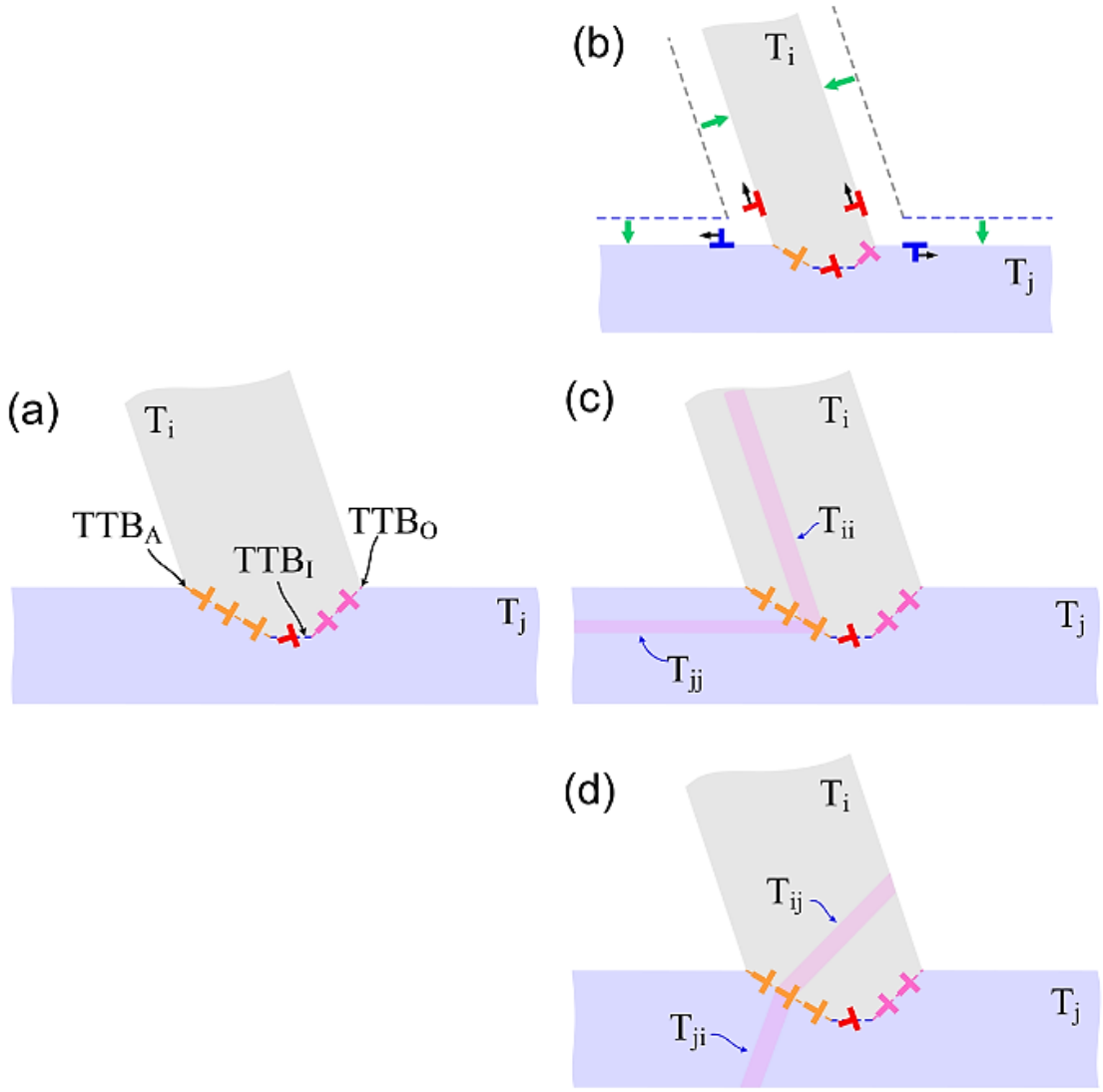

Figure 47 Detwinning, retwinning and secondary twinning mechanisms related to twin-twin boundaries under reversed loading: (a) at the start of load reversal; (b) detwinning through dissociation of a single TTB dislocation into twinning dislocations; (c) secondary twinning with the same twin variant as the primary twin (or referred to as "detwinning from inside") accompanying nucleation of twins from TTBs; (d) secondary twinning with a different twin variant from the primary twin (or referred to as double twinning) accompanying nucleation of twins from TTBs.

Table 8 Dissociation process associated with three detwinning mechanisms, the energy associated with the dissociated secondary twin dislocation and the residual dislocation, and the Schmid factor for secondary twinning under reversed loading in [000 $\bar{1}$] direction.

Dissociation	E_1	E_2	E_1 - E_2	$b_{tw}^{T_{ij}} \bullet b_r /(n\lambda a)^2$	m
Mechanism 1 and 2: (n = 1 for Mechanism 1, n = 3 for Mechanism 2)					
Type I					
$nb_A \Rightarrow nb_{tw}^{T_{44}} + nb_{tw}^{T_{11}}$	10.56	11.23	0.67	-0.36	0.5
$nb_O \Rightarrow nb_{tw}^{T_{44}} + nb_{tw}^{T_{11}}$	11.97	11.23	-0.74	0.36	0.5
Type II(a)					
$nb_A \Rightarrow nb_{tw}^{T_{22}} + nb_{tw}^{T_{11}}$	19.54	11.23	-8.31	4.12	0.5
$nb_O \Rightarrow nb_{tw}^{T_{22}} + nb_{tw}^{T_{11}}$	2.99	11.23	8.24	-4.12	0.5
Type II(b)					
$nb_A \Rightarrow nb_{tw}^{T_{33}} + nb_{tw}^{T_{11}}$	13.54	11.23	-2.31	1.13	0.5
$nb_O \Rightarrow nb_{tw}^{T_{33}} + nb_{tw}^{T_{11}}$	9.00	11.23	2.23	-1.13	0.5
Mechanism 3 (n=3)					
Type I					
$nb_I \Rightarrow nb_{tw}^{T_{41}} + nb_r$ (or $nb_I \Rightarrow nb_{tw}^{T_{14}} + nb_r$)	5.62	17.59 (or 27.99)	11.97 (or 22.37)	-5.98 (or -11.19)	0.49
$nb_A \Rightarrow nb_{tw}^{T_{41}}(\text{or } nb_{tw}^{T_{14}}) + nb_r$	10.56	33.60	23.04	-11.55	0.49
$nb_O \Rightarrow nb_{tw}^{T_{41}}(\text{or } nb_{tw}^{T_{14}}) + nb_r$	11.97	33.60	21.63	-10.83	0.49
Type II(a)					
$nb_I \Rightarrow nb_{tw}^{T_{21}} + nb_r$ (or $nb_I \Rightarrow nb_{tw}^{T_{12}} + nb_r$)	5.62	8.61 (or 7.01)	2.99 (or 1.39)	-0.266 (or -0.124)	0.12
$nb_A \Rightarrow nb_{tw}^{T_{21}}(\text{or } nb_{tw}^{T_{12}}) + nb_r$	19.54	12.64	-6.90	3.43	0.12
$nb_O \Rightarrow nb_{tw}^{T_{21}}(\text{or } nb_{tw}^{T_{12}}) + nb_r$	2.99	12.64	9.65	-4.82	0.12
Type II(b)					
$nb_I \Rightarrow nb_{tw}^{T_{31}} + nb_r$ (or $nb_I \Rightarrow nb_{tw}^{T_{13}} + nb_r$)	5.62	14.64 (or 18.22)	9.02 (or 12.60)	-4.49 (or -6.29)	0.12
$nb_A \Rightarrow nb_{tw}^{T_{31}}(\text{or } nb_{tw}^{T_{13}}) + nb_r$	13.54	23.85	10.31	-5.16	0.12
$nb_O \Rightarrow nb_{tw}^{T_{31}}(\text{or } nb_{tw}^{T_{13}}) + nb_r$	9.00	23.85	14.85	-7.42	0.12

Notes: b_I - Burgers vector of the impinged twining dislocation on the T_1 twin boundary; b_A - Burgers vector of the TTB_A boundary dislocation; b_O - Burgers vector of the TTB_O boundary dislocation; $b_{tw}^{T_{ij}}$ - Burgers vector of the dissociated secondary twinning dislocation; b_r - Burgers vector of the dissociated residual dislocation; m - Schmid factor for secondary twinning under reversed loading in $[000\bar{1}]$ direction. $E_1 = |b_{TTB}|^2/(n\lambda a)^2$, and $E_2 = (|b_{tw}^{T_{ij}}|^2 + |b_r|^2)/(n\lambda \mathrm{a})^2$.

The feasibility of the three detwinning deformation modes are further analyzed. For each dissociation process, the interaction energy is computed between the dissociated dislocations, the change in the elastic energy of the dislocations, and the Schmid factor associated with the dissociated twinning dislocations. The results are summarized in Table 8. The Schmid factor for secondary twinning was computed for compression along the $[000\bar{1}]$ direction. It is clearly observed that (1) most of dissociation processes are energetically unfavorable resulting in a retarding behavior for detwinning and TTB-induced detwinning hardening; (2) the first mode (detwinning) is the easiest among the three modes; and (3) secondary twinning is easiest for Type II(a) twin-twin boundaries and the most difficult for Type I co-zone twin-twin boundaries.

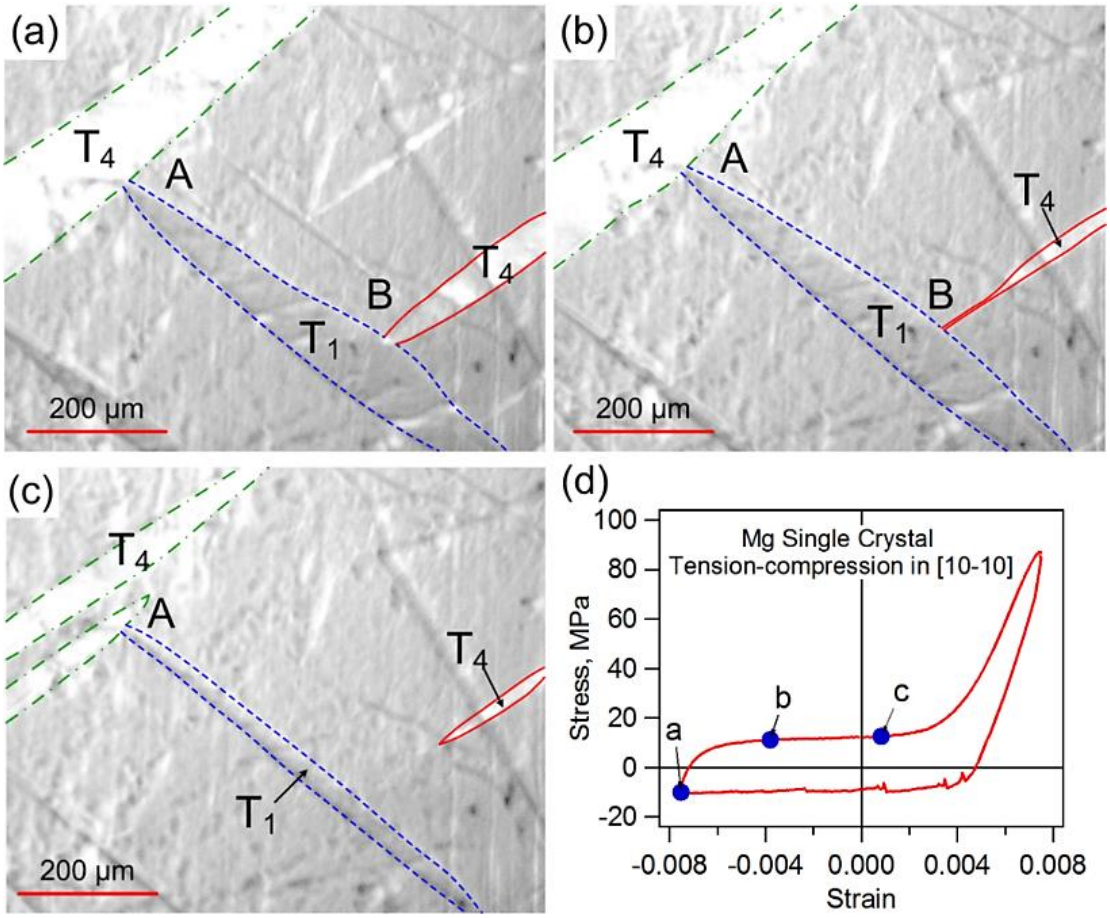

Figure 48 *In situ* optical micrographs showing different stages (a, b, and c) of detwinning and their corresponding stress-strain states (d) in the $[10\bar{1}0]$-oriented magnesium single crystal subjected to fully reversed compression-tension at the strain amplitude of 0.75%.

An *in situ* observation of the hindering effect of the TTB on detwinning can be illustrated in the $[10\bar{1}0]$-oriented magnesium single crystal. Figure 48 includes three snapshots from *in situ* optical micrographs that show an evidence of retardation in detwinning. Figure 48a shows three fully formed twins at the compressive peak strain of -0.75% (Point a in Figure 48d). Twin T_1 (outlined by the blue dashed line) impinges on one T_4 twin (outlined by the green dashed line) at the contact site A. The other T_4

twin (outlined by the red solid line) impinges on the T_1 twin at the contact site B. It is observed that the T_1 twin boundary exhibits enhanced twin growth at the contact site B as compared to other locations on the boundary. The proposed model in Figure 44 can explain this observation. During detwinning and until the loading reaches Point b in Figure 48d, an *in situ* optical microscopic observation indicates that the T_4 twin (red solid line) shrinks in thickness but one end remains attached to the T_1 twin at site B (Figure 48b). The T_4 twin (red solid line) detaches from the T_1 twin at site B when the loading exceeds Point b in Figure 48d. After the detachment (Figure 48c), the T_4 twin quickly becomes elliptical, while the T_1 twin detwins partially and shrinks but remains attached to T_4 (green dashed line) because of the pinning effect of the tilt boundary at site A. The detachment of one twin from the tilt boundary accompanying detwinning involves the dissociation of the tilt boundary into two sets of twinning dislocations and is energetically unfavorable.

4.5.3 Effect of Twinning, Detwinning, and Secondary Twinning on Cyclic Hardening

In order to quantify the effect of twinning and detwinning upon cyclic hardening, a mean flow stress (σ_{twin} and σ_{detwin}) and a mean hardening rate ($\left(d\sigma / d\varepsilon_p\right)_{twin}$ and $\left(d\sigma / d\varepsilon_p\right)_{detwin}$) are defined as follows (Figure 49a). A mean plastic strain ($\varepsilon_{p,mean}$) is computed as the average of the tensile peak plastic strain and the compressive peak plastic strain in each loading cycle. The mean flow stress is the stress corresponding to the mean plastic strain for each cycle. The mean hardening rate is the slope of the stress-strain curve at the mean plastic strain. For each full loading cycle, the mean

twinning stress, the mean detwinning stress, and the mean strain hardening rates are computed. The results clearly show two hardening features (Figure 49b): the mean stress and hardening rate during detwinning are greater than those associated with twinning and both of them increase with the number of cycles. The higher flow stress for detwinning can be attributed to the energetically unfavorable dissociation of TTBs, which require a higher stress to be reversed.

The enhanced flow stress with loading cycles can be attributed to the accumulation of un-reversed TTBs and the formation of secondary twins. During twinning, twinning dislocations associated with the incoming twin are blocked at the pre-existing twin boundary, and quilted-looking twin structures form. A backstress is resulted from the pileup of these boundary dislocations and will hinder the motion of twinning dislocations toward the TTB, producing stronger repulsion force near the TTB. A further growth of twins thus requires a higher stress, corresponding to strain hardening during twinning. During detwinning, in addition to the effect due to energetically unfavorable dissociation, more secondary twins form from TTBs as the loading cycles increase. The nucleation and growth of secondary twins suppress detwinning of the primary twin because the plastic deformation associated with secondary twinning decreases the local stress. Consequently, the mean stress and the mean strain hardening rate during detwinning increase more rapidly than those during twinning. A clear evidence of secondary twin development after cyclic loading is shown in Figure 28 .

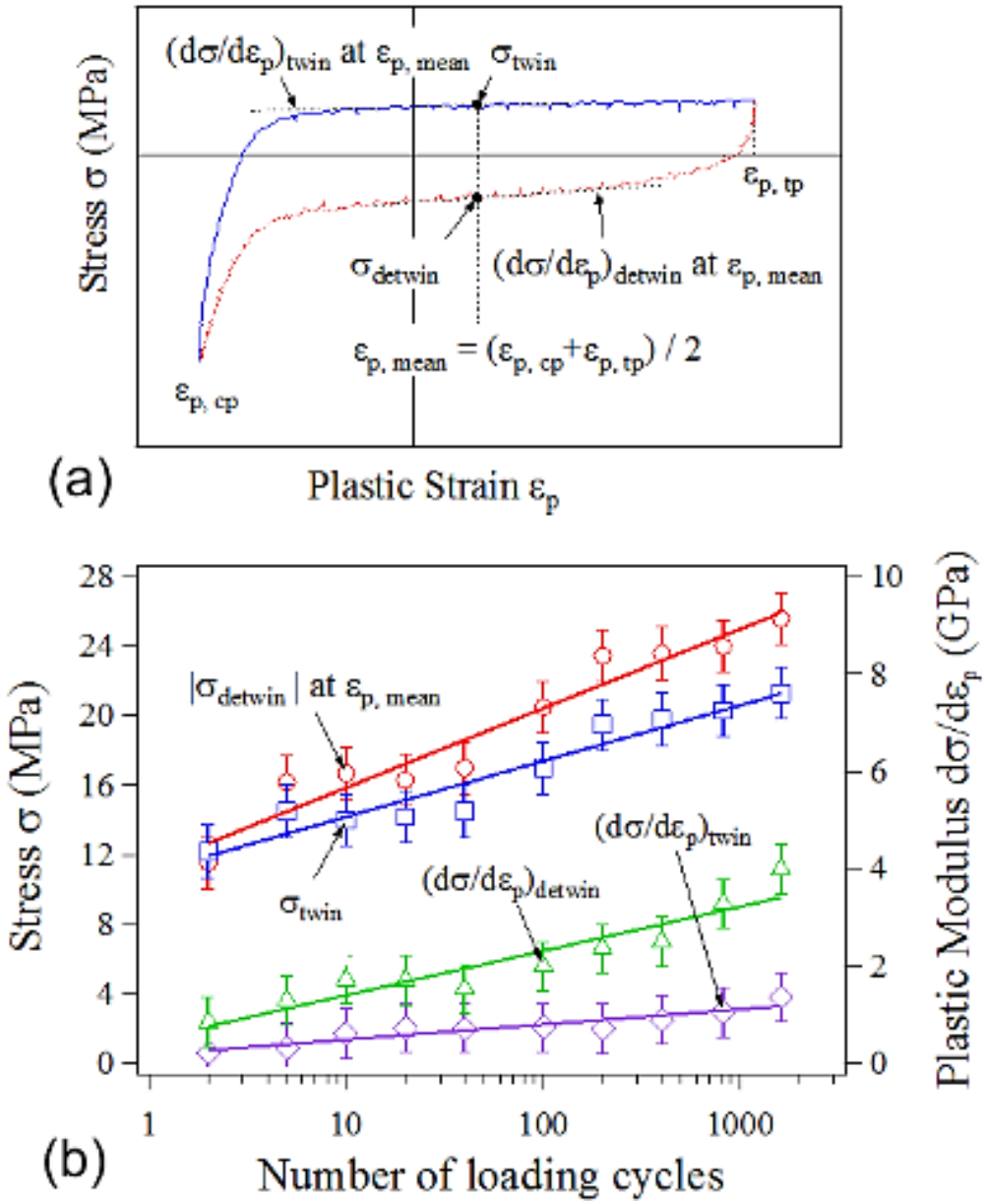

Figure 49 Cyclic hardening of the [0001]-oriented magnesium single crystal subjected to fully reversed tension-compression at a strain amplitude of 0.5%: (a) twinning stress (σ_{twin}), detwinning stress ($|\sigma_{detwin}|$) and their corresponding plastic moduli ($(d\sigma/d\varepsilon_p)_{twin}$ and $(d\sigma/d\varepsilon_p)_{detwin}$) at the mean plastic strain ($\varepsilon_{p,mean}$) as indicated in a typical stress-plastic strain hysteresis loop; (b) variation of twinning stress, detwinning stress and their corresponding plastic moduli with the number of loading cycles.

4.6 Summary

Theoretical analyses of twin-twin interaction structure in magnesium single crystal under cyclic loading were carried out based on crystallography of magnesium and the dislocation theory. Multiple twin variants interact with each other, consequently forming quilted-looking twin structures, "apparent crossing" twin structures, and double twin structures. The microstructures associated with twin-twin interaction are found to correlate with cyclic hardening. The following are the major conclusions from the analyses.

(1) According to a crystallographic analysis, twin-twin interactions can be classified into two types: Type I corresponding to two twins that share a $\langle 11\bar{2}0 \rangle$ zone axis and Type II interactions that share a different zone axis.

(2) When loading favors the growth of two tension twins, one twin cannot transmit into the other to cross a twin boundary through the secondary twinning path. Consequently, twin-twin boundary forms.

(3) According to a Schmid analysis, for a Type I twin-twin interaction, a loading direction activates twinning (or detwinning) of both twins at the same time. Twin transmission cannot occur. For Type II twin-twin interactions, twinning is activated for one twin while detwinning is activated for the other under certain loading directions. However, twin transmission is unlikely. Of all the twin-twin structures characterized in the EBSD experiments conducted, crossing twin structures through secondary twinning path were not observed when the external loading favors the growth of two primary twins.

(4) A twin-twin boundary can form through three mechanisms by reaction of twinning dislocations: impinging, zipping, and dissociating. All of these processes create twin-twin boundary dislocations. For a Type I twin-twin interaction, the twin-twin boundary is a low angle tilt boundary with the habit plane being parallel either to the basal or the prism planes in each twin. For Type II twin-twin interactions, the twin-twin boundary adopts a high index crystallographic plane according to a geometry analysis and could thus evolve to be a complex boundary following thermodynamic relaxation. Twin-twin boundary dislocations can be characterized by reactions of twinning dislocations associated with the two twin variants.

(5) "Apparent crossing" twin structures are a result of twin-twin boundary formation. The crystal in the intersection region experiences a tilt induced by the pileup of twin-twin boundary dislocations.

(6) Under reversed loading, detwinning is hindered because of the energetically unfavorable dissociation of twin-twin boundary dislocations. Secondary twinning can be activated at Type II twin-twin boundaries under reversed loading.

(7) Under cyclic loading, three kinds of twin structures (quilted-looking, "apparent crossing", and double tensile twin) form as a consequence of twin-twin interactions. These microstructures correlate with the observed cyclic hardening due to twinning and detwinning.

5. Cyclic Deformation and Fatigue Damage Development in Extruded Polycrystalline Pure Magnesium

5.1 Materials and Specimen Preparation

The pure polycrystalline magnesium was commercially acquired in the form of hot extruded round solid bar with a diameter of 32.9 mm (Figure 50a). Small dog-bone shaped plate specimens with a rectangular cross section of 5.0 mm × 3.0 mm within a gage length of 6.4 mm were cut from the outer circular layer of the material for fatigue experiments. The loading direction (LD) of the testing specimen was aligned parallel to the extrusion direction of the material bar. The extrusion direction (ED), the traverse direction (TD), and the normal direction (ND) are referred to as the three orthotropic axes of the sample coordinate system (Figure 50a).

A cubic material block was cut from the outer circular layer of the extruded bar for initial microstructure and texture analysis (Figure 50a). In order to visualize the grain boundaries and the twin boundaries, three orthotropic surfaces of the cubic material block were carefully ground and mechanically polished following the same procedure as that utilized for magnesium single crystal specimens. The polished samples were soaked in the etchant made of Acetic-Picral solution (10 mL acetic acid, 4.2 g picric acid, 10 mL distilled water, and 70 mL ethanol (95 pct)) for about 5 seconds. Figure 50b shows a three-dimensional stereography of optical microstructure for the extruded pure magnesium in the as-receive state. The material consists of equiaxed grains with an average grain size of 120 μm, measured using the Mean Lineal Intercept Method. No initial twins were detected before mechanical testing.

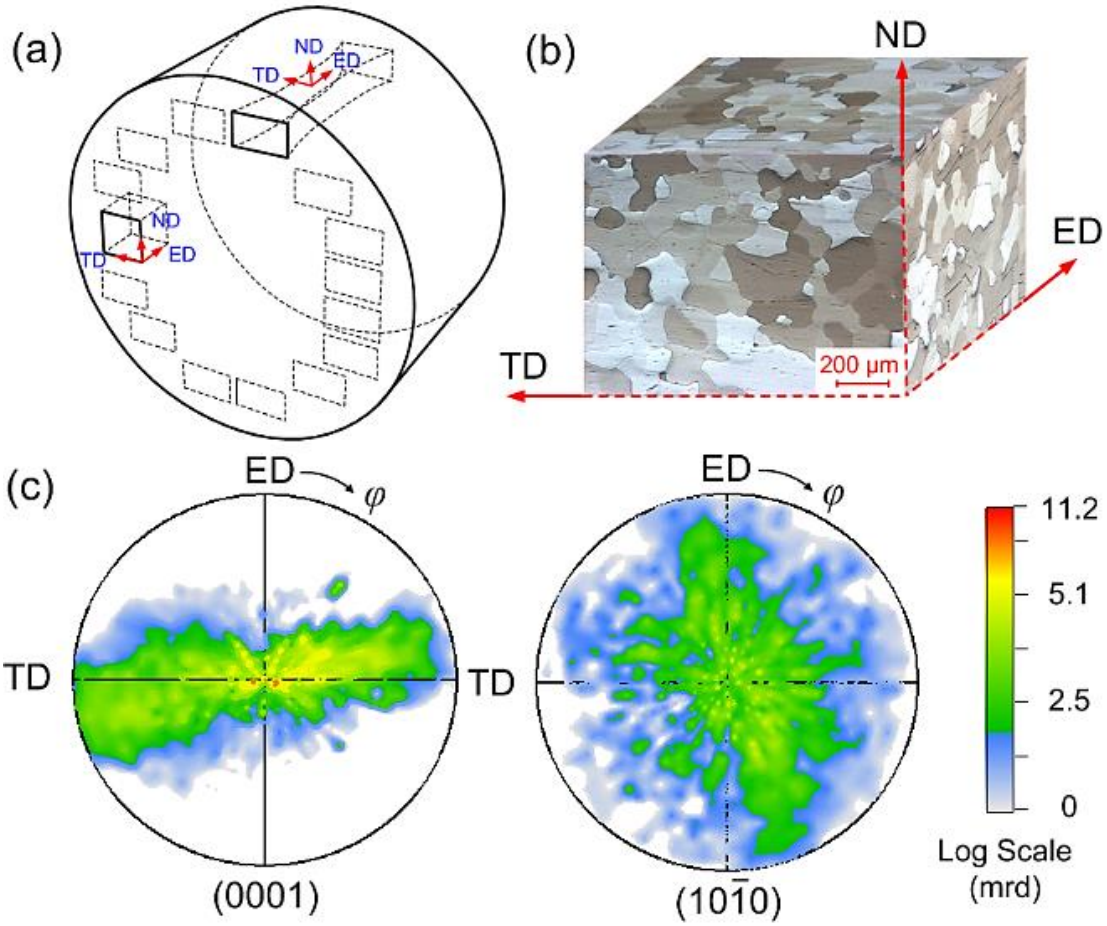

Figure 50 Initial microstructure and texture of the extruded polycrystalline pure magnesium: (a) schematic drawing of the testing specimen and the cubic material block for initial microstructure and texture analysis; (b) three-dimensional stereographic optical microstructure; and (c) (0001) and $(10\bar{1}0)$ pole figures measured by Lab X-ray diffraction.

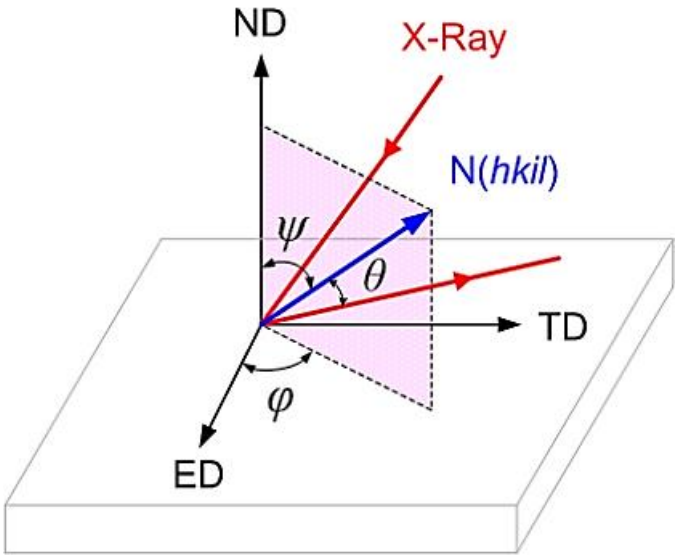

Figure 51 Principle of pole figure measurement by X-ray diffraction [164].

The plane perpendicular to the ND direction in the material block was analyzed for initial texture using Panalytical XPERT MPD PRO diffractometer. A quick GONIO scan was first performed to determine the precise 2θ positions of the $(10\bar{1}0)$, (0002), and $(10\bar{1}1)$ diffraction peaks. As schematically illustrated in Figure 51, the intensity of $(hkil)$ pole was collected on the diffraction plane which was designated by a plane normal $N(hkil)$. The orientation of the diffraction plane normal is described by the azimuth angle (φ) and the polar angle (ψ) of a sphere coordinates fixed on the sample coordinates. The diffraction plane is changed by rotating the azimuth angle (φ) from 0 °to 360 °in a 5 °incremental step and rotating the polar angle (ψ) from 0 °to 85 °in a 5 ° step. On each diffraction plane, the intensities of $(10\bar{1}0)$, (0002) and $(10\bar{1}1)$ diffraction peaks were collected at three corresponding 2θ positions, and used to construct the pole figures. The directly measured pole intensity is corrected as follows [164]:

$$I_{corr}(\varphi,\psi)=\frac{I_{meas}(\varphi,\psi)-BG(\varphi)}{U(\varphi)} \quad (10)$$

where $I_{meas}(\varphi,\psi)$ and $I_{corr}(\varphi,\psi)$ are the measured and corrected pole intensity, respectively. $BG(\varphi)$ and $U(\varphi)$ are the background error and defocusing error, respectively. After the correction, the intensity is normalized to the standard units – "multiples of a random orientation distribution (mrd)" using the following equation:

$$I_{norm}(\varphi,\psi)=\frac{I_{corr}(\varphi,\psi)}{\left[\int I_{corr}(\varphi,\psi)\sin(\varphi)d\varphi d\psi\right]/\left[\int \sin(\varphi)d\varphi d\psi\right]} \quad (11)$$

so that the integration of the normalized intensity (or mrd) over the full area of the pole figure satisfies the following equation,

$$\frac{1}{2\pi}\int I_{norm}(\varphi,\psi)\sin(\varphi)d\varphi d\psi=1 \quad (12)$$

where $0\le\varphi\le 360^{\circ}$ and $0\le\psi\le 90^{\circ}$. The (0001) and $(10\bar{1}0)$ pole figures in Figure 50c are finally represented in the standard unit of mrd. From the pole figures, a typical basal texture of extruded magnesium bar is exhibited. The *c*-axes of most grains lie approximately within the plane perpendicular to the ED direction.

5.2 Mechanical Experiments and Microscopic Observations

Fully reversed total strain-controlled tension-compression experiments were conducted to study cyclic deformation and fatigue damage development of pure polycrystalline magnesium in its extrusion direction. Two strain amplitudes (0.12% and 1%) were employed in the experimental investigation. The corresponding testing frequencies were 10 Hz and 0.2 Hz, respectively. For each loading cycle, a minimum

of 200 data points were recorded. The true stress and true strain were calculated and reported for all the tests conducted.

To investigate the fatigue damage development, the flat specimen surface perpendicular to the ND direction was pre-etched prior to fatigue tests by using the same procedure as that used for optical microstructure observation. A series of experiments using companion specimens were performed and interrupted at the specified loading cycles corresponding to different stages of cyclic deformation. The loading cycle at which the testing specimen was separated into two pieces is referred to as the "separation fatigue life" and is denoted as N_{sep}. Due to the scattering nature of fatigue data, the "separation fatigue life" is taken as the average from testing several companion specimens at the same strain amplitude. The separation fatigue lives at the strain amplitude of 1% and 0.12% were identified to be 1110 and 154100, respectively. These two values will be used as the reference loading cycles by which the loading cycles at the corresponding strain amplitude are normalized. For the strain amplitude of 1%, companion specimens were interrupted at the specified loading cycles of 2, 890, and 1110, which correspond to 0.18% N_{sep}, 80% N_{sep}, and 100% N_{sep}, respectively. For the strain amplitude of 0.12%, companion specimens were designed to be interrupted at the loading cycles of 76900, 107700, and 154100, which correspond to 50% N_{sep}, 70% N_{sep}, and 100% N_{sep} at this strain amplitude.

The surfaces of testing specimens after the termination of mechanical test at different stages of fatigue life were examined by high resolution scanning electron microscopy (SEM) for microcracks. To study the propagation mechanism of early-

stage transgranular microcrack at the strain amplitude of 0.12%, the crystallographic plane on which the propagated microcrack is located should be determined. To achieve this goal, crystal orientations of neighboring grains surrounding the microcrack propagation path were determined by electron backscatter diffraction (EBSD) scan on the specimen surface. By knowing the geometry relationship between the microcrack and the grain orientation, the habit plane of the propagated microcrack can be identified, which provides an important clue for the propagation mode of early-stage transgranular microcrack at low strain amplitude.

5.3 Basic Characteristics of Cyclic Deformation

Figure 52 shows the cyclic stress-strain hysteresis loops at the strain amplitudes of 1% and 0.12%. A clear difference is observed on the shapes of the cyclic stress-strain hysteresis loops between these two strain amplitudes. At 1% strain amplitude, the stress-strain hysteresis loops show a typical asymmetric shape as those for wrought magnesium alloys. During the compressive reversal, when the compressive stress reached approximately -50 MPa, the material showed an abrupt yielding point, beyond which massive $\{10\bar{1}2\}$ tension twins were formulated. During the initial portion of the tensile reversal, the stress-strain curve shows a concave-down shape with a low and decreasing hardening rate. An inflection point is exhibited at a strain of ~0.5%. Beyond the inflection point, a concave-up shape can be observed and the strain hardening rate increased gradually. The shape change of the stress-strain curve at the inflection point indicates a gradual exhaustion of detwinning and the activation of nonbasal slip [165, 166]. The asymmetric stress-strain hysteresis loops were persistently held for the second and the successive loading cycles. However, with

increasing number of loading cycles, the value of the compressive peak stress increased slightly while the value of the tensile peak stress decreased significantly. Additionally, the shape-asymmetry of the stress-strain hysteresis loops tended to evolve to a less degree. The observed cyclic softening behavior at the tensile peak stress on pure magnesium disagrees with the general observation of significant cyclic hardening at the tensile peak stress for most wrought magnesium alloys at a similar strain amplitude [16, 111, 128, 130, 132].

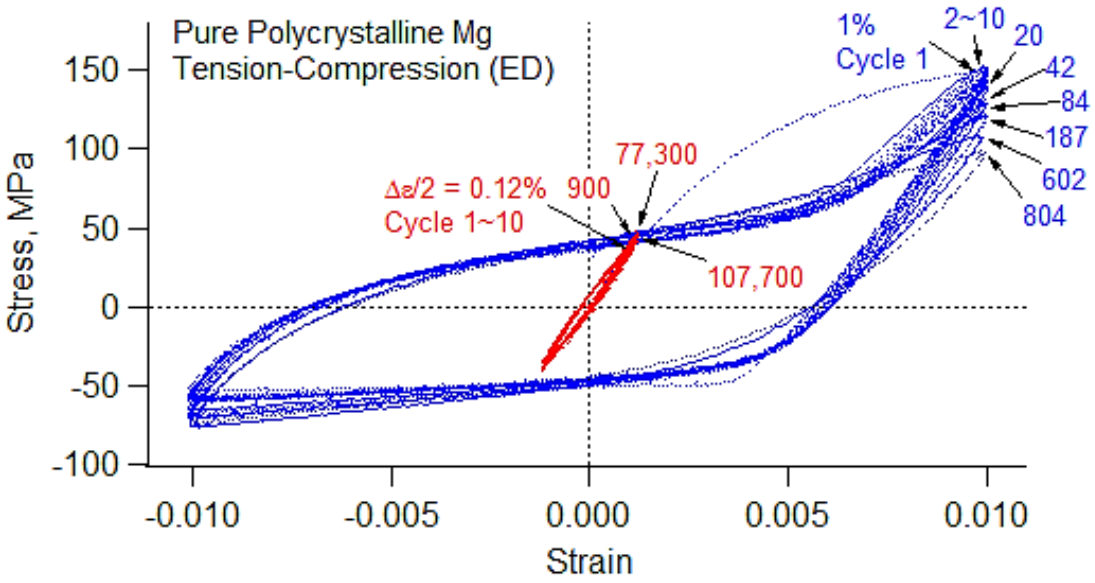

Figure 52 Cyclic stress-strain hysteresis loops for the extruded polycrystalline pure magnesium subjected to fully reversed tension-compression at strain amplitudes of 1% and 0.12%.

At a strain amplitude of 0.12%, the stress-strain hysteresis loops show a symmetric shape with almost zero mean stress during most of the loading cycles. Although marginal cyclic hardening occurred, the compressive peak stress never exceeded the value of -50 MPa which was insufficient to activate the formulation of massive tension

twins. Cyclic deformation at this strain amplitude is predominantly operated by basal slip. Small fraction of twinning might occur at local regions where the incompatibility stress is concentrated [167]. However, the presence of local tension twins does not result in any asymmetric shape of the macroscopic stress-strain hysteresis loop.

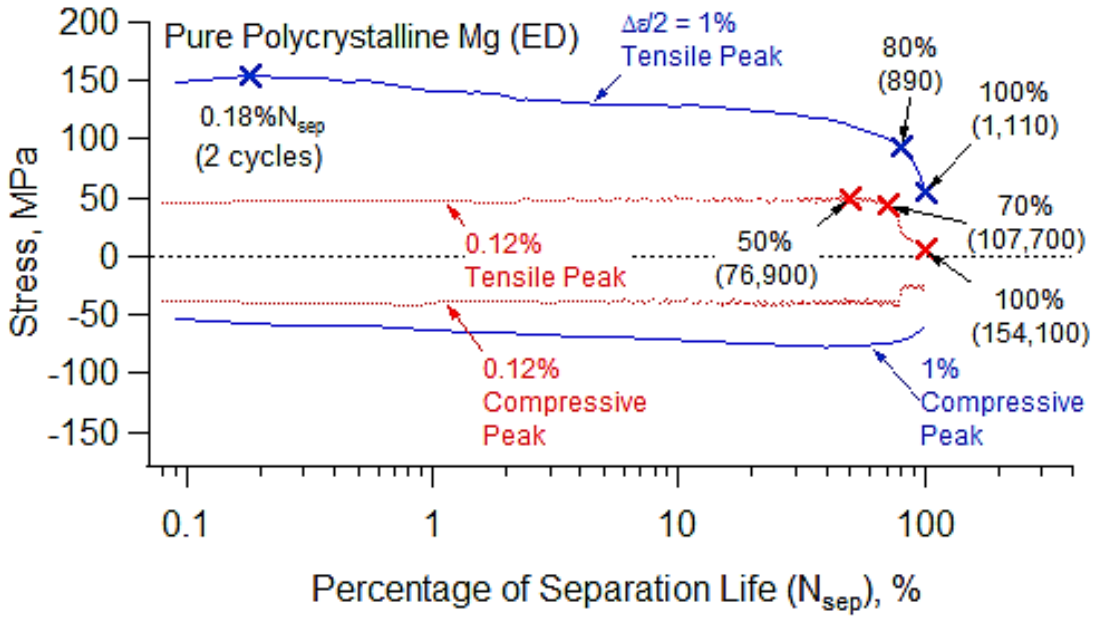

Figure 53 Variation of the tensile and compressive peak stresses with the normalized loading cycles in terms of the percentage of the separation life (N_{sep}) in the extruded polycrystalline pure magnesium loaded at strain amplitudes of 1% and 0.12%.

Figure 53 shows the variation of the tensile and compressive peak stresses with the normalized loading cycles in terms of the percentage of the separation fatigue life at the strain amplitudes of 1% and 0.12%. Pronounced differences can be found in the cyclic hardening/softening behavior between these two strain amplitudes. At 1% strain amplitude, right after the second loading cycle, the tensile peak stress displayed consistent cyclic softening until the specimen was separated into two pieces. A detailed

examination of the tensile peak stress curve shows that there existed three stages: a transient stage with an average cyclic softening rate of 8 MPa/cycle during the initial ~2% N_{sep}, a steady state stage with a constant cyclic softening rate of 0.5 MPa/cycle from the loading cycle of ~2% N_{sep} to that of ~80% N_{sep}, and a tertiary stage showing a gradually increasing cyclic softening rate during the last ~20% N_{sep}. On the other hand, the compressive peak stress showed a moderate cyclic hardening with a decreasing rate during the initial ~70% N_{sep}. During the last ~30% N_{sep}, accelerating cyclic softening was observed. It is established that with increasing number of loading cycles, the residual twin boundaries are gradually accumulated, which contributes to cyclic hardening by applying the barrier effect on the dislocation motions [117]. This cyclic deformation mechanism is macroscopically reflected on the moderate cyclic hardening at the compressive peak stress. However, for the cyclic softening at the tensile peak stress, a correlation with the fatigue damage development will be discussed in the next section.

At 0.12% strain amplitude, the material exhibits marginal symmetrical cyclic hardening at both tensile and compressive peak stresses (Figure 53). An examination of the tensile peak stress reveals that the tensile peak stress increased only 4 MPa within the initial ~5% N_{sep}. Afterwards, the tensile peak stress kept constant until the loading cycle of ~70% N_{sep}. During the rest of ~30% N_{sep}, the material demonstrated a gradual loss of cyclic loading capacity with an increasing softening rate. The marginal cyclic hardening behavior at 0.12% strain amplitude for pure magnesium is consistent with the results from most wrought magnesium alloys tested in the high-cycle fatigue

regime. However, there exists a noticeable difference in the final fracture behavior between the pure magnesium and wrought magnesium alloys. For wrought magnesium alloys tested at low stress/strain amplitudes, the testing specimen usually shows a quick and drastic drop of stress amplitude which is followed by a sudden final fracture [122, 124, 125, 130]. However, for the pure magnesium as shown in Figure 53 (logarithmic scale should be noticed for the loading cycles), the stress drop was detected relatively early at the loading cycle of ~70% N_{sep}. During the remaining ~30% N_{sep}, the material was cyclically softened gradually until the final separation occurred.

5.4 Microscopic Observation of Fatigue Damage Development

5.4.1 Strain Amplitude of 1%

Figure 54 presents the SEM images showing the fatigue damage development on the specimen surface after the second loading cycle at 1% strain amplitude. The loading direction is horizontal as being indicated in Figure 54. Figure 54a characterizes an observation window with a size of 1.25 mm × 0.75 mm on the central area of the gage section. It can be seen that several microcracks (or damaged sites) were detectable at local regions. To identify the concrete inhabited locations and the morphologies, three featuring regions, namely “b”, “c” and “d”, were focused and magnified, as illustrated in Figure 54b, Figure 54c and Figure 54d, respectively.

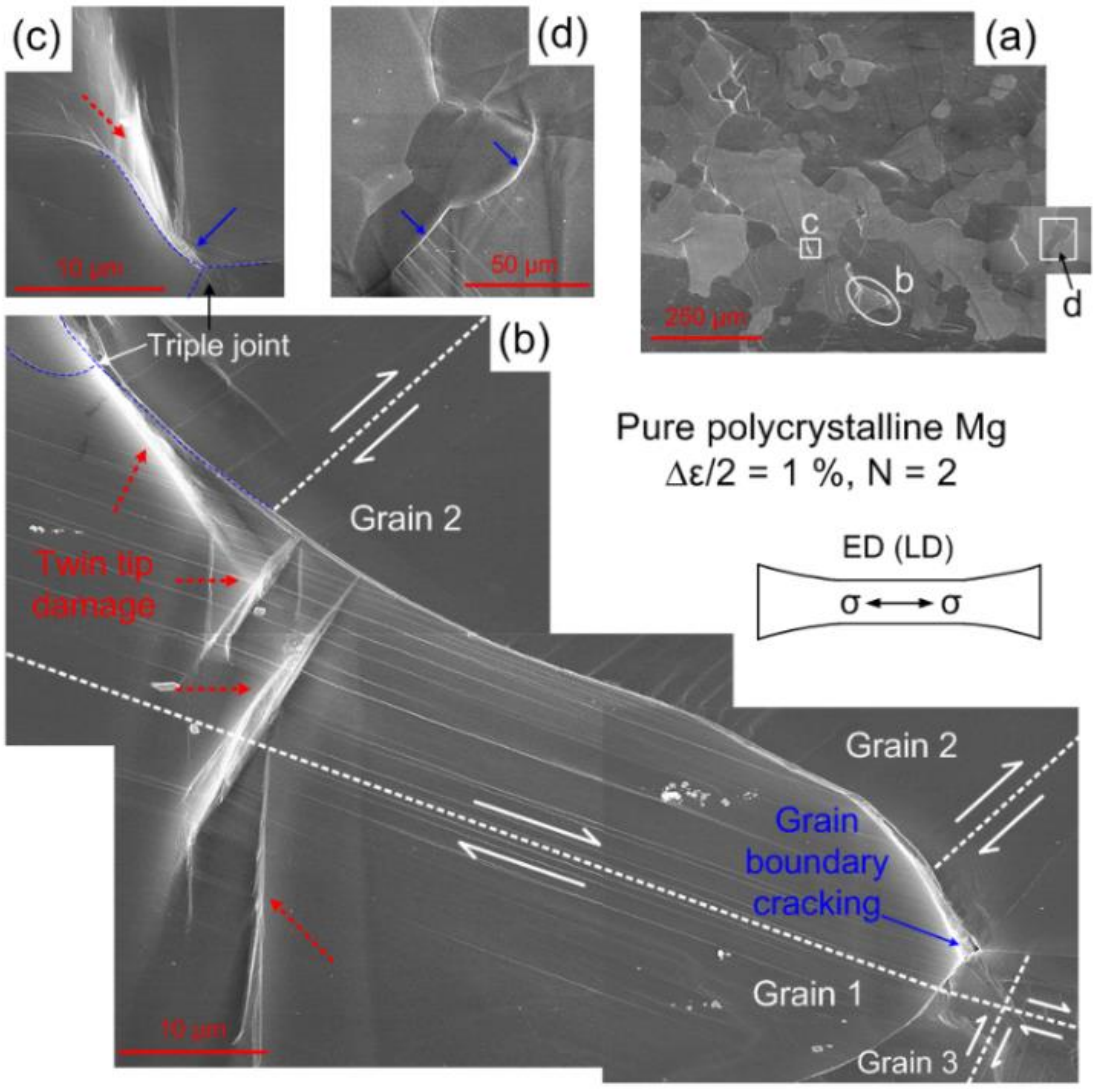

Figure 54 SEM examination of surface damage morphology after the second loading cycle in the extruded polycrystalline pure magnesium at 1% strain amplitude: (a) low magnification; and (b, c, d) high magnification (solid blue arrows indicating the locations of grain boundary cracking; dashed red arrows indicating the locations of twin tip damage; dashed white lines indicating the in-plane orientation of cyclic slip bands).

In Figure 54b, three neighboring grains were observed, namely “Grain 1”, “Grain 2” and “Grain 3.” Grain boundary cracking was detected at the triple joint of the three

neighboring grains (as indicated by the solid blue arrow right lower in Figure 54b). Further examination of the grain surface showed that, on Grain 1, densely-spaced cyclic slip bands were observed. The in-plane orientation of the cyclic slip bands was 19 ° with respect to the loading direction, as schematically represented by a dashed white line on the grain. Similarly, on Grain 2, cyclic slip bands which orientated in-plane 42.3 °with respect to the loading direction were detected. Compared with the slip bands on Grain 1, the amount of cyclic slip bands on Grain 2 was much reduced. Noticing that cyclic slip bands with only one orientation type were observed on Grain 1 and Grain 2, it is suggested that these slip bands were of basal type, knowing that basal slip was easiest to be activated as compared to the nonbasal slip for HCP magnesium at room temperature [28]. Unlike Grain 1 and Grain 2, two traces of cyclic slip bands were visible on Grain 3, locally close to the triple joint. The presence of cyclic slip bands with two orientations indicates that additional deformation mode of nonbasal slip was activated due to the highly concentrated stress near the triple joint [168]. Although the orientation of individual grains cannot be exactly determined without further investigation using EBSD, the in-plane orientation angle and the amount of cyclic slip bands observed on each grain can be regarded as the fingerprint of the direction and magnitude of local cyclic slipping in an individual grain. Cyclic slip bands locally observed with two orientations suggests that cyclic plastic deformation was most aggravated at such region in Grain 3. The least amount of sparsely distributed cyclic slip bands observed in Grain 2 indicates that Grain 2 was the area with the least cyclic plastic deformation. Apart from the triple joints, local sites on the two neighboring grain boundaries were also observed as the initiation sites. A direct evidence is shown

in Figure 54d. Local damaged sites on the grain boundaries were highly contrasted and attached with the cyclic slip bands terminated at the boundary. This observation implies that a pile-up of slip dislocation on the boundary was presented and served as the initiation sites for microcracks.

In addition to the grain boundary cracking, fatigue damage associated with the deformation twin was found at both Region "b" (Figure 54b) and Region "c" (Figure 54c). From Figure 54b, four damaged sites were developed on the newly formed twins. For these four twins, one was attached to the triple joint at one of its twin tips. Two others were connected to the two neighboring grain boundaries at one of their twin tips. The fourth one was embedded inside the grain with one of its twin tips attached to a nearest twin boundary. Due to the relatively narrow twinned areas, the damaged sites were generally found to be located at the twin boundaries close to one of the twin tips. A clearer image of the damaged region inhabiting on a twin is presented in Figure 54c, where the twinned area remained relatively large. It is revealed that, unlike the grain boundary cracking, the damaged region on a twin after the second loading cycle was more likely to be described as a narrow damaged zone, which inhabited on the parent grain side of the twin boundary near one of the sharp twin tips. This twin tip was frequently found to attach to either a grain boundary or a conjugate twin boundary. The narrow damaged zone near the twin tip is referred to as "twin tip damage" and is indicated by the dashed red arrow in Figure 54c.

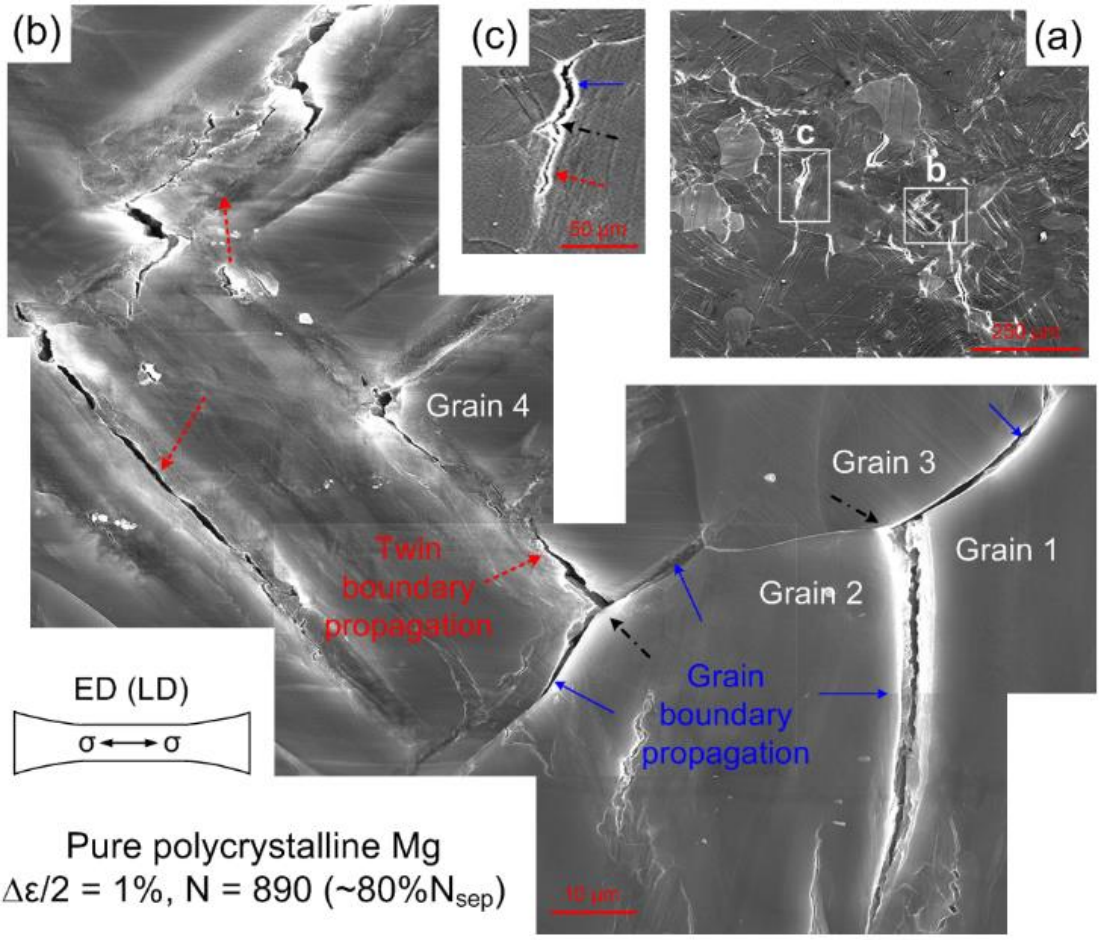

Figure 55 SEM examination of surface damage morphology after 890 loading cycles (~80% separation life) in the extruded polycrystalline pure magnesium at the strain amplitude of 1%: (a) low magnification; and (b, c) high magnification (dot dashed black arrows indicating the initiation sites; solid blue arrows indicating the propagation by grain boundary cracking; dashed red arrows indicating the propagation by twin boundary cracking).

Figure 55 presents the SEM images of the fatigue damage development after 890 loading cycles at 1% strain amplitude. The loading direction in the specimen is horizontal as indicated at the bottom left corner in Figure 55. Figure 55a shows a surface area with a size of 1.25 mm ×0.75 mm located at the center of the gage section.

Short microcracks can be detected to distribute randomly on this area. The microcrack density was significantly increased compared to that after the second loading cycle. The lengths of the microcracks generally varied from ~10 μm to ~100 μm, and no cracks longer than 100 μm were observed. A statistical analysis shows that only ~30% of the microcracks had the lengths longer than 40 μm. Noting that the average grain size of the pure magnesium under investigation is 120 μm, the observed crack lengths at ~80% N_{sep} suggest that propagation of microcracks is often limited within the size of a gain.

Observations after second loading cycle (Figure 54) and after ~80% N_{sep} (Figure 55) lead to the following implications with regard to the fatigue damage process. First, microcracks from preferred sites at grain boundaries or twin boundaries are initiated as early as after the second loading cycle. The majority of the loading cycles up to ~80% N_{sep} is spent on initiating microcracks with very insignificant growth in crack length. The crack growth of the microcracks is limited within the range of a single grain. In other words, most of the fatigue life at a strain amplitude of 1% is spent on increasing the number of crack initiation sites. The increased density of microcracks caused by the incessant initiation acts as a cyclic softening mechanism which suppresses the cyclic hardening effect due to dislocation immobilization by accumulated residual twin boundaries.

Owing to the relatively short propagation paths constrained in a single grain, propagation (or branching) behavior can be characterized more clearly. There are three main modes of propagation (or branching) observed at 1% strain amplitude:

propagation on grain boundary (intergranular), propagation on twin boundary (transgranular), and propagation by mixed types. Region "b" and Region "c" in Figure 55a were magnified as Figure 55b and Figure 55c, respectively. In Figure 55b, three neighboring grains were observed, namely "Grain 1", "Grain 2," and "Grain 3." A much larger grain ("Grain 4") surrounded by Grain 2 and Grain 3 was also detected. The first propagation mode as purely on grain boundary can be observed on the right part of Figure 55b. A microcrack initiated from the triple joint (as indicated by a dash-dot black arrow) propagated in two directions (as indicated by two solid blue arrows). The propagation path in one direction was along the boundary between Grain 1 and Grain 2 approximately perpendicular with respect to the loading direction. Another propagation path orientated with approximate in-plane 45 ° from the loading direction on the boundary between Grain 1 and Grain 3. The second propagation mode as purely on twin boundary can be detected from two sites inside Grain 4. One microcrack initiated from the twin boundary propagated continuously along its inhabited twin boundary. Rather than a smooth shape, the twin boundary microcrack has a serrated and irregular shape. Another microcrack initiated from twin boundary deviated from its proceeding path at the intersection of two twin sets. The microcrack followed a "zigzag-like" route on the twin boundaries by switching between two sets of twins. The shape of the "zigzag-like" microcrack was rather serrated, and most severe at the intersection of two twin sets. The third propagation mode as mixed types can be observed in the mid region in Figure 55b. A microcrack which originated from the twin tip attached to the boundary of Grain 2 and Grain 4 was detected to grow in three directions. Two branches were along the boundary between Grain 2 and Grain 4, being

inclined approximate in-plane 45 ° with respect to the loading direction. The third branch intended to penetrate into Grain 4 along a twin boundary. A similar mix-type propagation mode was noticed as shown in Figure 55c. The microcrack initiated from the twin tip on the grain boundary propagated perpendicular with respect to the loading direction into two branches. One branch was along the grain boundary and the other branch penetrated into the grain along the twin boundary.

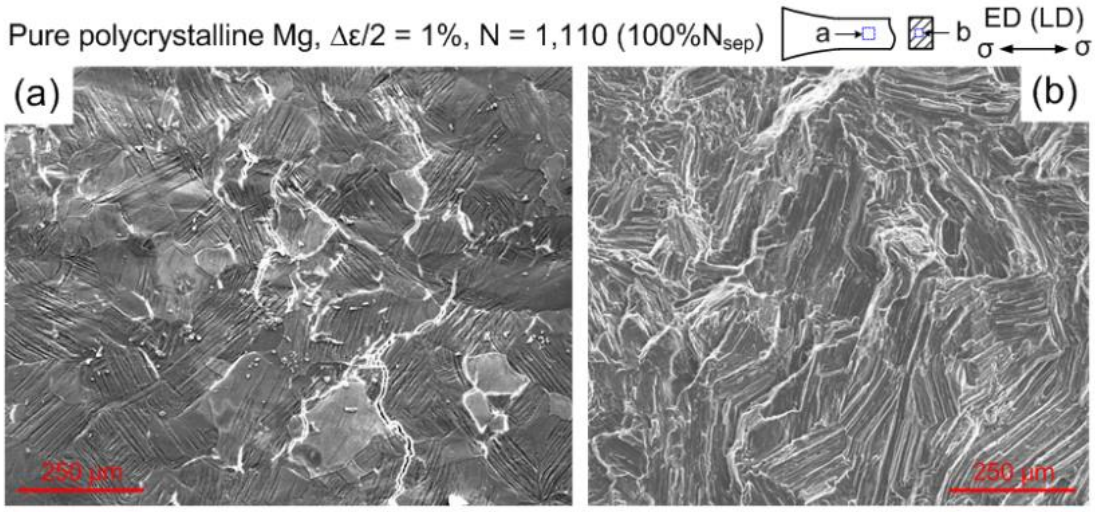

Figure 56 Fatigue damage development in the extruded polycrystalline pure magnesium after fatigue failure at the strain amplitude of 1%: (a) surface damage morphology far away from the fracture surface; and (b) fracture surface.

Figure 56 presents the SEM examination of fatigue damage development after fatigue failure. Figure 56 characterizes the surface damage morphology far away from the fracture surface. Figure 56b shows the morphology of the fracture surface. From Figure 56a, it can be observed that high density of microcracks was developed. Coexistence of short and long microcracks was frequently observed. More microcracks propagated. A careful examination reveals that the longer microcracks usually spanned

over two or three grains. Rather than a preferred global orientation, the overall propagation paths were very winding. It should be emphasized that along the propagation paths of some microcracks, two-fold (bifurcation) or three-fold (trifurcation) branches can be observed. The propagation or branching modes are found to be pure transgranular, pure intergranular, or of a mix-type. The transgranular paths were found mostly inhabiting on the twin boundaries. Three types of propagation modes occurred in a randomly alternating sequence on the propagation paths. Although the propagated microcracks were separated from one another, there existed chances that two or more close-separated long microcracks would coalesce and formulate a longer crack or a crack cluster. Through further propagation or branching, secondary coalescence had more probability to occur. It is suggested that the most severely propagated and coalesced surface crack (or crack cluster) would take the priority to serve as the potential initiation site for final fracture.

Figure 56b shows the morphology of the fracture surface at 1% strain amplitude. Similar to the fracture surface of wrought magnesium alloys tested at high stress/strain amplitudes [123, 130], most areas of the fracture surface were covered by densely distributed cleavage facets (parallel-aligned dark lamella area) together with the bright and rough ridges. No specified initiation sites can be found. The existence of cleavage facets and the similarity between these facets and the twin lamella structure indicated that cleavage cracking occurred along the twin boundaries. The bright and rough ridges were probably tearing/shearing regions at grain boundaries or cleavage steps to connect parallel cleavage facets. Further investigation of the fatigue crack growth behavior will help to elucidate the formulation process of the fracture surface.

5.4.2 Strain Amplitude of 0.12%

At the strain amplitude of 0.12%, SEM examination shows that no damage is detected on the specimen surface after the loading cycle of ~50% N_{sep}. Therefore, only the fatigue damage developments after ~70% N_{sep} and at 100% N_{sep} will be discussed. Figure 57 shows the surface fatigue damage development for a specimen which was fatigue tested after 10,770 loading cycles (~70% N_{sep}) at a strain amplitude of 0.12%. Figure 57a shows a low magnification SEM image covering the center surface area on the gage section with a size of 3 mm × 2 mm. It can be observed that several microcracks have been developed and distributed randomly on the surface. Most microcracks were isolated from one another. However, at the Region "b" in Figure 57a as magnified in Figure 57b, two microcracks were found to start coalescence at their propagation fronts.

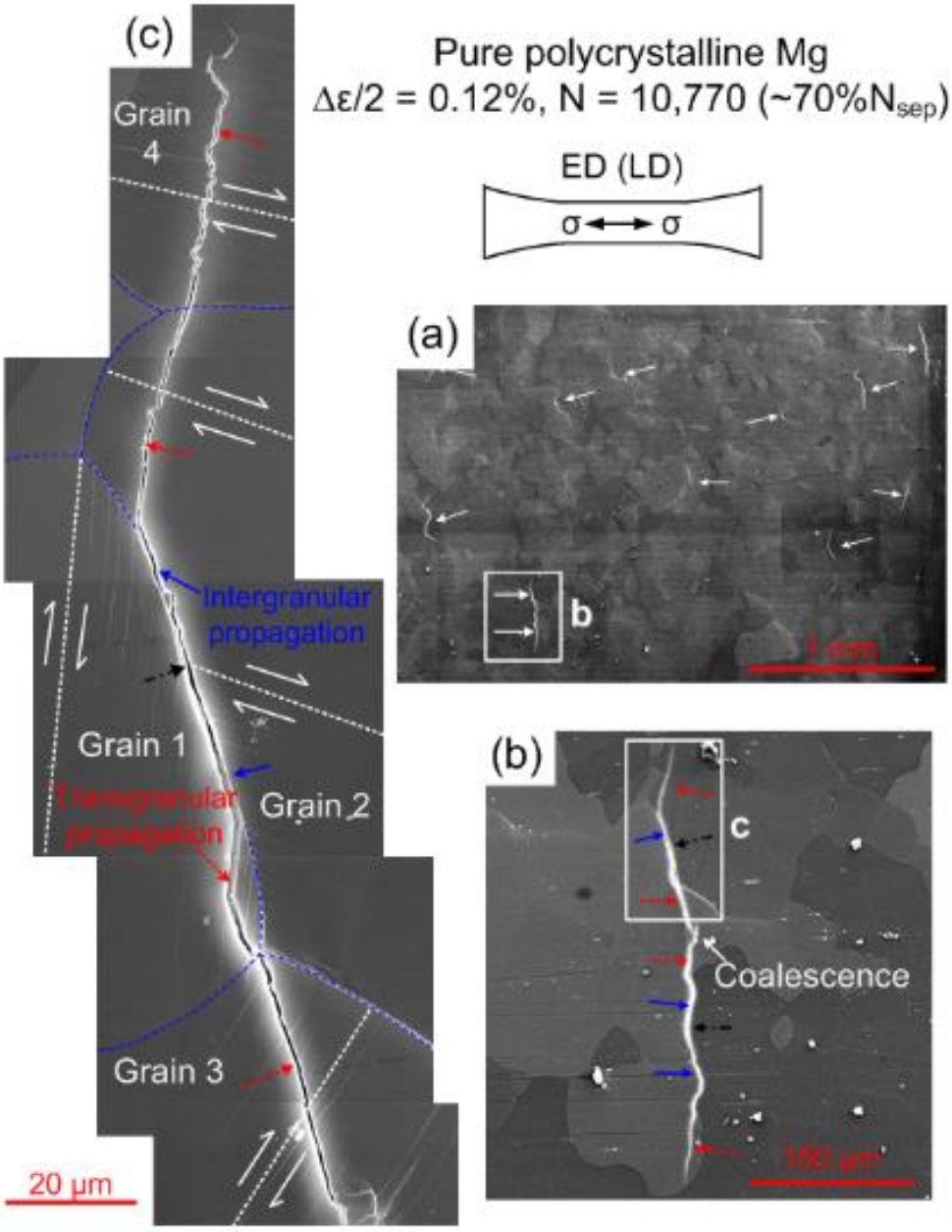

Figure 57 SEM examination of surface fatigue damage in the extruded polycrystalline pure magnesium after 10,770 loading cycles (~70% separation life) at the strain amplitude of 0.12%: (a) low magnification; and (b, c) high magnification (dot dashed black arrows indicating the possible initiation sites; solid blue arrows indicating the propagation by intergranular cracking; dashed red arrows indicating the propagation by transgranular cracking).

From Figure 57a, the coexistence of short and long microcracks with the lengths ranging from ~10 μm to ~150 μm was observed. Noting that no microcrack was detected at the loading cycle of ~50% N_{sep}, it is suggested that the visible microcracks were developed successively during the period between ~50% N_{sep} and ~70% N_{sep}. By examining the mid-point of the short microcracks having the lengths less than 40 μm, it was found that all these mid-points coincided to be located either at the triple joint or on the boundary of two neighboring grains. Based on this observation, the microcrack initiation mode at the strain amplitude of 0.12% can be clearly identified as being grain boundary cracking.

To investigate the morphology of early-stage propagation, one of the microcracks in Figure 57b was further magnified, as shown in Figure 57c. The microcrack propagated in either intergranular or transgranular mode, spanning over four grains, namely “Grain 1”, “Grain 2”, “Grain 3” and “Grain 4.” Unlike the winding and branched propagation paths at the strain amplitude of 1%, the propagation path at the strain amplitude of 0.12% shows a preferred global orientation having small tilted angles from the direction perpendicular to the loading direction. No branching on the propagation path was found at this stage of cyclic deformation. Referring to Figure 57c, after propagating ~15 μm downwards from the initiation site (as indicated by the dash-dot black arrow) on the boundary between Grain 1 and Grain 2, the microcrack front changed its path and penetrated into Grain 1 along the cyclic slip band. Following a certain propagation distance of 10 μm, the microcrack deviated from the cyclic slip band and propagated by cutting through the parallel cyclic slip bands on a less straight path. Noting that the visible cyclic slip band is of basal type and no deformation twin

at the microcrack front is presented, the cutting path should inhabit on the cleavage planes, which are most likely to be nonbasal slip planes [26]. Such transgranular propagation continued in Grain 3. It is noticed that the less straight path had certain tendency to cut the cyclic basal slip bands in a shearing manner. On the other direction of propagation, the crack front penetrated into both Grain 2 and Grain 4 after following a certain distance on the boundary between Grain 1 and Grain 2. Unlike the transgranular morphologies in Grain 1 and Grain 3, the transgranular propagation paths within Grain 2 and Grain 4 showed a "zigzag" route, which is most severely in Grain 4. Schematically, the crack front proceeded alternatively by either following on the cyclic basal slip bands or propagating perpendicular to the cyclic basal slip bands. To summarize, early-stage propagation in either intergranular or transgranular mode was observed at the strain amplitude of 0.12%. Three morphologies of transgranular propagation were exhibited: straight path, less straight path, and a "zigzag" path.

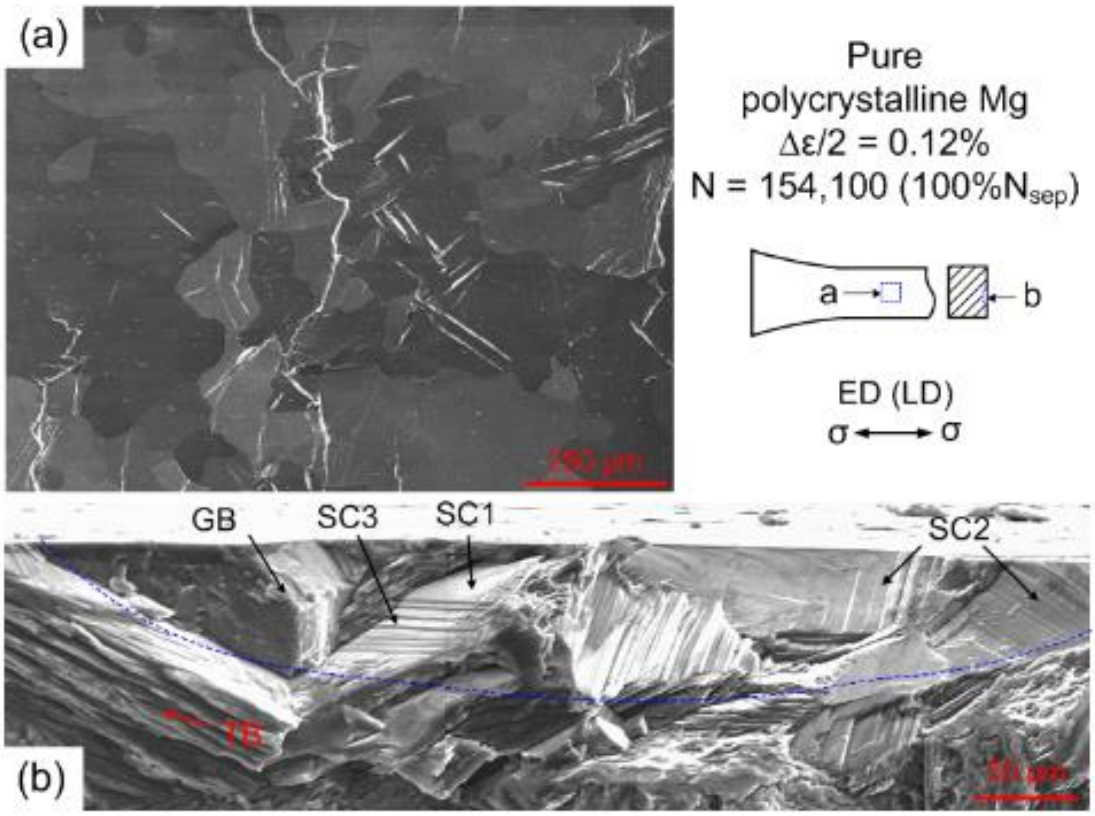

Figure 58 Fatigue damage after 154,100 loading cycles (100% separation life) in the extruded polycrystalline magnesium at the strain amplitude of 0.12%: (a) surface damage morphology away from the fracture surface; and (b) initiation site on the fracture surface (GB: grain boundary cracking; SC1, SC2, SC3: slip-induced cleavage cracking; TB: twin boundary cracking).

Figure 58 shows the fatigue damage both on the surface area far away from the fracture surface (Figure 58a) and on the initiation site on the fracture surface (Figure 58b) after the specimen tested after 154,100 loading cycles (100% N_{sep}) at a strain amplitude of 0.12%. From Figure 58a, it can be seen that microcracks have propagated across two or more grains. Coalescences and secondary coalescence of the long-propagated cracks were observed (refer to the mid part of Figure 58a). It is suggested

that there existed a competition in the growth among the coalesced cracks at different sites. The "twinning" propagated and coalesced crack would serve as the potential initiation site for final fracture. Different from the absence of twin microcracks after the loading cycle of ~70% N_{sep}, small amount of twin microcracks were found to distribute at local areas surrounding the propagated or coalesced long cracks. This observation implies two underlying fatigue processes. In the first place, when the microcrack propagates and coalesces into a longer one, the cyclic plastic zone ahead of the crack front gradually grows. Once the cyclic plastic zone reaches a sufficient large size to cover the surrounding grains, deformation twin is activated in favorably orientated grains due to the local high concentrated stress in the plastic zone. In the second place, residual twins are developed after sufficient number of loading cycles. The concentrated local stress at the residual twin boundary leads to the development of microcracks, as being observed in Figure 58a.

Figure 58b showed the initiation site on the fracture surface. It can be observed that the fracture morphology on a semi-ellipse shaped area (as circumscribed by the dashed blue curve in Figure 58b) was very different from the rest of the area. Two kinds of fracture structures can be identified: a crystal sugar-like structure resulted from grain boundary cracking and the cleavage facets resulted from slip-included cleavage cracking. Unlike the cleavage facets along twin lamella boundaries at the strain amplitude of 1%, the cleavage cracking at strain amplitude of 0.12% occurred along the basal and non-basal slip planes. Cleavage facets can be classified into three morphologies: smooth flat cleavage facet, less smooth flat cleavage facet with parallel marks observed, and the "ladder-like" step cleavage facets. The fracture morphologies

due to grain boundary cracking and slip-induced cleavage cracking were consistent with the surface microcrack morphologies as shown in Figure 57. It is noted that, at the rest propagation zone on the fracture surface, only the densely distributed cleavage facets together with bright and rough ridges was observed. This indicates that during the later propagation of the newly formed macroscopic crack, the twinning/detwinning mechanism dominates the formulation of the fracture surface.

5.5 Further Discussions

5.5.1 Crack Initiation Modes

Based on the experimental observations of surface damage morphology after the second loading cycle at 1% strain amplitude and that after the loading cycle of ~70% N_{sep} at 0.12% strain amplitude, two crack initiation modes are proposed. These two modes are applicable to the early stage of cyclic deformation, namely "grain boundary cracking" and "twin tip damage," as being illustrated schematically in Figure 59a and Figure 59b, respectively. Grain boundary cracking is applicable to both low and high cyclic loading magnitudes whereas twin tip damage only prevails under high cyclic loading magnitudes where the compressive stress exceeds the yielding stress that activates massive formulation of tension twins.

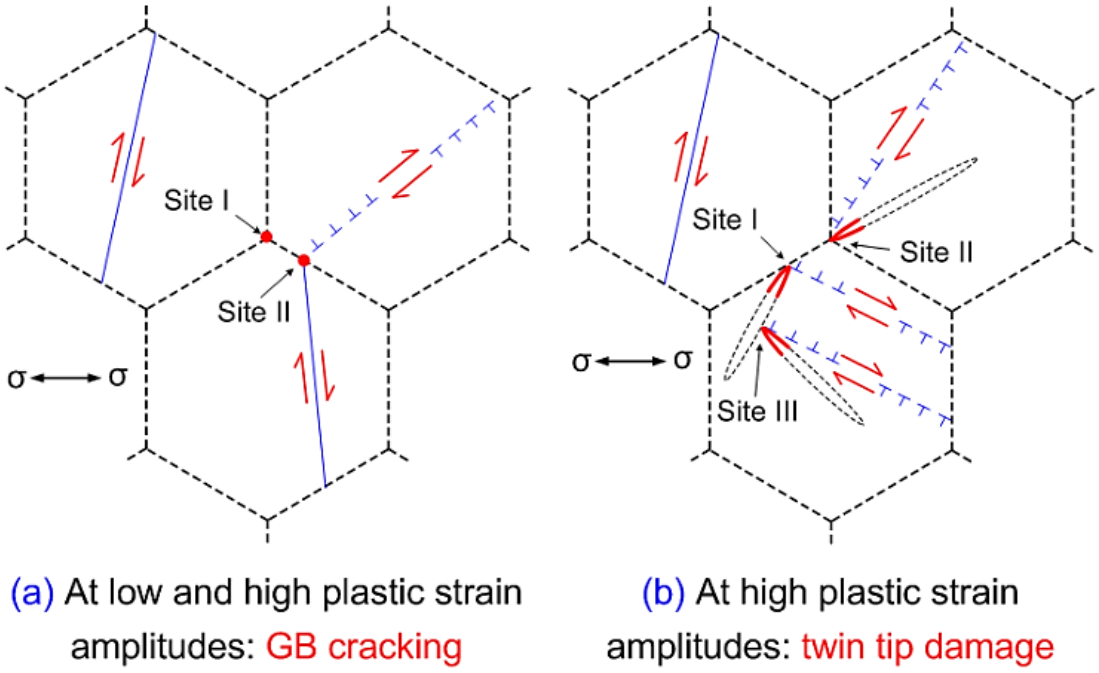

Figure 59 Schematics of the proposed microcrack initiation modes in the coarse-grained pure polycrystalline magnesium at early stage of fatigue life: (a) grain boundary cracking under low and high cyclic loading magnitudes ($\Delta\varepsilon/2$ = 0.12% and 1%); and (b) twin tip damage under high cyclic loading magnitude ($\Delta\varepsilon/2$ = 1%).

Grain Boundary Cracking ($\Delta\varepsilon/2$ = 1% and $\Delta\varepsilon/2$ = 0.12%): As shown in Figure 59a, grain boundary cracking has two preferred local initiation sites, namely the triple joint of three neighboring grains (Site I) and the local sites on the boundary of two neighboring grains (Site II). From mechanics viewpoints, the driving force for crack initiation at these local sites is the concentrated cyclic intergranular stress which is raised to accommodate the incompatible cyclic plastic deformation in the neighboring grains. Inherently, the incompatible plastic deformation between the neighboring grains roots in the limited independent slip systems for HCP magnesium at room temperature [169]. At certain low cyclic loading magnitudes where only two

independent basal slips are operated, the grains with higher degree of cyclic slipping can be regarded as plastically “soft-orientated” grain and the grain having lower degree of cyclic slipping can be considered as plastically “hard-orientated” grain [136]. The misfit capability of load bearing between plastically “hard-orientated” and “soft-orientated” neighboring grains will lead to a cyclic stress concentration at local regions on their boundary and most severely at the triple joint. As the external loading magnitude is increased, the local concentration of intergranular stress is much aggravated. This highly concentrated stress at local sites on grain boundaries activates two additional deformation modes. First, nonbasal slip is raised, favorably during the later stage of tensile reversal [165, 166]. Due to the large difference in critical resolved shear stress (CRSS) between the basal slip and the non-basal slip [170], the attendance of nonbasal slip retains a high-level stress concentration [171]. Therefore, the grain boundary crack initiation is very easy to be activated under a high cyclic loading magnitude (as observed in Figure 54b). As the second additional deformation mode, tension twins are nucleated due to the increased concentrated stress exceeding its CRSS in some favorably orientated grains. Unlike the nonbasil slip, once the tension twin is nucleated and starts to grow, the average internal stress in grains containing the growing twins will be abruptly relaxed [136]. Consequently, stress redistribution on the grain level is invoked: the intergranular stress between the twin-containing neighboring grains is reduced and the intergranular stress between the twin-containing grain and the twin-free grain remains high [172]. Such a high intergranular stress will lead to the grain boundary cracking.

Twin Tip Damage ($\Delta\varepsilon/2 = 1\%$): Twin tip damage can be found at three different sites: the twin tip attached to the boundary of two neighboring grains (Site I), the twin tip attached to the triple joint of three neighboring grains (Site II) and the twin tip connected to the conjugate twin boundary (Site III). It is interesting to note that the observed site of twin tip damage coincides with the nucleation site of deformation twin. The nucleation of deformation twin has been recently addressed by several investigators using statistical analysis of the EBSD data [173–177] and atomic simulation [149, 163, 174, 178]. A general conclusion is that twin nucleates most probably from the nuclei produced at the grain boundaries where grain boundary defects (GBDs) are subjected to sufficiently high local stress due to dislocation pile-ups or other defects terminating at the grain/twin boundary [174, 176, 177, 179, 180]. These researches not only explain why twin tip damage is located from the three sites as shown in Figure 59b, but also suggest that the highest stress concentration on the nucleated deformation twin is located at its twin tip which is attached to its nucleation site at the grain/twin boundary. However, a further understanding of the mechanism on twin tip damage requires a local stress analysis during the detwinning process by both experimental and numerical methods. The complex interaction between the "movable" twin boundary and the slip dislocations should be also considered.

5.5.2 Early-Stage Crack Propagation Modes

Two modes of early-stage crack propagation can be proposed: intergranular propagation and transgranular propagation, as shown in Figure 60. Intergranular propagation was observed at both strain amplitudes of 0.12% and 1%. Nevertheless, the transgranular propagation route depends on cyclic loading magnitude. To simply

the discussion, only the early-stage transgranular propagation within the range of a single grain is emphasized.

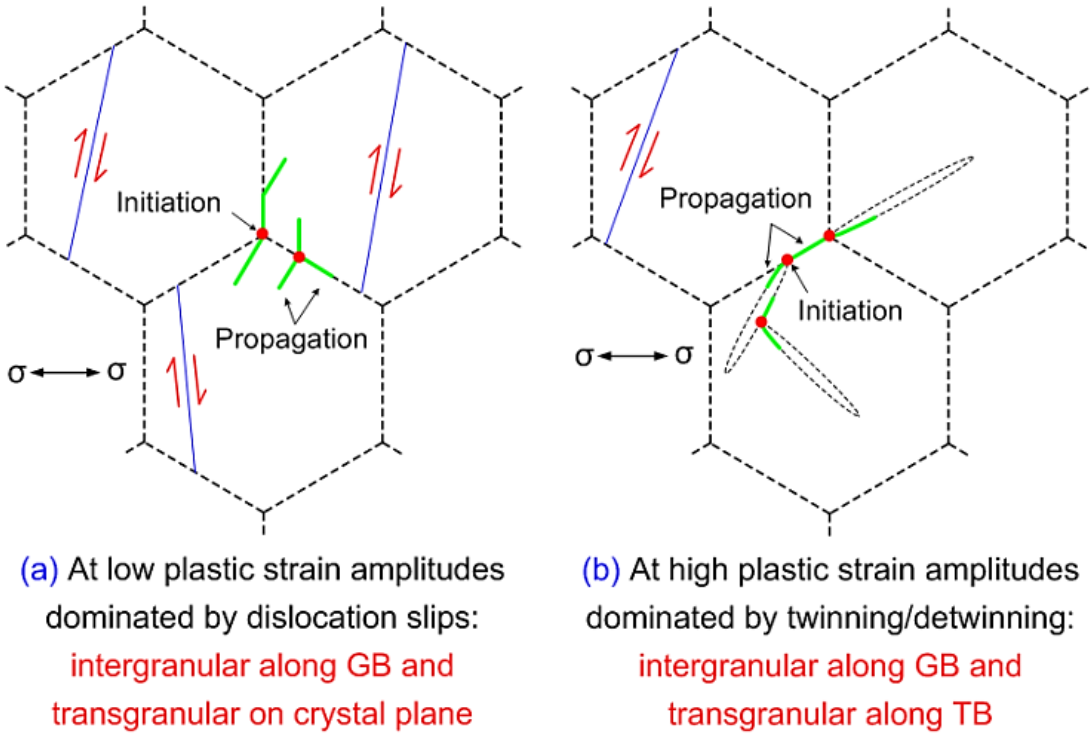

Figure 60 Schematics of the proposed crack propagation modes in the coarse-grained pure polycrystalline magnesium at early stage of fatigue life: (a) intergranular propagation along grain boundary and transgranular propagation on crystal plane under low cyclic loading magnitudes dominated by dislocation slips ($\Delta\varepsilon/2 = 0.12\%$); and (b) intergranular propagation along grain boundary and transgranular propagation along twin boundary under high cyclic loading magnitudes dominated by twinning/detwinning ($\Delta\varepsilon/2 = 1\%$).

Transgranular Propagation on Twin Boundary ($\Delta\varepsilon/2 = 1\%$): Transgranular propagation at the strain amplitude of 1% is characterized by cleavage cracking along the twin lamella boundary. The most prominent morphological feature can be

identified as the serrated and irregular crack profile as shown in Figure 55b. Partridge [99, 101] was the first to observe such a phenomenon which is prevailing in HCP metals subjected to cyclic loading. By inducing the deformation twins into the coarse-grained pure magnesium prior to the fatigue tests, Partridge [99, 101] found that microcracks are mostly found at the serrated boundaries of the irregular twin fragments.

Transgranular Propagation on $\{\bar{1}2\bar{1}0\}$ *Plane (Δε/2 = 0.12%):* At the low strain amplitude as 0.12%, the observation of the surface microcrack and the initiation site on the fracture surface indicates that the early-stage transgranular propagation is dominated by slip-induced cleavage cracking (see Figure 57 and Figure 58). As pointed out by Schmid and Boas [97] for HCP magnesium, the observed cleavage takes place on different crystal planes: $\{0001\}$, $\{10\bar{1}1\}$, $\{10\bar{1}2\}$, and $\{10\bar{1}0\}$. Without the presence of the $\{10\bar{1}2\}$ tension twin during the early-stage transgranular propagation, cleavage cracking at 0.12% strain amplitude most probably inhabits on the basal or nonbasal slip planes.

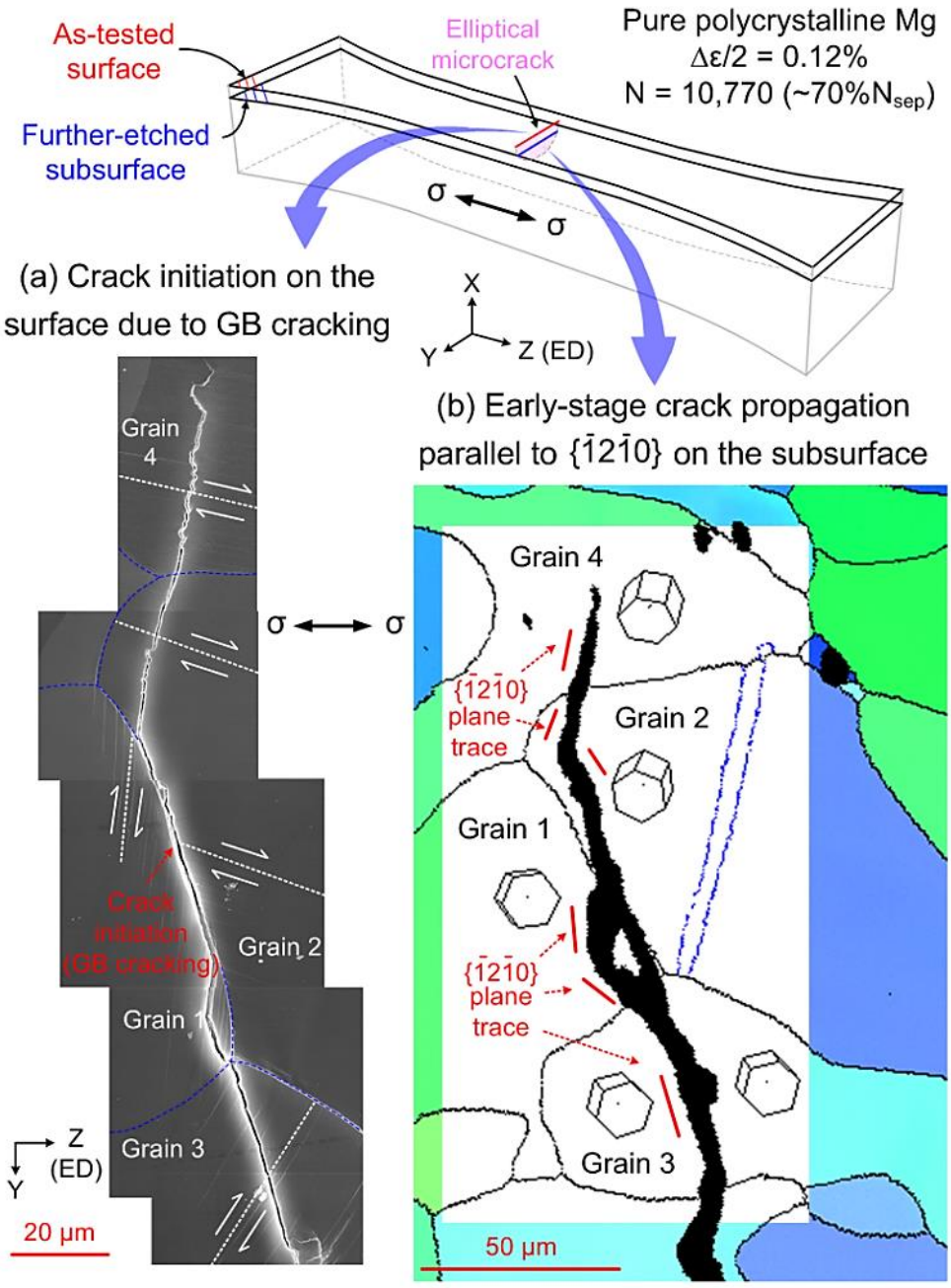

Figure 61 SEM observation of microcrack on the as-tested specimen surface and EBSD observation on the further-etched subsurface in the coarse-grained pure polycrystalline magnesium: (a) crack initiation on the surface due to GB cracking; (b) stage I microcrack propagation parallel to the $\{\bar{1}2\bar{1}0\}$ plane on the subsurface (HCP unit cells are embedded in the grains to indicate the crystal orientation of each grain).

To identify the crystal plane on which microcrack propagates, an investigation of the habit plane of the early-stage crack was carried out. Following further etching of the as-tested surface by removing ~20 μm-thick surface material, the propagated crack trace on the subsurface was subjected to EBSD scan and the crystal orientation surrounding the crack traces is determined (Figure 61). Figure 61b shows the crystal orientation map on subsurface beneath the as-tested specimen surface (Figure 61a). The HCP unit cells are delineated in the grains surrounding the microcrack to indicate the crystal orientation of each grain. Figure 61b shows all the traces of crack (and the branches) coincide with those of the $\{\bar{1}2\bar{1}0\}$ plane (see the bold black crack traces and the red solid lines in Figure 61b). This finding indicates that a microcrack propagates by habiting on $\{\bar{1}2\bar{1}0\}$ planes. The finding in pure magnesium is consistent with the results obtained from the crack propagation experiments of magnesium single crystal conducted by Ando et al. [102–106].

Figure 62 schematically illustrates the probable transgranular propagation routes of microcrack driven by a proposed alternative slip mechanism [103]. When the crack is initiated at the grain boundary on the specimen surface, two symmetric sets of second-order <*c*+*a*> pyramidal slip can be activated in the cyclic plastic zone at the crack front. The synergized slips by two sets of <*c*+*a*> pyramidal slips during a loading reversal (tensile or compressive) and the reversed slips during subsequent loading in the opposite direction act as a driving force to break the crystal on the $\{\bar{1}2\bar{1}0\}$ plane (see Figure 62b). The favorability of crack propagation on the $\{11\bar{2}0\}$ crystal planes can generate crack branches at different orientations, as schematically shown in Figure 62a.

Due to the HCP crystal symmetry, the $\{11\bar{2}0\}$ plane family has three distinctive planes having an angle of 60 °between any two. It is speculated that the crack has a tendency to grow on two possible directions which have an angle of 30 °from the $\{1\bar{1}00\}$ plane (see Figure 62a). When a crack front reaches point A in Figure 62a, branching might occur by propagating on the three possible $\{11\bar{2}0\}$ crystal planes. The proposed branching of crack by switching on three distinctive $\{\bar{1}2\bar{1}0\}$ planes can even occur inside the grain, as experimentally observed in Grain 2 in Figure 61b.

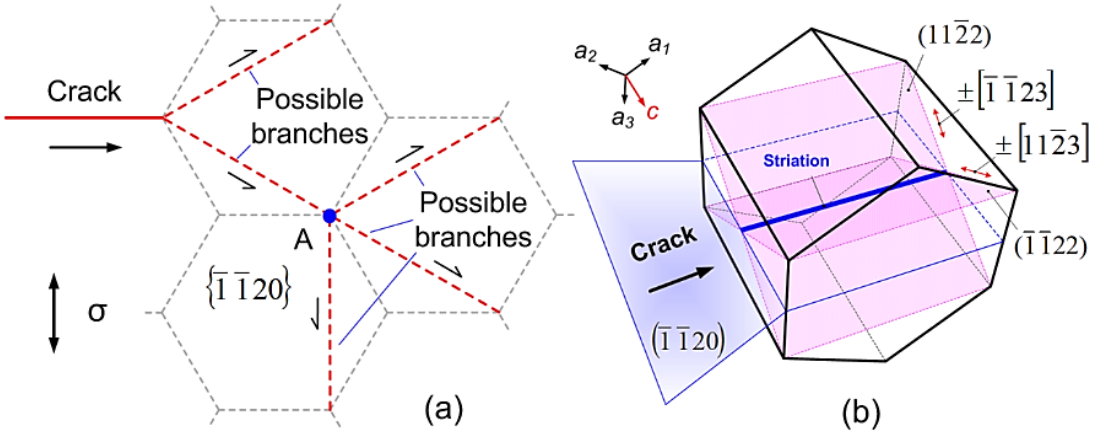

Figure 62 Schematics of the proposed early-stage (stage I) microcrack propagation mode in the pure polycrystalline magnesium under low cyclic loading magnitude dominated by dislocation slips: (a) potential propagation routes parallel to $\{\bar{1}2\bar{1}0\}$ plane; and (b) crack propagation driven by alternative slip mechanism by two sets of second-order <*c*+*a*> pyramidal slip [103].

5.6 Summary

Fully reversed strain-controlled cyclic tension-compression experiments were conducted on an extruded coarse-grained polycrystalline pure magnesium at two strain

amplitudes, 1% and 0.12%, in ambient air. Morphology of surface damage development was examined by SEM on companion specimens interrupted at different stages of cyclic deformation. Major experimental observations and the mechanisms are summarized as follows:

(1) At a strain amplitude of 1%, pure magnesium displays cyclic softening at the tensile peak stress right after the second loading cycle but moderate cyclic hardening at the compressive peak stress. At a strain amplitude of 0.12%, the material exhibits marginal cyclic hardening symmetrically for both the tensile and the compressive peak stresses.

(2) At a strain amplitude of 1%, a majority of the fatigue life (up to ~80% N_{sep}, where N_{sep} denotes the fatigue life corresponding to total separation of the testing specimen into two pieces) is spent on initiating microcracks with insignificant crack growth. The incessant initiation of microcracks is responsible for the cyclic softening observed at the tensile peak stress. At a strain amplitude of 0.12%, a majority of the fatigue life (50% ~70% N_{sep}) is spent on initiating microcracks.

(3) Early-stage microcrack initiation modes are dependent on the cyclic loading magnitude. Grain boundary cracking is persistent under both high and low loading amplitudes. Twin tip damage occurs under high cyclic loading magnitudes where massive tension deformation twins are activated.

(4) Both intergranular and transgranular crack growth modes exist at different loading amplitudes. However, the mechanisms of early-stage transgranular crack propagation are different at high and low strain amplitudes. At a strain amplitude of 1% where massive tension twins are formulated, transgranular crack growth is

due to cleavage cracking along twin boundary. At a strain amplitude of 0.12%, early-stage transgranular crack propagation is dominated by slip-induced cleavage cracking on $\{\bar{1}2\bar{1}0\}$ crystal planes driven by alternative slip mechanism on two sets of second-order <*c*+*a*> pyramidal slip.

(5) Fracture surface at a strain amplitude of 1% is characterized by densely distributed cleavage facets along twin lamella boundaries and tearing/shearing ridges without showing obvious initiation sites. At a strain amplitude of 0.12%, the fracture surface exhibits a semi-ellipse shaped initiation area where crystal sugar-like structure and cleavage facets on slip planes are detected.

6. Conclusions

In the current research, cyclic plastic deformation and the detailed morphology evolution of twinning-detwinning-retwinning in magnesium single crystal are obtained for the first time. Fundamental issues of twin-twin interaction under twinning/detwinning process are studied by combining experimental observations with the analytical methods based on crystallography of magnesium and the dislocation theory. Fatigue damage processes depending on different cyclic loading magnitudes are systematically investigated in an extruded polycrystalline pure magnesium. Microcrack initiation modes and the early-stage propagation modes in magnesium polycrystal are proposed. Based on the experimental results, major conclusions are drawn as follows:

(1) Typical cyclic stress-strain hysteresis loop for magnesium single crystal subjected to easy twinning and detwinning contains three featured deformation stages: twinning, easy detwinning, and hard detwinning accompanied by nonbasal slip. Repeated twinning-detwinning-retwinning in magnesium single crystal generates residual twin boundaries accumulated over the entire gage section. Residual twins are formed on the vicinities of pre-expanded twin boundaries during the detwinning reversal. With increasing loading cycles, the material exhibits cyclic hardening while the activities of fresh twinning, retwinning, and detwinning are reduced. Cyclic hardening is attributed to the accumulated barrier effect of the increased residual twin boundaries to the mobile slip dislocations and the twin-twin interactions. Particularly for the $[10\bar{1}0]$-oriented magnesium single crystal, a plastic instability phenomenon is found in the first tensile loading reversal

where the initial detwinning process accompanied by non-basal slips approaches exhaustion.

(2) After the termination of the fatigue experiments of [0001]-oriented and $[10\bar{1}0]$-oriented magnesium single crystals, microcracks with limited propagation are developed over the entire gage section at slip band extrusions, residual twin boundaries, and the intersection area of primary twins. For the $[10\bar{1}0]$-oriented magnesium single crystal, final fracture is dominated by the sudden cleavage cracking on $\{10\bar{1}1\}$-$\{10\bar{1}2\}$ double twin boundary and the shearing fracture on the basal plane.

(3) The matrix region in magnesium single crystal having experienced repeated twinning and detwinning cannot completely reverse to the original crystal orientation, which implies the existence of stable dislocation substructures due to dislocation-twin boundary interactions. Secondary tension twin fragments predominately occur at the interaction sites among primary twins and are more difficult to be detwinned as compared to the parent primary twins.

(4) Two types of twin-twin interaction can be categorized in magnesium: Type I corresponding to two twins that share the same zone axis and Type II interactions that share a different zone axis. Twin transmission in Type I twin-twin interaction is prohibited since both twins either twin or detwin under the same loading condition. For Type II twin-twin interaction under certain loading conditions, although secondary twinning can occur in one twin while the other twin experiences primary twinning, twin transmission is not observed in the experiments.

(5) Formation mechanism of twin-twin boundary is proposed as impinging, zipping, and dissociating of twinning dislocations. For Type I twin-twin interaction, the twin-twin boundary is a low angle tilt boundary with the habit plane being parallel either to the basal or the prismatic planes in both twins. For Type II twin-twin interactions, the twin-twin boundary adopts a high index crystallographic plane according to geometry analysis and could thus evolve to form a complex boundary following thermodynamic relaxation. Twin-twin boundary dislocations can be characterized by reactions of twinning dislocations associated with the two twin variants. "Apparent crossing" twin structure observed in experiment is interpreted as a result of twin-twin boundary formation. The intersection region bounded by a pair of twin-twin boundaries experiences a tilt induced by the pileup of twin-twin boundary dislocations.

(6) Under reversed loading, detwinning and retwinning are hindered due to the energetically unfavorable dissociation of twin-twin boundary dislocations. Under local concentrated stress, twin-twin boundary dislocation at Type II twin-twin boundaries can dissociate into secondary twinning dislocation and leave a residual dislocation, resulting in a double tension twin structure.

(7) Crack initiation and early-stage propagation in the extruded coarse-grained polycrystalline pure magnesium are dependent on the magnitude of the cyclic loading. Under cyclic loading dominated by twinning/detwinning, grain boundary cracking and twin tip damage are two initiation modes. Microcracks propagate very limitedly on both the grain boundaries and the twin boundaries. Under cyclic loading controlled by dislocation slips, microcrack initiates

predominantly at grain boundaries due to the incompatibility caused by the anisotropic elastic/plastic deformation between neighboring grains. Both intergranular and transgranular propagation modes are observed. The early-stage transgranular propagation mode is identified as cleavage cracking on the $\{\bar{1}2\bar{1}0\}$ crystal planes driven by alternative slip mechanism on two sets of second-order <*c*+*a*> pyramidal slips.

Appendix A

A.1 Crystal Direction and Crystal Plane in Hexagonal Close Packed Crystal Structure

In the direct lattice of hexagonal close packed crystal structure, an arbitrary direction $\mathbf{r}$ can be expressed in the rhombohedral system using the Miller indices $[U\,V\,W]$ with respect to three basis vectors $\mathbf{a_1},\mathbf{a_2},\mathbf{c}$. The direction $\mathbf{r}$ can also be expressed in the hexagonal system with four basis vectors ($\mathbf{a_1},\mathbf{a_2},\mathbf{a_3},\mathbf{c}$) using the Miller-Bravais indices $[u\,v\,t\,w]$.

$$\mathbf{r} = U\mathbf{a_1} + V\mathbf{a_2} + W\mathbf{c} \qquad \text{(A1a)}$$

$$\mathbf{r} = u\mathbf{a_1} + v\mathbf{a_2} + t\mathbf{a_3} + w\mathbf{c} \qquad \text{(A1b)}$$

The transformation between the Miller indices $[U\,V\,W]$ in the rhombohedral system and the Miller-Bravais indices $[u\,v\,t\,w]$ in the hexagonal system is:

$$U = u - t, \qquad V = v - t, \qquad W = w \qquad \text{(A2a)}$$

$$u = \frac{1}{3}(2U - V),\ v = \frac{1}{3}(2V - U),\ t = -(u + v),\ w = W \qquad \text{(A2b)}$$

To index the crystal planes, the reciprocal lattice needs to be introduced. The vector $\mathbf{r}^*$ in the reciprocal lattice lies along the normal of a set of parallel planes (HKL) in the direct lattice. The norm of the vector in the reciprocal lattice is inversely proportional to the spacing of the planes:

$$\left|\mathbf{r}^{*}_{HKL}\right| = \frac{n}{d_{HKL}} \qquad (A3)$$

where $\mathbf{r}^{*}_{HKL}$ is a vector in the reciprocal lattice. d_{HKL} is the spacing of a set of parallel planes $(H\ K\ L)$ in the direct lattice. n is a constant. The reciprocal basis vectors in the rhombohedral system and the hexagonal system are denoted as $\mathbf{A}^{*}_{1},\mathbf{A}^{*}_{2},\mathbf{C}^{*}$ and $\mathbf{a}^{*}_{1},\mathbf{a}^{*}_{2},\mathbf{a}^{*}_{3},\mathbf{c}^{*}$, respectively. Direct and reciprocal basis vectors in the rhombohedral and the hexagonal systems satisfy the following conditions:

$$a_i \cdot A^{*}_{j} = \delta_{ij},\ i, j = 1,3 \qquad (A4a)$$

$$a_i \cdot a^{*}_{j} = \delta_{ij},\ i, j = 1,4 \qquad (A4b)$$

where δ_{ij} is the Kronecker delta. To this end, a crystal plane $\mathbf{n}$ can be described by the Miller indices $(H\ K\ L)$ and by the Miller-Bravais indices $(h\ k\ i\ l)$ using the reciprocal basis vectors in the rhombohedral and the hexagonal systems, respectively:

$$\mathbf{n} = \mathbf{n}_{HKL} = H\mathbf{A}^{*}_{1} + K\mathbf{A}^{*}_{2} + L\mathbf{C}^{*} \qquad (A5a)$$

$$\mathbf{n} = \mathbf{n}_{hkil} = h\mathbf{a}^{*}_{1} + k\mathbf{a}^{*}_{2} + i\mathbf{a}^{*}_{3} + l\mathbf{c}^{*} \qquad (A5b)$$

The transformation between the Miller indices $(H\ K\ L)$ in the rhombohedral system and the Miller-Bravais indices $(h\ k\ i\ l)$ in the hexagonal system follows:

$$H = h, \quad K = k, \quad L = l \qquad (A6a)$$

$$h = H, \quad k = K, \quad i = -(h + k), \quad l = L \qquad (A6b)$$

The indices of a normal to a crystal plane $(h\,k\,i\,l)$ in the direct lattice are $\left[h\;\;k\;\;i\frac{3}{2}\left(\frac{a}{c}\right)^2\;\;l\right]$. If a direction vector $\mathbf{r}$ lies within the crystal plane $\mathbf{n}$, orthogonality condition is satisfied, i.e. that, $\mathbf{r}\cdot\mathbf{n}=0$ or $uh+vk+ti+wl=0$ or $UH+VK+WL=0$. The interplanar spacing of a set of $(H\,K\,L)$ (or $(h\,k\,i\,l)$) crystal planes is given by [181]:

$$d_{HKL}=a\left[\frac{4}{3}\left(h^2+hk+k^2\right)+\left(\frac{c}{a}\right)^{-2}\cdot l^2\right]^{-\frac{1}{2}} \qquad (A7)$$

To facilitate the description of the crystal orientation, an orthonormal coordinate system ($\mathbf{e_1},\mathbf{e_2},\mathbf{e_3}$) can be introduced as embedded on the rhombohedral system ($\mathbf{a_1},\mathbf{a_2},\mathbf{c}$), where:

$$\begin{aligned}\mathbf{e_1}&=\mathbf{a_1}/a\\ \mathbf{e_2}&=\left(\frac{1}{2}\mathbf{a_1}+\mathbf{a_2}\right)/\left(\frac{\sqrt{3}}{2}a\right)\\ \mathbf{e_3}&=\mathbf{c}/c\end{aligned} \qquad (A8)$$

In Equation A8, a and c are lattice parameters. The transformation matrix $\mathbf{L}$ from the rhombohedral system ($\mathbf{a_1},\mathbf{a_2},\mathbf{c}$) to the orthonormal system ($\mathbf{e_1},\mathbf{e_2},\mathbf{e_3}$) can be written as [164, 182]:

$$\mathbf{L}=\begin{pmatrix}1 & -\frac{1}{2} & 0\\ 0 & \frac{\sqrt{3}}{2}a & 0\\ 0 & 0 & \frac{c}{a}\end{pmatrix} \qquad (A9)$$

With the transformation matrix $\mathbf{L}$, the transformation between the direction vector described by $\mathbf{r}_{[e_1e_2e_3]}=[e_1\ e_2\ e_3]$ in the orthonormal system and the same vector described by $\mathbf{r}_{[UVW]}=[U\ V\ W]$ in the rhombohedral system can be realized [182]:

$$\mathbf{r}_{[e_1e_2e_3]}=\mathbf{L}\,\mathbf{r}_{[UVW]} \qquad (A10a)$$

$$\mathbf{r}_{[UVW]}=\mathbf{L}^{-1}\mathbf{r}_{[e_1e_2e_3]} \qquad (A10b)$$

where $\mathbf{L}$ is the transformation matrix from the rhombohedral system $\mathbf{a_1},\mathbf{a_2},\mathbf{c}$ to the orthonormal system $\mathbf{e_1},\mathbf{e_2},\mathbf{e_3}$. $\mathbf{r}_{[e_1e_2e_3]}=[e_1\ e_2\ e_3]$ and $\mathbf{r}_{[UVW]}=[U\ V\ W]$ are column vectors.

Following a similar fashion, the transformation between the crystal plane described by $\mathbf{n}_{(e_1e_2e_3)}=(e_1\ e_2\ e_3)$ in the orthonormal system and the same plane described by $\mathbf{n}_{(HKL)}=(H\ K\ L)$ in the rhombohedral system can be realized by means of the transformation matrix $\mathbf{L}$ [182]:

$$\mathbf{n}_{(e_1e_2e_3)}=\mathbf{n}_{(HKL)}\,\mathbf{L}^{-1} \qquad (A11a)$$

$$\mathbf{n}_{(HKL)}=\mathbf{n}_{(e_1e_2e_3)}\,\mathbf{L} \qquad (A11b)$$

where $\mathbf{L}$ is the transformation matrix from the rhombohedral system $\mathbf{a_1},\mathbf{a_2},\mathbf{c}$ to orthonormal system $\mathbf{e_1},\mathbf{e_2},\mathbf{e_3}$. $\mathbf{n}_{(e_1e_2e_3)}=(e_1\ e_2\ e_3)$ and $\mathbf{n}_{(HKL)}=(H\ K\ L)$ are row vectors.

A.2 Schmid Criterion

The activation of a specific slip/twinning system is strongly dependent on the orientation of the stress axis. According to the Schmid criterion, a slip/twinning system is activated when the resolved shear stress on the slip/twinning plane exceeds its associated critical resolved shear stress (CRSS). The resolved shear stress on a slip/twinning plane can be calculated by:

$$\tau = \sigma_{ij}\left(\frac{m_i n_j + n_i m_j}{2}\right) \qquad \text{(A12)}$$

where σ_{ij} is the stress tensor with respect to the sample coordinate system. $\frac{m_i n_j + n_i m_j}{2}$ is the Schmid factor (SF) for the slip/twinning system. m_i and n_i are the unit vector of slip/twinning plane normal and the unit vector of slip/twinning direction with respect to the sample coordinate system, respectively.

As an application of the Schmid criterion, the Schmid factors for all the potential slip systems in HCP magnesium single crystal were calculated under a tensile stress oriented in an arbitrary direction. Such work can facilitate the design of single crystal orientation under which a preferred slip/twinning system has a higher value of Schmid factor than those of the other slip/twinning modes, so that an individual deformation mode can be easily studied. Figure A1 illustrates inverse pole figures showing Schmid factors for various slip systems in magnesium single crystal under uniaxial loading in an arbitrary orientation. All SFs are plotted in their absolute values. It can be seen that basal slip has its highest SF value when the loading axis is oriented approximately 45° from *c*-axis or the basal plane. When the loading axis is along *c*-axis or lying on the

basal plane, basal slip is suppressed since its SF value is zero. For prism $<a>$ slip and first-order pyramidal $<a>$ slip (Figure A1b and Figure A1c), their activation is suppressed when the loading direction is along *c*-axis. Second-order pyramidal $<c+a>$ slip has its highest SF value when the loading axis is oriented along the *c*-axis or *a*-axis, as seen in Figure A1d.

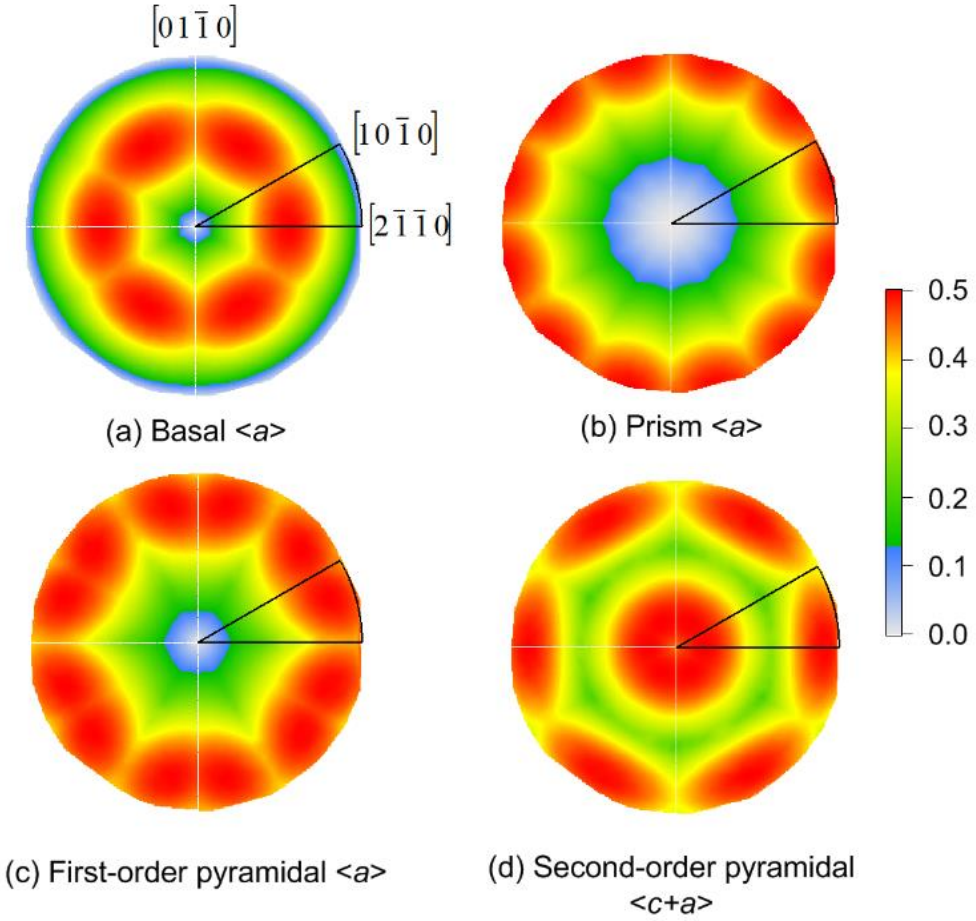

Figure A1 Inverse pole figures showing Schmid factors for various slip systems in magnesium single crystal under a uniaxial tensile loading oriented in an arbitrary direction (the solid black lines indicate the standard stereographic triangle for HCP magnesium): (a) basal $<a>$; (b) prism $<a>$; (c) first-order pyramidal $<a>$; (d) second-order pyramidal $<c+a>$.

Qin Yu's Journal Publications

1. **Yu, Q.**, Jiang, Y., Wang, J., 2015, "Cyclic Deformation and Fatigue Damage in Magnesium Single Crystal under Fully Reversed Strain-Controlled Tension-Compression in [10-10] Direction," *Scripta Materialia*, Vol.96, pp.41-44 (doi:10.1016/j.scriptamat.2014.10.020).
2. Dong, S., **Yu, Q.**, Jiang, Y., Dong, J., Wang, F., Ding, W., 2015, "Electron backscatter diffraction observations of twinning-detwinning evolution in a magnesium alloy subjected to large strain amplitude cyclic loading," *Materials & Design*, Vol.65, pp.762-765 (doi:10.1016/j.matdes.2014.09.079).
3. Gibson, R.F., Jang, H.-K., Simkhada, S., **Yu, Q.**, Kim, H.-I., Suhr, J, 2014, "The use of nanoindentation, finite element simulations and a combined experimental/numerical approach to characterize elastic moduli of individual porous silica particles," *Particulate Science and Technology*, in press, (doi:10.1080/02726351.2014.950396).
4. Cao, Q.P., Jin, J.B., **Yu, Q.**, Wang, X.D., Zhang, D.X., Jiang, Y.Y., Jiang, J.Z., 2014, "Tensile Elastic Behavior of a Zr-Cu-Ag-Al Bulk Metallic Glass," *Journal of Materials Science & Technology*, Vol.30, pp.595-598 (doi: 10.1016/j.jmst.2013.12.020).
5. **Yu, Q.**, Wang, J., Jiang, Y., McCabe, R.J., Tomé, C.N., 2014, "Twin-twin interactions in magnesium," *Acta Materlia*, Vol.77, pp.28-42 (doi: 10.1016/j.actamat.2014.05.030).

6. **Yu, Q.**, Wang, J., Jiang, Y., McCabe, R.J., Tomé, C.N., 2014, "Co-zone $\{\bar{1}012\}$ twin interaction in magnesium single crystal," *Material Research Letter,* Vol.2, pp.82-88 (doi:10.1080/21663831.2013.867291).
7. Wang, J., **Yu, Q.**, Jiang, Y., Beyerlein, I.J., 2014, "Twinning-associated boundaries in hexagonal close-packed metals," *JOM,* Vol.66, pp.95-101 (doi: 10.1007/s11837-013-0803-0)
8. Xiong, Y., **Yu, Q.**, Jiang, Y., 2014, "An experimental study of cyclic plastic deformation of extruded ZK60 magnesium alloy," *International Journal of Plasticity*, Vol.53, pp.107-124 (doi: 10.1016/j.ijplas.2013.07.008).
9. **Yu, Q.**, Wang, J., Jiang, Y., 2013, "Inverse slip accompanying twinning and de-twining during cyclic loading of magnesium single crystal," *Journal of Materials*, Vol. 2013, Article ID 903786, 8 pages (doi:10.1155/2013/903786).
10. Zheng, S., **Yu, Q.**, Jiang, Y., 2013, "Loading history effect on fatigue crack growth of extruded AZ31B magnesium alloy," *Engineering Fracture Mechanics,* Vol.114, pp.42-54 (doi:10.1016/j.engfracmech.2013.10.012).
11. Zheng, S., **Yu, Q.**, Jiang, Y., 2012, "An experimental study of fatigue crack propagation in extruded AZ31B magnesium alloy," *International Journal of Fatigue,* Vol.47, pp.174-183 (doi: 10.1016/j.ijfatigue.2012.08.010).
12. **Yu, Q.**, Zhang, J., Jiang, Y., Li, Q., 2012, "Effect of strain ratio on cyclic deformation and fatigue of extruded AZ61A magnesium alloy," *International Journal of Fatigue,* Vol.44, pp.225-233 (doi: 10.1016/j.ijfatigue.2012.04.013).

13. Xiong, Y., **Yu, Q.**, Jiang, Y., 2012, "Multiaxial fatigue of extruded AZ31B magnesium alloy," *Material Science and Engineering: A,* Vol.546, pp.119-128 (doi:10.1016/j.msea.2012.03.039).
14. **Yu, Q.**, Zhang, J., Jiang, Y., 2011, "Direct observation of twinning-detwinning-retwinning on magnesium single crystal subjected to strain-controlled cyclic tension-compression in [0001] direction," *Philosophical Magazine Letters,* Vol.91, pp.757-765 (doi:10.1080/09500839.2011.617713).
15. **Yu, Q.**, Zhang, J., Jiang, Y., and Li, Q., 2011, "An experimental study on cyclic deformation and fatigue of extruded ZK60 magnesium alloy," *International Journal of Fatigue,* Vol.36, pp.47-58, (doi:10.1016/j.ijfatigue.2011.08.016)
16. **Yu, Q.**, Zhang, J., Jiang, Y., 2011, "Fatigue damage development in pure polycrystalline magnesium under cyclic tension-compression loading," *Materials Science and Engineering A,* Vol.528, pp.7816-7826, (doi:10.1016/j.msea.2011.06.064).
17. **Yu, Q.**, Zhang, J., Jiang, Y., Li, Q., 2011, "Multiaxial fatigue of extruded AZ61A magnesium alloy," *International Journal of Fatigue*, Vol.33, pp.437-447 (doi:10.1016/j.ijfatigue.2010.09.020).
18. Zhang, J., **Yu, Q.**, Jiang, Y., Li, Q., 2011, "An experimental study of cyclic deformation of extruded AZ61A magnesium alloy," *International Journal of Plasticity*, Vol.27, pp.768-787 (doi:10.1016/j.ijplas.2010.09.004).
19. Li, Q., **Yu, Q.**, Zhang, J., Jiang, Y., 2011, "Microstructure and deformation mechanism of Mg6Al1ZnA alloy experienced tension–compression cyclic

loading," *Scripta Materialia*, Vol.64, pp.233-236 (doi:10.1016/j.scriptamat.2010.10.017).

20. Li, Q., **Yu, Q.**, Zhang, J., Jiang, Y., 2010, "Effect of strain amplitude on tension–compression fatigue behavior of extruded Mg6Al1ZnA magnesium alloy," *Scripta Materialia*, Vol.62, pp.778-781 (doi:10.1016/j.scriptamat.2010.01.052).

References

1. Eliezer, D., Aghion, E., and Froes, F. H. (Sam), 1998, "Magnesium Science, Technology and Applications," Advanced Performance Materials, Vol. 5(3), pp. 201–212.

2. Mordike, B. ., and Ebert, T., 2001, "Magnesium: Properties — applications — potential," Materials Science and Engineering: A, Vol. 302(1), pp. 37–45.

3. Bettles, C., and Gibson, M., 2005, "Current wrought magnesium alloys: Strengths and weaknesses," JOM, Vol. 57(5), pp. 46–49.

4. Agnew, S. R., 2004, "Wrought magnesium: A 21st century outlook," JOM, Vol. 56(5), pp. 20–21.

5. Luo, A. A., 2002, "Magnesium: Current and potential automotive applications," JOM, Vol. 54(2), pp. 42–48.

6. Froes, F. H., 1994, "Advanced metals for aerospace and automotive use," Materials Science and Engineering: A, Vol. 184(2), pp. 119–133.

7. Ball, E. A., and Prangnell, P. B., 1994, "Tensile-compressive yield asymmetries in high strength wrought magnesium alloys," Scripta Metallurgica et Materialia, Vol. 31(2), pp. 111–116.

8. Kleiner, S., and Uggowitzer, P. J., 2004, "Mechanical anisotropy of extruded Mg–6% Al–1% Zn alloy," Materials Science and Engineering: A, Vol. 379(1-2), pp. 258–263.

9. Barnett, M., 2007, "Twinning and the ductility of magnesium alloys, Part I: 'Tension' twins," Materials Science and Engineering: A, Vol. 464(1-2), pp. 1–7.

10. Barnett, M., 2007, "Twinning and the ductility of magnesium alloys, Part II. 'Contraction' twins," Materials Science and Engineering: A, Vol. 464(1-2), pp. 8–16.

11. Stephens, R. I., Fatemi, A., Stephens, R. R., Fuchs, H. O., and Faterni, A., 2000, Metal Fatigue in Engineering. Wiley-Interscience.

12. Suresh, S., 1998, Fatigue of Materials. Cambridge University Press.

13. Manson, S. S., and Halford, G. R., 2009, Fatigue and durability of metals at high temperatures. ASM International.

14. Kennedy, A. J., 1963, Processes of Creep and Fatigue in Metals. Oliver and Boyd.

15. Miller, K. J., 1991, "Metal fatigue—past, current and future," ARCHIVE: Proceedings of the Institution of Mechanical Engineers, Part C: Journal of Mechanical Engineering Science, Vol. 205(53), pp. 291–304.

16. Wu, L., Jain, A., Brown, D. W., Stoica, G. M., Agnew, S. R., Clausen, B., Fielden, D. E., and Liaw, P. K., 2008, "Twinning-detwinning behavior during the strain-controlled low-cycle fatigue testing of a wrought magnesium alloy, ZK60A," Acta Materialia, Vol. 56(4), pp. 688–695.

17. Wu, L., Agnew, S. R., Brown, D. W., Stoica, G. M., Clausen, B., Jain, A., Fielden, D. E., Liaw, P. K., 2008, "Internal stress relaxation and load redistribution during the twinning-detwinning-dominated cyclic deformation of a wrought magnesium alloy, ZK60A," Acta Materialia, Vol. 56(14), pp. 3699–3707

18. Tokaji, K., Kamakur, M., Ishiizumic, Y., and Hasegawad, N., 2004, "Fatigue behaviour and fracture mechanism of a rolled AZ31 magnesium alloy," International Journal of Fatigue, Vol. 26(11), pp. 1217–1224.

19. Xu, D. K., Liu, L., Xu, Y. B., and Han, E. H., 2007, "The crack initiation mechanism of the forged Mg-Zn-Y-Zr alloy in the super-long fatigue life regime," Scripta Materialia, Vol. 56(1), pp. 1–4.

20. Yang, F., Yin, S. M., Li, S. X., And Zhang, Z. F., 2008, "Crack initiation mechanism of extruded AZ31 magnesium alloy in the very high cycle fatigue regime," Materials Science and Engineering: A, Vol. 491(1-2), pp. 131–136.

21. Yin, S. M., Yang, F., Yang, X. M., Wu, S. D., Li, S. X., And Li, G. Y., 2008, "The role of twinning–detwinning on fatigue fracture morphology of Mg–3%Al–1%Zn alloy," Materials Science and Engineering: A, Vol. 494(1-2), pp. 397–400.

22. Partridge, P. G., 1967, "The crystallography and deformation modes of hexagonal close-packed metals," Metallurgical Reviews, Vol. 12, pp. 169–194(26).

23. Yoo, M. H., 1967, "Slip modes of hexagonal-close-packed metals," Journal of Applied Physics, Vol. 38(11), pp. 4317.

24. Von Mises, R., 1928, Z. angew. Math. Mech., Vol. 8, pp. 161.

25. Reed-Hill, R. E., and Robertson, W. D., 1957, "Additional modes of deformation twinning in magnesium," Acta Metallurgica, Vol. 5(12), pp. 717–727.

26. Schmid, E., and Boas, W., 1968, Plasticity of crystals: with special reference to metals. Chapman and Hall.

27. Bakarian, P. W., and Mathewson, C. H., 1943, "Slip and twinning in magnesium single crystals at elevated temperatures," Transactions of the American Institute of Mining, Metallurgical, and Petroleum Engineers, Vol. 152, pp. 226.

28. Burke, E. C., and Hibbard, W. R., 1952, "Plastic deformation of magnesium single crystals," Transactions of the Metallurgical Society of AIME, Vol. 194, pp. 295–303.

29. Asada, H., and Yoshinaga, H., 1959, "Temperature and orientation dependence of the plasticity of magnesium single crystals," The Journal of the Japan Institute of Metals, Vol. 23(11), pp. 649–652.

30. Bhattacharya, B., and Niewczas, M., 2011, "Work-hardening behaviour of Mg single crystals oriented for basal slip," Philosophical Magazine, Vol. 91(17), pp. 2227–2247.

31. Reed-Hill, R. E., and Robertson, W. D., 1957, "Deformation of magnesium single crystals by nonbasal slip," Journal of Metals, Vol. 209, pp. 496.

32. Wonsiewicz, B. C., and Backofen, W. A., 1967, "Plasticity of magnesium single crystals," Trans. Metall. Soc. AIME, Vol. 239, pp. 1422–1431.

33. Chapuis, A., and Driver, J. H., 2011, "Temperature dependency of slip and twinning in plane strain compressed magnesium single crystals," Acta Materialia, Vol. 59(5), pp. 1986–1994.

34. Obara, T., Yoshinga, H., and Morozumi, S., 1973, "{11-22}<-1-123> Slip system in magnesium," Acta Metallurgica, Vol. 21(7), pp. 845–853.

35. Abbaschian, R. A., and Reed-Hill, R. E., 2008, Physical Metallurgy Principles. Cengage Learning.

36. Cahn, R. W., 1953, "Plastic deformation of alpha-uranium; twinning and slip," Acta Metallurgica, Vol. 1(1), pp. 49–70.

37. Christian, J. W., and Mahajan, S., 1995, "Deformation twinning," Progress in Materials Science, Vol. 39(1-2), pp. 1–157.

38. Miura, H., Yang, X., Sakai, T., Nogawa, H., Miura, S., Watanabe, Y., and Jonas, J. J., 2005, "High temperature deformation and extended plasticity in Mg single crystals," Philosophical Magazine, Vol. 85(30), pp. 3553–3565.

39. Yu, Q., Zhang, J., and Jiang, Y., 2011, "Direct observation of twinning–detwinning–retwinning on magnesium single crystal subjected to strain-controlled cyclic tension–compression in [0 0 0 1] direction," Philosophical Magazine Letters, Vol. 91(12), pp. 757–765.

40. Yoshinaga, H., and Horiuchi, R., 1963, "Deformation mechanisms in magnesium single crystals compressed in the direction parallel to hexagonal axis," Transactions of the Japan Institute of Metals, Vol. 4(1), pp. 1–8.

41. Reed-Hill, R. E., and Robertson, W. D., 1957, "The crystallographic characteristics of fracture in magnesium single crystals," Acta Metallurgica, Vol. 5(12), pp. 728–737.

42. Yoshinaga, H., Obara, T., and Morozumi, S., 1973, "Twinning deformation in magnesium compressed along the c-axis," Materials Science and Engineering, Vol. 12(5-6), pp. 255–264.

43. Hartt, W. H., and Reed-Hill, R. E., 1967, "The irrational habit of second-order {10-11}-{10-12} twins in magnesium," Trans. Metall. Soc. AIME, Vol. 239, pp. 1511–1517.

44. Kelley, E. W., and Hosford, W. F., 1968, "Plane-strain compression of magnesium and magnesium alloy crystals," Trans. Metall. Soc. AIME, Vol. 242, pp. 5–13.

45. Reed-Hill, R. E., 1960, "A study of the {10-11} and {10-13} twinning modes in magnesium," Trans. AIME, Vol. 218, pp. 554.

46. Hartt, W. H., and Reed-Hill, R. E., 1968, "Internal deformation and fracture of second-order {10-11}-{10-12} twins in magnesium," Trans. Metall. Soc. AIME, Vol. 242, pp. 1127–1133.

47. Hartt, W. H., and Reed-Hill, R. E., 1968, "Shear accommodation kinking at second order {10-11}-{10-12} twins in magnesium," Trans. Metall. Soc. AIME, Vol. 242, pp. 2207–2210.

48. Maruyama, S., and Kiho, H., 1956, "Intersection of {301}, {101} twin bands in Tin," Journal of The Physical Society of Japan, Vol. 11(5), pp. 516–521.

49. Mahajan, S., Barry, D. E., and Eyre, B. L., 1970, "A thin twin and its interaction with a coherent twin boundary in copper," Philosophical Magazine, Vol. 21(169), pp. 43–52.

50. Mahajan, S., and Chin, G. Y., 1973, "Twin-slip, twin-twin and slip-twin interactions in Co-8 wt.% Fe alloy single crystals," Acta Metallurgica, Vol. 21(2), pp. 173–179.

51. Mahajan, S., and Chin, G. Y., 1974, "The interaction of twins with existing substructure and twins in cobalt-iron alloys," Acta Metallurgica, Vol. 22(9), pp. 1113–1119.

52. Rajan, K., 1982, "Twin-twin interaction in a Co-Cr-Mo alloy," Journal of Materials Science Letters, Vol. 1(11), pp. 482–484.

53. Pratt, P. L., 1953, "Cleavage deformation in zinc and sodium chloride," Acta Metallurgica, Vol. 1(6), pp. 692–699.

54. Reed-Hill, R., and Buchanan, E., 1963, "Zig-zag twins in zirconium," Acta Metallurgica, Vol. 11(1), pp. 73–75.

55. Reed-Hill, R. E., 1964, "Twin intersections and Cahn's continuity conditions," Trans. Metall. Soc. AIME, Vol. 230, pp. 809–813.

56. Roberts, E., and Partridge, P. G., 1966, "The accommodation around {10-12} <-1011> twins in magnesium," Acta Metallurgica, Vol. 14(4), pp. 513–527.

57. Ecob, N., and Ralph, B., 1983, "The effect of grain size on deformation twinning in a textured zinc alloy," Journal of Materials Science, Vol. 18(8), pp. 2419–2429.

58. Nave, M., and Barnett, M., 2004, "Microstructures and textures of pure magnesium deformed in plane-strain compression," Scripta Materialia, Vol. 51(9), pp. 881–885.

59. Jiang, J., Godfrey, A., and Liu, Q., 2005, "Influence of grain orientation on twinning during warm compression of wrought Mg–3Al–1Zn," Materials Science and Technology, Vol. 21(12), pp. 1417–1422

60. Jiang, L., Jonas, J., Luo, A., Sachdev, A., and Godet, S., 2007, "Influence of {10-12} extension twinning on the flow behavior of AZ31 Mg alloy," Materials Science and Engineering: A, Vol. 445-446, pp. 302–309.

61. Yang, X., and Zhang, L., 2009, "Twinning and twin intersection in AZ31 Mg alloy during warm deformation," Acta Metallurgica Sinica (China), Vol. 45(11), pp. 1303–1308.

62. Hong, S.-G., Park, S. H., and Lee, C. S., 2010, "Role of {10–12} twinning characteristics in the deformation behavior of a polycrystalline magnesium alloy," Acta Materialia, Vol. 58(18), pp. 5873–5885.

63. Hong, S.-G., Park, S. H., and Lee, C. S., 2011, "Strain path dependence of {10−12} twinning activity in a polycrystalline magnesium alloy," Scripta Materialia, Vol. 64(2), pp. 145–148.

64. Oppedal, A. L., El Kadiri, H., Tomé, C. N., Kaschner, G. C., Vogel, S. C., Baird, J. C., and Horstemeyer, M. F., 2012, "Effect of dislocation transmutation on modeling hardening mechanisms by twinning in magnesium," International Journal of Plasticity, Vol. 30-31, pp. 41–61.

65. Ma, Q., El Kadiri, H., Oppedal, A. L., Baird, J. C., Li, B., Horstemeyer, M. F., and Vogel, S. C., 2012, "Twinning effects in a rod-textured AM30 Magnesium alloy," International Journal of Plasticity, Vol. 29, pp. 60–76.

66. El Kadiri, H., Kapil, J., Oppedal, A. L., Hector, L. G., Agnew, S. R., Cherkaoui, M., and Vogel, S. C., 2013, "The effect of twin–twin interactions on the nucleation and propagation of twinning in magnesium," Acta Materialia, Vol. 61(10), pp. 3549–3563.

67. Chun, Y. B., Yu, S. H., Semiatin, S. L., and Hwang, S. K., 2005, "Effect of deformation twinning on microstructure and texture evolution during cold rolling of CP-titanium," Materials Science and Engineering: A, Vol. 398(1–2), pp. 209–219.

68. Yu, Q., Wang, J., and Jiang, Y., 2013, "Inverse slip accompanying twinning and detwinning during cyclic loading of magnesium single crystal," Journal of Materials, Vol. 2013, pp. 1–8.

69. Zhang, J.-B., Fan, D., Yu, S.-R., and Wang, J.-Y., 2003, "Influence of mechanical surface treatments on fatigue strength of commercial purity titanium," Journal of Materials Science, Vol. 38(16), pp. 3455–3459.

70. Li, H., Duan, Q., Li, X., and Zhang, Z., 2007, "Compressive and fatigue damage behavior of commercially pure zinc," Materials Science and Engineering: A, Vol. 466(1-2), pp. 38–46.

71. Zhu, K. Y., Vassel, A., Brisset, F., Lu, K., and Lu, J., 2004, "Nanostructure formation mechanism of α-titanium using SMAT," Acta Materialia, Vol. 52(14), pp. 4101–4110.

72. Zhang, L., and Han, Y., 2009, "Twins formation and their role in nanostructuring of zirconium," Materials Science and Engineering: A, Vol. 523(1–2), pp. 130–133.

73. Jäger, A., Ostapovets, A., Molnár, P., and Lejček, P., 2011, "{10-11}-{10-12} Double twinning in magnesium," Philosophical Magazine Letters, Vol. 91(8), pp. 537–544.

74. Hou, X., Cao, Z., Sun, X., Wang, L., and Wang, L., 2012, "Twinning and dynamic precipitation upon hot compression of a Mg−Gd−Y−Nd−Zr alloy," Journal of Alloys and Compounds, Vol. 525(0), pp. 103–109.

75. Al-Samman, T., and Gottstein, G., 2008, "Room temperature formability of a magnesium AZ31 alloy: Examining the role of texture on the deformation mechanisms," Materials Science and Engineering: A, Vol. 488(1-2), pp. 406–414.

76. Choi, S.-H., Kim, J. K., Kim, B. J., and Park, Y. B., 2008, "The effect of grain size distribution on the shape of flow stress curves of Mg-3Al-1Zn under uniaxial compression," Materials Science and Engineering: A, Vol. 488(1-2), pp. 458–467

77. Jain, J., Zou, J., Sinclair, C. W., and Poole, W. J., 2011, "Double tensile twinning in a Mg-8Al-0.5Zn alloy.," Journal of microscopy, Vol. 242(1), pp. 26–36.

78. Xin, Y., Wang, M., Zeng, Z., Nie, M., and Liu, Q., 2012, "Strengthening and toughening of magnesium alloy by {10−12} extension twins," Scripta Materialia, Vol. 66(1), pp. 25–28.

79. Park, S. H., Hong, S.-G., Lee, J. H., and Lee, C. S., 2012, "Multiple twinning modes in rolled Mg–3Al–1Zn alloy and their selection mechanism," Materials Science and Engineering: A, Vol. 532, pp. 401–406.

80. Fernández, A., Jérusalem, A., Gutiérrez-Urrutia, I., and Pérez-Prado, M. T., 2013, "Three-dimensional investigation of grain boundary–twin interactions in a Mg AZ31 alloy by electron backscatter diffraction and continuum modeling," Acta Materialia, Vol. 61(20), pp. 7679–7692.

81. Bian, M. Z., and Shin, K. S., 2013, "{10-12} twinning behavior in magnesium single crystal," Metals and Materials International, Vol. 19(5), pp. 999–1004.

82. Yoshinaga, H., and Horiuchi, R., 1962, "Work hardening characteristics of the basal slip of magnesium single crystals," Transactions of the Japan Institute of Metals, Vol. 3(4), pp. 220–226.

83. Hirsch, P. B., and Lally, J. S., 1965, "The deformation of magnesium single crystals," Philosophical Magazine, Vol. 12(117), pp. 595–648.

84. Basinski, Z. S., 1960, "The influence of temperature and strain rate on the flow stress of magnesium single crystals," Australian Journal of Physics, Vol. 13, pp. 284.

85. Akhtar, A., and Teghtsoonian, E., 1969, "Solid solution strengthening of magnesium single crystals--I alloying behaviour in basal slip," Acta Metallurgica, Vol. 17(11), pp. 1339–1349.

86. Buchanan, E. R., and Reed-Hill, R. E., 1969, "The stress-strain behavior of magnesium single crystals deformed by rotational slip," Trans. Metall. Soc. AIME, Vol. 245, pp. 1929–1935.

87. Lavrentev, F., and Pokhil, Y., 1975, "Relation of dislocation density in different slip systems to work hardening parameters for magnesium crystals," Materials Science and Engineering, Vol. 18(2), pp. 261–270.

88. Yoshinaga, H., and Horiuchi, R., 1964, "On the nonbasal slip in magnesium crystals," Transactions of the Japan Institute of Metals, Vol. 5(1), pp. 14–21.

89. Reed-Hill, R. E., and Robertson, W. D., 1958, "Pyramidal slip in magnesium," Trans. Metall. Soc. AIME, pp. 256–259.

90. Kitahara, T., Ando, S., Tsushida, M., Kitahara, H., and Tonda, H., 2007, "Deformation behavior of magnesium single crystals in c-axis compression," Key Engineering Materials, Vol. 345-346, pp. 129–132.

91. Ando, S., Tsushida, M., and Kitahara, H., 2010, "Deformation behavior of magnesium single crystal in c-axis compression and a-axis tension," Materials Science Forum, Vol. 654-656, pp. 699–702.

92. Byer, C. M., Li, B., Cao, B., and Ramesh, K. T., 2010, "Microcompression of single-crystal magnesium," Scripta Materialia, Vol. 62(8), pp. 536–539.

93. Kutsukake, A., Ando, S., Tsushida, M., Kitahara, H., and Tonda, H., 2007, "Influence of impurities to deformation behavior in magnesium single crystal," Key Engineering Materials, Vol. 345-346, pp. 137–140.

94. Ando, S., and Tonda, H., 2000, "Non-basal slips in magnesium and magnesium-lithium alloy single crystals," Materials Science Forum, Vol. 350-351, pp. 43–48.

95. Stevenson, R., and Sande, J. B. V., 1974, "The cyclic deformation of magnesium single crystals," Acta Metallurgica, Vol. 22(9), pp. 1079–1086.

96. Kwadjo, R., and Brown, L. M., 1978, "Cyclic hardening of magnesium single crystals," Acta Metallurgica, Vol. 26(7), pp. 1117–1132.

97. Armstrong, R. W., and Horne, G. T., 1963, "Fatigue behaviour in shear of oriented magnesium single crystals," Journal of the institute of metals, Vol. 91, pp. 311–315.

98. Partridge, P. G., 1965, "Irregular twin growth and contraction in hexagonal close packed metals," Acta Metallurgica, Vol. 13(12), pp. 1329–1335

99. Partridge, P. G., 1969, "Effect of cyclic stresses on the microstructures of hexagonal close packed metals," Czechoslovak Journal of Physics, Vol. 19(3), pp. 323–332.

100. Partridge, P. G., 1965, "Slip band extrusion in fatigued close packed hexagonal metals," Acta Metallurgica, Vol. 13(5), pp. 517–525.

101. Partridge, P. G., 1965, "Cyclic twinning in fatigued close-packed hexagonal metals," Philosophical Magazine, Vol. 12(119), pp. 1043–1054.

102. Iida, N., Ando, S., Tsushida, M., Kitahara, H., and Tonda, H., 2007, "Crack orientation dependence for fatigue behavior of magnesium single crystals," Key Engineering Materials, Vol. 345-346, pp. 307–310.

103. Ando, S., and Tonda, H., 2003, "Fatigue crack propagation in magnesium single crystals," Materials Science Forum, Vol. 419-422, pp. 1031–1036.

104. Ando, S., Iwamoto, N., Hori, T., and Tonda, H., 2001, "Fatigue crack propagation in magnesium crystals," Journal of the Japan Institute of Metals, Vol. 65(3), pp. 187–190.

105. Ando, S., Ikejiri, Y., Iida, N., Tsushida, M., and Tonda, H., 2006, "Orientation dependence of fatigue crack propagation in magnesium single crystals," Journal of the Japan Institute of Metals, Vol. 70(8), pp. 634–637.

106. Ando, S., Saruwatari, K., Hori, T., and Tonda, H., 2003, "Fatigue crack propagation behavior in magnesium single crystals," Journal of the Japan Institute of Metals, Vol. 67(5), pp. 247–251.

107. Gehrmann, R., Frommert, M. M., and Gottstein, G., 2005, "Texture effects on plastic deformation of magnesium," Materials Science and Engineering: A, Vol. 395(1-2), pp. 338–349.

108. Wang, Y. N., and Huang, J. C., 2003, "Texture analysis in hexagonal materials," Materials Chemistry and Physics, Vol. 81(1), pp. 11–26.

109. Zenner, H., and Renner, F., 2002, "Cyclic material behaviour of magnesium die castings and extrusions," International Journal of Fatigue, Vol. 24(12), pp. 1255–1260.

110. Hasegawa, S., Tsuchida, Y., Yano, H., And Matsui, M., 2007, "Evaluation of low cycle fatigue life in AZ31 magnesium alloy," International Journal of Fatigue, Vol. 29(9-11), pp. 1839–1845.

111. Yin, S. M., Yang, H. J., Li, S. X., Wu, S. D., and Yang, F., 2008, "Cyclic deformation behavior of as-extruded Mg–3%Al–1%Zn," Scripta Materialia, Vol. 58(9), pp. 751–754.

112. Matsuzuki, M., and Horibe, S., 2009, "Analysis of fatigue damage process in magnesium alloy AZ31," Materials Science and Engineering: A, Vol. 504(1-2), pp. 169–174.

113. Begum, S., Chen, D., Xu, S., And Luo, A., 2009, "Low cycle fatigue properties of an extruded AZ31 magnesium alloy," International Journal of Fatigue, Vol. 31(4), pp. 726–735.

114. Begum, S., Chen, D. L., Xu, S., and Luo, A. A., 2009, "Effect of strain ratio and strain rate on low cycle fatigue behavior of AZ31 wrought magnesium alloy," Materials Science and Engineering: A, Vol. 517(1-2), pp. 334–343.

115. Huppmann, M., Lentz, M., Brömmelhoff, K., and Reimers, W., 2010, "Fatigue properties of the hot extruded magnesium alloy AZ31," Materials Science and Engineering: A, Vol. 527(21-22), pp. 5514–5521.

116. Lv, F., Yang, F., Duan, Q. Q., Luo, T. J., Yang, Y. S., Li, S. X., and Zhang, Z. F., 2009, "Tensile and low-cycle fatigue properties of Mg–2.8% Al–1.1% Zn–0.4% Mn alloy along the transverse and rolling directions," Scripta Materialia, Vol. 61(9), pp. 887–890.

117. Park, S. H., Hong, S.-G., Bang, W., and Lee, C. S., 2010, "Effect of anisotropy on the low-cycle fatigue behavior of rolled AZ31 magnesium alloy," Materials Science and Engineering: A, Vol. 527(3), pp. 417–423.

118. Park, S. H., Hong, S.-G., Lee, B. H., Bang, W., and Lee, C. S., 2010, "Low-cycle fatigue characteristics of rolled Mg–3Al–1Zn alloy," International Journal of Fatigue, Vol. 32(11), pp. 1835–1842.

119. Lv, F., Yang, F., Duan, Q. Q., Yang, Y. S., Wu, S. D., Li, S. X., and Zhang, Z. F., 2011, "Fatigue properties of rolled magnesium alloy (AZ31) sheet: Influence of specimen orientation," International Journal of Fatigue, Vol. 33(5), pp. 672–682

120. Lin, X. Z., and Chen, D. L., 2008, "Strain controlled cyclic deformation behavior of an extruded magnesium alloy," Materials Science and Engineering: A, Vol. 496(1–2), pp. 106–113.

121. Lou, X., Li, M., Boger, R., Agnew, S., And Wagoner, R., 2007, "Hardening evolution of AZ31B Mg sheet," International Journal of Plasticity, Vol. 23(1), pp. 44–86.

122. Li, Q., Yu, Q., Zhang, J., and Jiang, Y., 2010, "Effect of strain amplitude on tension–compression fatigue behavior of extruded Mg6Al1ZnA magnesium alloy," Scripta Materialia, Vol. 62(10), pp. 778–781.

123. Li, Q., Yu, Q., Zhang, J., and Jiang, Y., 2011, "Microstructure and deformation mechanism of Mg6Al1ZnA alloy experienced tension–compression cyclic loading," Scripta Materialia, Vol. 64(3), pp. 233–236.

124. Zhang, J., Yu, Q., Jiang, Y., and Li, Q., 2011, "An experimental study of cyclic deformation of extruded AZ61A magnesium alloy," International Journal of Plasticity, Vol. 27(5), pp. 768–787.

125. Yu, Q., Zhang, J., Jiang, Y., and Li, Q., 2011, "Multiaxial fatigue of extruded AZ61A magnesium alloy," International Journal of Fatigue, Vol. 33(3), pp. 437–447

126. Begum, S., Chen, D. L., Xu, S., and Luo, A. A., 2008, "Strain-controlled low-cycle fatigue properties of a newly developed extruded magnesium alloy," Metallurgical and Materials Transactions A, Vol. 39(12), pp. 3014–3026.

127. Fan, C. L., Chen, D. L., and Luo, A. A., 2009, "Dependence of the distribution of deformation twins on strain amplitudes in an extruded magnesium alloy after cyclic deformation," Materials Science and Engineering: A, Vol. 519(1-2), pp. 38–45.

128. Luo, T. J., Yang, Y. S., Tong, W. H., Duan, Q. Q., and Dong, X. G., 2010, "Fatigue deformation characteristic of as-extruded AM30 magnesium alloy," Materials and Design, Vol. 31(3), pp. 1617–1621

129. Chen, L., Wang, C., Wu, W., Liu, Z., Stoica, G. M., Wu, L., and Liaw, P. K., 2007, "Low-cycle fatigue behavior of an as-extruded am50 magnesium alloy," Metallurgical and Materials Transactions A, Vol. 38(13), pp. 2235–2241.

130. Yu, Q., Zhang, J., Jiang, Y., and Li, Q., 2012, "An experimental study on cyclic deformation and fatigue of extruded ZK60 magnesium alloy," International Journal of Fatigue, Vol. 36(1), pp. 47–58.

131. Xiong, Y., Yu, Q., and Jiang, Y., 2014, "An experimental study of cyclic plastic deformation of extruded ZK60 magnesium alloy under uniaxial loading at room temperature," International Journal of Plasticity, Vol. 53(0), pp. 107–124.

132. Wu, L., Agnew, S. R., Ren, Y., Brown, D. W., Clausen, B., Stoica, G. M., Wenk, H. R., and Liaw, P. K., 2010, "The effects of texture and extension twinning on the low-cycle fatigue behavior of a rolled magnesium alloy, AZ31B," Materials Science and Engineering: A, Vol. 527(26), pp. 7057–7067.

133. Bauschinger, J., 1886, "On the change of the position of the elastic limit of iron and steel under cyclic variations of stress," Mitt. Mech. Tech. Lab, Vol. 13, pp. 1.

134. Lee, S. Y., and Gharghouri, M. A., 2013, "Pseudoelastic behavior of magnesium alloy during twinning-dominated cyclic deformation," Materials Science and Engineering: A, Vol. 572, pp. 98–102.

135. Cáceres, C. H., Sumitomo, T., and Veidt, M., 2003, "Pseudoelastic behaviour of cast magnesium AZ91 alloy under cyclic loading–unloading," Acta Materialia, Vol. 51(20), pp. 6211–6218.

136. Muránsky, O., Carr, D. G., Šittner, P., and Oliver, E. C., 2009, "In situ neutron diffraction investigation of deformation twinning and pseudoelastic-like behaviour of extruded AZ31 magnesium alloy," International Journal of Plasticity, Vol. 25(6), pp. 1107–1127.

137. Muránsky, O., Carr, D. G., Šittner, P., Oliver, E. C., and Dobroň, P., 2008, "In situ neutron diffraction studies of the pseudoelastic-like behaviour of hydrostatically extruded Mg-Al-Zn alloy," Materials Science Forum, Vol. 571-572, pp. 107–112.

138. Mann, G. E., Sumitomo, T., Cáceres, C. H., and Griffiths, J. R., 2007, "Reversible plastic strain during cyclic loading–unloading of Mg and Mg–Zn alloys," Materials Science and Engineering: A, Vol. 456(1-2), pp. 138–146.

139. Brown, D. W., Agnew, S. R., Bourke, M. A. M., Holden, T. M., Vogel, S. C., and Tomé, C. N., 2005, "Internal strain and texture evolution during deformation twinning in magnesium," Materials Science and Engineering: A, Vol. 399(1-2), pp. 1–12.

140. Wu, L., 2009, Mechanical Behavior and the Role of Deformation Twinning in Wrought Magnesium Alloys Investigated Using Neutron and Synchrotron X-ray Diffraction. The University of Tennessee, Knoxville.

141. Chou, J.-T., Shimauchi, H., Ikeda, K., Yoshida, F., and Nakashima, H., 2005, "Preparation of samples using a chemical etching for SEM/EBSP method in a pure magnesium polycrystal and analysis of its twin boundaries," Journal of Japan Institute of Light Metals, Vol. 55(3), pp. 131–136.

142. Blewitt, T. H., Coltman, R. R., and Redman, J. K., 1957, "Low-temperature deformation of copper single crystals," Journal of Applied Physics, Vol. 28(6), pp. 651–660.

143. Hirose, M., 1972, "The strain distributions within and around deformation twin bands of iron single crystals," Japanese Journal of Applied Physics, Vol. 11(3), pp. 309–318.

144. Overcash, D. R., Stillwell, E. P., Skove, M. J., and Davis, J. H., 1972, "Deformation twinning in Zn, Sn and Bi single crystal whiskers," Philosophical Magazine, Vol. 25(6), pp. 1481–1488.

145. Brunton, J. H., and Wilson, M. P. W., 1969, "The kinetics of twinning in zinc and tin crystals," Proceedings of the Royal Society A: Mathematical, Physical and Engineering Sciences, Vol. 309(1498), pp. 345–361.

146. Clausen, B., Tomé, C. N., Brown, D. W., and Agnew, S. R., 2008, "Reorientation and stress relaxation due to twinning: Modeling and experimental characterization for Mg," Acta Materialia, Vol. 56(11), pp. 2456–2468.

147. Ma, B.-T., and Laird, C., 1989, "Overview of fatigue behavior in copper single crystals—I. Surface morphology and stage I crack initiation sites for tests at constant strain amplitude," Acta Metallurgica, Vol. 37(2), pp. 325–336.

148. Serra, A., and Bacon, D. J., 1996, "A new model for {10-12} twin growth in hcp metals," Philosophical Magazine A, Vol. 73(2), pp. 333–343.

149. Wang, J., Beyerlein, I. J., Hirth, J. P., and Tomé, C. N., 2011, "Twinning dislocations on {1$\bar{1}$011} and {1$\bar{1}$013} planes in hexagonal close-packed crystals," Acta Materialia, Vol. 59(10), pp. 3990–4001.

150. Wang, J., Beyerlein, I. J., and Hirth, J. P., 2012, "Nucleation of elementary {-1 0 1 1} and {-1 0 1 3} twinning dislocations at a twin boundary in hexagonal close-packed crystals," Modelling and Simulation in Materials Science and Engineering, Vol. 20(2), pp. 024001.

151. Hirth, J. P., and Lothe, J., 1992, Theory of Dislocations. Krieger.

152. Wang, J., and Huang, H., 2006, "Novel deformation mechanism of twinned nanowires," Applied Physics Letters, Vol. 88(20), pp. 203112.

153. Wang, J., Beyerlein, I. J., Mara, N. A., and Bhattacharyya, D., 2011, "Interface-facilitated deformation twinning in copper within submicron Ag–Cu multilayered composites," Scripta Materialia, Vol. 64(12), pp. 1083–1086.

154. Hirth, J. P., Pond, R. C., Hoagland, R. G., Liu, X.-Y., and Wang, J., 2013, "Interface defects, reference spaces and the Frank–Bilby equation," Progress in Materials Science, Vol. 58(5), pp. 749–823.

155. Wang, J., Hirth, J. P., Pond, R. C., and Howe, J. M., 2011, "Rotational partitioning at two-phase interfaces," Acta Materialia, Vol. 59(1), pp. 241–251.

156. Kang, K., Wang, J., and Beyerlein, I. J., 2012, "Atomic structure variations of mechanically stable fcc-bcc interfaces," Journal of Applied Physics, Vol. 111(5), pp. 053531.

157. Bilby, B. A., Bullough, R., and Smith, E., 1955, "Continuous distributions of dislocations: a new application of the methods of non-Riemannian geometry," Proceedings of the Royal Society A: Mathematical, Physical and Engineering Sciences, Vol. 231(1185), pp. 263–273.

158. Frank, F. C., 1953, "Martensite," Acta Metallurgica, Vol. 1(1), pp. 15–21.

159. Wang, J., Hirth, J. P., Pond, R. C., and Howe, J. M., 2011, "Rotational partitioning at two-phase interfaces," Acta Materialia, Vol. 59(1), pp. 241–251.

160. Yu, Q., Wang, J., Jiang, Y., McCabe, R. J., and Tomé, C. N., 2014, "Co-zone $\{1\bar{0}12\}$ twin interaction in magnesium single crystal," Materials Research Letters, Vol. 2(2), pp. 82–88.

161. Wang, J., and Beyerlein, I. J., 2012, "Atomic structures of symmetric tilt grain boundaries in hexagonal close packed (hcp) crystals," Modelling and Simulation in Materials Science and Engineering, Vol. 20(2), pp. 024002.

162. Wang, J., and Beyerlein, I. J., 2012, "Atomic Structures of [0 -1 1 0] Symmetric Tilt Grain Boundaries in Hexagonal Close-Packed (hcp) Crystals," Metallurgical and Materials Transactions A, Vol. 43(10), pp. 3556–3569.

163. Wang, J., Hirth, J. P., and Tomé, C. N., 2009, "(1¯012) Twinning nucleation mechanisms in hexagonal-close-packed crystals," Acta Materialia, Vol. 57(18), pp. 5521–5530.

164. Engler, O., and Randle, V., 2009, Introduction to Texture Analysis: Macrotexture, Microtexture, and Orientation Mapping. CRC Press.

165. Agnew, S. R., and Duygulu, Ö., 2005, "Plastic anisotropy and the role of non-basal slip in magnesium alloy AZ31B," International Journal of Plasticity, Vol. 21(6), pp. 1161–1193.

166. Agnew, S., Brown, D., And Tome, C., 2006, "Validating a polycrystal model for the elastoplastic response of magnesium alloy AZ31 using in situ neutron diffraction," Acta Materialia, Vol. 54(18), pp. 4841–4852.

167. Koike, J., Kobayashi, T., Mukai, T., Watanabe, H., Suzuki, M., Maruyama, K., and Higashi, K., 2003, "The activity of non-basal slip systems and dynamic recovery at room temperature in fine-grained AZ31B magnesium alloys," Acta Materialia, Vol. 51(7), pp. 2055–2065.

168. Koike, J., 2005, "Enhanced deformation mechanisms by anisotropic plasticity in polycrystalline Mg alloys at room temperature," Metallurgical and Materials Transactions A, Vol. 36(7), pp. 1689–1696.

169. McG. Tegart, W. J., 1964, "Independent slip systems and ductility of hexagonal polycrystals," Philosophical Magazine, Vol. 9(98), pp. 339–341.

170. Hutchinson, W. B., and Barnett, M. R., 2010, "Effective values of critical resolved shear stress for slip in polycrystalline magnesium and other hcp metals," Scripta Materialia, Vol. 63(7), pp. 737–740.

171. Chino, Y., Kimura, K., And Mabuchi, M., 2008, "Twinning behavior and deformation mechanisms of extruded AZ31 Mg alloy," Materials Science and Engineering: A, Vol. 486(1-2), pp. 481–488.

172. Choi, S.-H., Kim, D. H., Park, S. S., and You, B. S., 2010, "Simulation of stress concentration in Mg alloys using the crystal plasticity finite element method," Acta Materialia, Vol. 58(1), pp. 320–329.

173. Beyerlein, I. J., and Tome, C. N., 2010, "A probabilistic twin nucleation model for HCP polycrystalline metals," Proceedings of the Royal Society A: Mathematical, Physical and Engineering Sciences, Vol. 466(2121), pp. 2517–2544.

174. Wang, J., Beyerlein, I. J., and Tomé, C. N., 2010, "An atomic and probabilistic perspective on twin nucleation in Mg," Scripta Materialia, Vol. 63(7), pp. 741–746.

175. Beyerlein, I. J., Capolungo, L., Marshall, P. E., McCabe, R. J., and Tomé, C. N., 2010, "Statistical analyses of deformation twinning in magnesium," Philosophical Magazine, Vol. 90(16), pp. 2161–2190.

176. Beyerlein, I. J., and Tome, C. N., 2010, "A probabilistic twin nucleation model for HCP polycrystalline metals," Proceedings of the Royal Society A: Mathematical, Physical and Engineering Sciences, Vol. 466(2121), pp. 2517–2544.

177. Beyerlein, I. J., McCabe, R. J., and Tomé, C. N., 2011, "Effect of microstructure on the nucleation of deformation twins in polycrystalline high-purity magnesium: A multi-scale modeling study," Journal of the Mechanics and Physics of Solids, Vol. 59(5), pp. 988–1003.

178. Wang, J., Hoagland, R. G., Hirth, J. P., Capolungo, L., Beyerlein, I. J., and Tomé, C. N., 2009, "Nucleation of a $(1\bar{0}12)$ twin in hexagonal close-packed crystals," Scripta Materialia, Vol. 61(9), pp. 903–906.

179. Wang, J., Beyerlein, I. J., and Tomé, C. N., "Reactions of lattice dislocations with grain boundaries in Mg: Implications on the micro scale from atomic-scale calculations," International Journal of Plasticity, Vol. 56, pp. 156-172.

180. Wang, J., Yu, Q., Jiang, Y., and Beyerlein, I. J., 2013, "Twinning-Associated Boundaries in Hexagonal Close-Packed Metals," JOM, Vol. 66(1), pp. 95-101.

181. Otte, H. M., and Crocker, A. G., 1965, "Crystallographic Formulae for Hexagonal Lattices," physica status solidi (b), Vol. 9(2), pp. 441–450.

182. Niewczas, M., 2010, "Lattice correspondence during twinning in hexagonal close-packed crystals," Acta Materialia, Vol. 58(17), pp. 5848–5857.

183. Hall, E.O., 1970, "Yield point phenomena in metals and alloys," Plenum Press, New York.

184. Jiang, Y., 2001, "An experimental study of inhomogeneous cyclic plastic deformation," ASME Journal of Engineering Materials and Technology, Vol. 123, pp. 274-280.

185. Chatelier, F. Le, 1909, Rev. de Métal Vol. 6, pp. 914-917.

186. Portevin, A. and Chatelier, F. Le, 1923, C.R. Acad. Sci. Vol. 176, pp. 507.

187. Yilmaz, A., 2011, "The Portevin–Le Chatelier effect: a review of experimental findings," Science and Technology of Advanced Materials, Vol. 12, pp. 063001.

188. Yu, Q., Zhang, J., and Jiang, Y., 2011, "Fatigue damage development in pure polycrystalline magnesium under cyclic tension–compression loading," Materials Science and Engineering: A, Vol. 528, pp. 7816–7826.

189. Yu, Q., Wang, J., Jiang, Y., McCabe, R.J., Li, N., and Tomé, C.N., 2014, "Twin–twin interactions in magnesium," Acta Materialia, Vol. 77, pp. 28–42.